A STUDY ON END FORMING OF METALLIC TUBES

A Thesis Submitted in Partial Fulfillment of the Requirements

for the Degree of

DOCTOR OF PHILOSOPHY

by

ARVIND KUMAR AGRAWAL

(Roll No.: 136103008)

Department of Mechanical Engineering

Indian Institute of Technology Guwahati

Guwahati – 781039

September 2019

Department of Mechanical Engineering

Indian Institute of Technology Guwahati

Guwahati-781039 INDIA

CERTIFICATE

It is certified that the work contained in the thesis entitled **"A STUDY ON END FORMING OF METALLIC TUBES"** submitted by Mr. Arvind Kumar Agrawal to the Indian Institute of Technology Guwahati for the award of the degree of the Doctor of Philosophy has been carried out under my supervision in the Department of Mechanical Engineering, Indian Institute of Technology Guwahati. This work has not been submitted elsewhere for the award of any other degree or diploma.

(Dr. R Ganesh Narayanan)

Associate Professor

Department of Mechanical Engineering

Indian Institute of Technology Guwahati

Guwahati-781039

INDIA

Dedicated to

My Family,

My Teachers,

and

My Nation

Acknowledgement

First of all, I am deeply grateful to my supervisor, Dr. R. Ganesh Narayanan for his guidance and constant encouragement throughout my PhD work. There were tough moments during my PhD work, but finally i could get rid of those moments and now in a position to write this thesis. The credit goes a lot to him. His innovative ideas and the amount of confidence he put in me reflects in this thesis.

I would like to pay my special thanks to my doctoral committee chairman Prof. U. S. Dixit. His suggestions helped a lot in improving the quality of the work. Other members Dr. Sachin D. Kore, Dr. Swarup Bag and Dr. A. Murali Krishna (Civil department) are also architect of my PhD Work. Their valuable suggestions helped me a lot not only from technical aspects but also in improving presentation and writing skills.

I would like to thank Dr. Arun C. Borsaikia to allow me to do tube joining experiments in Civil department lab (IIT Guwahati). In those experiments Mr. Pranab Hazarika and Mr. Saurabh Mudoi helped me. I will also like to thank Mr. Sidananda Sarma (Technical staff in Physics department) to help me in XRD analysis of my samples.

I am extremely grateful to Dr. Satish V. Kailas, IISc Bengaluru. I spent two productive months in SIAM (Surface Interaction and Manufacturing) Lab, IISc Bengaluru. Processing of all aluminium tubes has been conducted in this lab. Within a short time I could understand the research culture. My special thanks goes to Madhu, Ganesh, Rajneesh, Himanshu, Amlan, Swami Babu, Suresh and others who helped me to accomplish such a lengthy work in a short duration.

I am thankful to staffs of MSME TOOL ROOM, Amingaon (Guwahati) for fabricating a complex set-up for mechanical joining. My special thanks to Mr. Sanjeev and Mr. Rajasarkar who held the responsibility of making my experimental set-up.

I thank IIT Guwahati administration to provide all facilities to complete my PhD work. I would like to mention technical staffs and other staffs of Mechanical department, without their help this work could not have been completed. They helped me in academic related work and in other experiments such as tensile testing, microstructure analysis and laser cutting of samples. In this context, I would like to extend my thanks to Mr.

Saiffuddin Ahmed, Mr. Jiten Basumatary, Mr. Nip Borah, Mr. Nabajyoti Dutta, Mr. Sanjib Sarma and Mr. Raju Talukdar. I fabricated many tools in the institute workshop for my PhD work. Sometimes it was really difficult to manufacture job as per drawing. But finally skill of Mechanical workshop staffs proved useful in fabricating my experimental tools and in many other small works related to my work. I would like to pay my thanks to Mr. N. K. Das (Workshop superintendent), Mr. Manoj K. Baishya, Mr. Chandan Banikya, Mr. Dilip Chetri, Mr. Bijoy K. Choudhury, Mr. Dulumoni Das, Mr. Amjad, Mr. Gakul Das, Mr. Dipak K. Deka, Mr. Lakhinath Gogoi, Mr. Gautam Gogoi, Mr. Upen Gohain, Mr. Dhaneswar Khaklary, Mr. Minesh C. Medhi, Mr. Ratan Medhi, Mr. Ganesh Nath, Mr. Joykrishna Saikia, Mr. Nidul Saikia and Mr. Mrinal Sarma.

Last but not the least, the patience and forbearance of my wife, my parents, my brothers and sister need special attention. In difficult times, their continued moral support and blessings, allowed me to concentrate on my work for long hours.

The company of my friends at IIT Guwahati make my five and half years of stay enjoyable. I would like to thank my senior Dr. Satheeshkumar V and my juniors Mr. Pritam, Mr. Tinu, Mr. Saibal, Mr. Priyabrata, Mr. Sukanta, Mr. Nitish, Mr. Girish, Mr. Yogendra, Mr. Premananda, Mr. Arun Krishnan and Mr. Vishnu Ganesh from my lab. Throughout my PhD work they helped me in various ways. Apart from that I would like to convey my special thanks to Dr. Asish, Mr. Manish, Mr. Amit, Mr. Soumya, Mr. Rashmi Ranjan, Mr. Getu, Mr. Sundarlal, Mr. Debabrata Gayen, Mr. Dipendra, Dr. Ramesh Kumar, Dr. Chandan Kumar, Mr. Anupam Alok, Mr. Pankaj, Mr. Devarshi, Mr. Sunil, Mr. Kishor, Mr. Vignesh. Each of them deserves special thanks.

Arvind Kumar Agrawal

Abstract

End forming of tubes generally refer to making of simple or complex shapes such as expansions, reductions, flares, flanges, tapers, and beads made at the end of the tube by single or multiple metal forming operations. These end formed tubes have plenty of applications in our day-to-day life, agriculture and automobile sectors. End formed tubes are carrier of fluids such as oil, refrigerant and water for agriculture etc. They also act as interconnection between individual tubular parts. Tube flange joints are widely used in pipeline and petrochemical industry. Tube inversion operations are used in manufacture of double-walled tubes for heat exchangers, driving elements and other components. In the last decade increasingly interest in the safety and crashworthiness of vehicles has resulted in extensive researches on the structural response of thin-walled metallic tubes, which are conventionally most effective energy-absorbing devices.

Earlier research (in 60's) in the field of tube end forming was focused on identification of main process parameters, especially tube inversion methods. Later on and here after finite element (FE) simulations based prediction of forming load and formability played an important role in the field of tube end forming. In the last two decades some newer products have been manufactured using tube end forming as well as newer materials have been tried to end form. With the further advancement of tube end forming technology some innovative methods of joining involving tube end forming have been proposed and it was observed that joint strength of end formed joints is at par with the joints obtained from conventional methods. Joining using plastic deformation (tube end forming) is an environmental friendly process. No harmful gases are ejected during the process.

Tubes are manufactured mainly from two ways. First is extrusion from metal billet and second from welding. Though there is always a debate over the strength of welded tubes and seamless tubes, welded tubes have other advantages. Welding of tubes are possible in larger diameters and thinner walls. It has been mentioned that welding of tubes with diameter lying in the range of 0.006-2.5 m and in the thickness range of 0.5 to 40 mm can be accomplished (Hashmi et al., 2006). Tailor made tubes for industry use are also feasible. It has been observed that friction stir welding (FSW), invented in 1991 in TWI (UK) became popular for welding of low melting point alloys such as aluminium and magnesium in a short duration and substituted fusion and arc welding processes

where the workpiece material is melted. In FSW the material is not melted but recast. After, some duration friction stir processing (FSP) based on basic principles of FSW has been developed, which basic aim is to modify microstructures and properties in the processed region of a single workpiece rather than joining two metal pieces together.

In this context, joining using tube end forming and end forming of joint (FSPed) tubes are conducted in the present thesis work. In the first part, tube end forming behaviour has been studied through mechanical joining operations. Novel method of joining of a tube to a sheet and a tube to a tube has been proposed. The tube and sheet material used are 'steel'. The joining method has been proposed through CAE analyses. To propose such joining method experimentally is both costly and time consuming. Hence with the help of finite element (FE) software, methods have been proposed. The FE simulation software used is ABAQUS explicit (version 6.7-6/6.17). Important parameters influencing the joint quality have been identified. Die groove radius and friction conditions are found to affect the joint quality significantly in case of tube-sheet joint, while circular arc radius and projected section of punch height affect the joint quality significantly in case of tube-tube joint. A number of criteria have been proposed to decide the quality (successful or unsuccessful) of the joint. These criteria are simple and specific to the proposed technologies. Using these criteria quality of the joint on shop floor can be decided without any complex measurements and calculations. Later, the proposed joining methods have been experimentally demonstrated through some selected cases. In case of tube-sheet joint the load evolution obtained by experiment and prediction showed some difference. It is felt that failure criteria need to be incorporated in the numerical model to improve the accuracy of predicted result. However, in case of tube-tube joint a good comparison between experiments and prediction is observed. Incorporation of anisotropic yield function in the model improved the accuracy of the result. The joining strategy for joining of longer tubes has been proposed and is successfully demonstrated through FE simulation. The results show that after implementing some minor modification in the proposed technology for joining of shorter tubes, longer tubes can also be joint.

Further, mechanical testing of end formed joints (tube-sheet and tube-tube) has been conducted. Strength of end formed tube-sheet joints has been compared with gas welded tube-sheet joint. The effect of inclination on joint strength has been observed. For that purpose, dies with different inclinations have been fabricated. Unlocking in the end

formed tube-sheet joint region has been observed during pull-out test, while physical failure is seen in the tube-sheet joint region in welded tube-sheet joint. End formed joints performed better on flat die, while welded joints performed better on inclined dies. 3D FE models simulating the pull-out tests at different die inclinations of end formed joints have been proposed. A significant difference in load displacement data has been observed between experimental and predicted results. Hence it is concluded that such models for strength evaluation need to be applied cautiously and need to be improved further. The strength evaluation of end formed tube-tube joint has been done through both pull-out test and compression test. Strength of end formed tube-tube joint has been compared with arc welded tube-tube joint. In pull-out test, strength of end formed tube-tube joint performed better than arc welded tube-tube joint, while in case of compression test, strength of both (end formed joints and welded joints) joints compared well.

The proposed methods for joining using tube end forming are simple and aimed at sustainable manufacturing. They are capable of producing joints with similar or larger strength as compared to that obtained from conventional methods. The proposed methods certainly remove some of the drawbacks of conventional joining technologies such as welding, joining by adhesive bonding and joining through fasteners. However, the proposed joining methods have certain limitations too. For example, for any change in material dimensions, the CAE analysis needs to be done each time. Further after joint formation, for easy disassembly of the joint from the experimental set-up, the die and punches need to be fabricated in split section.

The second part of the thesis is aimed at end forming operations of friction stir processed (FSPed) AA 6063-T6 tubes at different process parameters. It is believed that properties of the FSPed zone will change according to process parameters and their levels and the changed properties will also affect end forming behaviour of processed tubes. Few cases may yield better properties as compared to raw tube and can substitute raw tubes in its applications. Further, single line-single pass processing route has been used in the present work. Different combinations of processing routes like, single line-multi pass, multi line-single pass, multi line-multi pass, and whole surface processing can also be tried. The effect of FSP through these processing routes can be studied and at optimized processing conditions performance of FSPed tube can be enhanced in end forming operations.

Though many parameters influence friction stir welding or processing, the effect of tool rotational speed, tool traverse speed, tool pin profile and tool plunge depth has been studied in the present work during processing and end forming operations. The end forming operations conducted are expansion, reduction and beading. The effect has been seen in terms of, load evolution of processed and unprocessed tubes, thickness evolution in processed and unprocessed zones (processed tubes) and in unprocessed tubes, hardness variation along the processed zone before forming and after forming, and energy absorbed in processed and unprocessed tubes during end forming operations at different process parameters and their levels. Grain size measurement and dislocation density measurement into different zones of processed region have been done. At last, end forming simulations have been conducted with an aim of minimizing the experimental efforts. In this context, load evolution and instability prediction for processed as well as unprocessed tubes have been accomplished during different end forming operations.

From the present investigation it has been observed that formability of the FSPed zone improves after FSP in many cases, while flow strength decreases for different cases with respect to base metal. Hardness decreases in the FSPed zone after FSP. Heat experienced in the FS process is responsible for this. Hardness improves after end forming in FSPed zone. Strain hardening during end forming is responsible for this. For different process parameters and their levels it has been observed that strain hardening is larger in reduction as compared to expansion and beading except few cases. Further, it has been observed that grain size vary significantly in the processed region. Based on grain size, the processes region can be divided into three parts. A relatively smaller grain size is observed in the middle of the processed region known as stirred zone (SZ), a larger elongated grains have been observed in the area adjacent to stirred zone, known as theromomechanically affected zone (TMAZ). The region adjacent to the base metal region is known as heat affected zone (HAZ) and the grain size in this region is almost same as that of base metal. The amount of heat flux and plastic deformation experienced in these zones are different and also affect the grain size. However, it has been seen that there is no direct correlation between hardness and grain sizes into different zones after FSP. It indicates that microstructural behaviour does not affect the hardness of the FSPed zone. Later, it has been observed that SZ shows lower dislocation density as compared to other zones for most of the cases. TMAZ shows larger dislocation density among zones for most of the cases. In HAZ region dislocation density observed is comparable with that

of base metal. Similar results have been shown by Woo et al. (2008) for FSWed 6061-T6 alloy. For different parameters except few cases, FSPed zone having lower dislocation density results in larger *n* as well as ductility.

From end forming experiments of processed and unprocessed tubes, it has been concluded that the parent tube needs larger load to deform as compared to processed tubes during different end forming operations and process parameters. A larger strength of base metal as compared to FSPed zone is responsible for this. Within FSPed tubes made at different levels at different process parameters, maximum load obtained during load evolution depends mainly on strength of the FSPed zone except few cases such as during expansion and beading in case of rotational speed, and in expansion process for different plunge depths. In these cases, maximum load occurrence during load evolution depends on initial hardness and particularly on hardness index, *H*. Except for plunge depths, for other parameters displacement to failure during expansion depends on '*n*' value of different FSPed tubes. FSPed zone having larger *n* experiences larger displacement to failure. FSPed zone experiences larger thinning as compared to base metal in case of expansion and finally failure occurs at the middle of the FSPed zone. FSPed zone having larger ductility has thinned more. In reduction, FSPed zone experiences larger thickening as compared to corresponding base metal zone. Wrinkling and overlapping is observed in the FSPed zone during reduction. A softer FSPed zone as compared to base metal is responsible for these phenomena. A FSPed zone having lower flow strength has thickened more for different process parameters in reduction. In case of beading, base metal thickening is more than FSPed zone thickening in most of the cases. Relative strength of FSPed zone and base metal zone as well as respective strain hardening exponent '*n*' is responsible for this. Here fine cracks are seen at the peak bulged height of the base metal region. Larger hardness and reduced ductility of the base metal as compared to FSPed zone is responsible for this. For unprocessed tubes, in reduction, no wrinkling is observed. In beading, unprocessed tubes show larger cracks as compared to processed tubes.

Beading absorbs larger energy for raw and FSPed tubes among conducted end forming operations, while in expansion lesser energy is absorbed. Reduction lies in between the two. In expansion, parent tube absorbs larger energy as compared to FSPed tubes. Few FSPed tube cases reach closer to that of parent tube. In reduction, energy absorbed by FSPed tubes is comparable with parent tube with many FSPed tube cases

resulting in larger energy absorption capacity as compared to parent tube. In beading, energy absorbed by FSPed tubes is larger than that of the parent tubes in most of the cases. Large energy absorbed in case of FSPed tubes with lesser load requirement make the processed tubes an appropriate choice for energy absorbing devices in aircraft and shipbuilding industries in place of raw tube. However, instabilities incurred during end forming can restrict the uses of FSPed tubes.

End forming simulation is an encouraging attempt aimed at minimizing the experimental efforts. In most of the cases in expansion and reduction a closer comparison between experimental and prediction data is observed with respect to load evolution. Few cases show minor deviation especially in reduction of tubes. In beading, a significant difference is seen after bead initiation in load displacement data, when experimental and predicted results are compared. The larger load is observed in prediction. With respect to instability occurrence results obtain in reduction and beading compared well between experiments and prediction for different cases, while a difference is seen in most of the cases in end expansion. Modeling conditions, particularly strain rate and friction coefficient mismatch are responsible for such a difference. Modeling and simulation strategy needs to be improved further to minimize such a difference with respect to load evolution and instability prediction.

Abbreviations

YS	Yield Strength
UTS	Ultimate tensile strength
SZ	Stir zone
TMAZ	Thermomechanically affected zone
HAZ	Heat affected zone
BM	Base metal
wt. %	Weight %
FSW	Friction stir welding
FSP	Friction stir processing
FEA	Finite element analysis
PD	Plunge depth
FWHM	Full width at half maximum
VHN	Vickers hardness number
CAE	Computer aided engineering
AA	Aluminium alloy
OL	Overlapping
UTM	Universal testing machine
XRD	X-ray diffraction
FLD	Forming limit diagram
TCP	Tapered cylindrical pin
SCP	Straight cylindrical pin
STP	Stepped cylindrical pin

Nomenclature

σ	True stress in MPa
ε	True strain
k	Material strength coefficient in MPa
n	Strain hardening exponent
μ	Coefficient of friction
ΔF	Difference in peak load between experiments and simulations for different cases when tube-sheet joints tested under different die inclinations
r	Plastic strain ratio
r_x, r_y, r_{45}	Plastic strain ratio in 0°, 90, and 45° to the rolling direction of sheets
b	Burgers vector
B	Full width at half maximum
θ	Bragg's angle
λ	Wavelength of X-ray
C	Dislocation contrast factor
E	Energy absorbed by tubes during end forming operations
R_{11}, R_{22}, R_{33}, R_{12}, R_{13} and R_{23}	Yield factors in plane stress condition
H_i	Initial hardness of the processed zone before end forming
H_f	Final hardness of the processed zone after forming
$H(\%)$	Hardness index

Contents

List of Figures

List of Tables

Chapter 1

Introduction, Literature Review, Significance and Objective of Work

1.1 Introduction

End forming of tubes refers to making of simple or complex shapes such as expansions, reductions, flares, flanges, inversions and tapers made at the end of the tube by single or multiple metal forming operations. During 1960's research was focused on identification of main process parameters, development of theoretical models to explain the mechanics of the process and tube inversion methods. In 1990's, along with forming load evolution by experiments, forming load evolution with the help of finite element analysis was also performed. Some novel methods of tube end deformation aiming at fabrication of new products as well as new joining methodology (tube to sheet, tube to tube) have been developed. End forming of newer materials have been tried.

The main aim of the present work is to study the end forming behaviour of tubes. The whole thesis work can be divided into two sections. The first section discusses joining using end forming. Here novel methods of joining a tube to a sheet and a tube to a tube have been proposed based on finite element (FE) analyses. Steel grade material is used for demonstration. During the joining processes, the end forming operations conducted are, end curling, end inversion and end beading. Effect of important parameters influencing the joint formation has been studied. Selected cases from each joining process have been demonstrated at lab scale, and later based on critical findings important conclusions are drawn.

The second section discusses end forming of tubes after processing. In this section, end forming of friction stir processed (FSPed) AA 6063-T6 has been conducted. Tubes have been FSPed at different process parameters and at different levels. End forming operations conducted are tube expansion, tube reduction and tube beading. Generally, tubes are manufactured mainly from two ways. First is extrusion from metal billet, and the second is from welding. There is always a debate over the strength of welded tubes and seamless tubes, and welded tubes also have some advantages. Welded tubes can be manufactured in bigger diameters and thinner walls. Welding of tubes with diameter lying in the range of 0.006-2.5 m and in the thickness range of 0.5 to 40 mm can be accomplished (Hashmi et al., 2006). Tailor made tubes for industry use are also

feasible. Recently, it has been observed that friction stir welding (FSW) is more suited to welding of light-weight materials such as aluminium as compared to fusion and arc welding processes. The applications of light weight components is a central challenge in modern transportation engineering. Lightweight construction is crucial where mass is critical to enable the product function such as aeronautical applications. Depending on the actual alloy and grade, steel and aluminium are likewise 'light metals' as well as magnesium and titanium (Jeswiet et al., 2008). For welding of aluminium alloys, FSW has recently became popular due to its inherent properties such as low distortion of workpiece, no loss of alloying elements, absence of cracking and other environemental benefits over other fusion and arc welding processes (Mishra and Ma, 2005). Further, within different grades of aluminum alloys, Al alloys of 6000 series are known to have good formability, corrosion resistance, weldability and high strength-to-weight ratio (Al-Fadhalah et al., 2014) and hence 6000 series aluminium grade has been opted as investigating material in the present work.

Further, in fusion and arc welding processes, the workpiece material is melted and then solidification takes place. In the process, defects like pores, slag inclusion and cracks are developed in the workpiece material. Friction stir welding is a solid state welding process in which the material is not melted. Here the material below the workpiece is plastically deformed at a temperature below the melting point and joining takes place. Hence it is also called as solid state joining process. Friction stir welding (FSW) was invented in 1991 in TWI (UK) (Mishra and Ma, 2005). After few years, friction stir processing (FSP) has been developed, and the basic principle remains same as that of FSW (Mishra and Mahoney, 2001). Single monolithic workpiece is FSPed rather than joining two metal pieces. Initial aim of FSP was to locally modify the microstructures of the workpiece and thus to enhance its properties. Later, FSP found its utility in many other fields.

Rolled sheets are generally used to manufacture welded pipe or tube. However, instead of welding of rolled sheets to make a tube, a normal seamless tube has been processed in the present work and the effect of different process parameters on the processed zone has been studied. It is believed that the properties of FSPed zone are same as that of weld zone when a rolled sheet is welded in the form of a pipe, although the gap maintained between the two edges of the sheet affects the joining behaviour. It is believed

that FSP can modify the performance of end formed tubes, and as a result, a FSPed tube may replace raw tube in its applications. Moreover, a single line-single pass processing route has been adopted in the present work. Further, it will be interesting to see the effect of different processing routes such as, single line-multi pass, multi line-single pass, multi line-multi pass or whole surface processing, on the performance of end formed tube.

Literature review, significance of the work, objectives of the work, and tasks involved are presented in Chapter 1. A novel method of joining of a tube to a sheet has been discussed in Chapter 2. Successful experimental validation of few selected cases have been done. In addition, a detailed analysis on the strength evaluation of end formed tube-sheet joint based on experimental and numerical analysis has been presented in the same Chapter. The effect of important process parameters based on FE simulation and demonstration of few selected cases at lab scale for mechanical joining operations of two steel tubes has been discussed in Chapter 3. Chapter 4 details the effect of tool rotational speed on FSP of AA 6063-T6 tubes, and then on their end forming behaviour. In this context, load evolution, thickness evolution, hardness change along the processed zone, and energy absorption for processed as well as unprocessed tubes during end forming have been determined. Grain size and dislocation density measurement at different zones of processed region have also been conducted and validated with experimental data. FE modeling and simulation of end forming has also been conducted at last. Similarly, the effect of traverse speeds, tool pin profiles and tool plunge depths on FSP of AA 6063-T6 tubes, and then on their end forming behaviour have been shown in Chapters 5, 6 and 7 respectively. The conclusions from the thesis work and scope of further work have been summarized in Chapter 8.

1.2 Literature review

The literature review has been divided into sections. First part describes effect of important parameters in various end forming operations, joining using end forming and modeling and simulation of end forming. Second part describes effect of important parameters in FSW/FSP of sheets, plates and tubes and modeling and simulation of FSW/FSP.

1.2.1 Tube end forming

1.2.1.1 Influencing parameters in tube inversion, curling and flange formation

End formed tubes have a variety of applications in automobile, irrigation, shipbuilding and aircraft industries. They are good carriers of fluid such as liquid, oil and refrigerant etc. Hence they have been used in oil and pipeline industries. These end formed tubes are greatly used in chassis frames of automobiles, and can absorb impact kinetic energy when plastic deformation occurs under axial and lateral compression. Double-walled tubes manufactured through tube inversion methods are used in heat exchangers and driving elements. These structures are useful because of their low weight, high resistance and easy building (Rajabiehfard et al., 2018). Few research highlights in the field of tube inversion, curling and flange formation have been discussed here.

Invert-forming of tubes is a process in which tubes are subjected to axial compression and will undergo inside-out inversion or vice-versa to form a double-walled part (Rosa et al., 2003). Sekhon et al. (2003) studied the external inversion of round tubes made of aluminium. They studied the effect of die radius and friction between tube and die for the successful inversion of tube. The instability has been defined in terms of tube buckling and axial tube splitting. Rosa et al. (2004) conducted internal inversion of Al 6060 tubes. In their work local buckling was experimentally observed during the internal inversion of tubes having small ratio of radius of die and outer diameter of tube. Sun and Yang (2006) conducted tube inversion methods on a conical die and found a critical die angle above which tube can be curled. Further, they said that geometrical parameters of the tube have little effect on critical half conical angle. Later, Sun and Yang (2007) conducted experiments on tube axial compression using two types of dies, one is a conical shaped die and the other is a die having fillet section. They found a range of fillet radius and conical angle within which successful inversion of tube can be conducted. Luo et al. (2007) performed FEM analysis of external inversion and energy absorbing characteristics of 3A21 aluminium alloy tubes and 1Cr18Ni9Ti stainless steel tubes. The steady external inversion load for stainless steel tubes was almost 2.4 times that for 3A21 aluminium alloy tube. Rajabiehfard et al. (2018) investigated the internal inversion process of mild steel tubes under axial impact. It was concluded that if the projectile mass and geometrical parameters of tube and die remain constant, increasing impact velocity increases tube displacement. An increment in thickness up to half way mark in the

inverted tube section is observed and after that a decrement in thickness is observed. Alves and Martins (2009) comprehensively investigated invert-forming of thin walled PVC tubes. In case of external inversion, it was observed that for small value of the circular ratio r_d/r_o, formability is limited by the occurrence of plastic instability, while for larger value of r_d/r_o, restrictions are set by fracture. In case of internal inversion, for values of curling ratio $r_d/r_o < 0.18$, formability is limited by local buckling, while for values $r_d/r_o > 0.20$ formability is limited by excessive thickening. Here r_d is radius of die and r_o is reference radius of tube.

Leu (2000) derived the critical bending radius ρ_c to distinguish between curling and flaring on a conical die as a function of geometrical parameters and material properties such as strain hardening exponent, friction coefficient and half-apex angle of die. El-Domiaty (1997) conducted curling of thin tubes under compressive loads and found that the failure modes encountered in the curling process are tearing, buckling and flaring. Each failure mode occurs when specific conditions are satisfied. Kitazawa (1993) investigated outward curling of circular metal tubes made of copper, brass and mild steel. It is found that if the bending radius is less than critical bending radius (ρ_c), curling occurs. If the bending radius is more than critical bending radius, flaring occurs. It has also been observed that critical bending radius increases with increasing half-apex angle of die. Wang et al. (2001) studied the cold upsetting extruding process of a tube flange. It was observed that the friction factor affects the tube flange formation significantly. Huang et al. (2002) investigated the axial splitting and curling behaviour of mild steel and aluminium circular tubes that were pressed axially on conical dies with different semi angles. Thicker tubes require a larger force because of larger plastic deformation and/or tearing energy. The applied force linearly increases with die semi-angle in the range of 30° to 90°.

Yeh (2007) developed analytical models to predict the relation between the punch stroke, flaring process, tube thickness and flaring forming limit in the tube flaring process. It has been observed that strain hardening has little effect on the thickness ratio, r_k/r_o, where r_k is the final tube flare ratio and r_o is the reference radius of tube, although it has a marked effect on flaring load. The modification of the boss forming proposed previously by Alves at al. (2017a) has been attempted by Alves et al. (2017b). They introduced a new boss forming process for producing annular flanges in thin-walled tubes

by partial compression of the tube wall thickness along the longitudinal direction. The new design process allows piling-up more material without failure by buckling or cracking due to additional confinement and control, improves buckling resistance and, allows piling-up more material for producing flanges with larger outward radius r_d. Flaring of thin walled tube has been conducted through single point incremental forming (SPIF) by Movahedinia et al. (2018). It has been noticed that regardless of the SPIF strategy, the maximum semi angle achievable in incremental tube end flaring is higher than the one made by pressing. Huang and Huang (2001) studied the effects of size and the mechanical properties of tubes, lubricants and semi angle of punch on the flaring of aluminium alloy tube. It has been noticed that, the larger the punch semi angle, the larger is the forming load because of larger squeezing effect of the tube. Lu (2004) developed analytical expression relating the tube flaring ratio and tube strain rate to the tool stroke and velocity in tube flaring process on stainless steel tubes. Flaring ratio was found to be little larger in frictionless case as compared to the case having μ = 0.2. Mohamed et al. (2005) reported an innovative method of flange forming of Al tubes on the lathe utilizing a ball shaped tool attached to the lathe carriage and fed outwards radially, while the specimen is clamped to the lathe chuck and rotated. The radial flanging force increases with increase in tube thickness (t_o) and tool traverse speed (T_a).

From these studies it is understood that for a tube inversion die having fillet section, mainly its radius, and up to certain extent the geometrical parameters of tube play a key role. A critical bending radius is required to distinguish between tube curling and tube flaring. In tube flaring, forming load increases with increase in punch semi angle. Friction conditions always play a key role during end forming operations.

1.2.1.2 Influencing parameters in tube expansion and reduction

In the field of tube expansion and reduction, Gupta and Sahu (2013) discussed about contraction of aluminium tubes under conical entry dies. The dies were made with semiangles of 5°, 10°, 15° and 20°. The initial effort is more for bigger semiangle. Yang et al. (2010) studied the plastic energy absorption behaviour of expansion tubes under axial compression by a conical-cylindrical die. Modeling for the process has been done in non-linear finite element analysis code MSC.Marc. The tube material is 5A06 aluminium tubes with an internal radius fixed at 22.5 mm. Since the friction coefficient was not determined experimentally, value of μ ranging from 0 to 0.1 were tried and at μ = 0.05, a

good fit between experiments and simulations was obtained. Alves et al. (2006) studied the formability limits induced by fracture, local buckling and wrinkling during expansion and reduction of AA6060 aluminium alloy (naturally aged). It was concluded that the tube can be successfully expanded into a circular shape, while expansion into elliptical and square cross-sectional shapes witnessed ductile fracture. Almeida et al. (2006) presented a comprehensive theoretical and experimental investigation on tube expansion and reduction. The material used in the experimental tests was AA 6060 aluminum alloy (naturally aged). They pointed out that besides the formability window of process parameters, a successful mode of deformation can be easily changed into an unsuccessful mode simply by changing the lubrication. Jianguo and Makoto (2005) studied the forming properties of taper part experimentally. The taper is formed at one end of the aluminium tube (A1050, H24) having wall thickness 1mm in two different courses namely progressive taper region and progressive taper angle by computer numerically controlled spinning. The taper accuracy is better in the case of progressive taper angle as compared to the case of progressive taper region. Choi et al. (2012) studied the effect of impact velocity on the energy absorption characteristic of an expansion tube made from S20C carbon steel. The whole length of expansing tube has been divided into two different thicknesses, t_1 and t_2 ($t_1 > t_2$). The region with t_1 thickness requires larger load as compared to region having t_2 thickness. In addition it has been observed that impact force increases with an increase of impact velocities. Karrech and Seibi (2010) developed theoretical model for the expansion of metallic tubes subjected to large radial and circumferential plastic deformation and later a finite element analysis was used to validate the theoretical results. It is seen that the developed model predicts well the thickness variation for an expansion ratio up to 40 % and slightly diverges from the finite element results after that.

From these studies it is perceived that friction conditions play a key role during expansion and reduction. Apart from that it is also shown that instabilities like fracture, local buckling and wrinkling occur during these end forming operations, and optimum parametric design is crucial.

1.2.1.3 Influencing parameters in tube axial compression and crushing

In the field of tube axial compression and crushing, Ghamarian et al. (2011) conducted quasi-static tests to investigate the crush behaviour of the empty and poly-urethane foam filled end-capped conical tubes made of aluminium sheet of thickness 1

mm. It was observed that the load-displacement curve of polyurethane foam-filled conical tubes with higher density lie above the conical dies filled with lower foam density and empty conical tubes. The foam constrained the localized buckling of the conical tube wall and more energy was required to bend them. Ahmad and Thambiratnam (2009a) studied the axial crushing and energy absorption response of foam filled conical tubes under quasi-static loading. For filled tubes the load gradually increases with deflection and this is prominent with increase in semi-apical angle. Rezaei et al. (2015) studied the effect of polyurethane foam-filler on the axial splitting process of circular composite tubes. It has been observed that for polyurethane foam-filler tubes compressive stress after an initial linear part, remains constant which is due to crumbling pores wall of the foam. After the collapse of pores, the polyurethane foam is transformed to a rigid solid and because of that compressive stress acts by an intensive amount. Tarigopula et al. (2006) performed quasi-static and dynamic axial crushing tests on thin-walled square tubes and spot welded top-hat sections made of DP800. The average increase in energy absorption is about 4 kJ/kg for a 1 mm increase in thickness for quasi static as well as dynamic analysis. DiPaolo and Tom (2009) experimentally investigated the effects of ambient temperature on axial-crush response of steel, square box. For application purposes results of the current investigation indicate that, for constant geometry and for four different material types, axial-crush response can be obtained and restricted to the same configuration response mode for a wide range of ambient temperatures representative of vehicle design operating criteria. Jafarian and Rezvani (2019) studied the crushing behaviour of multi-component end-capped, non-capped and simple conical tubes made with aluminum sheet of thickness 4 mm. It is observed that in simple tubes (capped and non-capped), the maximum crushing load occurs during the formation of first fold and at the beginning of the crush range, while in the multi-component conical tubes, maximum load emerges at the end of the crush range.

Kim and Lee (1999) evaluated impact absorption energy of extruded 6061 aluminium tube and investigated the effect of cross-sectional shape on the compression behaviour under dynamic loading. For a thickness to width ratio in rectangular specimen or thickness to diameter ratio in circular specimen ranging in between 0.01 to 0.06, the circular specimen shows higher specific impact absorption energy than rectangular ones. The specific impact absorption energy linearly rises in both the cases. Azarakhsh and Ghamarian (2017) examined the crush response and energy absorption of empty and

foam-filled conical tubes clamped at both ends under axial and oblique loading. Test specimens were made of aluminum alloy 1050. It was found that increasing the load angle caused the formed lobes to be pushed laterally away from the upper rigid surface, thus reducing their amount of axial compression and hence energy absorption. Gouveia et al. (2006) conducted compression beading and nosing for AA 6060 aluminium alloy (naturally aged). For beading operation lower value of r_o/t_o is likely to achieve outward dominant material flow condition. Here r_o is the reference radius of tube and t_o is the thickness of tube. For nosing operation larger r_d/r_o promote lower growth rate of forming load. Here r_d is reference radius of forming die.

From these studies it is revealed that foam-filled tubes perform better than empty tubes during axial crushing. Further, with increase in density of foam its performance improves. It is also concluded that cross-sectional shapes also affect the crushing behaviour of tubes.

1.2.1.4 Influencing parameters in joining by tube end forming

Tube end forming has been utilized in formation of a new product. Few research highlights in this field have been discussed here. Alves et al. (2011a) introduced an innovative manufacturing process for shaping of seamless tubes into small size reservoirs. For the special case of spherical reservoir, they found that the internal mandrel which is basic component of the reservoir forming process plays a key role. Alves et al. (2010) proposed a new method of producing gas and liquid storage reservoirs that ensures a better utilization of raw materials as compared to currently available technologies to fabricate reservoirs. Tan et al. (2013) proposed a two-stage end expansion of round tube into a square section which has two main advantages over other conventional processes. The first advantage is the possibility of forming small corner radii and the second advantage is an improved square look around corners of the square section. Alves and Martins (2010) proposed an innovative forming process for shaping of thin walled industrial tubes into toroidal shells in a single-stage operation. Xia et al. (2014) proposed a new method of manufacturing tubes with nano/ultrafine grain structure by stagger spinning and recrystallization annealing. Here two experimental procedures are designed to refine the grains by considering material phase transformation, process optimization and heat treatment. The first method consists of five pass backward spinning where in the total thinning ratio of tubular blank achieved is 90 %. In the second phase, three pass

spinning followed by 580°C × 0.5 h static recrystallization, and 2 pass spinning and a 580°C × 1h static recrystallization have been followed. The second method provided good surface smoothness and an improved spin-formability of spun parts.

Fundamentals of tube end forming such as tube curling, bead formation, upsetting of tube wall, end expansion etc. has been utilized by researchers for joining of a tube to a tube or with a sheet. These end formed joints are found to be suitable in domestic as well industrial applications. The tube-sheet joints have found their applicability in the assembly of stair cases, roofs and floors made from sheet panels or simply the attachment of tubular posts to base support members in barriers for controlling and managing queues and safety auto part from the braking system (Alves et al. 2011b). One classical example of end formed tube to tube joints is exhaust pipe such that it can eliminate leakage of gases and other fluids at the joint cross-section as welded tube to tube joints are not appropriate for such application. In this context, Heidler et al. (2012) and Turk et al. (1991) emphasized a leak free exhaust system in a vacuum compatible gas bearing guide and radon control techniques in seven New Jersey houses with basements. Some critical findings in the field of mechanical joining using tube end forming have been addressed here. Alves et al. (2018a) joined a tube to a sheet in two stages. In the first stage, an annular flange is produced by partial compression of tube wall thickness along the longitudinal direction. In the second stage, the upsetting of tube's free end against a sheet with a beveled hole is done to lock the two parts together physically. Alves et al. (2011b) suggested a novel approach of joining a sheet to a tube which is accomplished by compression beading and external inversion. The load-displacement behaviour showed a sharp rise at the end of the joining process which is due to the result of compression of sheet panel against lower bead and upper external inverted end. Goncalves et al. (2014) investigated the deformation mechanics of inclined tube-sheet joints for a wide range of operating parameters. It is observed that slenderness ratio (l_{gap}/r_o) of the tube and inclination angle α of dies play a vital role in the formation of sound inclined tube-sheet joints. Here l_{gap} is the initial gap between the tubes and r_o is the reference radius of the tube. Zhang et al. (2014) used the principle of rotary swaging to join copper tubes having different diameters. The tensile strength of the joint made with different cases confirmed that the joint strength increases with increase in radial movement of the swaging die. Alves at al. (2014) joined two tubes at their ends using expansion and beading. Good joints are obtained when the slenderness ratio of tubes (l_{gap}/r_o) lies between 1.25 and

3.125. Later, Alves et al. (2017c) joined two tubes of different types namely S460MC (carbon steel) and AISI304 (stainless steel) welded tubes using the same technique. This time the range of acceptable slenderness ratio is found to be between 1.25 and 2.5 for a successful joint formation. Kitamura et al. (2012) developed a cold joining method for joining of a rotor shaft with a disc. Successful joining is possible when the hardness of the disc is less than nearly 1/3rd of the hardness of the shaft material. Alves et al. (2017a) utilized localized thickening of the tube wall for subsequent joining of function element (sheet) by forming. The deformation mechanics is limited by the occurrence of plastic instability for l_{gap}/t >10 between the initial gap length l_{gap} and final wall thickness t.

Alves et al. (2017d) joined two tubes at their ends, and the process consists of reduction, rounding and clamping by internal mechanical locking and the experiments were conducted on S460MC welded steel tubes. Later they performed the tensile test of newly formed joint and found that the maximum load the joint can withstand without failing is 30 kN. Silva et al. (2015) proposed a new process of joining two tubes which is based on the formation of lap joints by axisymmetric compression beading. The lap joints are capable of withstanding 64 MPa before sudden failure and a sharp spray of water is sent out during water tigntness test. Alves et al. (2018b) proposed a new joining by forming processes which involves forming an annular part with rectangular cross-section and performing the mechanical interlocking by upsetting the free tube end against the sandwich composite with a flaring punch. Destructive pull out tests have been performed upwards and not downwards because downward pull-out tests would provide larger pull-out forces and, therefore, would overestimate the performance of the joint. Alves et al. (2018c) illustrated the potential of mechanical joining by plastic buckling. It was observed that wrinkling formed in circular, hexagonal and square PVC profiles with a slenderness ratio l_{gap}/r_o= 0.94 are successfully utilized to produce a connection with a polycarbonate sheet of 3 mm thickness at room temperature. Alves and Martins (2013) fixed sheet panels against tubular profiles using fundamental modes of tube deformation such as flaring and compression beading. The raw material utilized in the investigation consisted of commercial S460MC (carbon steel) welded tubes and DC04 (carbon steel) sheet plates. They observed that under torsional testing conditions the joints made through proposed joining method and welding performed identically.

These studies reveal that, wherever compression beading is involved in joining process, the parameter l_{gap}/r_o plays an important role. Further it is also revealed that joints made using plastic deformation have strength equivalent to joints made through conventional joining processes. Tube end forming is capable of manufacturing products which have industrial as well as domestic applications.

1.2.1.5 Modeling and simulation in tube end forming

In this area, Zoghi et al. (2013) performed spinning for manufacturing a dome on 232.5 mm diameter and 5.5 mm thick 42CrMO (steel) tube and studied the strain distribution at different thickness layers and axial positions of the curved tube. The simulation of the process has been carried out in 3-D dynamic ABAQUS/explicit software. The comparison of the thickness distribution of the workpiece resulted from modeling and experiments shows a minor difference of 5 %. Nagel and Thambiratnam (2004) compared the energy absorption performance of tapered tubes with straight tubes. A model of straight and tapered tubes was developed using the FE code ABAQUS/explicit version (6.3). For impact velocities below 30 m/s, both straight and tapered tubes deform via dynamic progressive buckling with sequential fold formation starting at the impacted end. Increasing the velocity to 90 m/s causes a buckle to form near the fixed end of the straight tube. Pervez et al. (2012) conducted in-situ expansion of tube diameter by pushing or pulling through it depicting its major applications in oil and gas industry. The process has been modeled in ABAQUS 2D and it was found that a coefficient of friction of 0.07 matches the actual test condition. Excellent to good agreement were found between experimental and numerical results when the expansion ratio varied in the range 12 % to 28 %. Mohebbi and Akbarzadeh (2010) flow formed (a kind of metal spinning process) AA 6063 alloy of 2.5 mm thickness. Simulation in FE commercial code ABAQUS/Explicit showed that equivalent plastic decreases along the thickness of tube. High equivalent strain on the surface could be attributed to high shear strains. Tan et al. (2015) successfully developed axially displaced box-shaped ends having small corner radii from the experiments and simulation. The simulation software used is ABAQUS/standard version (6.10). The higher value of strain was observed around the corners which is due to the compression of the circular end into square corner radii. Masmoudi ei al. (2016) numerically investigated external curling process of thin-walled round tube made of copper having a thickness of 0.7 mm. The investigation was

performed using standard version of ABAQUS 2D. The interfacial friction between tube and die has been studied, and at higher μ a delay in deformation process and local buckling is observed. Daxner et al. (2005) numerically investigated the tube flaring process in the finite element code ABAQUS/Standard. The contact conditions were characterized by classical isotropic Coulomb friction, the coefficient of friction μ ranging from 0 to 0.2. An excellent fit was obtained for driving force at μ = 0.1. Hua et al. (2005) established three-dimensional elastic-plastic finite element model for three-roller backward spinning of a cylindrical workpiece of Hastelloy C alloy tube and simulated the model in ANSYS software. The distribution of the three normal stress components on the spun tube in a cylindrical coordinate system reveals that the three components in the region under the roller are all compressive stress. Ahmad and Thambiratnam (2009b) studied the dynamic response and energy absorption of empty and foam-filled conical tube using non-linear FE code LS-DYNA. It was observed that foam filling tends to shift the deformation mode of empty tube from diamond mode to concertina mode which is related to enhancement in energy absorption performance of foam-filled tube. Shakeri et al. (2007) studied the expansion of deformable tube by a rigid tube under axial compression. The simulation software used for the purpose is ABAQUS/Implicit (6.4). It is shown that in the initial stage of the expansion process, as the rigid tube moves down, the leading edge of the deformable tube bends. In the next stage of the expansion process, unbending takes place. As the compression of the rigid tube continues the leading edge of the deformable tube tends towards a straight profile. Praveen Kumar and Srivaathsav (2019) studied the influence of forming parameters of multi-stage deep drawing process on the axial crushing response of thin-walled capped cylindrical tubes numerically using LS-DYNA R-971^{R} finite element code and validated the results experimentally. It was observed that axial force-deformation history of tube geometry with constant thickness was inferior to that of tube with incorporated forming effects.

The information provided for FE simulation in these work reveal that deforming material was calibrated using Ludwik law or Hollomon's law. An updated Langragian method is used to formulate geometric non-linearity and the contact conditions were characterized by classical isotropic Coulomb friction. Further, a good agreement between predicted and experimental results is observed.

1.2.2 FSW/FSP of flat plates/sheets

1.2.2.1 Effect of tool rotational speed and tool traverse speed

Tool rotational speed and tool traverse speed significantly affect the weld quality or processed zone quality in FSW/FSP. Few contributions highlighting the effect of these parameters are discussed here. Balasubramanian (2008) proposed an empirical relationship for calculating tool rotational speed and tool traverse speed for defect free joint in terms of base metal mechanical properties using five different grades of aluminum alloys. The formation of defect free welds is taken as criterion to establish the relationship. The relationship established between base metal yield strength (YS) and tool rotational speeds for defect free weld is: Rotational speed $= 204YS^{0.31}$. Zapata et al. (2016) studied the effect of the rotational speed and traverse speed on the residual stress during FSW of AA2024-T3 and AA6061-T6 using X-ray diffraction. It has been observed that at a higher tool rotational speed, larger amount of heat is generated resulting in more uniform temperature distribution which ultimately causes lesser deformation and lesser residual stresses on the plates welded. Toktas and Toktas (2012) studied the effect of welding parameters like traverse speed and rotational speed, and the post weld aging process on the microstructural and the mechanical properties of the FSWed Al 6063-T4. With the increase of rotational speed, the grain size of the weld nugget increases, while there is not much effect of traverse speed on grain size.

Cui et al. (2010) discussed about torque developed in FSW and related it to major process parameters like rotation speed (ω) and forward speed (v). Torque is found to decrease as ω increases and increases as v increases. Ramesh et al. (2017) joined 3 mm thick high strength low alloy (HSLA) plates using FSW from a tool made of tungsten-rhenium alloy. The grain size decreases with increases in traverse speed. It has been explained that grain size is the net effect of frictional heat and deformation rate. Frictional heat decreases, hence grain size decreases and deformation rate also decreases, hence grain size increases with respect to increase in traverse speed. In the competition between frictional heat and deformation rate, frictional heat wins and as a result grain size decreases. Golezani et al. (2015) studied the effect of tool rotational speed on 4 mm thick plates of 7020-T6 aluminium alloy. The reduction of grain size, and accordingly increase in hardness values in the joints welded at lower rotational speeds, is because of the reduction of the heat input which leads to a decrease in both peak temperature and

exposure time with respect to higher amounts of rotational speeds. Barenji (2016) investigated the effect of tool traverse speed on microstructure and mechanical properties of friction stir welded 7020-T6 aluminium alloy at different traverse speeds. It was observed that welded joints have lower ultimate tensile strength than base metal. Due to lower heat input at higher traverse speed, the annihilation of the dislocation will be slower which may result in higher dislocation densities in the stir zone (SZ) of the joints, and hence higher UTS (ultimate tensile strength). Peel et al. (2003) investigated the effect of traverse speed on microstructural, mechanical property and residual stresses on AA 5083 aluminum alloy. Longitudinal full width at half maximum (FWHM) of the peaks with the hardness values at similar distances from the weld line has been compared. A strong correlation between the two with both showing an almost identical profile has been observed.

Carlone and Palazzo (2013) provided numerical and experimental investigation on the influence of rotating and welding speed on microstructure, mechanical properties, and joint quality in AA 2024-T3 friction stir welded butt joints. Increasing rotational speed results in a relatively coarser microstructure while opposite behaviour is related to the increase of traverse speed. Hariri et al. (2013) attempted to find an optimum combination of the welding tool rotation rate and traveling speed, concerning the corrosion and mechanical properties of FSWed AA5052 aluminium alloy. The presence of a fine microstructure in the stir zone and a perfect stir zone without any defects are essential to enhance the strength of the weld zone. Moshwan et al. (2015) studied the effect of tool rotational speed on force generation between 3 mm thick AA5052-O aluminium alloy plates. With the increase in rotational speed the longitudinal force was increased and downward force decreased. Sabari et al. (2016) studied the effect of tool traverse speed on tensile properties during underwater friction stir welding (UWFSW) of AA2519-T87. The UWFSW joint made using the higher tool traverse speed of 30 mm/min exhibited superior tensile properties. Rana and Badheka (2018) conducted FSP on the surface of aluminium alloy 7075 (AA 7075) by incorporating B_4C particles. For an increase in tool rotational speed value, T_{peak} grows for different processing conditions (same direction and coarse powder, change in tool travel direction and coarse powder, same direction and fine powder, change in tool travel direction and fine powder). Higher T_{peak} may be attributed to higher frictional heat and plastic deformation while FSP.

Through these research highlights it is understood that in general an increase in rotational speed, or decrease in traverse speed is favourable for more heat generation in the weld zone. Further, grain size also gets affected with change in rotational or traverse speed. Change in rotational speed or traverse speed also affect the longitudinal force as well as downward force and this in turn also affect the quality of the weld.

1.2.2.2 Effect of tool geometry and tool plunge depth

Effect of tool geometry and plunge depth on FSW/FSP has been discussed here. Imam et al. (2013) for their research used three different pin profiles namely, tapered cylindrical, tapered square and square tools for preparation of butt welds in 6 mm thick 6063-T4 aluminium plates. The welds have been characterized using macrographs, hardness contours in the weld cross-section, fractographs and tensile tests. It was observed that performance of square pin profile is better than the other two. Elangovan et al. (2008a) used 6 mm thick plates of AA6061 for FSP. Out of all the pin profiles, the square pin profiled tool provided better performance due to the acceptable dynamic orbit and pulsating action on the workpiece. Chen et al. (2009) used polycrystalline cubic boron nitride tool for FSP of 15 mm thick, 316L stainless steel plate. The tensile tests of FSPed zone showed that its tensile strength is equal to the base metal tensile strength. Colegrove and Shercliff (2003) studied friction stir welding of 7075-T7351 aluminium alloy with three different tool materials. The MP159 tool showed significant voiding on the top surface that did not occur with Dievar tool. The quality of the tool that used the 'combination' tool produced a weld with smooth voiding, but it was less than with the MP159 tool. Kumar et al. (2008) used two different tool geometries namely un-chamfered shoulder and cylindrical pin with a flat end and a chamfered shoulder and a frustum shaped pin having rounded ends to weld a 7xxx alloy. The shoulder diameter was varied at 10 mm, 15 mm and 20 mm. The joint fabricated using chamfered shoulder having a frustum shaped rounded end pin is better. Elangovan and Balasubramanian (2008) studied the effect of tool pin profile (straight cylindrical, tapered cylindrical, threaded cylindrical, triangular and square) and tool shoulder diameter on FSP zone formation of AA 6061 aluminium alloy. Of the five joints, the highest hardness value of 88 VHN has been recorded in the joint fabricated using square pin profile and the lowest hardness value of 60 VHN has been recorded in the joint fabricated using straight cylindrical pin profiled tool.

Vijay and Murugan (2010) joined Al-10 wt. % TiB_2 metal matrix composites using FSW process. The effect of tool pin profile, ratio of shoulder diameter/pin diameter and configuration of shoulder-workpiece interface surface has been studied during process. Out of all different pin profiles used only tapered hexagonal pin and straight square pin produced defect free weld. Leal et al. (2008) investigated material flow during heterogeneous FSW of 1 mm thick plates of AA 5182-H111 and AA 6016-T4 aluminium alloy. Two types of tool shoulders were used for the purpose, first is a shoulder with a conical cavity and the second is a scrolled shoulder. Crown appearance of the weld zone in the later case is rougher than the previous one. Rodrigues et al. (2009) conducted friction stir welds in 1 mm thick plates of AA 6016-T4 aluminium alloy with two different tools and compared the results such as microstructures, strength and hardness across the weld zone for both tools. The results plotted for hardness examination across FSPed zone shows very small difference in hardness between conical shoulder weld and the base material, and a strong decrease in hardness is observed for scrolled shoulder weld. Mastanaiah et al. (2018) FSWed AA2219-T6 rolled plates and the effect of two different tool pin profiles were studied on temperature profile, surface appearance, microstructure and microhardness. First tool pin has tapered cylindrical threaded configuration, and the other is specially designed hybrid FSW. The upper half length (base side) of hybrid tool pin is conical threaded, whereas lower half is of unthreaded triangular cross section. It is observed that lower hardness values are obtained in all zones of the weld joint made by conical threaded tool compared to those produced using the hybrid tool. Mugada and Adepu (2018) studied the flow of stirred material under ridges shoulder combined with various polygonal pin profiles during FSW of 6082 aluminium alloy. The average hardness in the stir zone is higher for hexagonal tool pin profile as compared to triangular tool pin profile. With increasing number of flats the pulsating action was increasing and amount of material sheared off decreasing. For triangular tool pin profile the static volume/dynamic volume ratio is more, and more amount of material was sheared generating larger temperature. Tongne et al. (2017) produced FSWed joints for 6 mm thick AA 6082-T6 plates using carbide trigonal pin. In case of defective welds (higher rotational speed or lower welding speed) a void type of defect is formed below the tool due to inappropriate heat generation. Modeling of this material separation requires development of damage model taking into account the mechanical and thermal loads undergone by the material under the tool.

Mandal et al. (2008) experimentally and numerically investigated the plunge stage during friction stir welding of Al 2024. It was observed that during plunge the peak load occurred slightly before the completion of the plunge. Zimmer et al. (2010) studied plunge processing parameters on maximum generated force and torque while performing successful welding operation in a 6 mm thick 6082-T651 aluminium alloy. They explained the special features of two mainly used plunge stage mode (i.e., displacement control mode and force control mode) while conducting FSW. Khan et al. (2015) conducted FSW for two dissimilar aluminium alloys such as AA5083-H6 and AA 6063-T6. According to them a lower plunge depth causes inadequate material flow which is responsible for defect formation such as tunneling defect and kissing bond. An excessively high plunge depth, however, causes overheating which leads to generation of inter-metallic compound. Ramulu et al. (2013) studied the influence of shoulder diameter and plunge depth on formability of FSWed sheets AA 6061-T6 of 2.1 mm thickness. With an increase in shoulder diameter and plunge depth, the forming limit is found to improve considerably. Kim et al. (2006) discussed about different defect types during FSW of aluminium die casting alloy of ADC 12. The main reason for defect formation during FSW is excess and insufficient heat input and abnormal stirring. Further, it has been derived mathematically that heat input during FSW is directly proportional to tool plunge downforce, rotational speed, and inversely proportional to welding speed. Mehta and Badheka (2015) studied the effect of two different tool design along with different process parameters such as tool pin offset, welding speed and axial plunge load to produce dissimilar copper to aluminum (6061-T651) friction stir welded joints. AA 6061-T651 and electrolytic – tough – pitch (ETP) Cu (of 6.3 mm thickness) were used as the base materials. Cylindrical pin profile performed better as compared to taper pin profile in terms of defect-free dissimilar joints because of uniform mixing of both the materials.

These studies reveal that a square pin profiled tool provided better performance over other pin profiles due to the acceptable dynamic orbit and pulsating action on the workpiece. Later it is also shown that an optimized plunge depth is necessary to get a defect free weld. During plunge stage, maximum axial force and torque occurs at the end of the plunge when shoulder touches the extruded material.

1.2.2.3 Other influencing parameters

Apart from tool rotational speed, tool traverse speed, tool pin profile and tool plunge depth, other parameters and factors affect FSW/FSP. The collective effect of different parameters and factors have been presented here. Al-Fadhalah et al. (2014) conducted FSP of 6063 aluminum plates and studied the effect of overlapping between consecutive passes. In their work, FSP has been conducted for three overlapping (OL) percentages: 25 %, 50 % and 75 % at constant tool rotational speeds and welding speeds. Regardless of the grain size refinement, all FSP samples show a reduction in the tensile strength in the following order: Base metal> Single pass>Multi pass (25 % OL)>Multi pass (50 % OL)> Multi pass (75 % OL). Behnagh et al. (2012) performed FSP of 6mm thick AA5083 sheet and investigated the microstructure evolution and its effect on hardness, wear resistance and corrosion resistance. Due to temperature rise and severe plastic deformation in nugget zone, the average grain size has decreased from 10 μm to 3 μm when compared with un-welded sheet. Sinclair et al. (2010) observed the effect of preheating on process forces during FSW of AA6061-T6. The preheating of the work-piece results in a 43 % reduction in the axial force experienced by the tool for a wide range of process parameters. Aval et al. (2015) friction stir welded 8 mm thick plates of AA6082-T6 and AA7075-T6 and studied the effect of welding heat input and post-weld natural aging on residual stress, microstructure and precipitate distribution in different zones of dissimilar friction stir welds. The results indicate that the dynamically recrystallized grain size is dependent upon plastic deformation rate and welding temperature.

Moreira et al. (2008) highlighted the influence of FSW on the fatigue life of 6063-T6 and concluded that FSW specimens display longer fatigue lives than non-welded specimens tested under the same loading conditions. Sato et al. (1999) studied the FSW of 6063 aluminium during post weld aging. The weld zone has been divided into four zones namely BM (the same hardness region as the base material), LOW (the lower hardness region than the base material), MIN (the minimum hardness region), and SOF (the softened region) which lie at a distance of 15, 12.5, 10 and 0 mm away from the weld centre. It is observed that precipitate-free region (i.e., SOF) and the MIN, LOW and BM regions were heated to about 402°C, 353°C, 302°C and 201°C. Barcellona et al. (2006) conducted FSW on AA2024-T4 and AA7075-T6 and investigated density of insoluble

particles across the weld zone between welded and post weld heat treated samples. Density of insoluble particles was found to be more in case of heat treated samples as compared to normal welded samples. Hwang et al. (2008) devised different types of thermocouple layout to measure the temperature histories during FSW at different locations on the workpiece involving butt joining of aluminium 6061-T6. For the case with thermocouple layout on same side and equal distance a quite steady thermal history in the welding direction has been obtained. Leal and Loureiro (2008) studied the effect of overlapping on the friction stir welding of 3 mm thick 5083-O and 6063-T6 alloy. Welds made with a single pass or two overlapping passes show some higher value of hardness on the retreating side than on the advancing side. Kumar and Kailas (2008) investigated the material flow pattern in FSW, where the interaction of the friction stir welding tool with the base material is continuously increased. It was concluded that primary reason for having defect in the weld, at the initial stages, where the axial load is less than 7.4 kN, is the lack of shoulder contact with the base material. Aktarer et al. (2019) FSWed AA 6061 alloy and interstitial-free (IF) steel plates with dimensions of 200 mm × 50 mm × 2mm and studied the microstructure, mechanical properties, and biaxial stretch formability. It was observed that the formability of the joint of AA 6061 and IF-steel substantially decreases with respect to the formability of IF-steel, however it increases in the case of the AA 6061 alloy. Formation of Fe-Al intermetallic at the joint interface is responsible for this.

Salari et al. (2014) investigated friction stir welding of AA 5456 aluminium alloy in lap joint configuration with two different tempers T321 and O, and different thicknesses, 5 mm and 2.5 mm. The influence of tool geometry and various rotational speeds on macrostructure, microstructure and joint strength have been studied. Hooking is observed as the most common defect in FSW lap joints and its slope is found to be minimum for stepped conical threaded pin. Sato and Kokawa (2001) welded 6063-T5 aluminium and examined local tensile properties corresponding to local microstructure and hardness. It was concluded that due to reprecipitation of the needle shaped precipitates a considerable increase in hardness is observed in post weld aged samples as compared to as-welded samples. Chen and Kovacevic (2003) presented a three-dimensional model based on finite element analysis to study the thermal history and thermomechanical process in the butt-welding of aluminium alloy 6061-T6. It was seen that at location 10 mm to the weld centerline, 1.6 mm below top surface of plate,

rotational speed 500 rpm and traverse speed 140 mm/min, the FE calculated values are higher than measured ones, but they are less than measured ones after maximum temp, which is explained to be caused by assumption of a constant temperature of backing plate. Song and Kovacevic (2002) developed a three dimensional heat transfer model for FSW of AA 6061-T6. Here a moving co-ordinate system is introduced to reduce the difficulty of modeling the moving tool. The comparison of the thermocouple measured and calculated temperature histories has been done at coordinate (114.4, 89.6, 2.5 mm). The calculated result is in good agreement with the measured one, but a little higher. Liu et al. (2014) FSWed AA 6061-T6 and advanced high strength steel successfully. SEM images of Al-Fe interface layer revealed a different color from either steel or aluminium, which indicates a newly formed phase of intermetallic compound (IMC). Sekban et al. (2019) investigated the microstructure, mechanical properties, formability and corrosion behaviour of FSWed low-carbon steel plates (ASTM 131 A) used in shipbuilding applications with dimensions 200 mm × 40 mm × 4 mm. The yield and tensile strength values of the SZ increased from 256 and 435 MPa to about 457 and 585 MPa, respectively, by the effect of FSW without a considerable decrease in ductility.

Mishra et al. (2003) developed a novel method for fabrication of surface composite, Al-SiC by friction stir processing (FSP). It was observed that for a target depth of 2.03 mm surface composite was formed with well distributed particles. A lower target depth (1.78 mm) and a higher target depth 2.28 resulted in no incorporation of particle (SiC) in the aluminium. Khodabakhshi et al. (2017) studied the unique microstructural features of Al-matrix nanocompsites reinforced by graphene nano-platelets (GNPs), fabricated by multi-pass friction stir processing (FSP). Yield strength of Al-Mg alloy improved from 68 to 148.7 MPa after nanocomposite fabrication. Maamoun et al. (2019) studied the FSP effect on the microstructure evolution, microhardness, and the residual stresses of as-built and hot isostatic pressed AlSi10Mg parts. The optical microscope observation indicated a considerable reduction in void zone inside the friction stirred area as compared to HIP (hot isostatic pressed) zone. Thankachan and Soorya Prakash (2017) demonstrated the strength improvement with addition of aluminium nitride in the copper matrix through FSP. It was observed that as-received copper has larger ultimate tensile strength and yield strength as compared to surface composites whereas strength increases with increment in dispersion of AlN particles into copper matrix. Charit and Mishra (2003) demonstrated an improvement in ductility of 400-500 %

via FSP of a commercial 2024 Al. Kurt et al. (2011) incorporated SiC particles, into the commercially pure aluminum by FSP to form particulates surface layers. The improved hardness of produced composite surface was attributed to grain structure and subgrain structure and dislocation distribution of the modified surface. Ma et al. (2006) performed FSP on cast A356 Al to modify the as-cast microstructure. Pores of size 1–2 μm in the as-received polished A356 Al casting is completely removed after FSP. Ahmad and Saha (2018) developed a simple mechanical fixture to overcome the peculiar fixturing issues present in FSW of thin aluminum sheets. The main parts of the developed fixture were, backing plate, top clamp, clamp support, cover plate, lateral clamps and front clamp. Ahmad et al. (2015) studied the micro-friction stir welding (μFSW) of 0.44 mm thick commercial grade 6xxx series aluminum alloys. The lap welds are having better tensile properties than the butt welds in both transverse and longitudinal tensile tests. Mehta and Badheka (2016) attempted dissimilar FSW between AA 6061-T651 and electrolytic tough pitch copper plates of 6.3 mm thickness. Experiments were carried for different tool tilt angles 0°, 1°, 2°, 3° and 4° keeping other parameters constant. Minor variations in tensile strength were observed for tilt angles of 0° to 3°, whereas the highest tensile strength of 116.6 MPa was noticed for a tilt angle of 4°. The reason for this may be attributed to higher axial plunge load recorded with a tilt angle of 4°. Mehta and Badheka (2017) conducted normal FSW (NFSW), heating assisted – FSW (HFSW) at different preheating currents of 40, 80 and 120 amps by applying tungsten inert gas torch ahead of stirring tool while, compressed air and water were brought into the effect behind the stirring tool in case of cooling enhanced FSW (CFSW). A maximum elongation of 4.4 % was reported at NFSW, while low fracture to elongation (1.2 % to 2.2 %) was reported for the rest of the conditions. The presence of large amounts of IMCs and the rapid cooling effect of the stir zone is responsible for such phenomena in HFSW and CFSW welds.

These studies show the effect of multi-pass FSW/FSP on weld/processed zone. How preheating affects the weld zone quality has also been shown. Material flow behaviour on weld/processed zone, as well as effect of post weld natural aging have been discussed also. It is also revealed that FSP improves ductility and also composite fabrication at the surface of workpiece improves hardness and flow strength of the processed zone.

1.2.3 FSW/FSP of tubes

The important parameters which affect the FSW/FSP process in flat plates and sheets such as tool rotational speeds, tool traverse speed, tool geometry (pin profile and shoulder geometry), tool plunge depth, tool tilt angle, tool axial force etc. also affect the FSW/FSP of tubes. However, FSW/FSP of circular tubes have their own challenges in terms of full contact of shoulder contact with the workpiece material, requirement of internal support to the workpiece such that it can sustain the large amount of vertical forces applied by tool holder and heavy duty clamping methods required to the workpiece. Despite these challenges, a number of research group attempted research in this field. Their contributions have been mentioned here.

Kang et al. (2016) joined oxide dispersion strengthened steel plug and F/M steel tube by FSW. It was observed that the hardness in the joint region is 1.5-2 times higher than that of base metal because of a faster cooling rate of the joint region after welding gets completed. Chen et al. (2015) butt welded small dimension Al3003 pipe and pure copper pipe circumferentially and measured the temperature across the weld seam with the help of thermal infrared camera. It was noticed that temperature was not uniform across weld seam which influenced the weld surface across the weld seam. Lammlein et al. (2011) achieved full penetration FSW on butt sections of 107 mm OD and 5.1 mm thick AA 6061-T6 pipe with the help of expandable mandrel. They explained that expandable inner mandrel exert the desired degree of support to the interior of the pipe without damaging the interior of the pipe. Maggiolini et al. (2016) joined 38 mm diameter tubes of 6082-T6 aluminium tubes in butt fashion and then conducted fatigue performance under tension, torsion and tension-torsion loading conditions. They concluded that under torsion testing condition for stress ratio $R = 0$, crack initiation site is primarily on retreating side, while for $R = -1$, crack initiation site is primarily on advancing side for selected shear stress range.

Susmel et al. (2017) joined some one hundred tubular specimens of Al 6082-T6 in butt fashion using FSW by double pass strategy, and tested them under pure axial, pure torsional and biaxial tension-torsional loading. The first pass improves the uniformity of the shoulder, and second pass improves the surface finish. Yuan et al. (2012a) produced ultra-thin wall tubes using a hybrid process combining friction stir welding and spinning. The base metal of as-welded tubes shows non-uniform grains with an average size of 200

μm, while fine-equiaxed grains about 4 μm in size are observed in the base metal of FSW after spinning. Wang et al. (2014) formed the 5 mm thick 2024-O aluminium alloy rolled plates into FSW tube. Further during thickness-reduction of as-welded tube from spinning operation it has been shown that the appropriate temperature can significantly improve the weld cracking during spinning. Later, Hu et al. (2015) also formed 5 mm thick 2024-O aluminium alloy rolled plate into circular shape and then FSWed. Welded tubes show an inhibitory effect for the generation of wrinkles during hydroforming. As the internal pressure increases the number of wrinkles also increases. The distribution and shape of wrinkles are improved. Yuan et al. (2012b) studied the effect of subsequent spinning combined with PWHT on the friction-stir welded tube. It is seen that the *K*-value of FSW tube decreases with increasing PWHT temperature up to 300°C, while the *n*-value increases with increasing PWHT.

A lack of literature has been observed in the field of FSW/FSP of tubes, especially in the field of lap welding of tubes. However, existing literature show that tubes are weldable with the help of appropriate mandrel design and later on spinning and PWHT can improve the performance of welded tube in terms of ductility.

1.2.4 Modeling and simulation in FSW/FSP

In the field of modeling and simulation in FSW and FSP, Ulysse (2002) modeled (three dimensional) FSW of 19.1 mm thick butt joints of AA 7050-T451 in commercial software FIDAP. Increasing the welding speed decreases the maximum temperature, while increasing the rotational speed has an opposite effect. Fratini and Buffa (2005) numerically modeled the continuous dynamic recrystallization phenomena (CDRX) in FSW of AA 6082-T6 using DEFORM. For low value of penetration depths in specimens, a good agreement is obtained between numerical predictions and experimental verifications is obtained in grain size. For larger penetration depths the difference increases. Colegrove and Shercliff (2005) used computational fluid dynamics code, FLUENT, to model the 3-dimensional metal flow in friction stir welding (FSW). The model assumed that the material sticks to the tool surface, so the material velocity equaled the rotational speed multiplied by radius. Buffa et al. (2006) modeled FSW of AA 7075 in DEFORM-3D with varying pin geometries and advancing speeds. The change in tool pin angle causes work hardening of the workpiece due to upsetting. If hardening of workpiece is prominent than the softening in the weld zone caused by

temperature increase, an increase in welding force is observed. Tutunchilar et al. (2012) employed DEFORM-3D to predict the material flow pattern, temperature distribution and effective plastic strain in the weld zone of LM13 eutectic Al-Si as-cast alloy. Simulation predicted the cavity at a higher traverse speed of 200 mm/min and the same was visible in experiment also. Buffa et al. (2011) proposed 3D FE model through FEA software DEFORM-3D to simulate the FSW of AA 6060-T4 in butt joining. From the residual stress contour it has been observed that in steady state, tensile stress is found at the centre of the joint all along the welding line and including the area interested by the tool action, while a compressive state can be observed at the periphery of the joint. Zhu and Chao (2004) conducted three-dimensional nonlinear thermal and thermo-mechanical numerical simulations for the FSW of 304 L stainless steel in FE code WELDSIM developed by authors. FEA results of temperature match with the experimental data very well for both top and bottom surfaces. Zhu et al. (2016) studied CFD models to simulate the material plastic flow during the FSW of AA 2024-T4 using commercial CFD Code, FLUENT. It was demonstrated that in the adjacent area of the welding tool, the simulated temperature history curve closely fit the experimental one.

These studies indicate that modeling softwares are capable of predicting grain size and material flow in weld zone. Further, with the help of appropriate modeling strategy and assumptions temperature distribution, effective plastic strain and residual stress in the weld/processed zone can be predicted. A good match between predicted and experimental result is observed.

1.3 Significance of work

A number of literature are available in the field of joining using end forming of tubes (e.g. a tube to a sheet, a tube to a tube or a tube to a disc etc.). Some novel methods of joining a tube to a sheet and a tube to a tube have been proposed by researchers in the past. Important process parameters influencing the joint quality have been determined and then range of parameters for successful joint formation is obtained. Strength evaluation of end formed joints has also been conducted. The following discussion highlights some of the important results related to end formed joints.

In the field of joining of a tube to a sheet, Alves et al. (2011b) joined sheet panels to tubular profiles using fundamental modes of tube end forming. They also demonstrated

that how joining sheet panels to tubular profiles by tube end forming can be successfully employed in industrial applications. They also concluded that joints made using tube end forming and welding performed identically under torsional loads. The major drawback of this work is that joining is completed in two stages. The first stage is compression beading, and the second stage is external inversion. Similarly, Alves et al. (2018a) joined a tube to a sheet in two stages. In the first stage, an annular flange is produced by partial compression of tube wall thickness along the longitudinal direction. In the second stage, the upsetting of free end of tube against a sheet with a beveled hole is done to lock the two parts. Alves and Martins (2013) proposed an innovative mechanical joining process for fixing sheet panels against tubular profiles with a single ram stroke. They also predicted the safe window of the operating variables. Strength of end formed joints and welded joints performed identically in their work. For joining of a tube to a tube, the work performed by Zhang et al. (2014), Alves et al. (2014), Alves et al. (2017c), Alves et al. (2017d) and Silva et al. (2015) needs special attention. In Zhang et al. work a big experimental set-up is required as they used rotary swaging method to join two tubes which will not be resource intensive. Alves et al. (2014) and Alves at al. (2017c) used the same method to join two tubes at their ends. Though authors claim that joining is possible in single stroke, chamfering needs to be done at the ends of the tube before start of joining experiments. Same is the case with Silva et al. (2015) work. Similary, in Alves et al. (2017d) work, the joining process consists of three stages. Strength of end formed joints has been conducted experimentally, as numerical prediction of strength of end formed joints is unavailable in literature. From these studies, it is found that there is scope to propose a new method of joining a tube to sheet and a tube to a tube. A simple one stroke joining solution for joining of a tube to a sheet or to a tube is the need of industry. Further, a new method may be advantageous when compared to available methods in many ways including accuracy of joint formation, strength of joint, ease of conducting joining experiments, feasibility of joining processes for different materials and dimensions, shop floor production of joints etc.

Although plenty of literature are available in the field of FSW/FSP of flat plates and sheets, literature available in the field of FSW/FSP of tubes is limited (Lammlein et al., 2011), (Kang et al., 2016), (Chen et al., 2015) and (Yuan et al., 2012a,b). Further, literature available in the field of end forming of FSPed tubes is not much. Moreover the end forming of tubes after FSW/FSP is not studied at all. As mentioned earlier, despite

challenges in FSW/FSP of tubes, few research groups such as Kang et al. (2016), Chen et al. (2015), Lammlein et al. (2011), Maggiolini et al. (2016), Susmel et al. (2017) and Yuan et al. (2012a,b) have attempted FSW of tubes. In this, Chen et al. (2015), Lammlein et al. (2011), Maggiolini et al. (2016) and Susmel et al. (2017) have attempted butt welding of tubes. Yuan et al. (2012a) converted a rolled sheet into a pipe via roll forming and then FSWed for joining. Further, they conducted spinning operation on them. But none of them carried out FSP of tubes.

As it has already been stated that FSP has been developed on the basic principles of FSW. The basic purpose of FSP is microstructural modification and mechanical properties enhancement in the processed zone. FSW can also be used to fabricate Aluminium tubes from raw sheet after roll forming. Instead of this route to study the effect of FSW parameters on the forming behaviour after tube fabrication, one can follow FSP of Aluminium tubes to study the effect. Both the results are equivalent. Tailor welded tubes can also be fabricated via longitudinal FSW of tubes of different diameters and materials. The routes are schematically shown in Fig. 1.1.

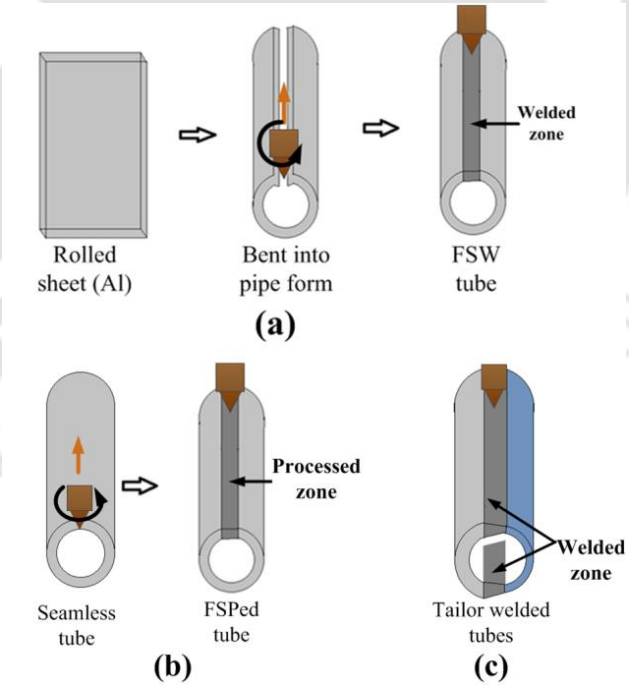

Fig. 1.1 (a) FSW of rolled sheet into pipe form, (b) FSP of normal tube, and (c) fabrication of tailor made tubes through FSW

In this context, FSP of AA 6063-T6 tubes at different levels of parameters in defect free environment has been carried out in the present work with an aim of getting an

optimum processing condition at which a processed tube can perform better than raw tube. Some interesting results have also been obtained through FSP of tubes.

1.4 Objectives of thesis

The main objective of the present thesis is two-fold – (i) To propose novel methods of joining metallic structures by end forming, and (ii) To study the effect of important FSP parameters during end forming of FSPed AA 6063-T6 tubes. Here process parameters are rotational speed, traverse speed, plunge depth and tool pin profile.

The sub-tasks involved to achieve the objectives of the present work are as follows:

(i) Proposing novel methods of joining of a tube to a sheet, and a tube to a tube by end forming and to study the effect of influencing parameters on the joint formation.

(ii) To study the end forming behaviour such as expansion, reduction and beading of friction stir processed aluminum tubes AA 6063-T6 at different tool rotational speeds.

(iii) To study the end forming behaviour such as expansion, reduction and beading of friction stir processed aluminum tubes AA 6063-T6 at different tool traverse speeds.

(iv) To study the end forming behaviour such as expansion, reduction and beading of friction stir processed aluminium tubes AA 6063-T6 at different tool pin profiles.

(v) To study the end forming behaviour such as expansion, reduction and beading of friction stir processed aluminium tubes AA 6063-T6 at different tool plunge depths.

1.5 Organization of thesis

The thesis consists of eight chapters which are organized as follows. Chapter 1 gives an introduction and literature review to the present work. Significance and objective of thesis has been discussed in the last section of the chapter. A novel method of joining a tube to a sheet has been proposed based on FE simulation in Chapter 2 and after that a detailed pull-out test scheme for end formed joints has also been presented both numerically and experimentally. A novel method of joining of two tubes has been

proposed in Chapter 3. Fabricated joints have been tested experimentally. End forming operations such as tube expansion, reduction and beading of friction stir processed AA 6063-T6 tubes at different tool rotational speeds, tool traverse speeds, tool pin profiles and tool plunge depths have been discussed in Chapter 4, 5, 6 and 7 respectively. Chapter 8 summarizes important conclusions from the thesis. Scope of future work has also been discussed in this Chapter.

भारतीय प्रौद्योगिकी संस्थान गुवाहाटी
Indian Institute of Technology Guwahati

Chapter 2

Joining of a tube to a sheet through end curling

2.1 Methodology

In this section, proposed joining method and different parameters involved, materials, finite element simulation strategy and lab scale demonstration methodology have been discussed. Later on, a detailed pull-out test methodology based on experimental approach and numerical approach has been discussed.

2.1.1 Proposed joining method and parameters

The important parts of the proposed joining method are punch, die with a groove, tube, sheet with bend, and upper blank holder. The punch supports the tube partially defined by supported length. The die contains a groove within which the tube deforms at the end. The blank holder applies a blank holding force on the sheet. The schematic of the proposed joining process and parameter definitions are shown in Fig. 2.1.

Initially, a thin sheet with a hole slightly smaller than the tube is machined in the sheet. A vertical bend is made at the edge of a circular hole with a specially designed die. For this, the sheet with a circular hole is placed on the die with a hole larger than the hole in the sheet. The punch is moved downwards into the die hole making a vertical bend. The vertical bend is further deformed into a curved bend using another die of required curvature. The sheet is then placed on the die fabricated for the proposed tube-sheet joining operation. A blank holder is used to clamp the sheet tightly. In the initial stage (Fig. 2.1a), the tube is kept just above the die and a part of the tube is clamped inside the punch. As the punch is given downward vertical displacement, the tube travels through the die groove in the next stage and then enters into the bent region of the sheet. With further vertical displacement of punch, a neck starts to form in the undeformed region of the tube above the sheet. The undeformed length of the tube is designed such that the neck is formed just above the bent part of the sheet. The idea for formation of neck here is that it just touches the upper surface of the sheet, so that a compact joint between the sheet and the tube is obtained. The main aim of producing such a sound joint is to keep the joined parts intact so that one cannot be detached from the other. The whole joining process is completed once the neck is formed above the sheet. Since a split die is used for

end curling of the tube (Fig. 2.1c), once the joining is completed, after unscrewing, the upper and lower die parts are separated. The tube to sheet assembly is removed after that. Fig. 2.2 depicts the process description of the proposed joining method.

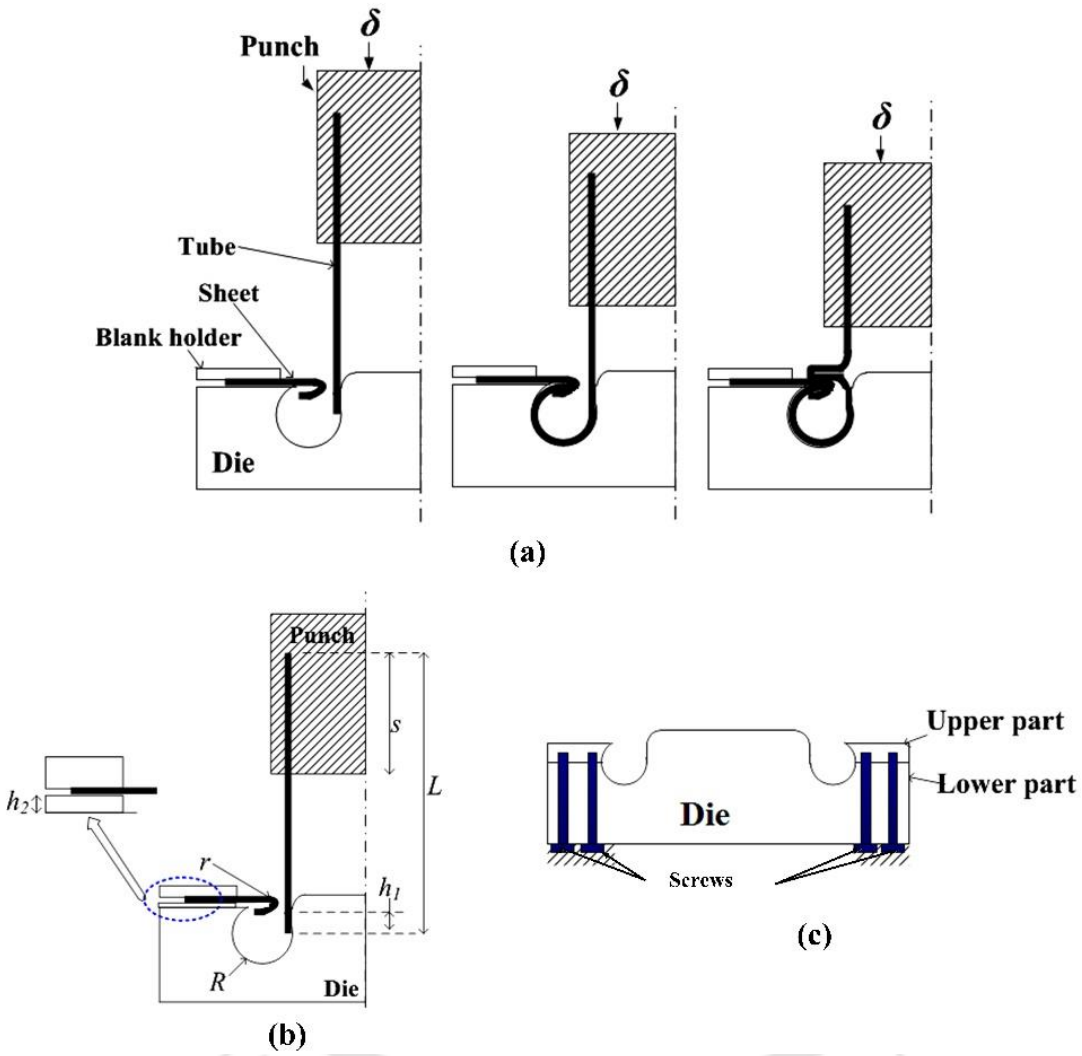

Fig. 2.1 Joining a tube to a sheet using end curling, (a) schematic of the proposed method, (b) parameter definitions, (c) split die for tube end curling (not to scale)

The groove design is crucial as it determines the plastic deformation of the end of the tube and channelizes the tube to enter into the sheet bend. The friction coefficient, in general, affects the plastic deformation. The unsupported tube length determines the formation of neck in the tube. Hence, tube length and tube support length are important parameters. Land height and lower blank holder height are important as they provide the necessary height adjustment for unsupported length of the tube for good interlocking. Optimizing bent sheet radius is important for good compact joint, as it determines the final interlocking.

The success of the joint fabricated depends on a set of process and tool parameters like total tube length, tube support length, die groove radius, sheet bend radius, friction coefficient, land height and height of lower blank holder. The influence of all these parameters can be studied to design the process of joining a tube to a sheet through experiments, which will be time consuming and resource intensive. Hence, a computer aided engineering (CAE) analysis based on FE simulations has been planned to understand the effect of all these parameters on the load-displacement behaviour and tube thinning. The details of FE simulations are described later.

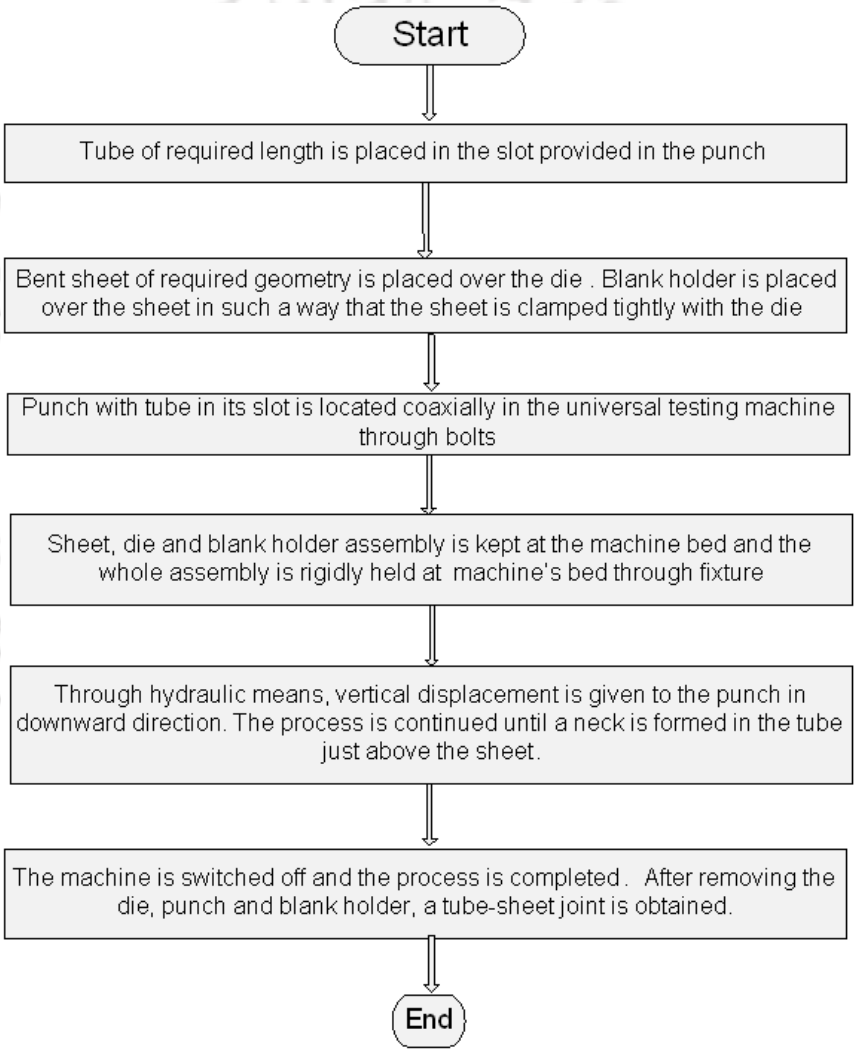

Fig. 2.2 Description of the proposed sheet to tube joining process

The levels of the seven parameters namely total tube length, die groove radius, Coulomb's friction coefficient, tube support length, sheet bend radius, land height and lower blank holder height are shown in Table 2.1. Fig. 2.1 shows the definition of

parameters. The various levels are decided based on extensive simulation trials yielding successful and unsuccessful joints. Finally, as given in Table 2.1, 33 number of FE simulations are planned to understand the influence of chosen parameters and to identify the successfully formed joints. Apart from this, 20 additional FE simulations are conducted to obtain some finer details of the joint formed.

Table 2.1 Variation of parameters during FE simulation of the proposed joining method

Case	Total Tube length (L)	Tube support length (S) (mm)	Sheet bend radius (r) (mm)	Die groove radius (R) (mm)	Coulomb's friction coefficient (μ)	Land height (h_1) (mm)	Lower blank holder height (h_2) (mm)
Cases with varying tube length, other parameters are kept constant							
1.	70	38	0.82	4	0.1	2	0
2.	76	38	0.82	4	0.1	2	0
3.	80	38	0.82	4	0.1	2	0
4.	85	38	0.82	4	0.1	2	0
5.	90	38	0.82	4	0.1	2	0
Cases with varying tube support length, other parameters are kept constant							
6.	76	30	0.82	4	0.1	2	0
7.	76	34	0.82	4	0.1	2	0
8.	76	36	0.82	4	0.1	2	0
9.	76	40	0.82	4	0.1	2	0
10.	76	42	0.82	4	0.1	2	0
Cases with varying sheet bend radius, other parameters are kept constant							
11.	76	38	0.74	4	0.1	2	0
12.	76	38	0.78	4	0.1	2	0
13.	76	38	0.8	4	0.1	2	0
14.	76	38	0.84	4	0.1	2	0
15.	76	38	0.9	4	0.1	2	0
Cases with varying die groove radius, other parameters are kept constant							
16.	76	38	0.82	3.4	0.1	2	0
17.	76	38	0.82	3.6	0.1	2	0
18.	76	38	0.82	3.8	0.1	2	0
19.	76	38	0.82	4.2	0.1	2	0
20.	76	38	0.82	4.4	0.1	2	0
Cases with varying Coulomb's friction coefficient, other parameters are kept constant							
21.	76	38	0.82	4	0.05	2	0
22.	76	38	0.82	4	0.08	2	0
23.	76	38	0.82	4	0.12	2	0
24.	76	38	0.82	4	0.14	2	0
Cases with varying land height, other parameters are kept constant							
25.	76	38	0.82	4	0.1	0	0
26.	76	38	0.82	4	0.1	1.5	0
27.	76	38	0.82	4	0.1	2.5	0
28.	76	38	0.82	4	0.1	3	0
Cases with varying lower blank holder heights, other parameters are kept constant							
29.	76	38	0.82	4	0.1	2	0.1
30.	76	38	0.82	4	0.1	2	0.15
31.	76	38	0.82	4	0.1	2	0.2
32.	76	38	0.82	4	0.1	2	0.25
33.	76	38	0.82	4	0.1	2	0.3

2.1.2 Materials

The sheet and tube materials are stainless steel (SS316L) and mild steel (C%: 0.17-0.23) respectively with dissimilar thicknesses. The tensile properties of the tube (thickness 1.64 mm ± 0.2) and sheet material (thickness 0.6 mm ± 0.1) are determined by tensile tests using a universal testing machine of 100 kN maximum tonnage. From the load-stroke behaviour, the engineering stress-strain values are obtained. The true stress and true strain values are calculated as per standard practice. About 20 different samples are tested to obtain the tensile properties. From the stress-strain data, the mechanical properties of the sheet and the tube are evaluated as per standard procedure and are given in Table 2.2. The true stress-true strain data are fit using the Hollomon's power law, $\sigma = k\varepsilon^n$ (Hollomon and Jaffe, 1947; Hollomon, 1945), and the obtained flow stress-strain behaviour (Fig. 2.3) is used for FE simulations of the proposed joining process. The strain hardening of the sheet during initial bending is not considered during FE simulations, rather the bent sheet is made as CAD data and imported for meshing in the solver. The effect of strain-rate and temperature on the flow stress-strain data has been ignored. Both sheet and tube has been considered to be isotropic.

Table 2.2 Mechanical properties of sheet and tube materials from tensile tests

Mechanical properties / Sheet/Tube	Yield strength, σ_{YS} (MPa)	Ultimate tensile strength, UTS (MPa)	Uniform elongation, e_u	Total elongation, e_t	Strain hardening exponent, n	Strength coefficient, K (MPa)	Plastic strain ratio 'r'
Sheet	229±5	610±5	0.58±0.1	0.6±0.1	0.57±0.013	1760±15	1
Tube	339±19	406±10	0.13±2.5	0.34±0.1	0.15±0.02	646±16	1

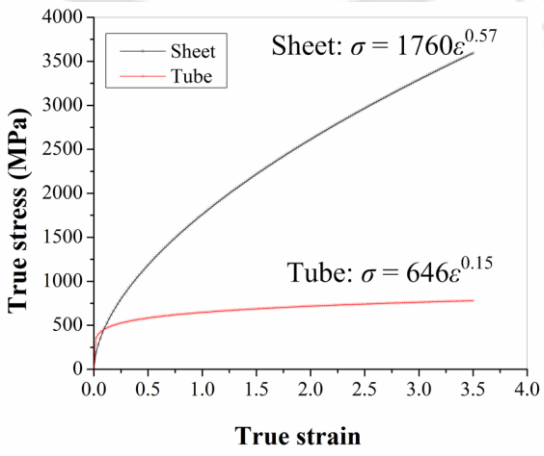

Fig. 2.3 True stress-strain curve of tube and sheet used for FE simulations

2.1.3 Finite element simulation details

2.1.3.1 Standardizing the FE simulation strategy of tube end forming and joining

The proposed method is a novel method of joining tube to sheet, hence similar work is unavailable in the existing literature. In order to standardize the FE simulation strategy for joining tube to sheet, some initial FE simulations and modeling are validated with available literature results on conventional tube expansion and tube reduction. The load-displacement behaviour and thinning behaviour are predicted and validated. Both two dimensional (axisymmetric) and three dimensional FE simulations are carried out for tube expansion and reduction.

Almeida et al. (2006) work has been used for initial validation. The load-displacement data for tube expansion and thinning behaviour for tube reduction are predicted and validated. For this, two cases are considered as given in Table 2.3. Here r_o is the reference radius of the tube (i.e., tube inner radius in case of tube expansion and tube outer radius in case of tube reduction), t_o is the thickness of the tube, α is the conical surface of the punch, r_p is radius of expanded section of the punch, r_d is the radius of reduced section of the punch. The tube length is taken as 90 mm.

Table 2.3 Conditions of tube expansion and tube reduction from Almeida et al. (2006)

Case	r_o (mm)	t_o (mm)	α (°)	r_p/r_o	r_d/r_o	t_o/r_o
Tube expansion	18	1	15	1.67	-	0.055
Tube reduction	20	2	15	-	0.75	0.10

The FE simulations are carried out in ABAQUS/explicit (ver. 6.7-6) code. For three dimensional and two dimensional (axisymmetric) modeling purposes, the conditions used by Almeida et al. (2006) are used exactly. The total time period used for simulation is 0.3 s. In the case of three dimensional modeling, C3D8R and C3D4 have been used. In the case of two dimensional modeling, CAX4R and CAX3 are used. The element type C3D8R and CAX4R are used for deformable domains, while the element type C3D4 and CAX3 are used for rigid domains. The element size of 2 mm has been used for tube. For punch, an element size of 4 mm, and for die an element size of 2 mm have been chosen. A small element size of 2 mm for die represents the die corner appropriately and hence used. The penalty type contact has been used at the interacting surfaces with a constant Coulomb's friction coefficient of 0.11. Almeida et al. (2006) has characterized the

friction coefficient by means of law of constant friction and a friction coefficient of 0.11 was found through calibration by finite element simulations. The tube material used is AA6060 grade alloy (naturally aged) with a hardening behaviour described in Almeida et al. (2006) and it is modeled as isotropic. The tube is modeled as elasto-plastic material, while tools are modeled as rigid. The last stages of FE simulation of tube expansion and reduction are shown in Fig 2.4(a, b) and Fig 2.5(a, b) respectively.

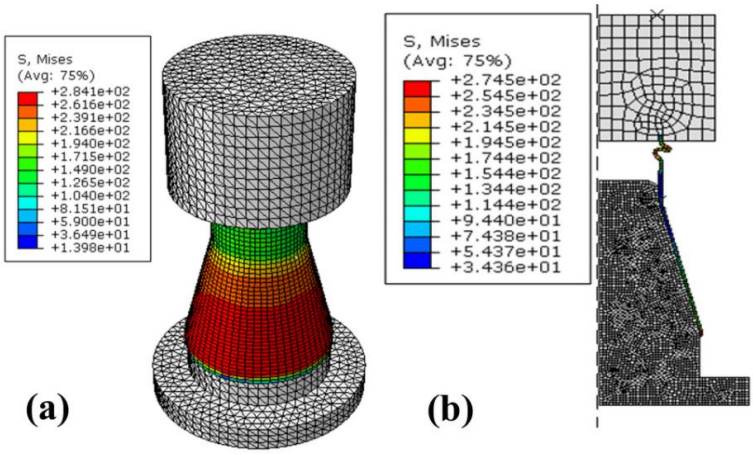

Fig. 2.4 FE simulation of tube expansion, (a) three dimensional modeling, (b) two dimensional modeling

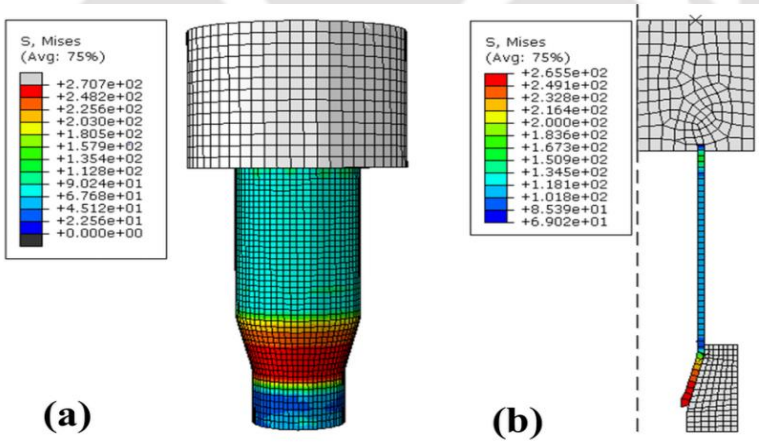

Fig. 2.5 FE simulation of tube reduction, (a) three dimensional modeling (die not shown), (b) two dimensional modeling

2.1.3.2 FE simulation of the proposed tube to sheet joining operation

A two dimensional finite element axisymmetric model has been followed for simulating the proposed joining method using ABAQUS/explicit (ver. 6.7-6) FE code.

The large mesh distortion involved in the large deformation process has been modeled using arbitrary Lagrangian Eulerian formulation (ALE) (Pantale et al., 2004), already used by Rakotomalala et al. (1993) and Pantale (1996). ALE equations involved in simulations have been shown in appendix at the end of the thesis. The total time period for simulation has been taken as 0.3 s. The punch and die has been defined as rigid parts, while tube and sheet has been defined as deformable parts. The true stress-strain behaviour obtained from Hollomon's strain hardening equation as shown in Fig. 2.3 has been incorporated during FE simulations. The sheet and tube are modeled isotropic following von-Mises yield criterion. The effect of strain-rate and temperature are ignored.

For interaction between surfaces, a surface-to-surface contact (explicit) method has been used. A penalty type contact has been defined between surfaces with a Coulomb's friction coefficient of 0.1 simulating dry friction and is varied depending on the cases 21-24 as given in Table 2.1. The die is fixed, and the punch has been given a downward vertical displacement of 40 mm. The element type used is CAX4R and CAX3, first order reduced integration elements. CAX4R is used for deformable part, while CAX3 is used for rigid part. The total number of elements created is approximately 3100, while the total number of nodes created is approximately 3400. Here the mesh size for tube has been taken as 0.8 mm, for sheet material as 0.6 mm, for punch as 4 mm and for die as 1 mm respectively. A small element size of 1 mm for the die represents the die groove appropriately and hence used. The tube has been assigned two elements in thickness direction, and sheet has been assigned one element in thickness direction. Time scaling factor of 1 has been given in steps with a time period of 0.3 s. A mesh sensitivity analysis of tube and sheet for Case 28 (Table 2.1) has been done, as tube and sheet are plastically deforming in the process. The mesh size effect on load-progression behaviour and total CPU time has been studied. For the same case, the effect of time period which is an input parameter during simulation on total CPU time has also been studied.

The maximum time increment has been kept as unlimited. A blank holding force of 20kN has been applied in downward vertical direction to restrict the movement of sheet. The amplitude for simulation has been provided in tabular format. The amplitude has been defined as zero for zero step time, while the amplitude has been defined as 1 for 0.3 s step time. The different stages of simulation are shown in Fig. 2.6 for a typical case. In Fig. 2.6a, the initial stage of the simulation is shown, while the intermediate and final

stages of simulation are shown in Fig. 2.6b and Fig. 2.6c respectively. As discussed earlier, the tube has been kept vertically above the die groove at the start of the simulation. As simulation progresses, the tube travels through the die groove as the punch is given 40 mm downward vertical displacement.

The geometry of the die groove has been designed such that the tube travels through the groove undergoing plastic deformation and a stage comes when the tube enters directly into the bent sheet region (Fig. 2.6b). With further vertical movement of the tube, a bend (or neck) is formed in the undeformed region, just above the sheet. The length of the tube is kept such that the bend is formed just above the sheet and it presses the sheet so as to produce a mechanically interlocked joint (Fig. 2.6c). It is expected that the locking is perfectly formed so as to deliver a structurally strong joint. As pointed out earlier, the effect of the seven parameters on load-progression behaviour and thickness strain at the edge of the tube will be studied through finite element simulations.

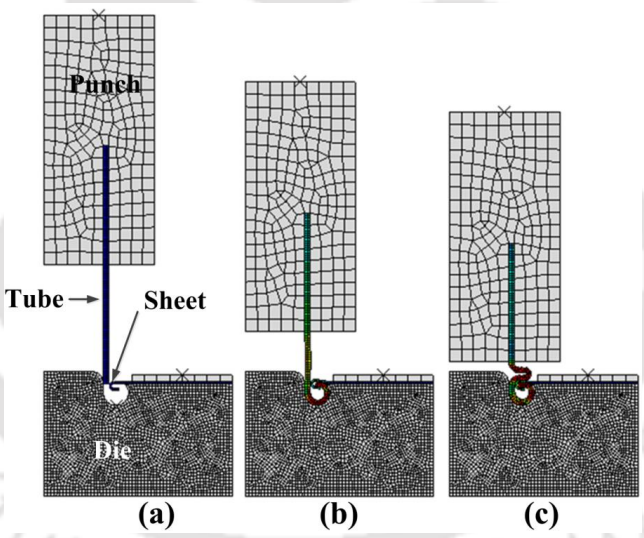

Fig. 2.6 FE simulation stages of the proposed joining method, (a) initial stage, (b) intermediate stage, (c) final stage

2.1.3.3 Description of used yield function

In the present work, von-Mises yield function has been used. According to this yield criterion, a materials is said to start yielding when the von-Mises stress reaches a value known as yield strength, σ_y. It is applicable for the analysis of plastic deformation for ductile materials such as metals (Kumar, 2008).

An equivalent von-Mises stress, σ_v is used to predict yielding of materials of under uniaxial loading conditions,

$$\sigma_V = \sqrt{\frac{(\sigma_{11}-\sigma_{22})^2+(\sigma_{22}-\sigma_{33})^2+(\sigma_{33}-\sigma_{11})^2+6(\sigma_{12}^2+\sigma_{23}^2+\sigma_{31}^2)}{2}} \quad (2.1)$$

In the case of pure shear stress,

$\sigma_{12} = \sigma_{21} \neq 0$, while all other $\sigma_{ij} = 0$, von-Mises criterion becomes,

$$\sigma_{12} = K = \frac{\sigma_Y}{\sqrt{3}} \quad (2.2)$$

This means that, at the onset of yielding, the magnitude of the shear stress in pure shear is $\sqrt{3}$ times lower than the yield stress in the case of simple tension. The von-Mises yield criterion for pure shear stress, expressed in principal stress is,

$$(\sigma_1 - \sigma_2)^2 + (\sigma_2 - \sigma_3)^2 + (\sigma_3 - \sigma_1)^2 = 2\sigma_y^2 \quad (2.3)$$

In the case of principal plane stress, $\sigma_3 = 0$ and $\sigma_{12} = \sigma_{23} = \sigma_{31} = 0$, the von-Mises criterion becomes,

$$\sigma_1^2 - \sigma_1\sigma_2 + \sigma_2^2 = 3k^2 = \sigma_y^2 \quad (2.4)$$

2.1.4 Criteria for assessing the quality of joint formed

In order to assess the quality of the joint formed, three different criteria are proposed. The aim of the criteria is to separate out successful and unsuccessful joints formed through visual inspection at the shop floor once the process is completed. The criteria should be simple and can be followed easily without the essentiality of measurements and calculations. The proposed criteria depend on certain features in the joint region without much concern of what happens elsewhere in the tube and the sheet. These are independent of the materials used for the tube and the sheet. Since there is no measurement involved, CAE analysis is sufficient to implement the proposed criteria before actual/shop floor trials are conducted. These are representative of the entire joint formed and depends on all the input parameters mentioned earlier (in Table 2.1) quantifying the joint quality as a function of these parameters (Fig. 2.7).

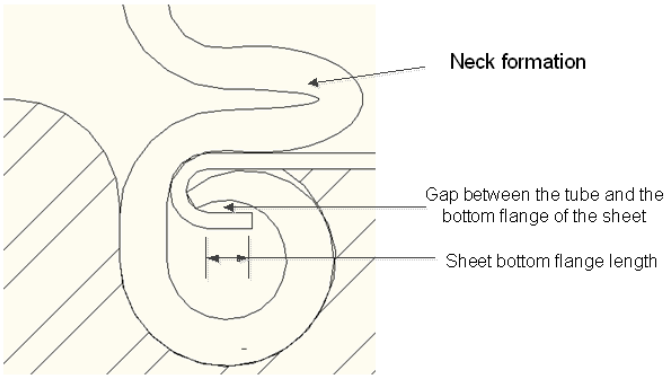

Fig. 2.7 Schematic representation of the proposed criteria for joint quality analyses

The criteria proposed to characterize a successfully formed joint are:

1. The neck should be formed just above the sheet such that it compresses the sheet to produce a tight and compact joint.

2. The gap between tube and bottom flange of the sheet should be as minimum as possible, about 0.1 to 0.3 mm, for good interlocking. Actually there should not be any gap between the tube bend region and bottom flange of the sheet. But practically it is found that a gap evolves when the tube bends into the sheet bend region because of straightening of bottom flange region. Hence a practical gap of 0.3 mm is allowed in terms of criterion. If the gap is larger than 0.3 mm, it is believed that the joint will be loose and weak.

3. The bottom flange length of the sheet should be optimized for good interlocking. Too long a sheet flange will restrict the movement of tube beyond the groove region and there are chances of the flange region to bend in the opposite direction. Too short a sheet flange will not support the tube against the neck and will finally yield a loose and weak joint.

All the criteria should be satisfied to obtain a successful joint. The joint is considered unsuccessful even if one of the criteria is unsatisfied.

2.1.5 Demonstration and validation of the proposed method at lab scale

For lab scale demonstration and validation purpose, three cases out of the thirty-three cases described in Table 2.1 are chosen. The chosen cases are given in Table 2.4. To check the repeatability of the process for each case, three experimental trials were conducted and for all cases the load-displacement data has been captured. The different

components of experimental set-up used for the proposed joining method and final joint fabricated are shown in Fig. 2.8. The load-displacement behaviour from FE simulations and experiments has been validated for all the three cases.

Table 2.4 Cases for which experimental demonstration have been conducted

Cases*	L (mm)	R (mm)	r (mm)	S (mm)	μ	h_1 (mm)	h_2 (mm)
1 (Case 2 in Table 2.1)	76	4	0.82	38	0.1	2	0
2 (Case 17 in Table 2.1)	76	3.6	0.82	38	0.1	2	0
3 (Case 4 in Table 2.1)	85	4	0.82	38	0.1	2	0

*refer Table 2.1

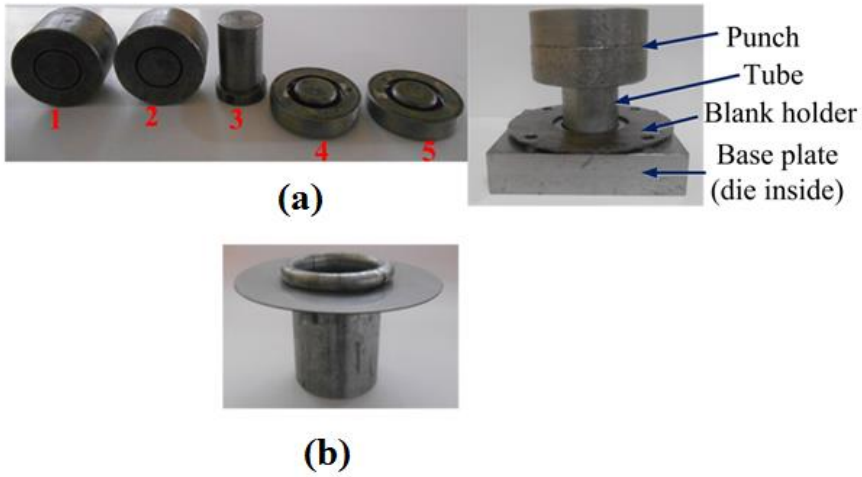

Fig. 2.8 (a) Disassembled and assembled view of different components of the experimental set-up (1: Punch with support length of 38 mm, 2: Punch with support length of 30 mm, 3: Tool used for sheet forming, 4: Die with groove radius of 3.6 mm, 5: Die with groove radius of 4 mm, (b) final joined component

2.1.6 Pull-out test of tube-sheet joint: experimental approach

For each case given in Table 2.4, six joints have been prepared for pull-out test purpose. Dies with three different slopes, i.e., 0°, 10° and 15° with horizontal have been fabricated for testing purpose of these end formed joints. Out of six joints fabricated for each case, two each will be tested with different angles. Totally 18 joints have been fabricated using the proposed method. The material used for dies is cast iron.

In addition to end formed joints, tube-to-sheet welded joints have been fabricated. Gas welding of tube-sheet has been conducted at a pressure of 0.5 bar. Acetylene and oxygen gas has been used for welding purpose. Galvanized iron has been used as the filler material during welding. Totally 6 welded joints have been fabricated such that 2 each

can be tested with different angles. Totally 24 joints have been fabricated (18 made using end forming technique and 6 made using welding). Fabricated joints with different end forming cases and welded tube-sheet joint have been shown in Fig. 2.9. Each experiment has been conducted twice for repeatability purpose. As it has been earlier mentioned that testing has been conducted on three different planes. First plane is flat die, second plane is on a die making an angle of 10° with the horizontal direction, and the third plane is on a die making an angle of 15° with the horizontal direction. The schematic of dies used for testing along with their dimensions and actual dies have been shown in Fig. 2.10.

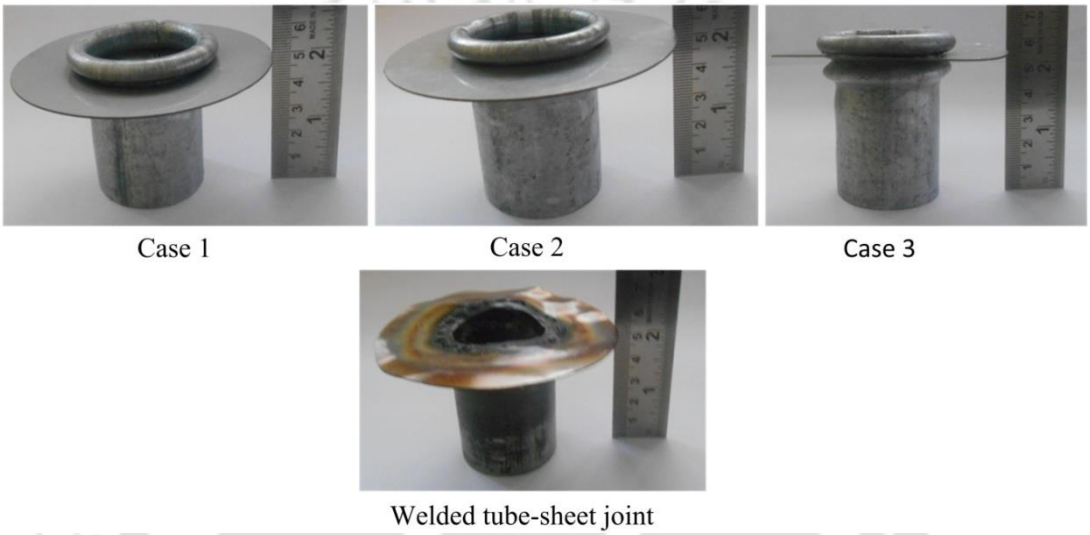

Fig. 2.9 Joints fabricated with different cases as given in Table 2.4 and tube-sheet welded joint

The schematic of pull-out test has been shown in Fig. 2.11. Fabricated tube-sheet joints have been kept on testing planes (either flat or angular) with the help of two blank holders supporting the sheet. These blank holders are bolted with the die such that the tube-sheet joint is intact. Now a punch is designed such that a part of length of the tube is inside the slot made in the punch and with the help of bolts the tube is tightened with the punch. The punch is connected to the ram of UTM which pulls the tube in vertical direction. Actually a shaft connects the punch and the ram and then pull-out test is conducted through the upward vertical movement of the ram. In case of angular dies, the inclination of shaft is same as that of inclination of die surface with the horizontal and pull-out test is conducted vertically.

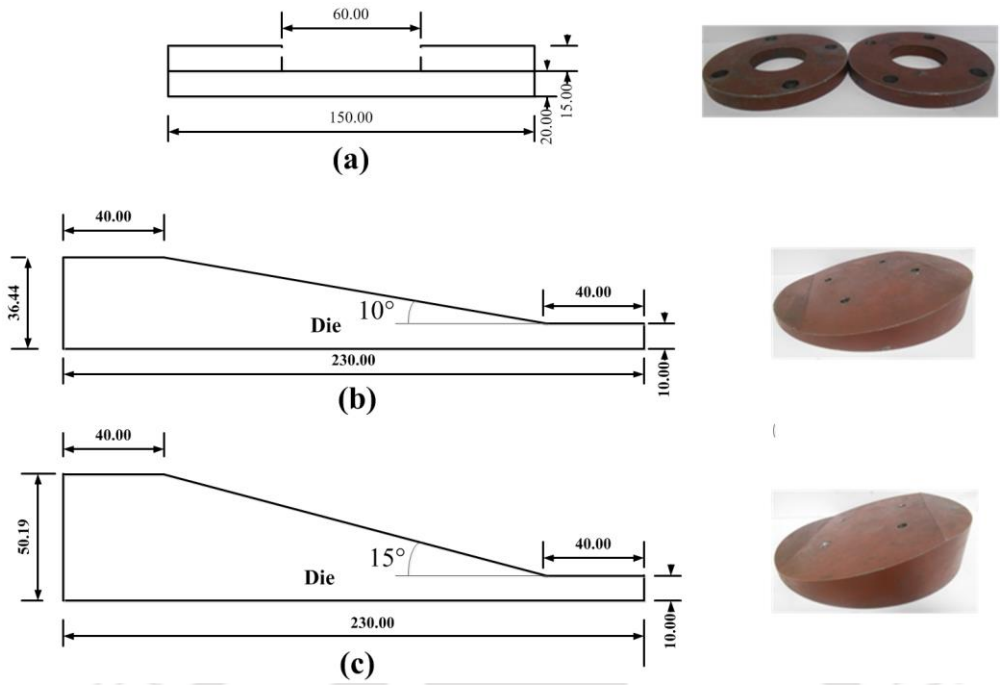

Fig. 2.10 Dies fabricated for pull-out test, (a) die with 0° angle, (b) die with 10° angle, (c) die with 15° angle (all dimensions in mm and not to scale)

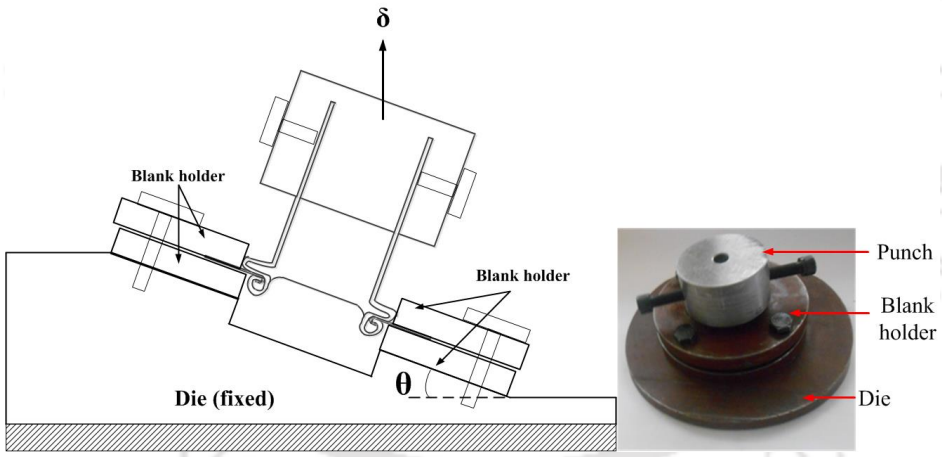

Fig. 2.11 Schematic and experimental set-up fabricated for pull-out test

2.1.7 Pull-out test of tube-sheet joint: FE simulations

Instead of fabricating such a set-up for testing purposes, a simpler way for testing evaluation is to rely on computational approach. The FE simulation prediction has been done through FE code ABAQUS/explicit (version 6.17). For this purpose, both two dimensional (2D) and three dimensional (3D) simulation has been done. To propose the joining method, 2D modeling has been done, since 3D modeling proves to be time consuming and number of experiments are quite high. However, for testing purpose

mainly 3D modeling has been conducted as the numerical experiments are less in number. Also 3D modeling provides a better visualization of the process.

For pull-out test simulations, punch and die are defined as rigid parts, while tube and sheet are defined as deformable ones. A tube element size of 0.6 mm and sheet element size of 0.4 mm has been used. For joining simulations, tube element size has been chosen as 0.8 mm and sheet element size has been chosen as 0.6 mm which has been standardized using mesh sensitivity analysis. A sheet element size of 0.6 mm makes only one element in thickness direction for sheet. Similarly, a tube element size of 0.8 mm makes only two elements in thickness direction for tube. During pull-out test simulations, when the deformed tube and sheet with these element sizes are pulled upwards, too much mesh distortion in the joint region is witnessed. Hence further refinement of mesh of tube and sheet has been done. For a tube mesh size of 0.6 mm and sheet mesh size of 0.4 mm simulation converges properly for all cases. Hence a tube mesh size of 0.6 mm and a sheet mesh size of 0.4 mm have been chosen for testing purpose. Element types used for 3D analysis are C3D8R and C3D10M. A friction coefficient of 0.01 has been applied between surfaces assuming lesser interaction between them during pull-out tests as compared to joining. Time period used for present analysis is 0.0005 s. Punch has been given downward vertical displacement during simulation till the neck is formed above the sheet. For successful cases (Case 1 and 2, Table 2.4) neck forms above the sheet, while for unsuccessful case, Case 3, neck does not form above the sheet. In this case neck forms slightly above the sheet because of longer length of the tube.

For pull-out tests the deformed part at the last stage of joining simulation is imported to another .cae file. Here after implementing all the modeling conditions the punch is given displacement in upward vertical direction to test the joint in flat die condition. The simulation is stopped when complete unlocking takes place. For pull-out tests on angular dies, after importing all the parts from joining simulation and then implementing all the modeling conditions for pull-out test, the whole model is rotated through the desired angle at which the test is to be conducted.

The predicted outcome is load-displacement behaviour. During the pull-out test, the tube inside the curled region comes out of the bent part of the sheet and unlocking phenomena starts in the joint region. During Pull-out test simulation, it has been observed that the initial distance between diametric opposite faces of the inside surface of the tube

in the curled region '*D*' decreases with the further vertical upward displacement of the punch. Actually it is an important phenomenon which describes the local deformation of the tube. The variation in '*D*' with respect to displacement has been further discussed. The schematic of FE simulation of pull-out tests along with the definition of '*D'* during pull-out tests has been described in Fig. 2.12.

Fig. 2.13 shows different stages during pull-out test of tube-sheet joint. The last stage of tube-sheet joint has been shown in Fig. 2.13a. When the punch is pulled in upward direction, an unlocking phenomena starts in joint region (Fig. 2.13b). The bead above the sheet is stretched upwards and the curled region is also stretched in the upward vertical direction. As a result of this '*D*' decreases. With further displacement the curled region of the tube comes out of the bent part of the sheet, and at the same time, the sheet is also bent in the vertical direction upwards (Fig. 2.13c).

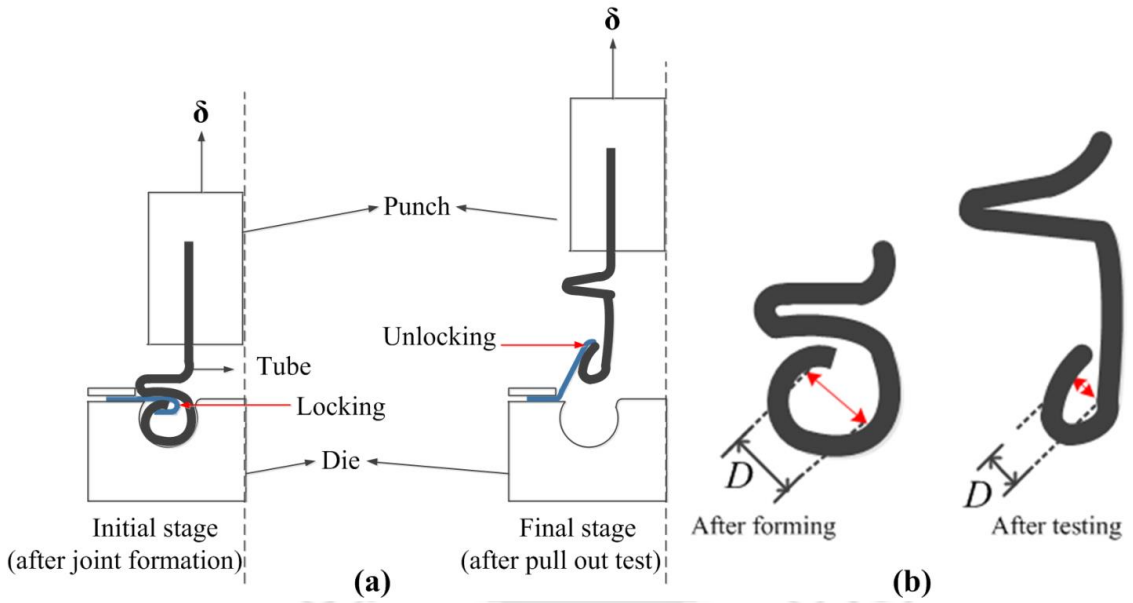

Fig. 2.12 Schematic of (a) pull-out test of end formed joints, (b) localized deformation of tube in curled region

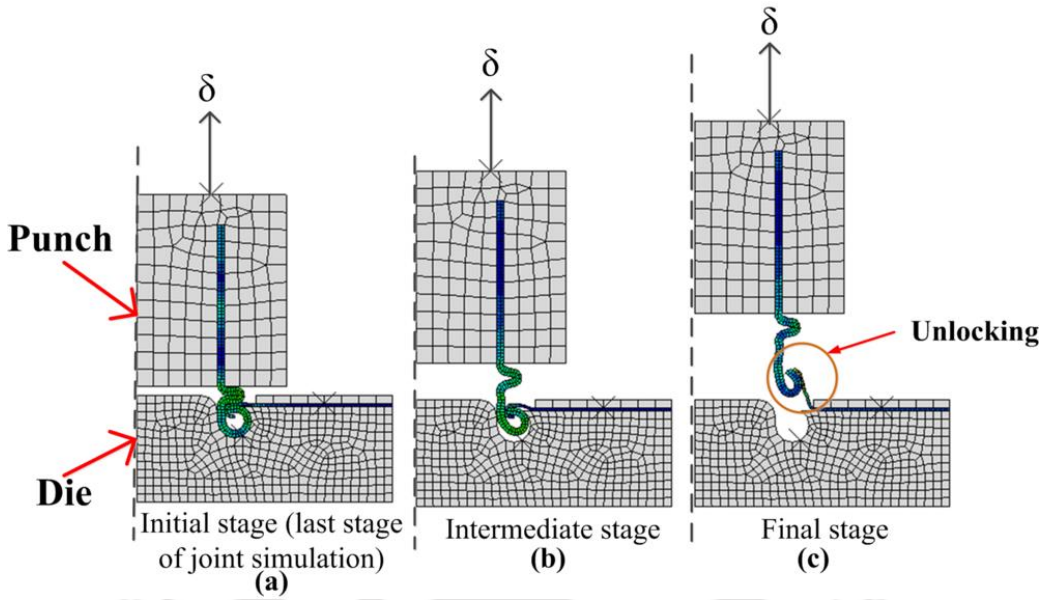

Fig. 2.13 Different stages as observed during pull-out test simulation of tube-sheet joint

2.1.8 Energy absorbed during pull-out tests

Energy absorbed by the end formed joint and welded joint during pull-out tests can be calculated as the area under the load-displacement curve (Spena et al., 2015) up to the peak load using following equation:

$$\text{Absorbed energy} = \int_0^x F dx \tag{2.5}$$

where F is the pull-out peak force and x is the displacement at the peak load. Energy absorbed during pull-out tests is an important output which should be monitored as failure occurs neither in the tube nor in the sheet, rather an unlocking phenomenon takes place. Now the complete unlocking can happen at different displacements for different joint formation and tests cases. Hence energy absorbed could be different under different testing conditions.

2.2 Results and discussion

2.2.1 Validation for standardizing the FE simulation of end forming of tubes

To standardize the FE simulation strategy, tube expansion and tube reduction processes have been modeled (in 2D, 3D) and the load-displacement behaviour and thickness strain at the end of the tube are predicted and validated with available results (Fig. 2.14 for tube expansion, and Fig. 2.15 for tube reduction).

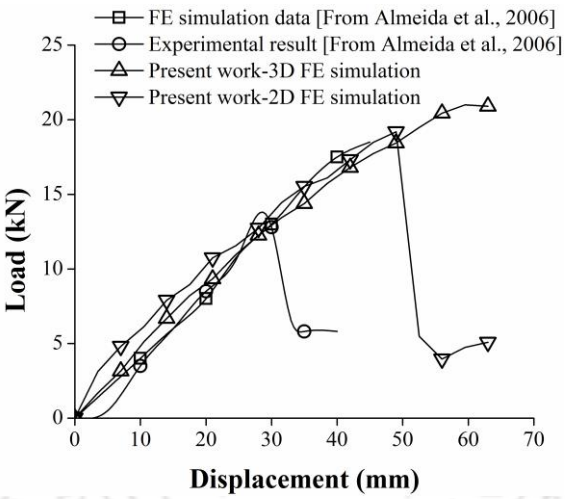

Fig. 2.14 Load-displacement behaviour validation for tube expansion

It is observed that the FE predictions (both 2D and 3D modeling) match well with the available experimental data and FE simulation data. In the case of load-displacement behaviour (Fig. 2.14), slight deviation is seen between the results of the present work and the available data from Almeida et al. (2006), mainly at the end of the process. Moreover, the experimental data from Almeida et al. (2006) for load-displacement behaviour has been characterized by tube failure and hence the load declines at an early stage (about 35-38 mm of displacement). This is not observed in the FE simulation data as a failure criterion is required for this purpose. In the case of thickness strain prediction (Fig. 2.15), the results match well with the available data, with the 2D model showing slight deviation. Since the FE simulation has been standardized with acceptable accuracy, a similar approach for modeling the proposed joining method will be followed.

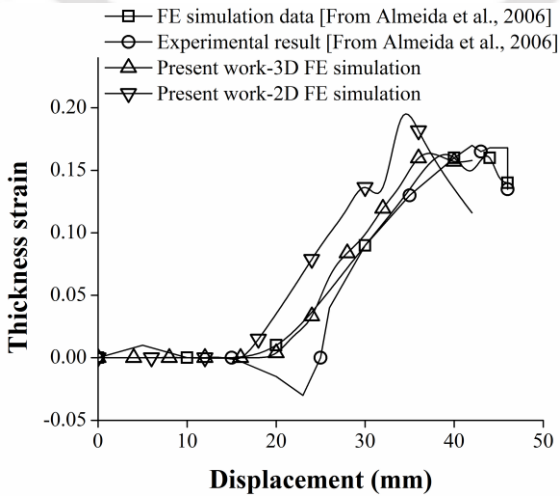

Fig. 2.15 Thickness strain evolution validation for tube reduction

2.2.2 Optimizing mesh size and time period during FE simulations of the proposed joining

The effect of the initial mesh size of the tube and sheet on the load-displacement behaviour and the total CPU time has been observed through mesh sensitivity analysis of tube (Fig. 2.16) for a particular case –Case 28 (refer Table 2.1). It is observed that the tube mesh size does not affect the load-displacement behaviour much, while sheet mesh size shows little effect on the maximum load. A sheet mesh size of 0.3 mm shows some deviation from other cases (Fig. 2.17). Moreover, it has been observed that lower the tube element size and sheet element size, larger the total CPU time (Table 2.5). Hence an optimum element size is required for FE simulation so that accurate forming behaviour is predicted with lesser CPU time. For the present analysis, tube mesh size of 0.8 mm has been chosen with two elements in thickness direction, while sheet mesh size of 0.6 mm has been chosen as there is not much difference present in the CPU time for mesh sizes of 0.6, 0.9 and 1.2 mm.

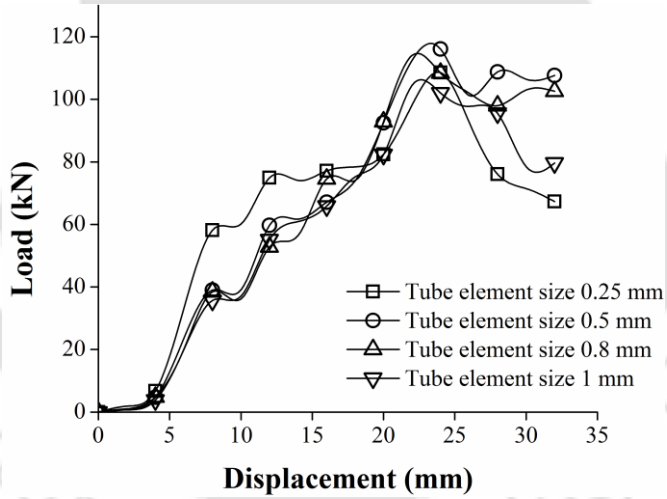

Fig. 2.16 Mesh sensitivity analysis of tube

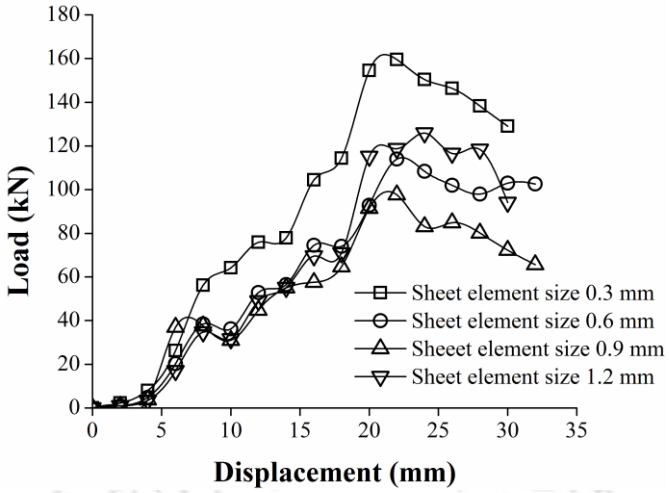

Fig. 2.17 Mesh sensitivity analysis of sheet

Table 2.5 Effect of tube and sheet element size on the total CPU time and joint quality

Mesh size (mm)	Total CPU time (min)	Joint quality
Tube		
0.25	156.6	Successful
0.5	28.91	Successful
0.8	20.98	Successful
1	23.11	Successful
Sheet		
0.3	61.02	Successful
0.6	20.93	Successful
0.9	18.45	Successful
1.2	17.02	Successful

The effect of time period which is given as input during FE simulation in ABAQUS has been varied and its effect on total CPU time and joint quality has been studied. It is observed from Table 2.6 that with increase in time period, the CPU time increases considerably. Moreover, the case of 0.1 s delivered an unsuccessful joint, while other cases have delivered a successful joint. The quality of the joint is assessed by the criteria proposed earlier. Finally, a time period of 0.3 s has been chosen for the entire FE analysis as minimum computational time is seen and it produces a successful joint.

Table 2.6 Effect of time period on CPU time and joint quality

Time period during FE simulation (sec)	CPU time (min)	Joint quality
0.1	6.71	Unsuccessful
0.3	21.51	Successful
0.5	35.16	Successful
0.7	51.14	Successful

2.2.3 Thickness strain evolution, thickness evolution and load-displacement behaviour of the proposed joining method

The thickness and thickness strain evolution and load-displacement behaviour during the proposed joining method for a typical case (Case 2, Table 2.1) has been described in Fig. 2.18. The joining process can be divided into three regions, region 'I', region 'II', region 'III', as a function of displacement. In region 'I', in less than 15 mm displacement, the tube moves down and curls along the die groove. In region 'II', between 15 to 26 mm, the tube moves into the sheet bend; for the rest of the displacement, i.e., above 26 mm, in region 'III', the unsupported length of the tube above the sheet bends and a neck is formed, completing the interlocking, and forming the joint.

The thickness strain and thickness evolution for Case 2 (Table 2.1) is shown in Fig. 2.18 (a) and 2.18 (b). From Fig. 2.18 (b) it is observed that maximum thinning at the end of the tube is observed at the completion of the tube curling region, region 'I', after which the thickness of the tube has increased showing tube thickening, although the tube thins down as compared to its initial thickness. Similarly, the maximum load is observed when the tube enters the bend region of the sheet, region 'II', and the necking starts (Fig. 2.18c). Similar behaviour is observed for all the FE simulation cases of the joining process proposed.

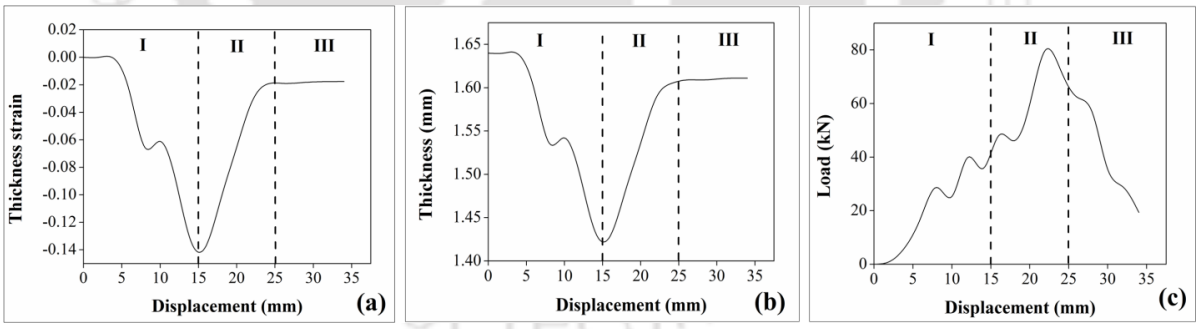

Fig. 2.18 Evolution of (a) thickness strain, (b) thickness, and (c) load, for Case 2 of the proposed joining method

2.2.4 Influence of parameters on the load-displacement behaviour

In this section, the influence of the seven parameters (cases 1-33, Table 2.1) on load-displacement behaviour is discussed. The motive of the following sections is to understand the effect of parameters and also to identify the successful cases of joint fabrication as per the criteria proposed. Actually the load-displacement behaviour is a

good representation of the process and it depends on the success and failure of the joint formed during the proposed process.

The influence of tube length (cases 1-5) on the load-displacement behaviour is shown in Fig. 2.19. It has been found that as the tube length increases, the maximum load decreases, except for Case 2 (Tube length = 76 mm). The case with 70 mm tube length exhibits larger maximum load, while 90 mm tube length needs lesser maximum load. The load requirement is almost same in all the cases, before the maximum load is reached. In case of 70 mm tube length, the tube length is not sufficient to form a full neck in the undeformed part of the tube. In case of tube lengths of 80 mm, 85 mm and 90 mm, the length of the tube is longer than the required tube length and neck is formed above the bent sheet and closer to the bottom surface of the punch and hence the upper surface of the sheet is not compressed. So cases 1, 3, 4 and 5 are the unsuccessful cases depending on the joint formed.

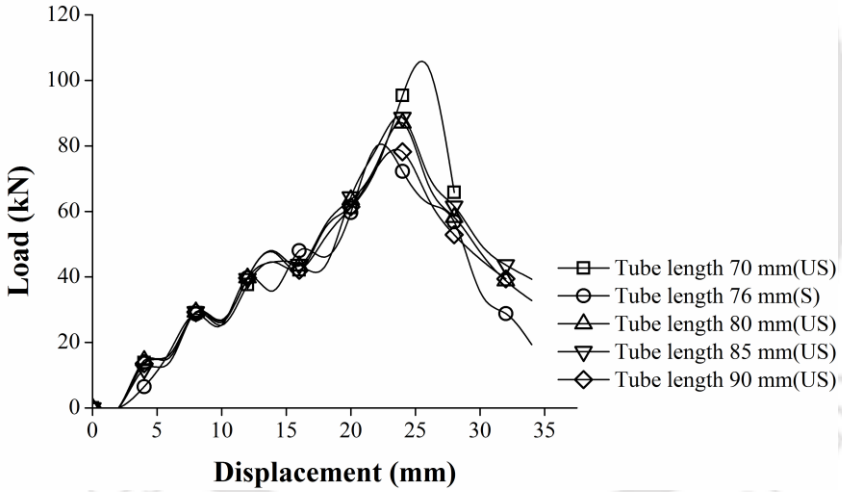

Fig. 2.19 Load-displacement behaviour for different tube lengths (cases 1 to 5, Table 2.1) (US: Unsuccessful, S: Successful)

The load-progression behaviour for different support lengths (cases 6-10) is shown in Fig. 2.20. The case with a tube support length of 34 mm requires minimum load, while that with 36 mm requires maximum. The tube support length of 30 mm delivers an unsuccessful joint. Although tube support length of 40 mm and 42 mm show inconsistent load-progression behaviour, all the four cases (7-10) belong to successful cases of joining and Case 6 is unsuccessful.

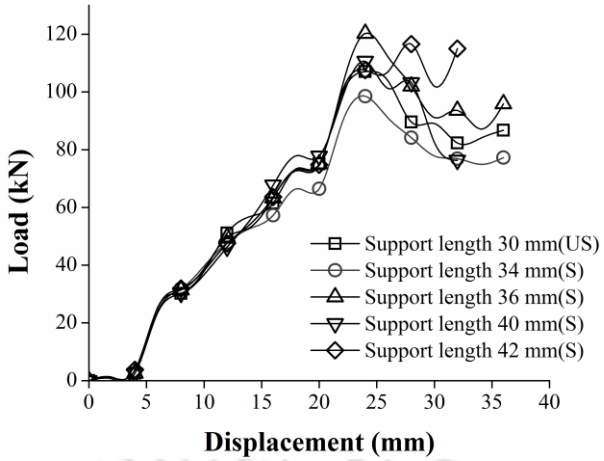

Fig. 2.20 Load-displacement behaviour for different tube support lengths (cases 6 to 10, Table 2.1) (US: Unsuccessful, S: Successful)

From the load-displacement behaviour of different sheet bend radius (cases 11-15, Fig. 2.21), it is observed that with the increase of sheet bend radius, the maximum load decreases, though the variation is small. The reason behind this is with the increase of sheet bend radius the ease with which tube is interlocked inside the bent region increases, so the load decreases, although the decrease in load is insignificant. All these cases belong to the successful cases of joining.

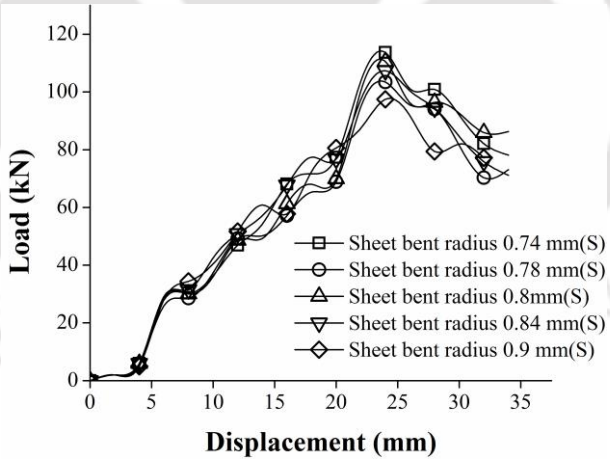

Fig. 2.21 Load-displacement behaviour for different sheet bent radius (cases 11 to 15, Table 2.1) (S: Successful)

It is clear from Fig. 2.22 that with the increase of die groove radius, the maximum load decreases. This is because of the fact that with the increase in die groove radius, the movement of tube across the die groove becomes easier reducing the maximum load. Out of these five cases, Case 17 (die groove radius: 3.6 mm) and Case 18 (die groove radius:

3.8 mm) are characterized by successful joints, while cases 16, 19 and 20 belong to the unsuccessful category.

It is observed from Fig. 2.23 that with the increase in Coulomb's friction coefficient, maximum load decreases. Here friction is provided between all the interacting surfaces. The decrease in maximum load can be explained with the successfulness and unsuccessfulness of the joint. Here the successful joint is obtained only for friction coefficient of 0.08. For the friction coefficients 0.12 and 0.14, the tube is not locking completely into the bend region of the sheet, so a decrease in maximum load is observed. For friction coefficient 0.05, the neck in the undeformed length of the tube is not formed just above the sheet; so a good joint has not been obtained. The influence of lower blank holder height and land height are insignificant and arbitrary as seen in Table 2.7.

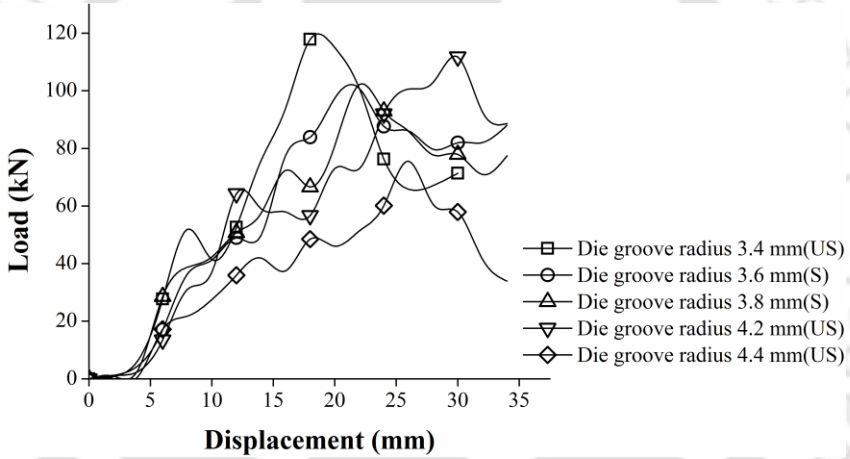

Fig. 2.22 Load-displacement behaviour for different die groove radius (cases 16 to 20, Table 2.1) (US: Unsuccessful, S: Successful)

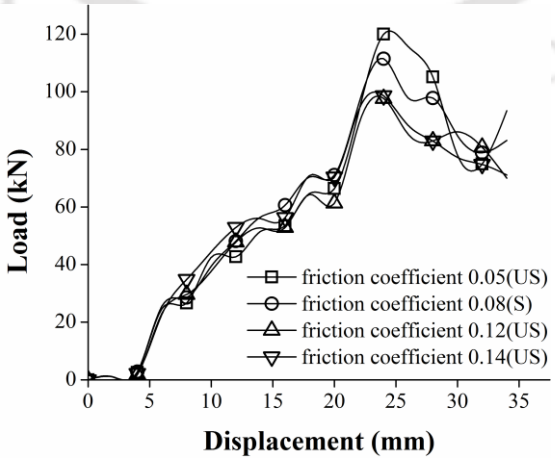

Fig. 2.23 Load-displacement behaviour for different Coulomb's friction coefficient (cases 21-24, Table 2.1) (S:Successful, US:Unsuccessful)

Table 2.7 Maximum load observed for different land heights and blank holder heights

Cases	Parameter	Maximum load (kN)
	Land height (mm)	
25.	0	95.52
26.	1.5	101.56
27.	2.5	95.49
28.	3	114.033
	Lower blank holder height (mm)	
29.	0.1	66.12
30.	0.15	65.00
31.	0.20	66.85
32.	0.25	67.78
33.	0.30	65.89

2.2.5 Influence of parameters on the thickness strain evolution

The thickness strain evolution at the edge of the tube for different tube lengths is shown in Fig. 2.24. It is observed that thickness strain at the edge of the tube is not affected much by different tube lengths. So the effect of tube length on thickness strain can be neglected.

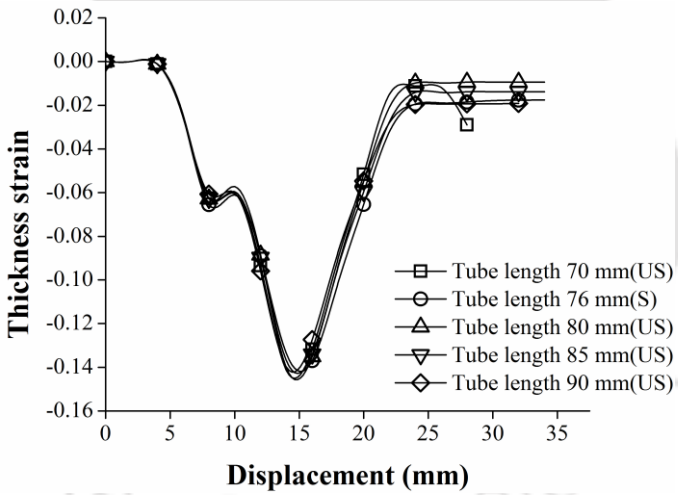

Fig. 2.24 Thickness strain evolution for different tube lengths (cases 1 to 5, Table 2.1) (S: Successful, US: Unsuccessful)

The thickness strain evolution for different die groove radius suggests that with the increase of die groove radius, the absolute value of thickness strain is increasing (Fig. 2.25). For die groove radius 3.4 mm, the peak thickness strain obtained is 0.125 (absolute), while for die groove radius 4.4 mm, the peak thickness strain obtained is 0.15 (absolute). So a decrement of thickness of 0.20 mm is observed in case of die groove radius 3.4 mm, while a decrement in thickness of 0.23 mm is observed in case of die

groove radius 4.4 mm. The decrease in thickness with increase in die groove radius is due to the severe plastic deformation taking place while covering a large die groove radius sustaining large compressive forces.

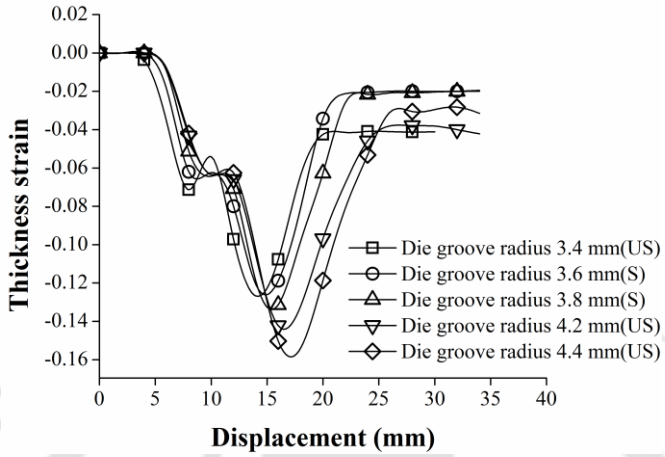

Fig. 2.25 Thickness strain evolution for different die groove radius (cases 16-20, Table 2.1) (S: Successful, US: Unsuccessful)

The thickness strain evolution for different Coulomb's friction coefficient is shown in Fig. 2.26 for cases 21-24. It is observed that the thickness strain increases with increase in friction coefficient. This shows that the thinning at the end of the tube increases with increase in friction coefficient. For a friction coefficient of 0.05, the peak thickness strain is 0.13 (absolute) and for 0.14, the peak thickness strain is 0.14 (absolute). A difference in thickness strain of 0.01 is observed. The reduction in thickness of tube with increase in friction coefficient is due to larger amount of frictional forces causing more plastic deformation at the edge of the tube.

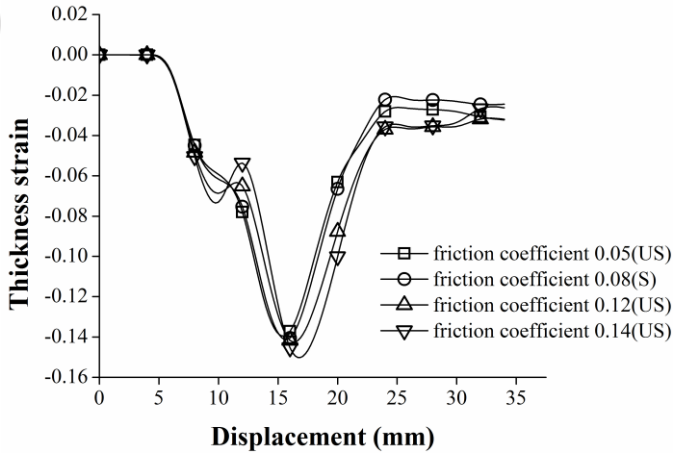

Fig. 2.26 Thickness strain evolution for different friction coefficients (cases 21-24, Table 2.1) (S: Successful, US: Unsuccessful)

The effect of land height, lower blank holder height, sheet bend radius and tube support lengths on thickness strain at the end of the tube is given in Table 2.8 in terms of maximum thickness strain. The effect is found to be insignificant. There is not much change in the entire thickness strain evolution depicting the ineffectiveness of these parameters.

Table 2.8 Maximum thickness strain for varying tube support length, sheet bend radius, land height and lower blank holder height

Case	Parameter	Peak thickness strain
	Tube support length (mm)	
6.	30	0.1449
7.	34	0.1444
8.	36	0.1456
9.	40	0.1491
10.	42	0.1454
	Sheet bend radius (mm)	
11.	0.74	0.1441
12.	0.78	0.1400
13.	0.80	0.1455
14.	0.84	0.1413
15.	0.90	0.1470
	Land height (mm)	
25.	0 mm	0.1410
26.	1.5 mm	0.1399
27.	2.5 mm	0.1353
28.	3 mm	0.1309
	Lower blank holder height (mm)	
29.	0.1	0.1416
30.	0.15	0.1438
31.	0.20	0.1418
32.	0.25	0.1452
33.	0.30	0.1466

2.2.6 Quality analysis of the formed joints

Based on the criteria proposed earlier to identify the successfully formed joints, the quality of the joints is analyzed and summarized in Table 2.9. The reason for quantifying the joint as unsuccessful is also given. There are twenty-two successful joints and eleven unsuccessful joints produced. Fig. 2.27(a, b) and Fig. 2.28(a, b) show the last stage of the joint fabricated in FE simulations. Fig. 2.27(a, b) shows two cases of successful joints. Both the cases satisfy all the three criteria as observed from the FE simulation images. Fig. 2.28(a, b) shows the unsuccessful cases. In the first case, because of smaller die groove radius, the bent edge of the tube contacts the lower flange of the

bend sheet, dislocating the bent region, not forming interlocking at all. In the second case, the neck is not formed above the sheet, producing a loose joint.

Table 2.9 Summary of quality analyses of the joints based on FE simulations

Case	Parameter description	Quality of the joint	Reason for unsuccessful joints
	Tube length (mm)		
1.	70	Unsuccessful	Criteria 1 and 2 not satisfied
2.	76	Successful	---
3.	80	Unsuccessful	Criterion 1 not satisfied
4.	85	Unsuccessful	Criterion 1 not satisfied
5.	90	Unsuccessful	Criterion 1 not satisfied
	Tube support length (mm)		
6.	30	Unsuccessful	Criterion 1 not satisfied
7.	34	Successful	---
8.	36	Successful	---
9.	40	Successful	---
10.	42	Successful	---
	Sheet bend radius (mm)		
11.	0.74	Successful	---
12.	0.78	Successful	---
13.	0.8	Successful	---
14.	0.84	Successful	---
15.	0.90	Successful	---
	Die groove radius (mm)		
16.	3.4	Unsuccessful	Criterion 3 not satisfied
17.	3.6	Successful	---
18.	3.8	Successful	---
19.	4.2	Unsuccessful	Criterion 2 not satisfied
20.	4.4	Unsuccessful	Criterion 2 not satisfied
	Coulomb's friction coefficient		
21.	0.05	Unsuccessful	Criterion 2 not satisfied
22.	0.08	Successful	---
23.	0.12	Unsuccessful	Criterion 2 not satisfied
24.	0.14	Unsuccessful	Criterion 2 not satisfied
.	**Land height (mm)**		
25.	0	Successful	---
26.	1.5	Successful	---
27.	2.5	Successful	---
28.	3	Successful	---
	Lower blank holder height (mm)		
29.	0.1	Successful	---
30.	0.15	Successful	---
31.	0.20	Successful	---
32.	0.25	Successful	---
33.	0.30	Successful	---

All the three criteria are satisfied in successful cases

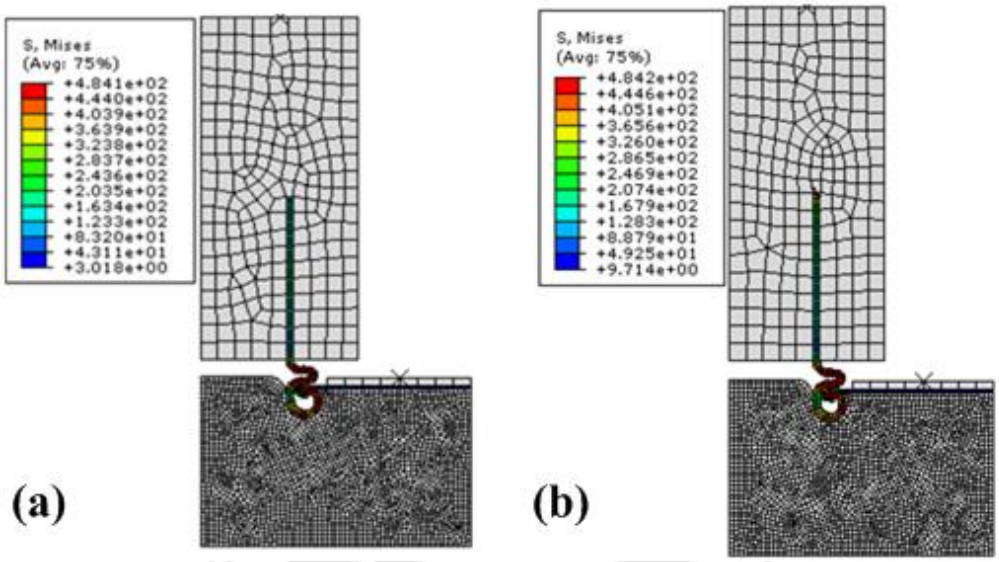

Fig. 2.27 Successfully formed joints through FE simulations (a) Case 2: *L*=76 mm, (b) Case 18: *R*=3.8 mm (refer Table 2.1)

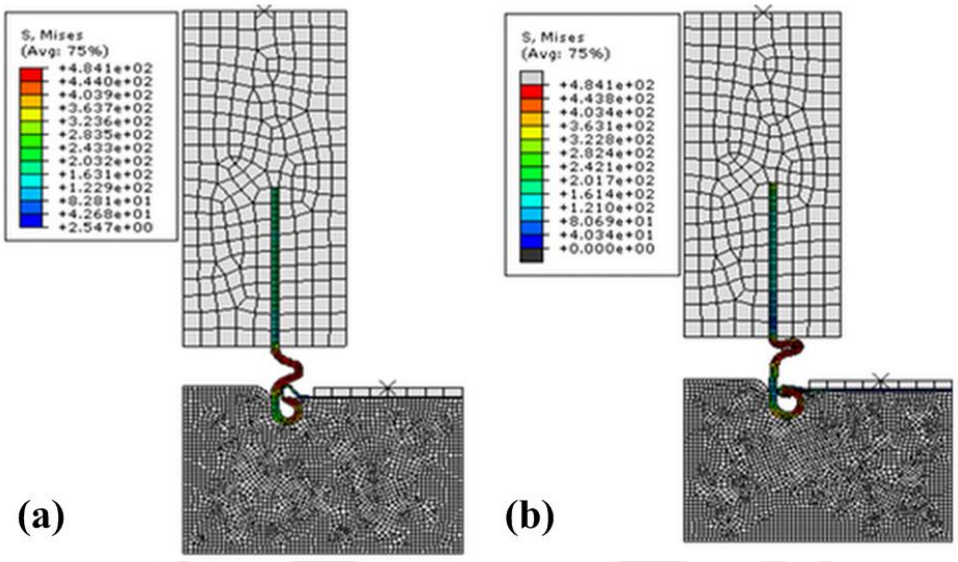

Fig. 2.28 Unsuccessfully formed joints from FE simulation (a) Case 4: *L* = 85 mm (b) Case 16: *R* = 3.4 mm (refer Table 2.1)

2.2.7 Experimental demonstration and validation at laboratory scale

The demonstration of the proposed joining method at laboratory scale has been conducted for three cases described earlier in Table 2.4. Fig. 2.29 shows the final joint fabricated, joining a tube to a sheet, for three different cases, of which Case 3 (Table 2.4) is unsuccessful. The other two cases are successful as per the criteria. In case 3, two necks are formed above the sheet, making it unsuccessful. Fig. 2.30 shows the sectioned view of

all the joint components. The FE simulation results agree well with the experimental results in terms of joint formation.

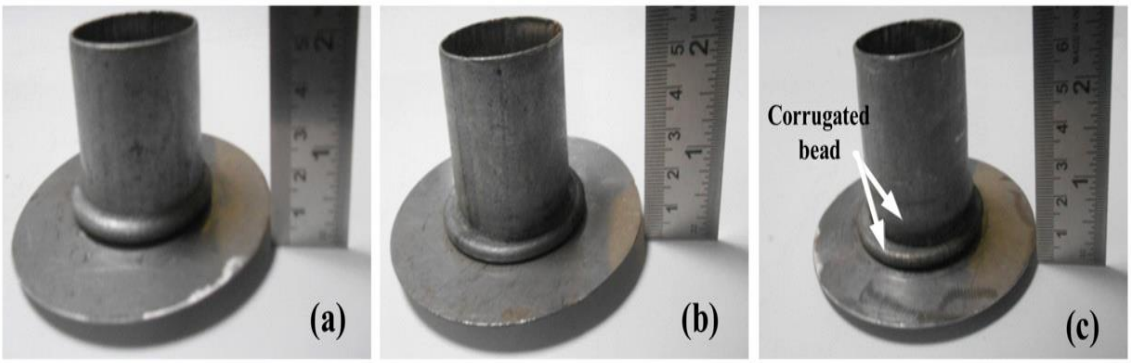

Fig. 2.29 Final joints fabricated (a) Case 1, Successful (b) Case 2, Successful (c) Case 3, Unsuccessful (refer Table 2.4)

The load-displacement behaviour obtained from the experimental trials is compared with the FE simulation results (Fig. 2.31) of the demonstrated joining method. Here a constant Coulomb's friction coefficient of 0.1 is assumed during FE simulations. It is observed that after the start of neck formation, some difference in load is found between the experimental and simulation results. Before that, the load requirement is almost the same. The error is because of the tube failure at the bend region while deforming in the die groove region. This is not captured in the simulations as a failure criterion is required for the purpose. Moreover, the Coulomb's friction coefficient has been assumed constant without experimental evaluation prevailing in the actual situation. This can also contribute to the error. The tube and sheet materials are assumed isotropic which is not actually true. Modeling anisotropy appropriately would improve the experimental validation.

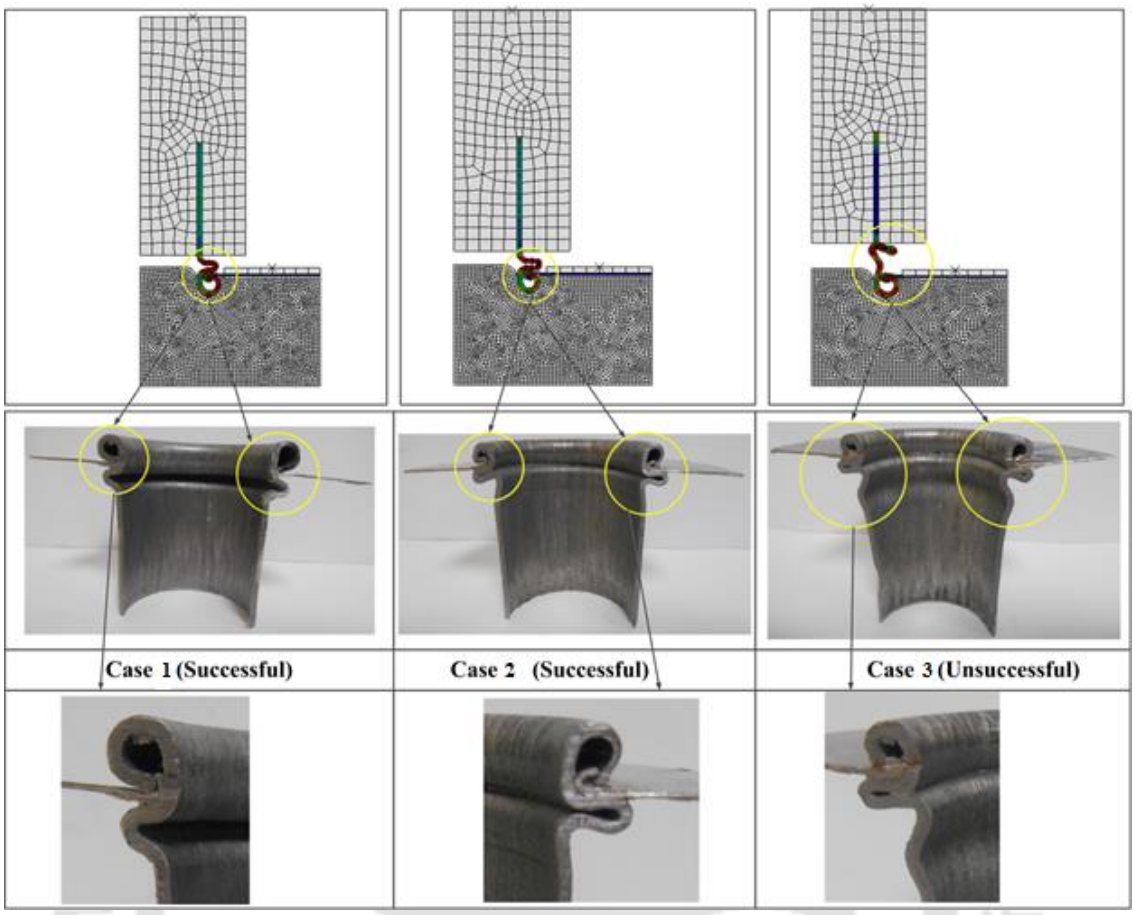

Fig. 2.30 Sectioned view of joints fabricated

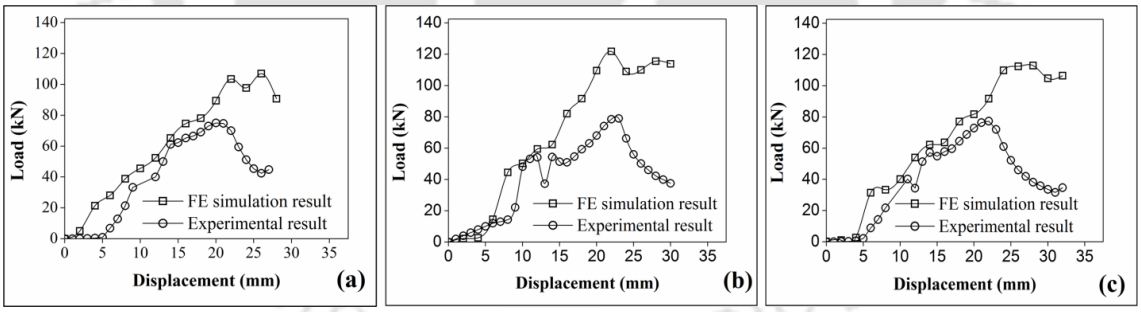

Fig. 2.31 Validation of the load-displacement behaviour for (a) Case 1, Successful (b) Case 2, Successful (d) Case 3, Unsuccessful (refer Table 2.4)

The technology proposed is a green and sustainable technology. A good compact, leakproof joint is obtained in one downward vertical stroke of the punch. The set-up required for the proposed method can be fabricated using existing machine tools. However, accuracy during fabrication is crucial. Mass production of joints using dissimilar materials (tube and sheet) with different sizes can be produced using this method. This technology certainly eradicates some of the major drawbacks of existing

technology like joining through welding, joining by adhesive bonding and joining through fasteners.

Alves et al. (2011b) proposed a different method of joining sheet to a tube using end forming of the tube. This process basically consists of two stages – first stage is compression beading and the second stage is tube inversion. When the proposed method is compared with the existing method, some advantages and limitations of the proposed method can be revealed. In the proposed method, the joining is performed in one downward vertical stroke of the punch and no tool is in contact with the joint location during the joining process, producing a better and compact joint. The preparation of sheet before the actual joining process and regular removal of punches and dies after the process completion are the major limitations of the proposed method.

2.2.8 Load-displacement behaviour and energy absorbed during pull-out tests

During Pull-out tests of the end formed joints and welded joints, it can be observed that joints have not failed, but the part of the sheet which is outside the upper blank holder area during testing is bent in the opposite direction because of the upward pulling force of the punch. Because of the upward pulling of the punch, the curled region of the tube comes out of the bent part of the sheet and unlocking phenomena happens in the tube-sheet joint region. Simultaneously the area of sheet which is outside the upper blank holder area is bent in the opposite direction and bent region (including curvature) is straightened. In case of welded joint, crack is observed closer to the welded region in the sheet. Fig. 2.32 shows the tested samples of end formed joint and weld.

Fig. 2.33 shows the load-displacement behaviour during pull-out tests when flat die is used. Case 3 (refer Table 2.4) takes the largest load to fail though it is unsuccessful in joint formation. The failure load is minimum for welded tube-sheet joints. Case 3 is an unsuccessful case as the bead did not form properly above the sheet. Since the load evolution during pull-out tests depends on the unlocking mechanism of tube-sheet joint below the sheet, locking of tube-sheet joint occurs properly in this case during forming, hence the fracture load for Case 3 does not depend on its unsuccessfulness. Up to a displacement of 6 mm, load evolution for welded joint is larger as compared to end formed joints, but at that point the welded joint cracks in sheet adjacent to the weld and load drops suddenly for the welded joint. For end formed joints complete unlocking needs

larger displacement and hence a larger maximum load is required to unlock the tube-sheet joint. Hence it can be said that since complete unlocking needs larger displacement in case of end formed joints, larger load is required as compared to welded structure in case of flat die.

Fig. 2.34 shows the pull-out data of joints tested for die inclination of 10°. The welded tube-sheet joint takes the largest fracture load among all type of joints. Among the end formed joints, joint made under Case 3 takes the largest load to fail. The fracture load reached for any case in end formed joints is a function of displacement on angular plane. In Case 3, the displacement to complete unlocking is larger and hence fracture load reached is also larger. For end formed joints no physical fracture or crack formation is observed in the joint region, rather an unlocking phenomenon takes place in the tube-sheet joint region. This unlocking phenomenon is considered as fracture in the end formed joint. When welded structure is compared with end formed joints, it is seen that it needs larger load as compared to end formed joints, despite the fact that it needs lesser displacement as compared to Case 1 and Case 3. Since welded structure undergoes physical fracture, it needs larger load as compared to end formed joints which exhibits joint unlocking.

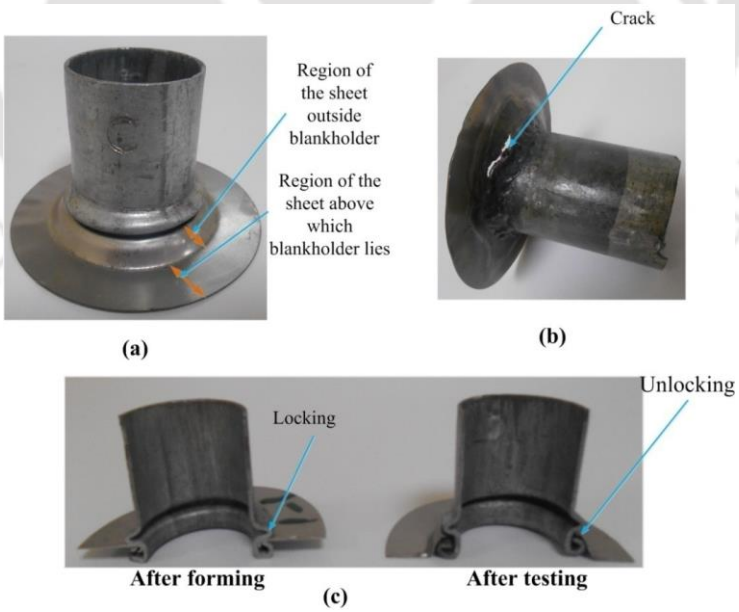

Fig. 2.32 Tested samples of (a) end formed joint, (b) welded joint, (c) sectioned view of end formed joints before and after pull-out tests

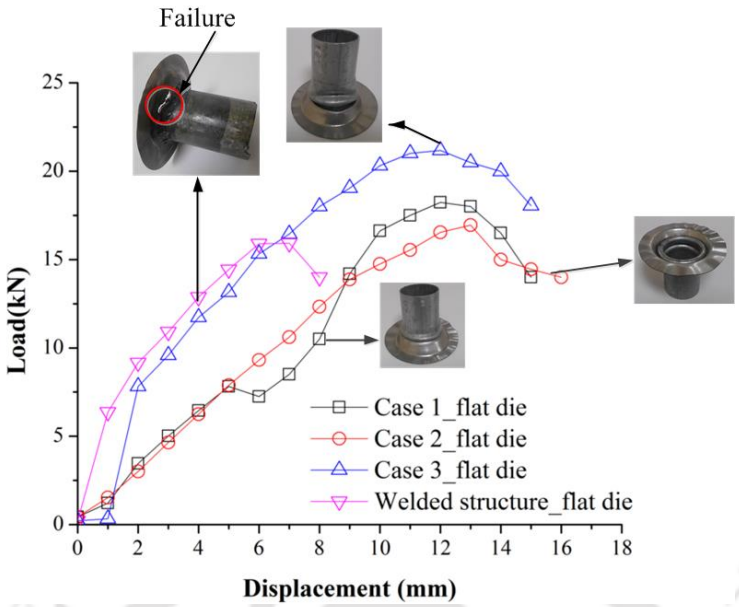

Fig. 2.33 Load-displacement behaviour of joints made under different conditions for flat die

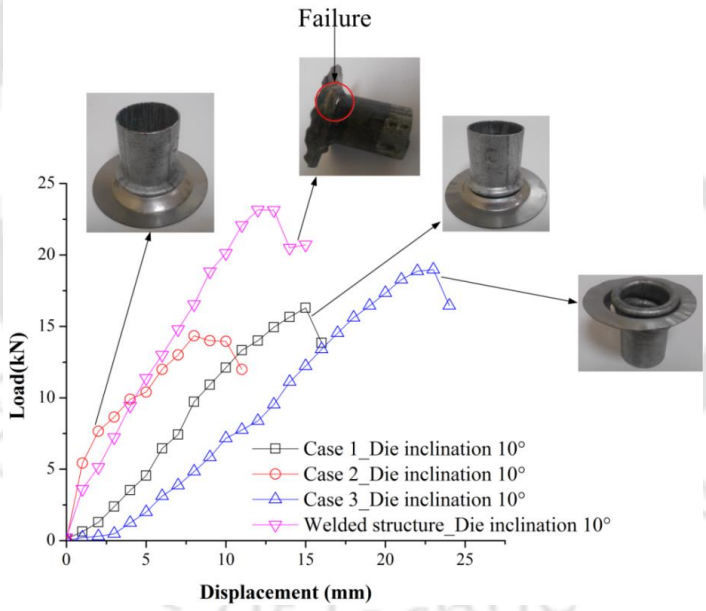

Fig. 2.34 Load-displacement behaviour of joints made under different conditions for die with inclination of 10°

Fig. 2.35 shows the pull-out test results of joints fabricated for die with inclination of 15°. The welded tube-sheet structure takes the largest load to fail. For end formed joints, as the displacement to failure increases, the maximum load required for failure also increases. In Case 3, larger displacement is observed for complete unlocking and hence larger load is required for failure in this case too. Since the welded structure fails near the weld zone, larger fracture load is observed for welded structure among all cases.

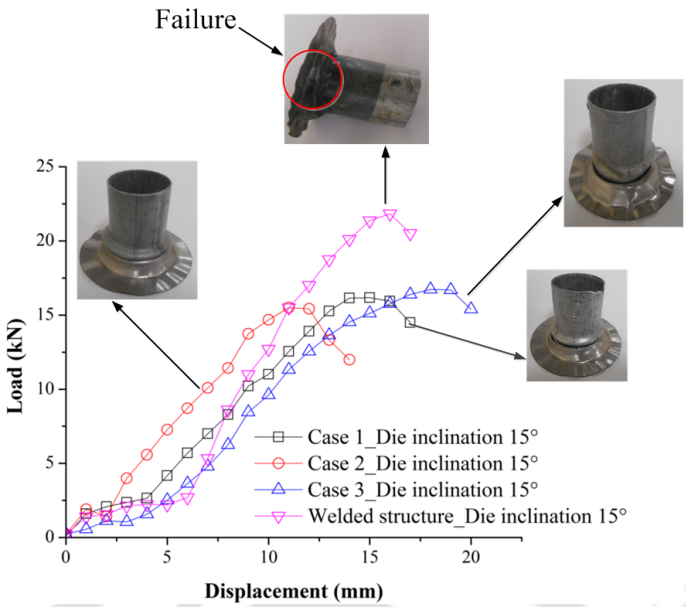

Fig. 2.35 Load-displacement behaviour of joints made under different conditions for die with inclination of 15°

In summary, it can be said that for end formed joints on inclined planes, lesser load is observed as compared to flat die. Here inclination helps in easy removal of the tube from the sheet. For welded structure, the fracture load increases for inclined dies as compared to flat dies. In this case, larger displacement to failure is needed when inclined planes are used and this holds responsible for larger peak load.

Fig. 2.36 shows the summary of variation of fracture load for welded and end formed joints. Though end formed joints perform better than welded joints in case of flat die, the welded joints performance is slightly better in other cases (like 10º and 15º die inclination). There is about 4 to 6 kN difference between the joints for inclined dies. Within end formed joints, Case 3 better performed. The joint performance in case of welded joints depend on metallurgical changes in the weld region as the raw tube is of mild steel category. On the other hand, the end formed joints depend only on mechanical interlocking and strain hardening undergone in the joint region. Though metallurgical changes during joint formation aides in joint strength, the end formed joints are advantageous in few ways.

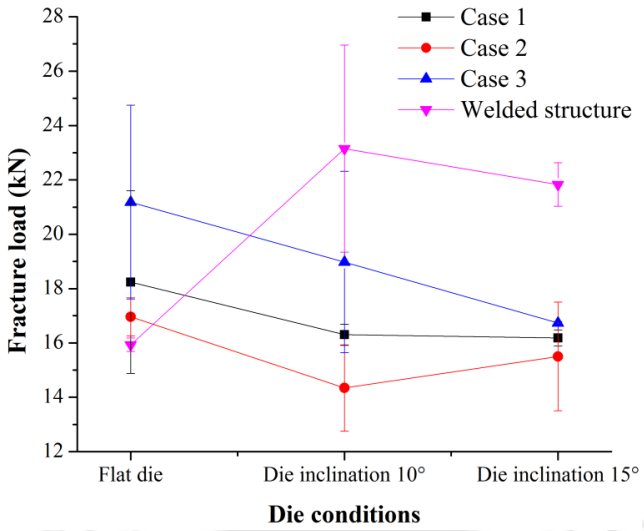

Fig. 2.36 Fracture load for joints made for different joint cases using different dies

There is no fume generation, consumable wastages, health hazards in the case of fabricated end formed joints as compared to arc welded joints or the fusion welding processes. In the case of welded joints, physical failure occurs at lower displacement during pull-out tests. But in end formed joints, since physical failure is not observed, even a slight pull-out displacement will keep the joint intact without quality loss. Complete unlocking takes larger displacement in this case.

Based on equation 2.1, the energy absorbed during pull-out tests of end formed joints and welded joints has been calculated. For this purpose, the load-displacement curves have been fit into a third order polynomial equation of the form A + B. x + C. x^2 + D. x^3. It is assumed that higher the order of fitting curve better would be the accuracy. The adjusting R-square value has also been calculated for different cases. The adjusting R-square value is more than 0.96 for different cases as shown in Table 2.11 which indicates that a better fit between load curve and fit polynomial curve has been obtained. The value of constant A and coefficients, B, C and D are given in Table 2.10 for different cases. Table 2.11 provides a summary of important data from pull-out tests.

Table 2.10 Values of A, B, C and D in the polynomial equation for different cases

Die conditions	Joining conditions	A	B	C	D
Flat die	Case 1(S)*	0.49843	1.34912	-0.02472	0.00354
	Case 2(S)*	0.35015	1.22723	0.08069	-0.0059
	Case 3(US)*	-0.75755	3.99625	-0.25876	0.00666
	Welded structure	0.62939	5.70865	-0.83953	0.04907

Die inclination 10°	Case 1(S)	0.07203	0.3552	0.15771	-0.00736
	Case 2(S)	0.45333	5.0773	-0.91827	0.06316
	Case 3(US)	-0.06013	0.06928	0.08156	-0.00209
	Welded structure	0.61269	2.41905	-0.06427	0.00175
Die Inclination 15°	Case 1(S)	0.7742	0.0498	0.16702	-0.00668
	Case 2(S)	0.3363	0.7465	0.1654	-0.00974
	Case 3(US)	0.57989	-0.40649	0.2027	-0.00729
	Welded structure	1.61041	-1.2201	0.36009	-0.0127

Table 2.11 Summary of important results from the joint pull-out tests

Die conditions	Joining conditions	Energy absorbed (J)	Adj. R-square	Maximum displacement at fracture load (mm)	Fracture load (kN)
Flat die	Case 1(S)*	107.23	0.9659	12	18.24
	Case 2(S)*	125.21	0.9993	13	16.96
	Case 3(US)*	164.12	0.9758	12	21.18
	Welded structure	81.65	0.9824	7	15.93
Die inclination 10°	Case 1(S)	125.32	0.99801	15	16.3
	Case 2(S)	74.05	0.98265	8	14.34
	Case 3(US)	201.50	0.99853	23	18.98
	Welded structure	153.57	0.99794	12	23.15
Die Inclination 15°	Case 1(S)	120.94	0.9945	15	16.18
	Case 2(S)	86.59	0.99106	11	15.5
	Case 3(US)	147.30	0.99707	18	16.73
	Welded structure	153.15	0.98681	16	21.83

*Cases 1,2,3 belong to end formed joint category

From Table 2.11, it is observed that the fracture load obtained and energy absorbed is minimum for welded structure in case of flat die. In case of die with inclination of 10°, the fracture load attained for welded structure is maximum amongst all joints, while energy absorbed for welded structure is intermediate as compared to end formed joints. The die inclination helps the tube to come out from the sheet due to slipping at tube-sheet interacting surface and also physical failure is not seen here. So a lesser load is required to unlock the tube from sheet despite the fact that Case 1 and Case 3 takes larger displacement to attain the peak load as compared to the welded structure. Within end formed joints, Case 3 takes largest load because it needs largest displacement to fracture. Case 3 absorbs more energy because the displacement attained by Case 3 is larger as compared to other cases (Case 1, Case 2 and welded structure). In case of die with inclination of 15°, the peak load attained and energy absorbed are larger for welded structure as compared to end formed joints. In this case, displacement to failure for

welded structure is quite high as compared to flat die and die with inclination of 10º. As a result, energy absorbed increases for welded structure.

2.2.9 FE simulation of pull-out tests of end formed joint

2.2.9.1 Variation in '*D*' for different cases

FE simulation of end formed joint has been performed in ABAQUS explicit (6.17). As it has been explained that '*D*' decreases with displacement. The variation of '*D*' with respect to displacement for different cases under flat die has been shown in Fig. 2.37.

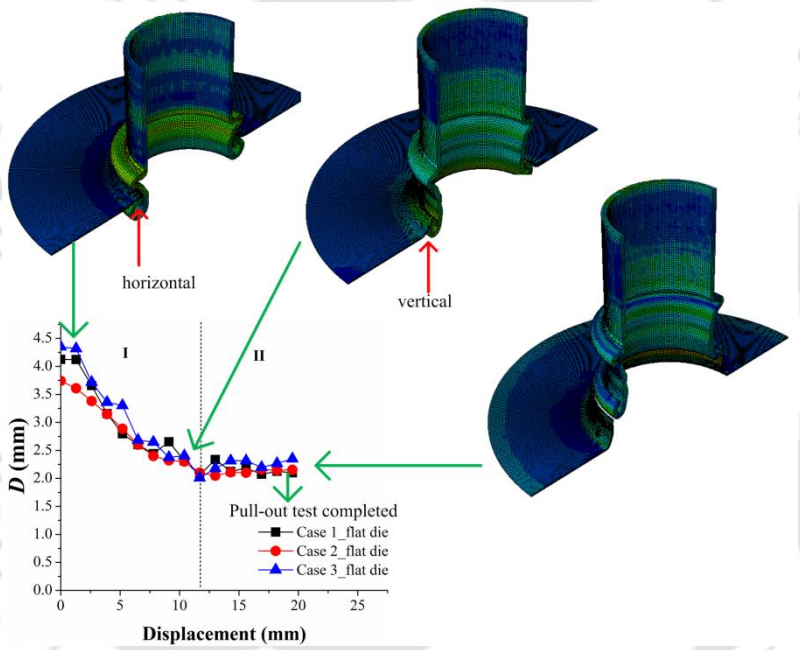

Fig. 2.37 Variation of '*D*' with respect to displacement for different cases tested under flat die

Up to a displacement of 12 mm, '*D*' decreases and then for further displacement it is almost constant. According to the variation in value of '*D*', whole deforming region can be divided into two regions. Region 'I' is that region in which '*D*' monotonically decreases, and region 'II' is that region in which '*D*' is almost constant. Initial value of '*D*' is lowest for Case 2, because of smaller die groove radius, while it is largest for Case 3. But at the end of region 'I', '*D*' is almost same for all the cases.

When the punch is given upward displacement, the curled part of the tube is pulled in upward vertical direction. As a result, the unsupported region (necked region

and curled region) is elongated in vertical direction. Neck slightly expands and after that rest of the deformation is concentrated in the curled region. '*D*' decreases up to a displacement about 12 mm. At this displacement the deforming end of the tube, which is initially horizontal due to designed geometry of the die becomes vertical and points in upward direction (Fig. 2.39). After this, deformation stops in the curled region of tube. As a result, '*D*' is maintained constant thereafter and with upward movement of tube, this vertical edge of tube pushes the bent sheet in the upward direction and sheet finally comes out of the curled part. During simulation studies complete unlocking is defined where the sheet finally comes out of the curled part of the tube. Inset images show the tube-sheet assembly at different stages of deformation for Case 1 during pull-out test simulation.

2.2.9.2 Validation of pull-out load-displacement results

Fig. 2.38 shows a comparison of load evolution between experimental and simulation trials. The nature of load evolution is slightly different for experimental and simulation trials. In case of experimental trials, load increases monotonically up to the displacement where complete unlocking takes place and after that load suddenly decreases. In case of simulation, peak load is attained either at the start of the process or at some intermediate displacement between start and end. For example, in the case of Case 1, peak load is attained at a displacement of 2.5 mm (Fig. 2.38a), while in case of Case 2 and 3 peak load is attained at a displacement of 8 mm ((Fig. 2.38(b, c)) under different testing conditions. Initial unlocking of tube from sheet needs larger load and once the joint becomes loose, load decreases monotonically up to the final unlocking displacement during simulation.

In case of experiments, though tube has been firmly bolted with punch, some slipping has been observed at the interaction of bolt and tube, while during simulation no slip condition has been defined between punch and tube surface. It can cause some deviation of load from the expected value during experiments. In experiments clamping has been done manually, which leads to different blank holding force. A difference in peak load between experimental and simulation trials have been observed. An average peak load difference 'ΔF (peal load)' for any case under different testing conditions has been calculated between experiments and simulations.

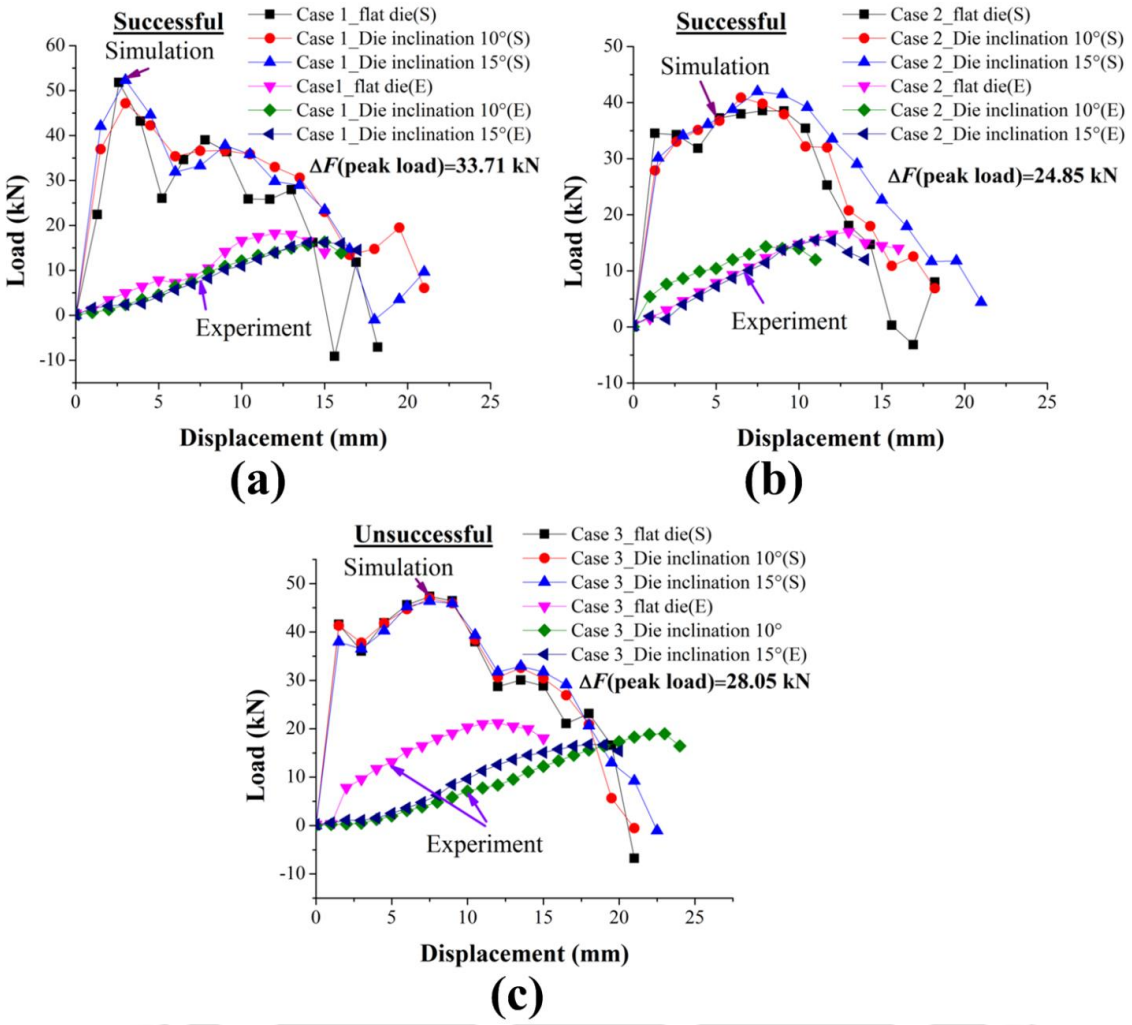

Fig. 2.38 Load-displacement curves for (a) Case 1, (b) Case 2, and (c) Case 3 of end formed joints during FE simulations and experiments (S: Simulation, E: Experiment)

Δ*F* (peak load) has been observed as 34 kN, 25 kN and 28kN in case of Case 1, 2 and 3 respectively. The difference is minimum in Case 2, while it is maximum in Case 1. Manual clamping, slip at the bolt-tube interface and modeling conditions attribute to such load difference. Load evolution during simulation for die inclination 10º and 15º is almost same for different cases and testing conditions, while a minor difference in load evolution is observed for flat die as compared to angular dies. Peak load experienced for different testing conditions do not follow any trend for different cases during simulation. For example, in case of Case 1 maximum load is observed for die inclination of 15º, in case of Case 2 maximum load is observed for die inclination of 15º, and in case of Case 3 maximum load is observed for flat die. During experiments, maximum load is experienced by flat die for different cases under different testing conditions, while during simulation for Case 1 and 2 same trend is not followed. Flat die takes lesser displacement

to completely unlock as compared to angular dies for different cases and testing conditions which is in agreement with experimental result.

Load evolution curve during simulation also conveys the quality of compactness of the joint. For example, for all cases and testing conditions, the load experienced by Case 1 under flat die and die inclination of 15º is largest. Also the displacement at which it is observed is minimum as compared to other cases. It means the most compact joint is obtained in case of Case 1.

Fig. 2.39 shows the completely unlocked images (sectioned view) of tube-sheet end formed joints during pull-out tests. Deformation behaviour of tube and sheet for different cases on different die inclination is clearly visible. The height between neck and curled part of tube for Case 3 (Fig. 2.39 (g-i)) is larger as compared to other cases.

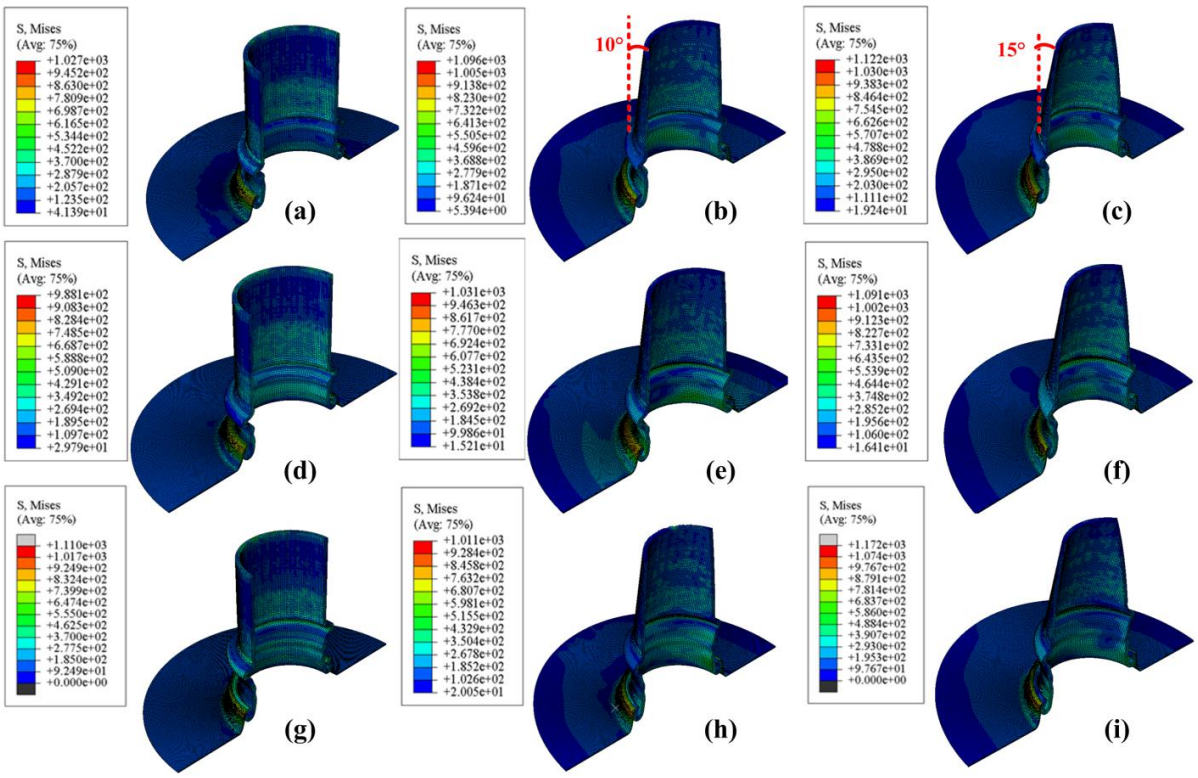

(a),(b),(c): Case1 (flat die, die inclination 10°,die inclination 15°)
(d),(e),(f): Case2 (flat die, die inclination 10°,die inclination 15°)
(g),(h),(i): Case3 (flat die, die inclination 10°,die inclination 15°)

Fig. 2.39 Sectioned and completely unlocked images (tube-sheet) for different cases at different testing conditions

von-Mises stress contour in the tube and the sheet is also different on angular dies as compared to flat dies. The equivalent stress generated in the supported region of tube

in flat dies is almost negligible, but on angular dies, the stresses are generated in the supported region of tube. It means that on flat dies, the whole deformation is concentrated in the joint region, while similar situation does not exist for angular dies.

2.3 Conclusions

From the present work, the following important conclusions are made:

1. A simple and novel method of joining a tube to a sheet through end curling has been proposed and the same has been successfully demonstrated in lab scale. In the context, generally, fusion welding of tubes and sheets is followed contaminating the environment and causing pollution. An alternative for such process towards sustainable manufacturing has been attempted.

2. A comprehensive CAE analyses of the proposed joining method has been performed through FE simulations for an efficient process design. In this, the influence of seven crucial parameters that decides the quality of the joint on the forming behaviour has been predicted. Out of all the parameters, the die groove radius, friction conditions, and tube support length are found to be significant.

3. Three different criteria that quantify the quality of the joints have been proposed. The criteria are simple and can be implemented through visual inspection at the shop floor. The essentiality of measurements and calculations is avoided. Using this, the successfully formed joints are identified through FE simulations. The relationship between the parameters and quality of the joints are brought forward.

4. The FE simulation results are validated with experimental results and the accuracy of the predictions are analyzed. It is also suggested to incorporate a failure criterion in FE simulations to have a much better model for predicting such joining methods.

5. Although the proposed joining technology eliminates the drawbacks of conventional joining technology such as joining through welding, joining by adhesive bonding and joining through fasteners, it has certain demerits like preparation of sheet before the actual joining process and regular disassembly of tools after the process completion.

6. In end formed joint, unlocking phenomenon is observed during pull-out tests, while in welded structure, physical failure is witnessed at tube-sheet joint region.

7. The performance of end formed joints in terms of maximum load is better when flat die is used. Larger displacement at failure required for complete unlocking is the main reason for this. On the other hand, the welded joint performed better when inclined dies are used. In this case, the slip at the tube-sheet interface resulting in easy disassembly of joint is responsible.

8. In end formed joints, for inclined dies, cases with larger displacement at failure required larger fracture load.

9. The trend in energy absorbed for different cases and testing conditions is almost same as that of fracture load.

10. 3D FE simulation of pull-out tests has been successfully done for end formed joints. There exists considerable difference in load-displacement data when compared with experiments. Hence by considering experiments as reference, the simulation accuracy should be improved. The pull-out test simulation method should be used cautiously.

Chapter 3

Joining steel tubes of different diameters by end forming operations

3.1 Methodology

In this section, influencing parameters affecting the proposed joining technology, materials and finite element simulation methodology have been discussed. Later on, few criteria have been discussed through which joint can be divided into successful and unsuccessful. Finally, methodology for lab scale demonstration of few selected joint cases and for strength evaluation of the joints have been discussed.

3.1.1 Parameters and mechanics of the proposed technology

The present joining technology involves tube external inversion and tube beading for joint formation. The schematic of the complete joining process, and the definition of process parameters have been shown in Fig. 3.1(a, b). Split punch and die are used for easy removal of tubes after joining.

Two active tool components have been used in the proposed technology. The first component is the punch or upper tool which houses the inner tube (tube having smaller outer diameter) and the second component is the lower tool or die which houses the outer tube (tube having larger outer diameter). When the punch is provided downward vertical displacement, the inner tube travels through the circular arc region in the die, and when it leaves the circular arc region, it is externally inverted. In the meantime, the outer tube comes in contact with the projected height of the punch and bead formation starts. With further vertical displacement, the inverted end of the inner tube makes contact with the inner surface of the outer tube during inside-out inversion. Finally, the inner tube is compressed within the bulged region of the outer tube to accomplish a successfully formed joint (Fig. 3.1a).

The inner tube has total length L_1 and supported length S, while the outer tube has total length L_2 and supported length S (Fig. 3.1b). In the present work, the supported length (S) is same for both tubes and is equal to 25 mm. The length of inner tube and outer tube decides the gap between projected section of the punch and upper free edge of outer tube. A larger gap will not be appropriate for a sound joint formation. Hence optimization of inner and outer tube lengths is necessary. A larger or shorter projected

height (H) is responsible for the early or late beading. Hence optimization of the projected height is also necessary. Coulomb's friction coefficient (μ) in general affects the metal forming processes. Local deformation such as inside buckling or outside buckling may take place in the inner tube when the load reaches its buckling limit during forming. Local deformation of the inner tube has been studied by providing an offset distance of punch h at the outer radius of the inner tube.

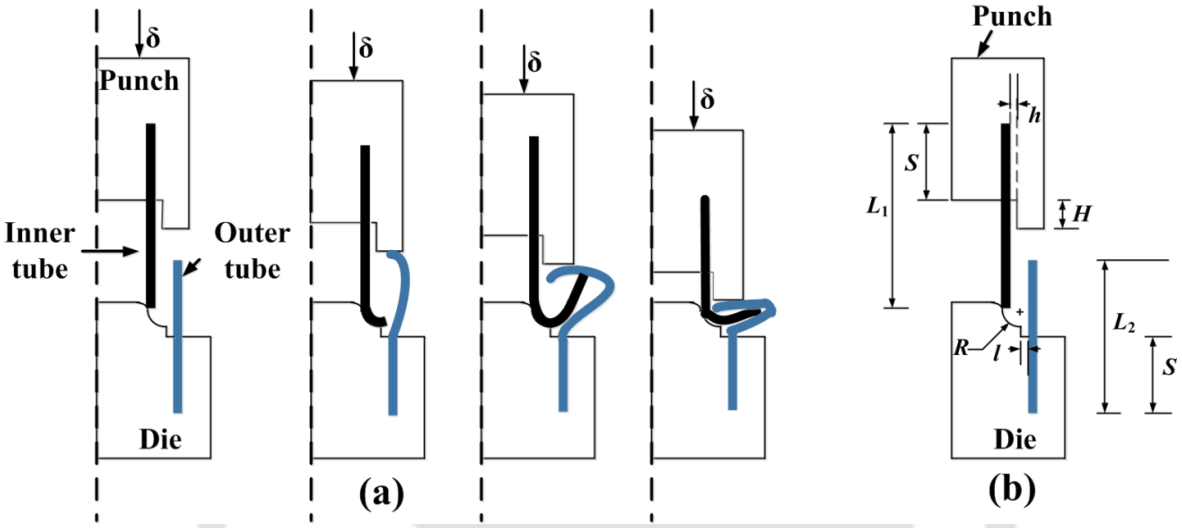

Fig. 3.1 End-to-end joining of tubes, (a) step by step schematic of tube-to-tube joining (not to scale), (b) definition of process parameters

Circular arc radius (R) of die is responsible for invertion of tube. Double walled gap (g) increases with increase in circular arc radius (Figs. 3.2(a-e)). This factor plays a key role in joint formation. Offset distance of outer tube l is the distance between the inner diameter of the outer tube and the point where circular arc ends. Keeping all other parameters constant, the variation of l influences the circular arc angle (α) as shown in Figs. 3.2(f-j). The influence of α on the forming of the inner tube has been shown in Figs. 3.2(f-j). As α increases, the inclination of the inverted section from vertical shifts from outward to the inward direction, and consequently the inclination angle (angle between vertical plane and plane of inverted section) shifts from outward to inward direction. Fixing vertical plane as the reference plane, the inclination angle (β) corresponding to Figs. 3.2(g-i) will be taken as positive and for Fig. 3.2j as negative, and will be referred henceforth throughout this chapter. The extreme conditions of α (Fig. 3.2f and 3.2j) and g (Fig. 3.2a and 3.2e) are not found to be appropriate for joint formation. Considering the influence of l on the joint formation, it has been considered as one of the parameters.

Selected process parameters along with their levels are shown in Table 3.1. The levels are selected based on extensive initial computational trials.

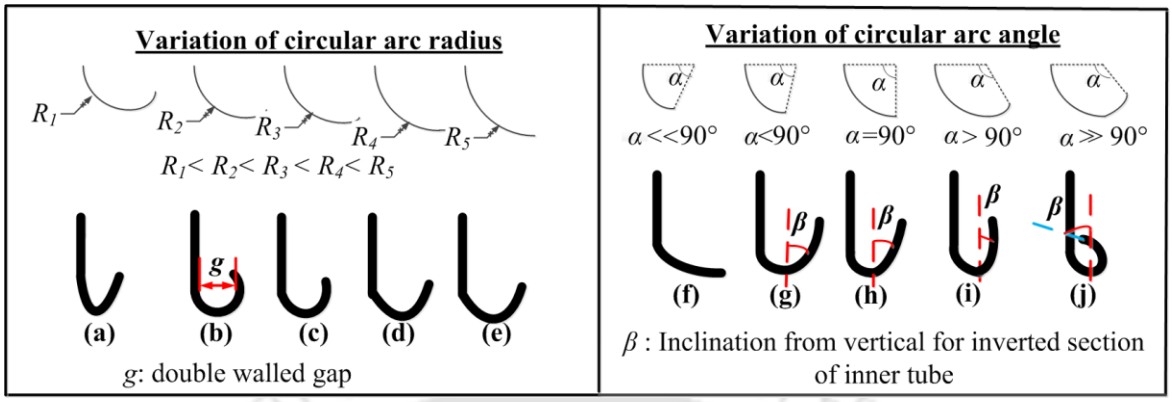

Fig. 3.2 Deformation behaviour of inner tube associated with variation in R and α, other parameters are kept constant

Table 3.1 Selected process parameters and their levels

Case no.	μ	L_1/S	L_2/S	h (mm)	H (mm)	l (mm)	R (mm)
Cases with varying μ, other parameters are kept constant							
1.	0.01	2.52	2.2	1	10.2	2	5
2.	0.05	2.52	2.2	1	10.2	2	5
3.	0.10	2.52	2.2	1	10.2	2	5
4.	0.15	2.52	2.2	1	10.2	2	5
5.	0.20	2.52	2.2	1	10.2	2	5
Cases with varying L_1/S, other parameters are kept constant							
6.	0.01	2.36(59/25)	2.2	1	10.2	2	5
7.	0.01	2.44(61/25)	2.2	1	10.2	2	5
8.	0.01	2.52(63/25)	2.2	1	10.2	2	5
9.	0.01	2.60(65/25)	2.2	1	10.2	2	5
10.	0.01	2.68(67/25)	2.2	1	10.2	2	5
Cases with varying L_2/S, other parameters are kept constant							
11.	0.01	2.52	2.04(51/25)	1	10.2	2	5
12.	0.01	2.52	2.12(53/25)	1	10.2	2	5
13.	0.01	2.52	2.20(55/25)	1	10.2	2	5
14.	0.01	2.52	2.28(57/25)	1	10.2	2	5
15.	0.01	2.52	2.36(59/25)	1	10.2	2	5
Cases with varying h, other parameters are kept constant							
16.	0.01	2.52	2.2	0	10.2	2	5
17.	0.01	2.52	2.2	1	10.2	2	5
18.	0.01	2.52	2.2	3	10.2	2	5
19.	0.01	2.52	2.2	5	10.2	2	5
20.	0.01	2.52	2.2	7	10.2	2	5
Cases with varying H, other parameters are kept constant							
21.	0.01	2.52	2.2	1	4.2	2	5
22.	0.01	2.52	2.2	1	7.2	2	5
23.	0.01	2.52	2.2	1	10.2	2	5
24.	0.01	2.52	2.2	1	13.2	2	5
25.	0.01	2.52	2.2	1	16.2	2	5
Cases with varying l, other parameters are kept constant							

26.	0.01	2.52	2.2	1	10.2	0	5
27.	0.01	2.52	2.2	1	10.2	1	5
28.	0.01	2.52	2.2	1	10.2	2	5
29.	0.01	2.52	2.2	1	10.2	3	5
30.	0.01	2.52	2.2	1	10.2	4	5
Cases with varying *R*, other parameters are kept constant							
31.	0.01	2.52	2.2	1	10.2	2	4
32.	0.01	2.52	2.2	1	10.2	2	5
33.	0.01	2.52	2.2	1	10.2	2	6
34.	0.01	2.52	2.2	1	10.2	2	7
35.	0.01	2.52	2.2	1	10.2	2	8

To propose such a joining method through lab experiments is costly and time-consuming. Hence the present technology has been proposed and analyzed through Computer Aided engineering (CAE) analyses using finite element (FE) simulations. Extensive FE simulations have been performed to design the joining method. FE simulation code used is ABAQUS (version 6.17). Based on the critical findings of initial preliminary simulations, process parameters and their levels have been decided. Totally 29 systematic simulations have been done for process analyses. Some extra simulations have also been done later on to obtain finer details.

3.1.2 Materials used

The tubes are made of carbon steel (0.20-0.22 %) and are used in as-received condition from the supplier. The inner tube has an outer diameter of 43 ± 0.1 mm and thickness of 3.48 ± 0.05 mm, while the outer tube has an outer diameter of 60.6 ± 0.1 mm and thickness of 3.35 ± 0.08 mm.

For calculation of mechanical properties of tubes, the tensile testing of tube material has been done in an INSTRON machine of load capacity 250 kN at a cross-head speed of 1 mm/min. The standard followed for preparation of tensile specimen is ASTM-E8 (subsize 3) (gauge length: 12.5 mm, gauge width: 3.2 mm, shoulder length: 30 mm and shoulder width: 10 mm). The captured load-displacement data has been converted into engineering stress-strain data with the help of initial dimensions of the specimen. Later on, yield strength, ultimate tensile strength, uniform and total elongation (at 12.5 mm gauge length), true stress, true strain, strain hardening exponent 'n' and strength coefficient 'K' have been calculated as per the established procedures. The mechanical properties of the inner tube and the outer tube have been shown in Table 3.2. The true stress-strain data are fit using the Hollomon's power law, $\sigma = K\varepsilon^n$ (Hollomon, 1945;

Hollomon and Jaffe, 1947). The constitutive data (true stress-strain data) from experiments and fit data from power law for both the tube materials are shown in Fig. 3.3. The true stress-strain curves of both the tubes are extended to larger strain values encountered in tube joining simulations by implementing the strain hardening laws $\sigma = 1368\varepsilon^{0.34}$ (for the outer tube) and $\sigma = 636\varepsilon^{0.23}$ (for the inner tube) during FE simulations in ABAQUS. Plastic strain ratio '*r*' (ratio of true width strain and true thickness strain) has been calculated for both the tubes (Table 3.2) by following E517-00 ASTM standards.

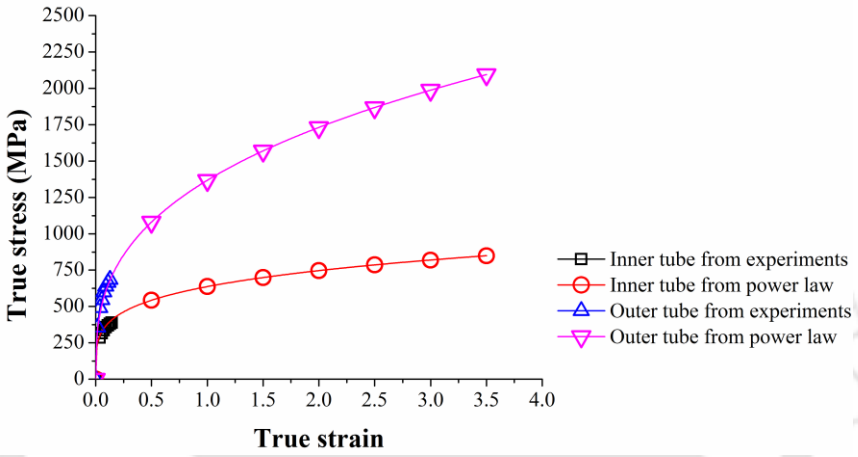

Fig. 3.3 True stress-strain curves for inner tube and outer tube

Table 3.2 Mechanical properties of tubes

Tube	Yield strength (MPa)	Ultimate tensile strength (MPa)	Uniform elongation (%)	Total elongation (%)	Strain hardening exponent, '*n*'	Strength coefficient, '*K*' (MPa)	Plastic strain ratio '*r*'
Inner	182±15	368±22	17±2	35±3	0.23±0.007	636±23	1.09±0.03
Outer	124±38	562±23	18.5±3	28±4	0.34±0.02	1368±83	0.69±0.02

3.1.3 FE simulation details

A dynamic explicit ABAQUS 6.17 FE code has been used for simulation purpose. Numerical simulations based on a dynamic explicit FE method can deal with complicated forming problems and can effectively show the effects of various process parameters. A 2D axisymmetric model has been used to analyze the joining method, as a 3D model takes longer computational time. Hence for the large number of simulations, 3D modeling is not appropriate.

Both the tubes are defined as deformable, while punch and die are defined as rigid parts. Four node bilinear axisymmetric quadrilateral solid elements with reduced integration (one integration point per element) and hourglass control (CAX4R) has been used to discretize the tube, while 3 node linear triangular elements along with 4 node quadrilateral elements (CAX3 and CAX4R) has been used for rigid ones. The time period used is 0.3 s. A penalty type contact between surfaces with a Coulomb's friction coefficient depending upon the cases as shown in Table 3.1 has been used. Die has been kept fixed during simulation, while punch has been provided a downward vertical displacement of 35 mm. An element size of 2 mm has been used for punch, while for die a mesh size of 0.25 mm has been used which appropriately defines the curved geometry of the die. Boundary constraints are applied by "displacement/rotation" option, while tabular amplitude curves have been used. Time scaling factor 1 has been used for the present problem. A mesh sensitivity analysis for tubes has been done, and an element size of 0.65 mm has been defined for tubes which results in five elements in thickness direction for both the tubes. For a typical simulation case, the total number of elements and nodes created for the whole model is 30807 and 31062 respectively.

Important steps for a successful joint formation in case of an axisymmetric model has been shown in Fig. 3.4. The joining mechanism successfully works here. The inner tube enters well inside the bulged region of outer tube after inside-out inversion (Fig. 3.4c) which upon compression through projected height of punch accomplishes a successful tube-tube joint (Fig. 3.4d).

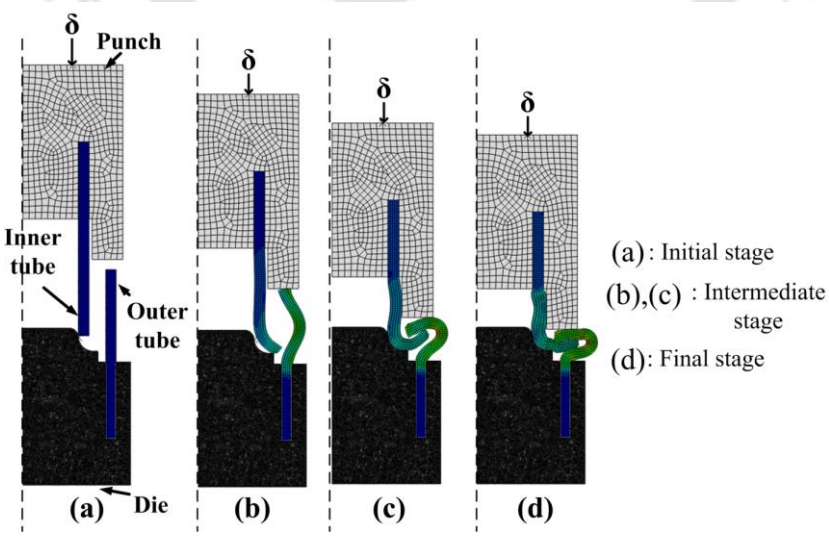

Fig. 3.4 Different stages during a successful tube-tube joining process

Hill's 1948 yield function is considered to model the plasticity of tubes through thickness. This model is explained as follows (Banabic, 2010),

$$f(\sigma) = \sqrt{F(\sigma_{22} - \sigma_{33})^2 + G(\sigma_{33} - \sigma_{11})^2 + H(\sigma_{11} - \sigma_{22})^2 + 2L\sigma_{23}^2 + 2M\sigma_{31}^2 + 2N\sigma_{12}^2} \quad (3.1)$$

where

$$\left.\begin{aligned} F &= \frac{1}{2}\left(\frac{1}{R_{22}^2} + \frac{1}{R_{33}^2} - \frac{1}{R_{11}^2}\right) \\ G &= \frac{1}{2}\left(\frac{1}{R_{33}^2} + \frac{1}{R_{11}^2} - \frac{1}{R_{22}^2}\right) \\ H &= \frac{1}{2}\left(\frac{1}{R_{11}^2} + \frac{1}{R_{22}^2} - \frac{1}{R_{33}^2}\right) \\ L &= \frac{3}{2R_{23}^2}, M = \frac{3}{2R_{13}^2}, N = \frac{3}{2R_{12}^2} \end{aligned}\right\} \quad (3.2)$$

According to the general form of Hill's quadratic yield criterion, the equivalent stress is given as follows,

$$\overline{\sigma_y} = \sqrt{\frac{3}{2}}\left[\frac{F(\sigma_2-\sigma_3)^2+G(\sigma_3-\sigma_1)^2+H(\sigma_1-\sigma_2)^2}{F+G+H}\right]^{\frac{1}{2}} \quad (3.3)$$

Where *F*, *G*, *H*, *L*, *M*, *N* are coefficients of Hill's 1948 yield function that can be imported to the ABAQUS by six yield factors R_{11}, R_{22}, R_{33}, R_{12}, R_{13} and R_{23}.

The equivalent strain and the ratio of incremental minor strain to the major strain are calculated using Hill's criterion as follows,

$$\bar{\varepsilon} = \frac{1+\bar{r}}{\sqrt{1+2\bar{r}}}\left[(\varepsilon_1)^2 + (\varepsilon_2)^2 + \frac{2\bar{r}}{1+\bar{r}}(\varepsilon_1)(\varepsilon_2)\right]^2 \quad (3.4)$$

$$\beta = \frac{d\varepsilon_2}{d\varepsilon_1} \quad (3.5)$$

Where the average value of the plastic strain ratio can be calculated by the following relation,

$$\bar{r} = \frac{r_0+2r_{45}+r_{90}}{4} \quad (3.6)$$

For plane stress condition, the six yield factors R_{11}, R_{22}, R_{33}, R_{12}, R_{13} and R_{23}, can be calculated using plastic strain ratios r_0 (r_x), r_{45} and r_{90} (r_y) by the following relations (equation 3.7) (Karajibani et al., 2015) and has been shown in Table 3.3.

$$\begin{aligned} &R_{11}= R_{13}= R_{23}=1 \\ &R_{22}=\sqrt{\frac{r_y(r_x+1)}{r_x(r_y+1)}} \\ &R_{33}=\sqrt{\frac{r_y(r_x+1)}{(r_x+r_y)}} \\ &R_{12}=\sqrt{\frac{3(r_x+1)r_y}{(2r_{45}+1)(r_x+r_y)}} \end{aligned} \qquad (3.7)$$

In the present model, the plastic strain ratio (r) has been calculated only along the length of the tube and has been assumed to be same in other directions. In circumferential direction r-value has not been calculated. The specimen needs flattening for circumferential material preparation before testing and this can affect its properties. Hence for present model,

$$r_x = r_y = r_{45} = r \qquad (3.8)$$

The r-value of the inner tube is close to unity, but for the outer tube it is less than 1 (Table 3.2). Hence to explain the anisotropic behaviour of tubes, the inclusion of anisotropic properties in the yield function is required and it gives better results over von-Mises yield function which is meant for an isotropic material. To model the anisotropic behaviour of tubes, a local material orientation has been assigned to tubes.

Table 3.3 Anisotropic parameters used for FE simulations

	R_{11}	R_{22}	R_{33}	R_{12}	R_{13}	R_{23}
Inner tube	1	1	1.023	0.9925	1	1
Outer tube	1	1	0.9191	1.032	1	1

3.1.4 Theoretical model for joining tubes

Yu et al. (2016) developed theoretical model of a metal tube inversion over circular dies (Fig. 3.5a). Since in the present work inner tube undergoes inside-out inversion, the model described by Yu et al., has been found appropriate for calculating

load theoretically. However, some modifications have been done in the existing model which is discussed in this section.

In Yu et al. work, a circular tube with original thickness t_o and average radius R_o is compressed along the axial direction under force P, over a circular die of radius $r_{d.}$ The tube is inverted from inside to outside with an outer radius R_e. For the theoretical load calculation they have divided the whole deforming region in two parts. First part is die contacting region AB and the second is free curling region CB. r_i is the curling radius in part AB and r_x is the curling radius in part CB.

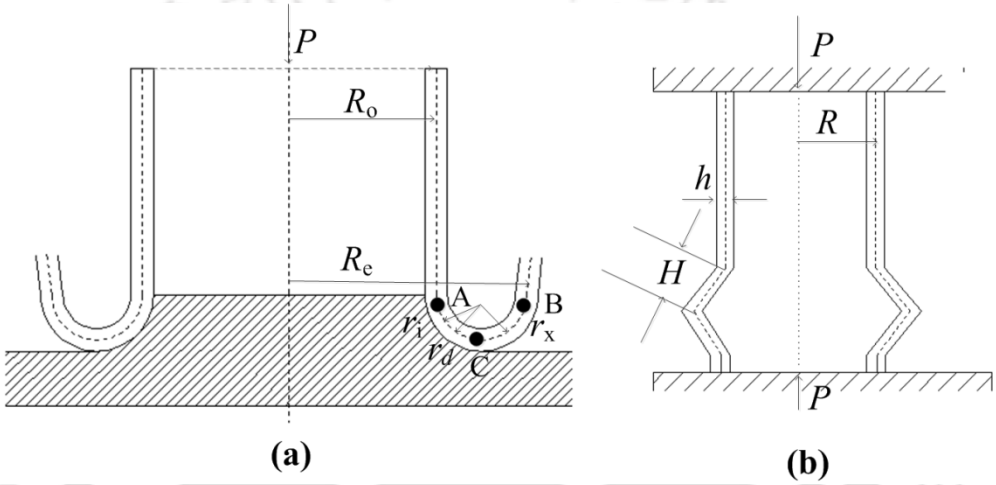

Fig. 3.5 Theoretical model for tube inversion and beading, (a) Schematic of tube inversion developed by Yu et al. (2016), (b) Schematic of tube axial beading process described by Abramowicz and Jones (1984)

The model developed by Yu et al. for theoretical load calculation is:

$$P = 2\Pi R_o t_o \,(E_{AC} + E_{CB})$$

where

E_{AC}= Density of plastic energy dissipation per unit volume in region AC

E_{CB}= Density of plastic energy dissipation per unit volume in region CB

$$E_{AC} = \frac{1}{t_o}\,(M_p K_A + N_p \varepsilon_{AC}) \qquad (3.9)$$

$$E_{CB} = \frac{1}{t_o}\,(M_p K_B + N_p \varepsilon_{CB})$$

here

M_p = Fully plastic bending moment= $Y\frac{{t_o}^2}{4}$

Y= Yield stress of the material

$N_p = Yt_o$= Fully plastic membrane force

$K_A, K_B = \frac{1}{r_i}, \frac{1}{r_x}$ =Curvature at point A and B for region AC and CB respectively

$\varepsilon_{AC}, \varepsilon_{CB}$= $\frac{r_i}{R_o}, \frac{r_x}{R_o + r_i}$ = Corresponding strain in the region AC and CB respectively

The assumptions followed are,

1. The material undergoing forming is considered rigid-perfectly plastic.

2. Tube thickness and material velocity in the meridional direction remain constant during the inverting process.

3. Friction between tube and die has been ignored.

The same model equation (3.9) is used in the present work for evaluating load in tube inversion process with the following modifications.

1. Instead of rigid-perfectly plastic model, a strain hardening model has been considered.

2. Instead of engineering strain, true strain has been considered in the modified model.

3. Anisotropy of both tubes has been considered for FE simulations.

After implementing all these modifications in the existing model by Yu et al., the final modified equation becomes:

$$P = 2\Pi R_o [K'(\frac{1}{\rho i})^n . \frac{{t_o}^{n+2}}{(n+2)2^{n+1}} . \frac{1}{r_i} + N_{p_{AC}} . ln(1 + \frac{r_i}{R_o}) + K'(\frac{1}{\rho x})^n . \frac{{t_o}^{n+2}}{(n+2)2^{n+1}} . \frac{1}{r_x} \quad (3.10)$$

$$+ N_{p_{CB}} ln(1 + \frac{r_x}{R_o + r_i})]$$

$K'(\frac{1}{\rho i})^n . \frac{{t_o}^{n+2}}{(n+2)2^{n+1}}$ = Bending moment applied in strain hardening model

K' = Strength coefficient in strain hardening model

ρi , ρx= Curvature at points A and B

$N_{PAC} = K\bar{\varepsilon}_{AC}^{\,n} t_o$ and $N_{PCB} = K\bar{\varepsilon}_{CB}^{\,n} t_o$ are fully plastic membrane force in region AC and CB respectively

$\bar{\varepsilon}$ is the plastic equivalent strain and is calculated over a range of elements in deforming region of tubes. Since FE simulations are performed with Hill's anisotropic yield function, anisotropic effect is included through such strain measurement/averaging

Abramowicz and Jones (1984) mentioned the mean crushing load (equation 3.11) required for dynamic axial crushing of tubes which is similar to the beading process of outer tube in the present work (Fig. 3.5b).

$$P_m = \frac{2\Pi\sigma_o h H^2 (1+\frac{H}{3R})}{2H} \tag{3.11}$$

where

σ_o = Uniaxial yield stress, h = Thickness of tube, $2H$ = Initial distance of free region which is bent, R = Average radius of tube

Equation (3.11) is used in the present work for load evaluation in tube beading process with the following modifications.

Instead of constant uniaxial yield stress, a strain hardening model has been followed. The expression for load becomes to be:

$$P_m = \frac{2\Pi(K\bar{\varepsilon}^n) H^2 h (1+\frac{H}{3R})}{2H} \tag{3.12}$$

Anisotropy has been considered in the equation by calculating averaged equivalent strain over a range of elements in the deforming region.

3.1.5 Criteria to assess the quality of joint formed

A number of criteria, specific to the proposed joining technology, have been developed to assess the quality of joint formed. The criteria developed are simple such that on the shop floor, by simple observation, the quality of joint (successful or unsuccessful) can be decided. The criteria developed are as follows:

1. Inner tube should be almost horizontal in the bulged region of the outer tube with no overlapping at the free end of the inner tube. Practically no gap is allowed between the

inverted edge of the inner tube, and the point which lies on the inner surface of the peak bulged region of the outer tube. However, some gap (*G*) is observed for most of the cases during simulation. Hence practically a gap of 3.5 mm is allowed. If the gap is more than 3.5 mm the joint will be considered unsuccessful.

2. Inner tube should be fully compressed within the bulged region of the outer tube for good joint formation. Hence practically the surfaces of inner tube should touch the inner surfaces of the bulged region of outer tube properly without leaving any gap between the surfaces (Fig. 3.6).

3. The free region of the inner tube should not buckle either externally or internally for a proper joint formation. If buckling happens, the joint formation is termed as unsuccessful, otherwise considered successful.

The criteria are summarized in Fig. 3.6. The gap between the free end of inner tube and peak bulged height (inner surface) is termed as '*G*' and should not be more than 3.5 mm. Length of inner tube entering the bulged region of the outer tube is denoted as '*Q*'. *Q* is defined as the distance between mid-thickness of the inner tube and inverted end of the inner tube. For successfully formed joints '*Q*' should be larger along with satisfying other criteria. It is expected that a larger *Q* will result in lower *G*, yielding a stronger joint.

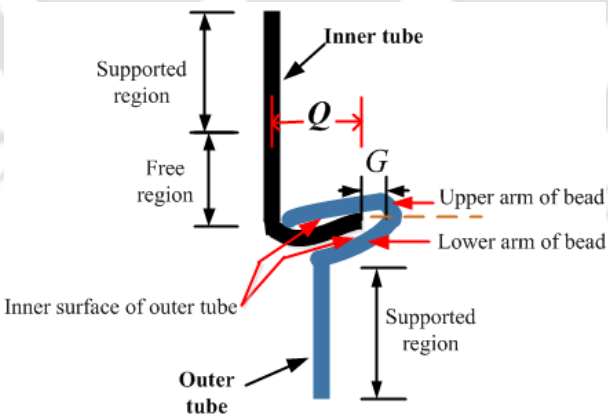

Fig. 3.6 Schematic representation of criteria developed for joint quality analyses

3.1.6 Laboratory scale demonstration

Three cases, Case 15, 21 and 29, have been chosen for lab scale demonstration of the proposed joining method. Out of these, cases 15 and 29 represent successful cases, while the case 21 represents unsuccessful one. Both the successful and unsuccessful cases are demonstrated in experiments. The joining experiments have been conducted in a UTM machine of load capacity 1000 kN at a cross-head speed of 1 mm/min. The fabricated tools for experiments along with the end product have been shown in Fig 3.7. Selected cases for lab scale demonstration have been shown in Table 3.4.

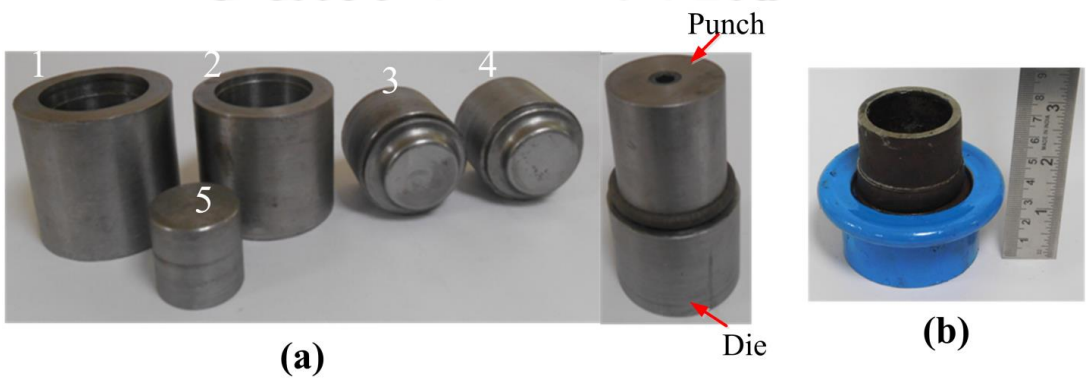

Fig. 3.7 End to end joining of tubes, (a) Disassembled and assembled view of active tools used in tube to tube joining process, (1: Punch with projected height 10.2 mm, 2: Punch with projected height 4.2 mm, 3: Die with offset distance for outer tube 2 mm, 4: Die with offset distance for outer tube 3 mm, 5: Cylindrical block used to support the inner tube inside punch), (b) Final tube-tube joint product

Table 3.4 Selected cases for lab scale demonstration from Table 3.1

Case	μ	L_1/S	L_2/S	h	H	l	R
15.	0.01	2.52	2.36(59/25)	1	10.2	2	5
21.	0.01	2.52	2.2	1	4.2	2	5
29.	0.01	2.52	2.2	1	10.2	3	5

(Case 15: Successful, Case 29: Successful, Case 21: Unsuccessful)

3.1.7 Mechanical testing of the fabricated joints

Pull out tests and compressive tests are performed on the joints fabricated. The schematic of the tests has been shown in Fig. 3.8(a, b). The performance of the tube to tube joints fabricated by end forming has been compared with tube to tube joints made by electric arc welding. Tubes have been welded at their ends using electric arc welding with mild steel as filler material. For pull out tests, inner and outer tubes have been supported through mandrel as shown in Fig. 3.8a. Mandrels are fastened through outer and inner

tubes using fasteners, while for compression test the fabricated joints have been compressed directly (Fig. 3.8b) in an UTM. Fig. 3.8c and 3.8d show the experimental set-up for the pull out tests and compression tests. The load-displacement data has been compared for analyses.

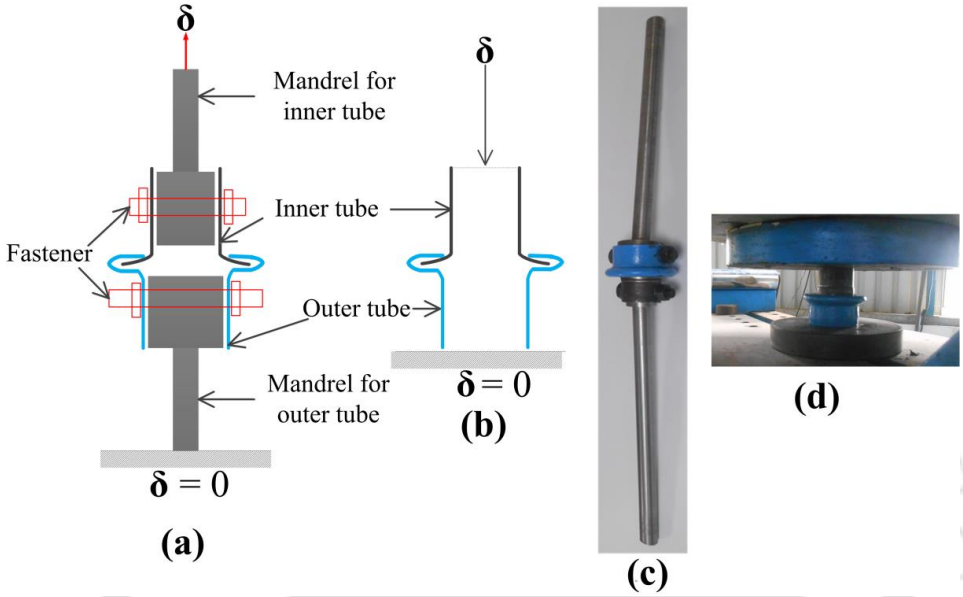

Fig. 3.8 Schematic of (a) pull-out tests, (b) compression tests, (c) experimental set-up fabricated for pull out test, (d) experimental set-up for compression test (not to scale)

3.2 Results and discussion

In this section, firstly, mesh size analysis for both the tubes has been discussed. The effect of parameters on load evolution and thickness evolution has been discussed after that. Later on, criteriawise division of the joints into successful and unsuccessful cases has been done. Laboratory scale demonstration for few selected cases has been presented. Finally, mechanical testing of the joints has been discussed.

3.2.1 Mesh sensitivity analysis

Element size affects the accuracy and the scale of computation time in FE simulation. Hence mesh sensitivity analysis has been done prior to main joining simulations to select the optimum element size. Case 15 (Table 3.1) has been chosen for mesh sensitivity analysis which is a successful case as per criteria provided earlier. Number of elements in through thickness direction has been varied between one to fourteen for both the tubes, keeping same number of elements for both tubes at a time. For number of elements lying in the range of 2-8 a successful joint is seen, whereas in

other cases (particularly with higher mesh density), a significant mesh distortion in the joint region results in simulation error before completion. Load–displacement behaviour (Fig. 3.9a) for successful cases is shown to find the optimum mesh size. Here n(O) is the number of elements through thickness in outer tube, n(I) is the number of elements through thickness in inner tube and *T* is the CPU time for completion of the simulation.

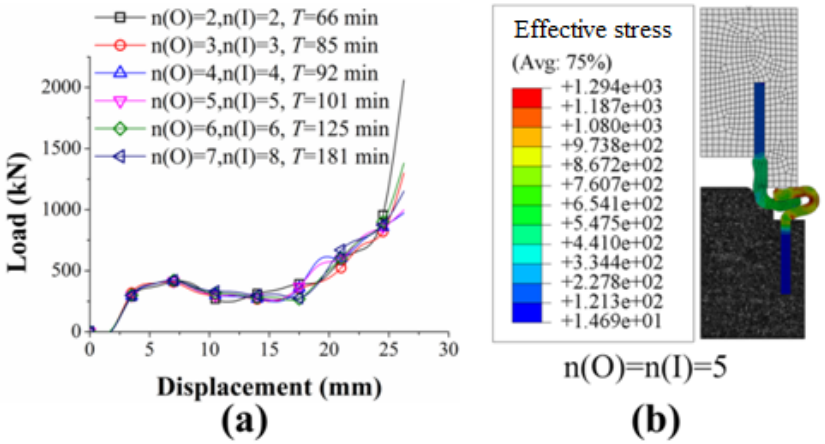

Fig. 3.9 Mesh size analysis, (a) load-displacement behaviour for varying number of elements (only successful cases), (b) simulation status in case of 5 elements through thickness for case 15

Different number of through thickness elements have almost no effect on the load evolution till the final step of joining (Fig. 3.9a). In the final step, slight difference in load is observed. It depends on factors such as mesh distortion, buckling and compression in the last stage. However, it is confirmed that mesh refinement shows load values within acceptable limits. It is seen that as the number of elements through thickness increases, computational time also increases. It has been stated in ABAQUS/explicit manual (2005) that hourglassing (deformation, but no strain) can occur in bending problems if the number of elements used through thickness is less than four. Hence considering computational efficiency, five elements in through thickness direction has been used for all the FE simulation trials which is appropriate to define the bending behaviour of tubes. Fig. 3.9b shows simulation status of Case 15 after successful completion stage using five elements through thickness along with the associated stress state.

3.2.2 Load-displacement behaviour and thickness evolution of tubes during joining

Different zones have been defined according to change in deformation behaviour of inner tube and outer tube during the joining process. Zone ‘1’ is defined up to the

displacement where outer tube touches the projected height of the punch. Zone 'II' is defined up to the displacement at which the inner tube touches the outer tube (upper arm of bead, refer Fig. 3.6) during its inside-out inversion. Zone 'III' is defined for rest of the displacement until joining gets completed. The zone wise representation of load-displacement behaviour for a typical case, Case 1 of Table 3.1, and the corresponding thickness evolution for both the tubes are shown in Fig. 3.10. Thickness has been measured at the bottom free edge of inner tube which is inverting whereas in case of outer tube it is measured at the upper free edge which touches projected section of the punch.

The load increases sharply at the end of zone '1', between 5 mm to 7.5 mm. In zone 'I' inner tube travels through the circular arc region of the die. At the end of this zone outer tube touches the projected section of the punch as a result of which bead starts to form in the outer tube. Bead initiation needs larger load and hence a sudden increase in load is observed towards the end of zone 'I'. With further displacement, continuation of bead initiation for outer tube as well as inversion of inner tube occur simultaneously. Here a sharp fall in load is observed (Fig. 3.10a). Continuation of bead formation needs lesser load as compared to its initiation. This region lies in the displacement range of 7.5 to 20 mm. Further when inner tube touches the outer tube (upper arm of bead) a simultaneous compression of both tubes is witnessed below the projected height of the punch (zone 'III'). For this compression, a larger load is needed and hence a monotonic rise in load is observed.

Because of compressive forces acting on the inner tube its thickness decreases almost throughout the forming region, however, rate of thinning is slightly less in zone 'II' as compared to other zones (Fig. 3.10b). In zone 'II' inner tube is freely inverting and it is not in contact with other surfaces. A slight increase in thickness is observed at the end of zone 'II' for inner tube. Here inner tube touches outer tube (Fig. 3.4c) which results in flattening at the edge of tube resulting in slight thickening. For outer tube, an increase in thickness is observed as soon as it touches the projected height of the punch and this thickening is continued till the inner tube touches outer tube during its inversion (Fig. 3.4c) or simultaneous compression of both tube starts.

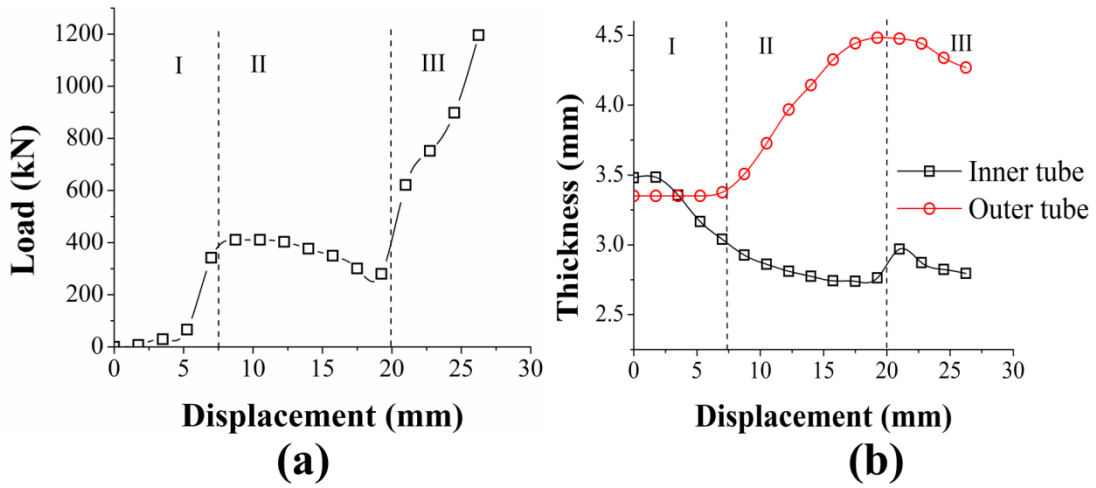

Fig. 3.10 Zonewise representation of, (a) load-displacement behaviour, and (b) thickness evolution of tubes, for Case 1 of Table 3.1

As the upper edge of outer tube touches the projected section, it is flattened by the compression provided by projected section and hence thickening is observed. In the last few steps, outer tube thins because of squeezing action between punch, inner tube and die (Fig. 3.4d). For all the successfully formed joints the nature of load and thickness evolution should follow as shown in Fig. 3.10. Thinning in the case of inner tube and thickening in the case of outer tube has been determined using following equation:

$$\Delta t = t_f - t_i \tag{3.13}$$

Here Δt is the change in thickness, t_f is final tube thickness and t_i is initial tube thickness. If Δt is positive, thickening occurs, and if it is negative, thinning occurs. For outer tube, Δt is positive, whereas it is negative for inner tube, in most of the cases.

3.2.3 Influence of parameters on the load evolution

FE simulations results were used to study the effect of parameters on load evolution. Coulomb's friction coefficient has been varied in the range of 0.01 to 0.20 (cases 1-5). Except for μ = 0.20, other μ values show successful joining processes. With increase in μ the curling and inversion phenomena for inner tube is restricted because of large frictional forces. For μ = 0.20, the tube is not able to invert properly and buckling is seen in inner tube above the curling region. The deformation behaviour of tubes in case of friction coefficient 0.05 (smooth joint) and 0.20 (buckling and distorted mesh) has been shown in Fig. 3.11(a, b). A lower μ value takes lower load up to the end of zone II, however, a similar final load at the last stage of joining is observed for different cases

(cases 1-5). The load corresponding to final stage for different cases has been shown in Table 3.5. A friction coefficient of 0.01 is used for other cases (case 6-35) which represents a lower friction condition or with lubrication. Experiments have also been conducted under properly greased surfaces.

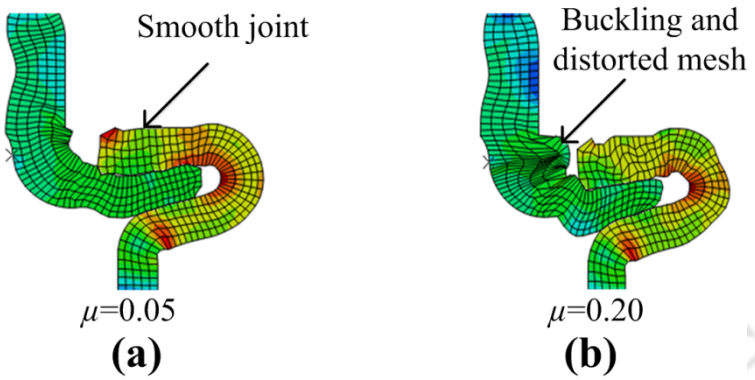

Fig. 3.11 Deformation behaviour of tubes in case of friction coefficient, (a) 0.05, and (b) 0.20

Table 3.5 Load at the last stage of simulation for cases 1-5, cases 11-15 and cases 16-20

Cases	Parameter description	Load (kN)
	μ	
1	0.01	1195.32
2	0.05	1289.83
3	0.10	1282.71
4	0.15	1263.29
5*	0.20	1284.8
	$\boldsymbol{L_2/S}$	
11	2.04(51/25)	2047.27
12	2.12(53/25)	1493.74
13	2.20(55/25)	1195.32
14	2.28(57/25)	1056.49
15	2.36(59/25)	998.22
	h	
16	0	1709.14
17	1	1195.32
18*	3	1043.1
19*	5	855.90
20*	7	794.34

(* Unsuccessful cases)

For different L_1/S, (cases 6-10), unsuccessful joints are seen in case of largest tube length of 2.68 (Case 10) (Fig. 3.12a). In this case the gap between projected section of the punch and free edge of outer tube is large enough that when the inner tube during inversion meets the outer tube, β becomes negative. As a result, tube is not able to enter properly inside bulged region of outer tube and unsuccessful joint is achieved. For smaller

inner tube lengths joining is completed well ahead because of early beading. There is not much difference in final load achieved for different successful cases, however, because of early bead formation, the load corresponding to beading and joining is reached well ahead in case of smaller inner tube lengths as compared to larger inner tube lengths (Fig. 3.12a).

For varying L_2/S, (cases 11-15), all the joining cases are successful. Here beading starts later for cases having smaller outer tube lengths. Inner tube touches the bottom unsupported region of outer tube during inversion after coming out of curling region. As soon as beading starts for outer tube, inner tube is pushed upwards by lower bead arm of outer tube (refer Fig. 3.6) to complete the inversion process. In all cases β is positive and successful joint is accomplished. Q is larger for smaller L_2 values indicating good (compact) joints in these cases. Final load obtained is also on the higher side for lower L_2 cases (Table 3.5).

Inner tubes have buckled outside for h values of 3, 5 and 7 mm (cases 18-20) and it is seen as unsuccessful joint formation. Slight inside buckling is also seen in the case of h = 0 mm, though it has been kept under successful category. Up to the end of zone II, load evolution is almost same for different cases. In the last phase of forming operation (zone III), load has dropped because of buckling for h values of 3, 5 and 7 mm as compared to h values 0 and 1 mm (Table 3.5).

For different H, (cases 21-25), in case of 4.2 mm, an unsuccessful joint is obtained. This is due to negative β. Even in case of H = 16.2 mm unsuccessful joint formation is seen. Despite being a successful joint, value of G is larger for H = 16.2 mm. Hence it is kept in unsuccessful category. All other cases provide successful joints. Highest final load is observed in case of H = 7.2 mm (Fig. 3.12b). In this case despite slight buckling of inner tube a compact joint ($G \approx 0$) is obtained. A load difference of about 800-1000 kN is experienced as compared to other successful cases.

In case of l = 0 mm, g is very low (Fig. 3.2a) and β is negative (Fig. 3.2j) and hence an unsuccessful joint is obtained. Slight buckling of inner tube is seen in this case. In all other cases successfully formed joints are obtained (cases 27-30). The load evolution remains almost same in all the cases, i.e., from l = 0 to 4 mm (Fig. 3.12c). Final load observed is larger for l = 1 mm and that too at a final displacement larger as

compared to other cases. A positive β helps in formation of successful cases in other cases at a lower load as compared to l = 1 mm. In this case, β is close to negative.

In case of R = 4 mm (Case 31) the value of g is very low (Fig. 3.2a) and a sound joint is not accomplished. Inner tube slightly buckles here. Similarly, in case of R = 8 mm (Case 35), though radius is larger unsuccessful joint is formed. The inner tube hits the bottom of the unsupported region of outer tube after leaving the curling region. The hitting point is so low that it fails to invert thereafter. In all other cases, successful joints are obtained. For R = 6 and 7 mm (cases 33, 34) load evolution obtained is almost same (Fig. 3.12d). Highest load is observed in case of circular radius of 6 mm.

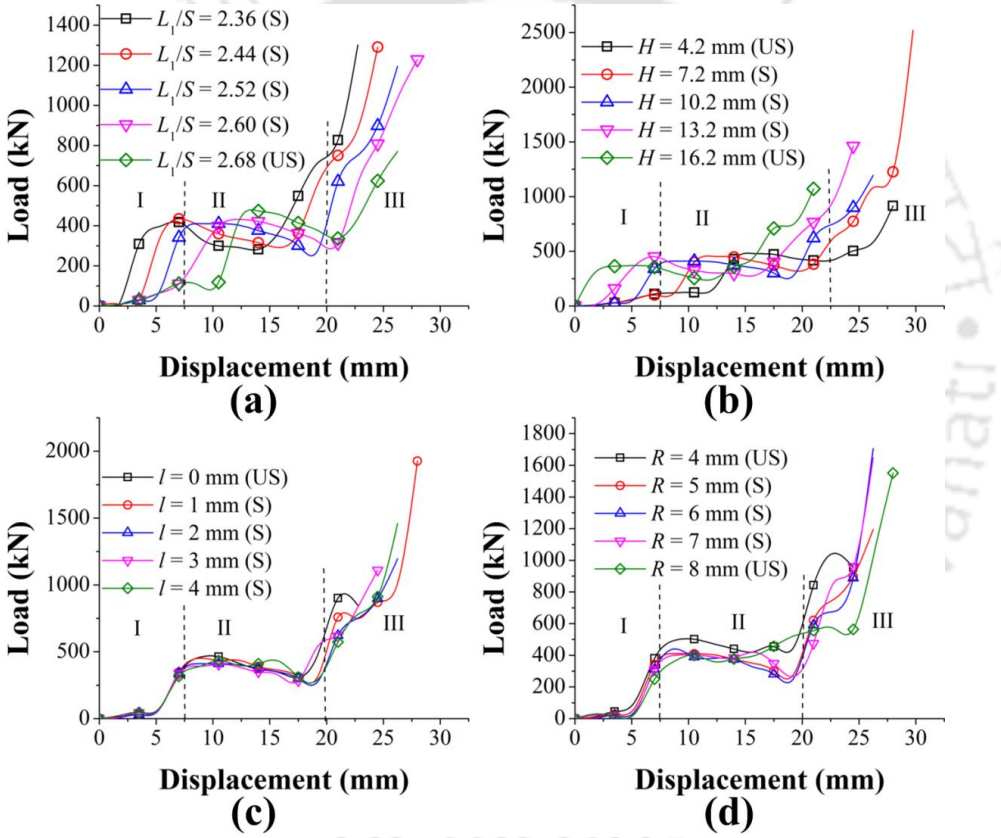

Fig. 3.12 Load-displacement behaviour for variation in, (a) L_1/S, (b) H, (c) l, and (d) R (S: successful, US: unsuccessful)

3.2.4 Effect of parameters on the thickness evolution at the end of the tube

Thickness evolution for outer tube is almost same for different friction coefficients except in zone III. In this zone slight variation is seen. As μ increases, thinning reduces in case of inner tube. With the increase in μ, buckling starts in inner tube. As a result, thinning severity decreases with increase in μ (Fig. 3.13a).

For different L_1/S cases, thickening for outer tube starts later for cases having larger inner tube lengths (Fig. 3.13b). Up to zone II, thickness evolution of inner tube for different L_1 is almost same. In zone III slight deviation is seen. Larger thinning for inner tube in zone III for lower L_1 values indicates a better tube compression and hence a compact joint. A negative β leads to a different thickness evolution for inner tube in case of L_1/S = 2.68 (unsuccessful case) in zone III. Here inner tube is compressed vertically from the upper arm of outer tube bead (refer Fig. 3.6) and because of which thickening is seen in last few stages.

For different L_2/S cases, thickening starts early for larger outer tubes (cases 11-15). Thickness evolution for inner tube is almost same up to zone II. In case of larger outer tube lengths, thinning observed in zone III is larger for inner tubes (Table 3.6). In these cases β is positive. It is seen that a larger positive β helps in compaction of joint.

Effect of h is almost negligible on thickness evolution of inner tube and outer tube for different values. Only in the case of h = 7 mm a slight difference in thickness evolution is seen as compared to other cases. In this case the width of projected height of punch is small, and in the last few stages, the end of outer tube is not in contact with projected section of punch at all. As a result, thinning severity is less for both tubes in last stages because of inappropriate compression (Table 3.6).

For different H values, outer tube thickening is almost same for different cases (cases 21-25) (Table 3.6). It is seen that thickening in outer tube starts earlier for higher H values. Inner tube thinning pattern is also observed to be same for different H up to zone II. In case of H = 4.2 mm, β is negative and hence thickening is seen in the last stage. In case of H = 7.2 mm, β is close to negative resulting in thickening in last stages, though this is a successful case as per criteria.

For different R and l values, outer tube thickening profile is almost same. For inner tube, thickness profile is almost same up to zone II for different R and l. Buckling in case of R = 4 mm affects thinning behaviour of inner tube (Fig. 3.13c). For l = 0 and 1 mm, a negative β is responsible for thickening in last stages (Table 3.6).

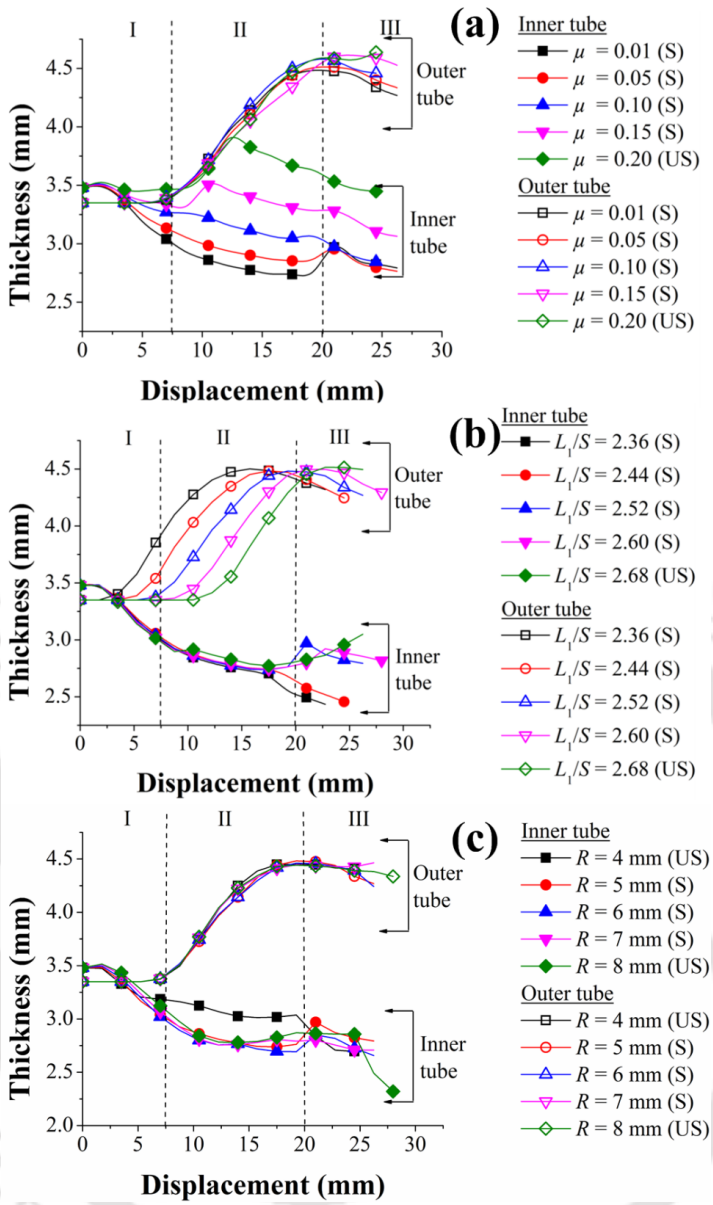

Fig. 3.13 Thickness evolution for variation in, (a) μ, (b) L_1/S, and (c) R (S: Successful, US: Unsuccessful)

Table 3.6 Δt for different L_2/S, h, H, and l

Cases	Parameter description	Δt (Inner tube)	Δt (Outer tube)
	L_2/S		
11	2.04(51/25)	−0.5840	0.6924
12	2.12(53/25)	−0.6686	0.7842
13	2.20(55/25)	−0.6859	0.9189
14	2.28(57/25)	−0.9876	1.0490
15	2.36(59/25)	−1.0621	1.0738
	h		
16	0	−0.7304	0.8252
17	1	−0.6859	0.9189
18*	3	−0.6732	0.9921
19*	5	−0.7364	1.0449

20*	7	−0.5185	1.1755
	H		
21*	4.2	−0.5199	0.9613
22	7.2	−0.3784	0.7322
23	10.2	−0.6859	0.9189
24	13.2	−1.0335	0.9326
25*	16.2	−0.8634	0.9849
	l		
26*	0	0.0457	1.1296
27	1	−0.2332	0.6352
28	2	−0.6859	0.9189
29	3	−0.9457	0.8326
30	4	−0.8840	0.9157

(* Unsuccessful cases)

In summary, thickness profile for outer tube largely remains unaffected for different cases for different process parameters. Inner tube thickness profile is same up to zone II for various cases. In zone III, few cases (both successful and unsuccessful) shows thickening. A negative or close to negative β is a major reason for this.

3.2.5 Joint quality analyses based on criteria

To analyse the quality of joints, two cases, one successful and one unsuccessful, have been discussed in this section. The successful case is Case 29 (l = 3 mm) and the unsuccessful case is Case 21 (H = 4.2 mm). FE simulation based results are used for the analysis.

In Case 29, after leaving the circular region the inner tube touches the bottom unsupported part of outer tube in the process of inversion (8^{th} step) in simulation. As beading has already started for outer tube, the lower bead arm of the outer tube also helps in inversion of inner tube (11^{th} step) as it is pushed upwards. As a result, the inner tube is clamped properly in the bulged region of outer tube. Finally, a successful joint is obtained in the later stage (Fig. 3.14a).

In Case 21, beading starts later for outer tube because of shorter projected section height. The difference in deformation can be seen clearly at 8^{th} step for cases 29 and 21 (Fig. 3.14(a, b)). However, inversion process continues for inner tube, but when it touches the upper bead arm of outer tube, β becomes negative (14^{th} step) in Fig. 3.14b. The free end of inner tube is not able to enter bulged region of outer tube, rather it is compressed vertically within upper and lower bead arms. Finally, an unsuccessful joint is seen at the end of 17^{th} step. Here criteria 1 and 2 are not fulfilled. Similarly, all the cases have been

categorized into successful and unsuccessful joints as per criteria. Table 3.7 describes the summary of joint quality analyses and reason for unsuccessful joint formation. Here it should be noted that a joint is termed as successful only when it satisfies all the three criteria.

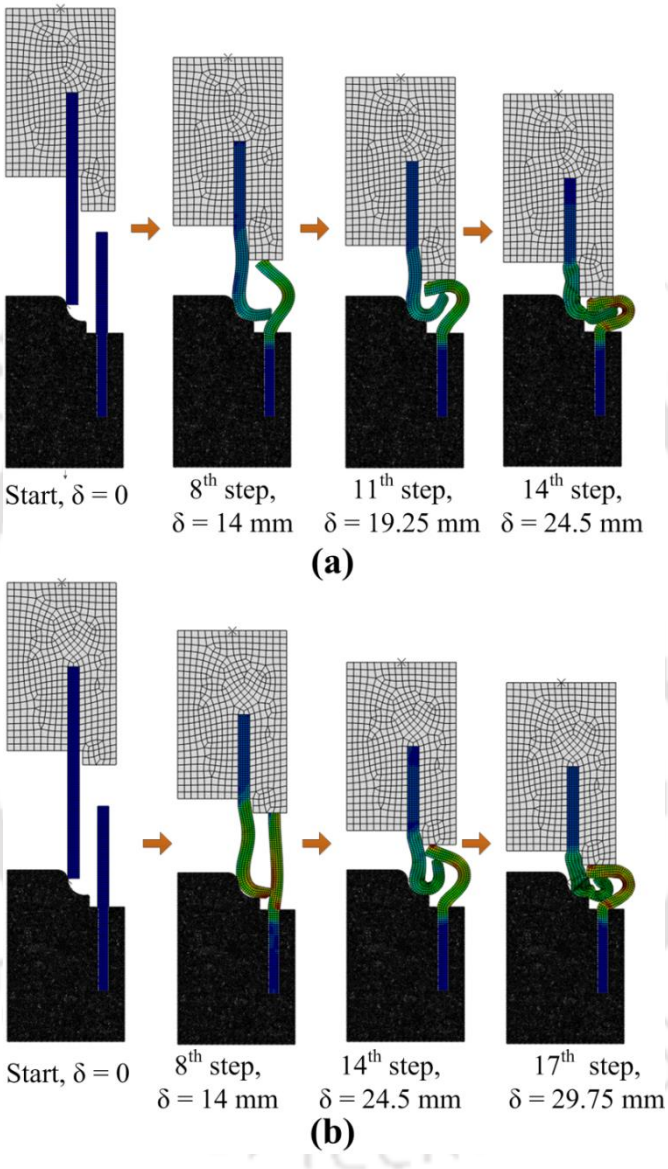

Fig. 3.14 Analysis of joint quality through FE simulations for (a) Case 29 (successful), and (b) Case 21 (unsuccessful)

Table 3.7 Summary of quality analyses of joints based on FE simulation

Case	Parameter description	Quality of the joint	Reason for unsuccessful joints
	μ		
1.	0.01	Successful	-
2.	0.05	Successful	-
3.	0.10	Successful	-

4.	0.15	Successful	-
5.	0.20	Unsuccessful	Criteria 3 not satisfied
	L_1/S		
6.	2.36	Successful	-
7.	2.44	Successful	-
8.	2.52	Successful	-
9.	2.60	Successful	-
10.	2.68	Unsuccessful	Criteria 1 and 2 not satisfied
	L_2/S		
11.	2.04	Successful	-
12.	2.12	Successful	-
13.	2.20	Successful	-
14.	2.28	Successful	-
15.	2.36	Successful	-
	h		
16.	0	Successful	-
17.	1	Successful	-
18.	3	Unsuccessful	Criteria 3 not satisfied
19.	5	Unsuccessful	Criteria 3 not satisfied
20.	7	Unsuccessful	Criteria 3 not satisfied
	H		
21.	4.2	Unsuccessful	Criteria 1 and 2 not satisfied
22.	7.2	Successful	_
23.	10.2	Successful	-
24.	13.2	Successful	-
25.	16.2	Successful	Criteria 1 not satisfied
	l		
26.	0	Unsuccessful	Criteria 1 and 3 not satisfied
27.	1	Successful	-
28.	2	Successful	-
29.	3	Successful	-
30.	4	Successful	-
	R		
31.	4	Unsuccessful	No criteria satisfied
32.	5	Successful	-
33.	6	Successful	-
34.	7	Successful	-
35.	8	Unsuccessful	No criteria satisfied

Successful cases: 19, Unsuccessful cases: 10

3.2.6 Lab scale demonstration for selected cases

Cases 15 and 29 satisfy all the criteria for successful joint formation (Fig. 3.15(a, b)). In Case 21 (Fig. 3.15c), although a joint is obtained, the inner tube has buckled outside making it defective. A clean, smooth joint has not been obtained. Even after buckling the inner tube has entered the bulged region of the outer tube. During compression test, the defect in Case 21 is more visible. '*G*' (refer Fig. 3.6) has been observed for experimental and simulation case studies. '*G*' compares well for experimental and simulation trials, for cases 15 and 29, while substantial deviation has been found for Case 21 (Table 3.8).

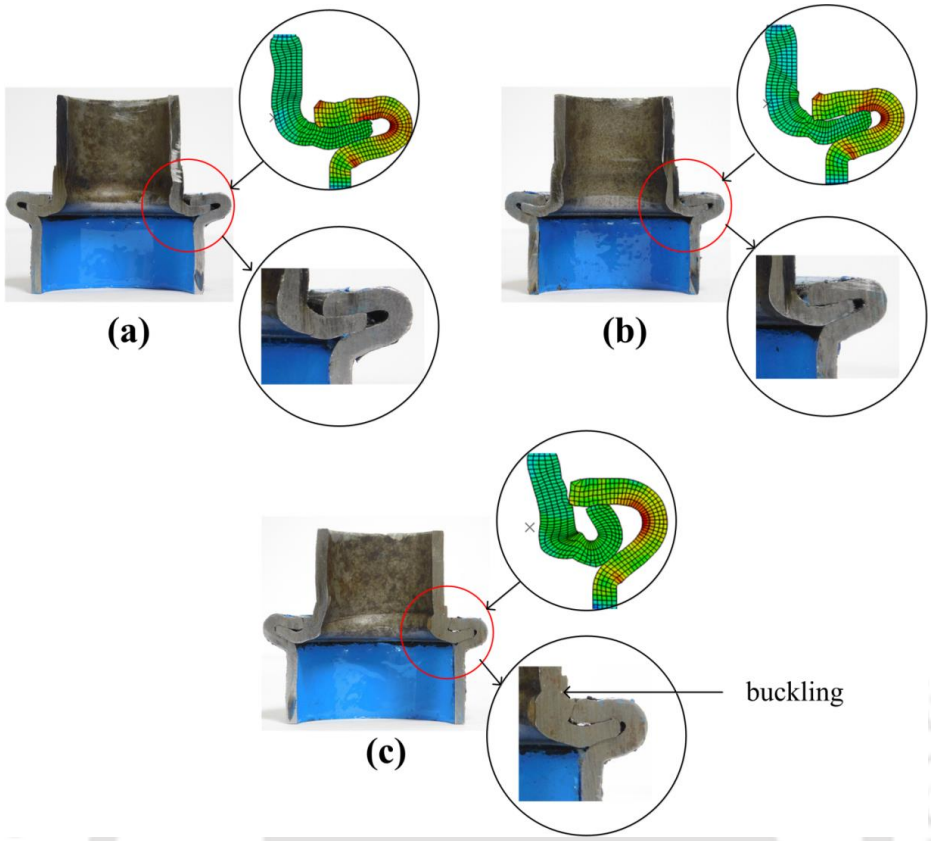

Fig. 3.15 Demonstration of joint formation at laboratory scale for, (a) Case 15 (successful), (b) Case 29 (successful), and (c) Case 21(unsuccessful)

Table 3.8 *G* (in mm) observed during simulation and experiment for demonstrated cases

	Case 15	Case 29	Case 21
FE simulation	3.07	0.724	7
From experiment	3	2	1.5

Fig. 3.16 shows a comparison between load-displacement behaviour for three selected cases. The load evolution compared well between simulation and experimental results. Anisotropic modeling has improved the accuracy of numerical result. The friction coefficient used during simulation is 0.01 and is not experimentally verified, which would have caused some difference in load evolution. Theoretical load has been evaluated for experimentally verified cases. Up to the displacement at which inner and outer tube comes in contact with each other theoretical prediction of load has been done. Load has been determined independently for inner tube and outer tube as described in section 3.1.4 and summed to obtain the theoretical load for different cases. Theoretically predicted load shows some difference in load with respect to numerical and experimental data (Case 15 and 29) (Fig. 3.16a,3.16b), while in case of Case 29 (Fig. 3.16c) the deviation is minor.

The deviation could have occurred because of strain averaging in FE simulations while using the models and assumption of constant tube thickness.

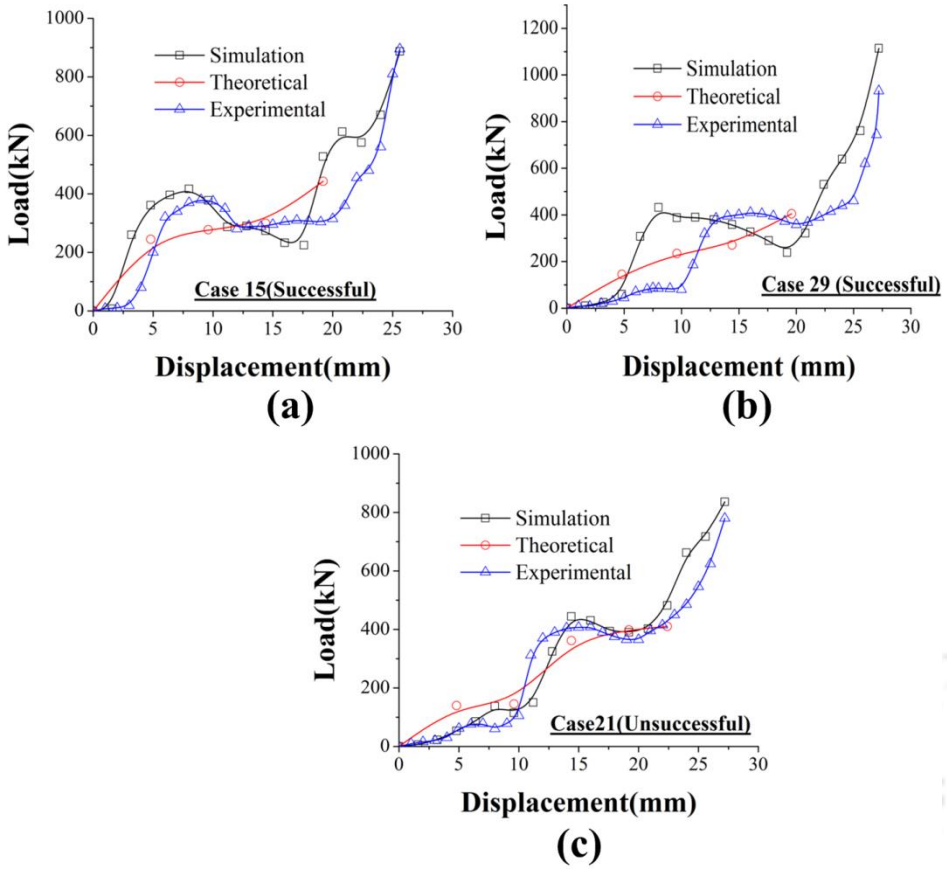

Fig. 3.16 Comparison of numerical, theoretical and experimental load-displacement behaviour for selected cases

3.2.7 Mechanical testing of joints

Destructive pull out test does not influence the joint region. The failure is observed in the free supported region of the inner tube and the outer tube. The joint formed is compact and tight and ultimately failure happens in holding region only. The failure pattern for the joints that underwent the pull out tests has been shown in Fig. 3.17. Failure happens in outer tube for successful cases (Case 15 and 29), while for Case 21(unsuccessful case) it happens in inner tube. Welded tube-tube joint fails along the weld seam. Since the joints made failed in the holding region of tubes for end formed joints, the load-displacement data obtained is not conclusive. But, from the failure pattern, it can be said that the joints fabricated are stronger than the welded joint as the welded joint failed in the weld seam itself.

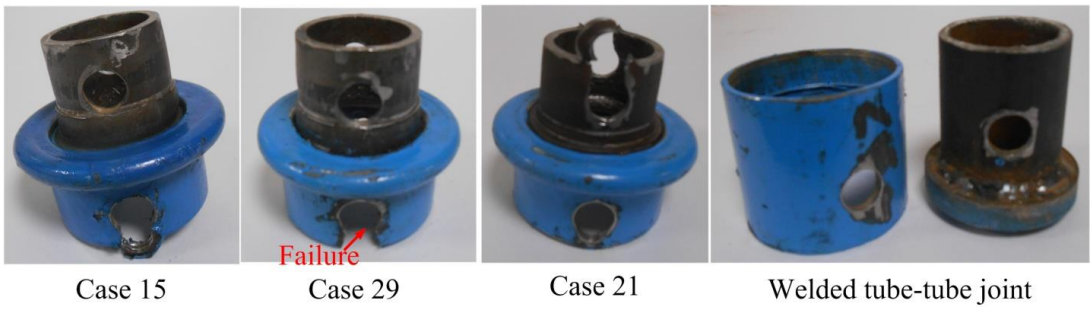

Fig. 3.17 Failure pattern of different end formed cases and welded tube-tube joint during destructive pull out test

Both the end formed tubes and welded tube performed equally well as seen from the load-displacement behaviour of compression test (Fig. 3.18). In successful cases (Case 15 and 29), disassembly of the inner tube and outer tube takes place in the joint region. The inner tube comes out of the bulged region. The joint formed is so strong that inner tube fails at the bent section where it enters inside the bulged region of outer tube during the process of disassembly (Fig. 3.18).

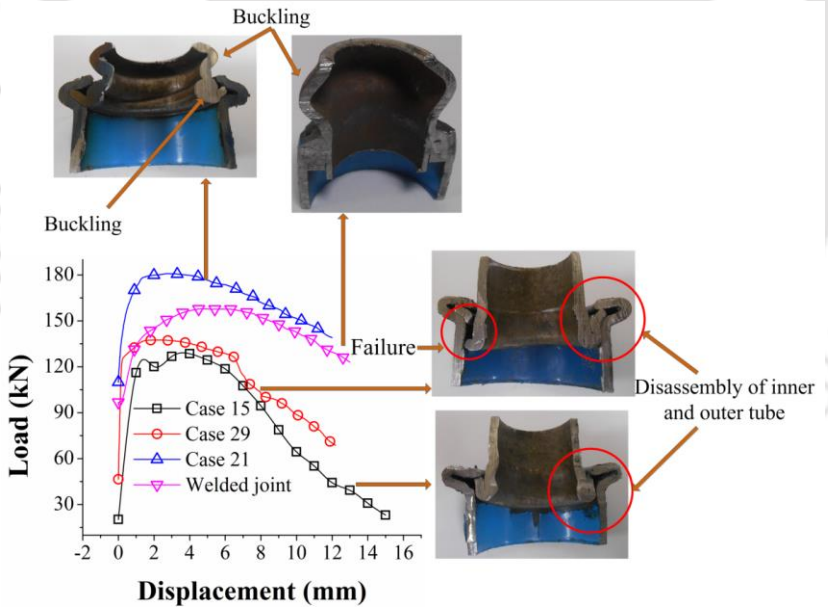

Fig. 3.18 Compression test results of joints made by end forming and welding

In Case 21 (unsuccessful case), the inner tube does not come out easily from the bulged region of the outer tube and buckling is observed in the supported and unsupported region for inner tube. In case of the welded joint, the weld is strong enough to prevent the failure at the weld interface. Buckling is observed in the free region of the

inner tube in this case. Peak load obtained for welded joint is slightly higher as compared to successful cases, but slightly lower as compared to unsuccessful case.

3.3 Merits and demerits of the proposed joining method

The following are some of the merits and demerits of the proposed joining method. The merits are,

- Even polymers can be joined
- Suitable to join lightweight materials which are difficult to join by conventional welding processes
- Consumes less energy
- Cost-effective process and mass production is possible
- No heat affected zone and hence a stronger joint is obtained
- Environmental friendly as no harmful gases are ejected during joining
- A leakproof joint capable of operating well in any climatic condition can be achieved
- No aesthetic issues and handling is easy

The demerits are,

- For joining different tubes, the optimized parameters are required and computations need to be conducted every time when different materials with different dimensions need to be joined
- Split dies are required such that after fabrication of joints, they can be easily taken out of the tools
- For joining of longer tubes the present die and punch system may not work. It will not be cost effective to fabricate a punch and die with larger support length

However, joining of longer tubes is possible by the proposed technology with the help of some modification in the design of existing die and punch. The complete schematic for joining of longer tubes after incorporating modification in the proposed technology has been shown in Fig. 3.19. For this purpose, FE simulations are performed in which all the parameters R, l, H, μ, h and S are kept same as that of Case 1 in Table 3.1. The only difference is the length of the tubes. The length of the tubes has been kept as 0.5 m. Die has been fabricated into parts. The inner die has circular arc profile responsible for

inversion of tube, whereas outer die is just a cylindrical capsule of desired length and width to hold the tube. Similarly, in punch there is no supporting region. Except the changes, the dimensions of the punch and die have been kept same as the original proposed for shorter tubes. Prior to conducting joining experiments, a slot of length, 25 mm in this case, and width, 2.48 mm for inner tube, 2.35 mm for outer tube need to be fabricated in the tubes. The modified punch and outer die is located in this slot.

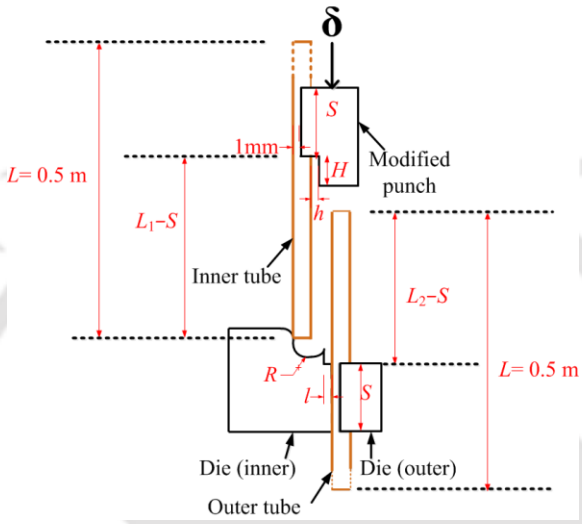

Fig. 3.19 Schematic (2D axisymmetric view) of joining of longer tubes (dimensions not to scale)

FE simulation strategy has been kept the same as that of discussed in section 3.1.3. The only difference is that a rough (no slip) interaction has been applied between contacting surfaces of outer tube and dies, so that outer tube does not slip during deformation. In actual practice the proposed method for joining of longer tubes needs preparation of a clamping system for outer tube between the dies, and application of load above the punch for compression. However, after fabrication of such set-up, mass production is possible even for tubes as long as 5-10 metres as only end of the tube deforms in both the longer and shorter tubes. Fig. 3.20 shows the different stages of joint formation obtained from FE simulations. Fig. 3.20 indicates appropriate forming of tubes required for compact joint formation. At the last step (Fig. 3.20c), slight buckling is seen below the offset distance of punch region. But it is not severe and can be avoided using a fillet section or optimizing the parameters, specifically '*h*'.

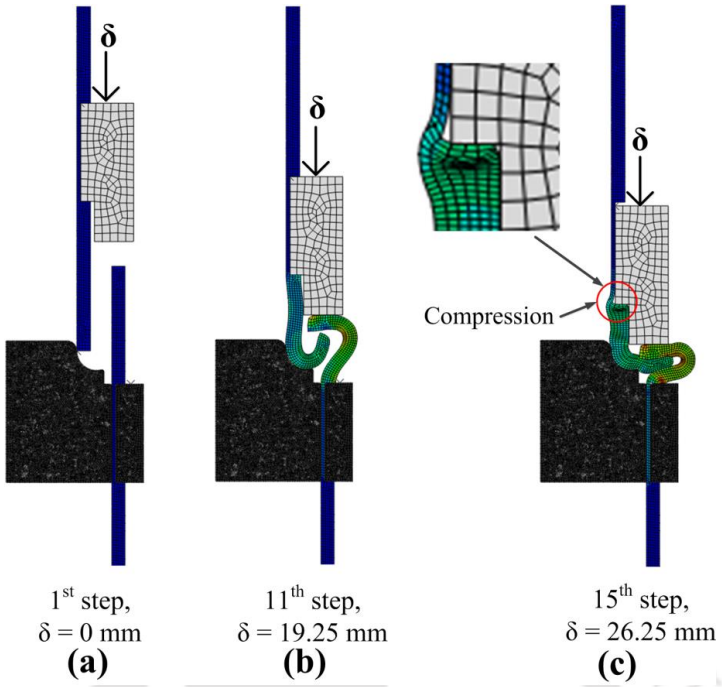

Fig. 3.20 Different stages during joining of longer tubes: FE simulation results

Tube-tube joint obtained using the proposed technology can be used in ground vehicle chassis design, light weight industry (building and trusses) etc. General uses like carrier of fluids (liquid, oil and refrigerant) is preferable as a good leakproof joint can be obtained. Aircraft and shipbuilding industries are potential users as longer tubes can also be joined using this method. Some peculiar features such as environmental friendliness, mass production, strength of the joint and requirement of minimum tools make the present method an alternative solution for current welding problems.

3.4 Conclusions

The main aim of the present work is to propose a tube to tube joining method using end forming. FE simulations are used to analyse the process. Finally, experimental validation is performed and mechanical performance of such joints are tested. The following conclusions can be drawn from the present work:

1. The proposed joining method using end forming is capable of fabricating stronger joints and can be considered as an alternative for conventional welding methods. A sudden rise in load and local thinning of tubes in last stages are seen due to compression of tubes under projected section of punch. Proper selection of parameters and their range leads to successful joint cases.

2. Important parameters have been identified which can influence the joining formation. Feasibility window of process parameters for successful joining is limited. Among all the parameters circular arc radius and projected height of punch are more influencing. Circular arc radius lying in the range of 5-7 mm and projected height of punch lying in the range of 7.2-13.2 mm is found to be suitable for proper joint formation.

3. A number of criteria have been developed through which quality of the joint can be predicted at the shop floor without any complex measurement and calculations. These criteria are specific to the proposed technology.

4. The predicted load-displacement behaviour matches well with few experimentally demonstrated cases with little variation.

5. Compression test and pull-out tests for the fabricated end formed joints have been conducted and the same have been compared with welded joints. During pull out tests, the end formed joints perform better as compared to the welded joint, while during compression test, the strength of the end formed joints and the welded joints are comparable.

6. Finally, a tube-tube joint method to join longer tubes has been proposed. The feasibility of the process has been demonstrated with FE simulation results. Few minor modifications in the process meant for shorter tubes are sufficient to join longer tubes successfully.

Chapter 4

End forming behaviour of FSPed Al 6063-T6 tubes at different tool rotational speeds

4.1 Methodology

In this section, firstly, methodology of FSP of tubes and mechanical properties evaluation of base metal and processed zones have been discussed. Dislocation density measurement and end forming experimentation methods have been discussed thereafter. Evaluation of specific energy absorption during end forming and FE simulation details of end forming have been described at last.

4.1.1 FSP of tube

The material used for the present work is AA 6063-T6, which has been used in as-received condition. A T6 heat treatment has been applied in the base material by the manufacturer. The outer diameter of tube is 50.8 mm and thickness is 3.17 mm. The chemical composition (% wt) of the alloy is: Si-0.496 %, Fe-0.149 %, Mg-0.549 %, Cu-0.008 %, Ti-0.009 %, Cr-0.002 %, Ni-0.007 %, V-0.011 %, Zn-0.002 %, Others<0.084 %, and Al-balance.

Single pass FSP of aluminium tubes has been conducted using a specially fabricated tool on a 5-axis friction stir welding machine. To support the tube against the large amount of forces applied by the tool holder, it is supported by a mandrel, located inside the tube. The diameter of mandrel is almost equal to inside diameter of the tube. The length of mandrel is larger than the length of the tube. The length of the tube used for FSP is 100 mm, while the length of the mandrel is 140 mm. Two capsules with threaded internal diameter are engaged with the mandrel. Both ends of mandrel are threaded up to a length of 25 mm at their ends. The designing of the capsule has been done in such a way that some part of it is covering the tube, so in this way tube, mandrel and capsules are providing a locking mechanism for tube. The tube has been processed up to a length of 65 mm. The schematic of the experimental set-up along with nomenclature of parts, the actual processing set-up, and the final processed tube are shown in Fig. 4.1.

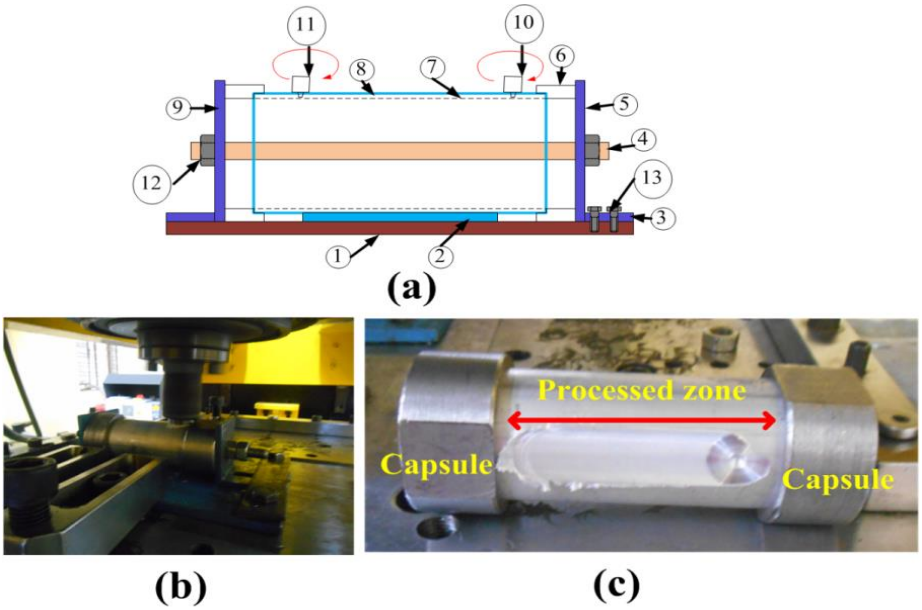

Fig. 4.1 FSP of tubes, (a) schematic of processing set-up for FSP of tubes, parts (1: base plate, 2: support plate, 3: slot, 4: inside rod, 5: movable angle plate, 6: capsule, 7: mandrel, 8: tube, 9: fixed angle plate, 10: FSP starts, 11: FSP ends, 12 and 13: bolts), (b) actual experimental set-up showing the processing operation, and (c) final FSPed tube

A tool with circular shoulder profile and a cylindrical tapered pin made of non-consumable H13 tool-steel has been used for the processing purpose. The shoulder diameter and shoulder length of the tool is 25 mm. The pin height is 2.9 mm. The diameter of the pin at its base is 4.5 mm and at its tip is 2.45 mm. The positioning of the tube on the base plate along with mandrel (not seen in the picture, since it is inside the tube) and capsules can be observed. Two angle plates have been kept at the opposite ends of mandrel-tube-capsule assembly and one through hole has been done in the mandrel and angle plates. One circular rod of particular dimension passes through this hole and bolted at the both ends with angle plates, such that any vibration of the set-up during processing can be avoided and processing could be conducted smoothly.

End forming of tubes have been conducted with defect free processed zones. To decide the defect free range, a tube has been processed, in which the rotational speed kept on varied from 500 rpm at one end to 1900 rpm at the other end. The other parameters such as tool traverse speed, tool plunge depth and tool tilt angle are kept constant at 90 mm/min, 3 mm and 2° respectively. The constant value of traverse speed has been decided by past experiences for defect free welding in case of traverse speed for 6xxx series aluminium alloys. Plunge depth has been kept at 3 mm such that a sufficient thickness of the tube could be penetrated and defects such as microscopic voids and other

root defects (kissing bond) could be avoided which happens due to lack of penetration. A tool tilt angle of 2° has been used.

After the processing has been completed, the tube has been taken out of the experimental set-up carefully. For metallographic examination, the entire processed length has been sectioned into suitable sizes of prescribed lengths perpendicular to processing direction. The sectioned specimen has been ground using standard procedures and polished with different grades of emery paper on a disc polishing machine. After the polishing is completed, the material is polished with velvet sheet (with 1μm particle size diamond). Finally, to reveal the macrostructure, etching is done with Keller's reagent (H_2O: 190ml, HNO_3: 5ml, HF: 3 ml, HCl: 2ml). The same procedure has been followed for grain size evaluation of processed zone later. Macrograph examination has been done at a low magnification of 10×. Micrograph examination has been done at a higher magnification of 20×. Some of the macrographs have been shown in Table 4.1.

Table 4.1 Macrographs of processed samples at different tool rotational speeds

S. No.	Tool rotational speed (ω, rpm) Tool welding speed (v, mm/min.)	Macrograph of weld cross-section	Defect and quality
1.	ω=566 v=90		Tunnel, defective
2.	ω=830 v=90	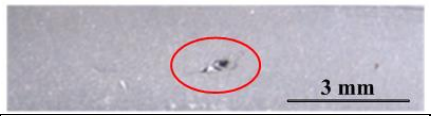	Pin hole, defective
3.	ω=1050 v=90		Worm hole, defective
4.	ω= 1200 v=90		Defect-free
5.	ω=1307 v=90		Defect-free
6.	ω=1535 v=90		Defect-free
7.	ω=1775 v=90		Rough surface, defective

It is observed from the macrographs that at lower rotational speed, below 1100 rpm, and higher rotational speeds, above 1600 rpm, tunnel defect, pin hole defect, worm hole defect and rough surfaces are observed at rotational speeds of 566 rpm, 830 rpm, 1050 rpm and 1775 rpm, due to inadequate or excessive heat input. So, for actual processing trials, the tool rotational speeds decided are 1200 rpm, 1350 rpm and 1500 rpm which lies in the defect free range of 1100 rpm to 1600 rpm and the same is confirmed from the macrographs (Table 4.1). A substantial gap between the two levels of tool rotational speeds has been maintained such that their effect on end forming behaviour could be identified.

Totally sixteen processing trials have been conducted for each rotational speed. Out of sixteen processed tubes for each rotational speed, four each will be utilized for expansion, reduction and beading and the two each will be utilized for tensile testing as well as plastic strain ratio, '*r*' value, calculation of processed zone. In total, 49 welding trials have been conducted. The scheme of utilization of sixteen tubes for a rotational speed has been shown in the form of flow chart (Fig. 4.2). Each experiment has been conducted twice to check the repeatability.

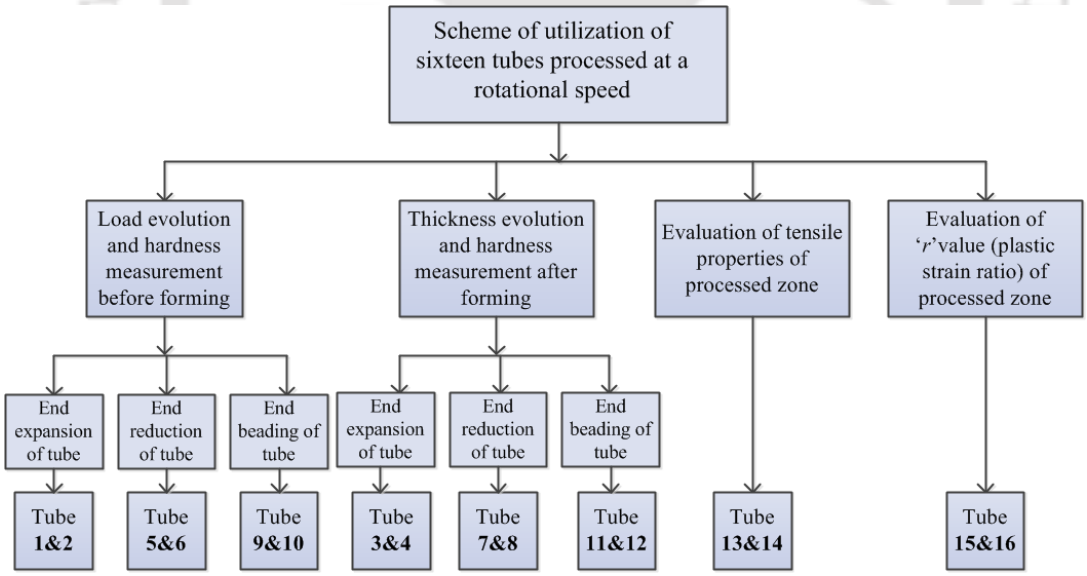

Fig. 4.2 Flow-chart of utilization of tubes for end forming operation

4.1.2 Hardness distribution, tensile properties and grain size evaluation

The hardness of base metal is measured through Vickers micro-hardness indenter at 500 gf load and a dwell time of 5 sec. The hardness is measured along the mid-

thickness of the tube along the circumference. For repeatability, four experiments for hardness measurement of base metal were conducted. The hardness has been measured at every 2 mm distance. Sixty-four hardness measurement have been performed for base metal during each trial.

The hardness of the processed zone has been measured before and after forming. The motive of measuring hardness after forming is to study the effects of deformation on the processed zone material. The hardness of the processed zone after end forming has been measured so that it can be compared with that of raw base material. Many applications require the final mechanical properties of the tube to be above necessary level. Because of FSP, it is believed that processed zone mechanical properties will be modified considerably. The decrease in strength (or hardness) of the processed zone as compared to raw base material can be improved during end forming. It is expected that the processed zone hardness will approach that of the base material because of strain hardening during end forming which is appropriate to most of the structural and automotive applications. The hardness of the FSPed zone before end forming and after end forming are measured at the mid-thickness of the sample.

The mechanical properties of base metal of the tube have been evaluated by tensile tests in an INSTRON machine of load capacity 100kN. For base material, the tensile specimen has been prepared following the ASTM-E8 standard (sub-size 3). The dimensions of tensile specimen for base material are: gauge length-12.5 mm, gauge width-3.20 mm, thickness-3.17 mm, shoulder length-30 mm, shoulder width-10 mm and total length-82.80 mm. Based on the availability of processed zone, the dimensions (non-standard) of the tensile sample have been decided for evaluating the processed zone properties. The dimension of tensile specimen for processed zone are: gauge length-12.5 mm, gauge width-10 mm, shoulder length-20 mm, shoulder width-18 mm and total length-60.50 mm. Tensile tests have been conducted at room temperature with a cross-head speed of 1 mm/min. After cutting the required dimensions of tensile samples from processed and unprocessed tube they have been fine polished to remove any burr or notches inside it. After polishing, the initial dimensions of the specimen have been measured with the help of profile projector. With the help of load-displacement data and initial dimensions of the specimen, other mechanical properties such as offset yield strength, ductility, strain hardening exponent and strength coefficient have been

calculated as per standard procedure. Plastic strain ratio '*r*' (ratio of true width strain to true thickness strain) has been calculated for base metal and FSPed zone at different conditions. The standard followed for calculation of plastic strain ratio is ASTM E517-00.

Grain size in the processed zone has been measured using line intercept method. Three different zones have been identified in the processed zone according to the size of the grain. The measurement has been done as per ASTM 112-113 standard.

The mechanical properties of the base metal are shown in Table 4.2. In the case of FSPed zone properties, yield strength, tensile strength, elongation, strain hardening exponent and strength coefficient are evaluated from tensile tests. The hardness distribution has been used to represent the strength of the FSPed zone for discussion.

Table 4.2 Mechanical properties of AA 6063-T6 tube base material

Yield strength (MPa)	Ultimate tensile strength (MPa)	Uniform elongation (%), at 12.5 mm gauge length	Total elongation (%), at 12.5 mm gauge length	Strain hardening exponent, *n*	Strength coefficient, *K* (MPa)	Plastic strain ratio '*r*'
152±11	258±12	20±0.6	31±0.02	0.17±0.01	407±13	0.11

4.1.3 Dislocation density measurement using X-ray peak profile analysis

Strain hardening behaviour is typically related to the accumulation and interaction of dislocations. Any material or region having lower dislocation density confirms better strain hardening behaviour resulting in higher ductility. It has been observed that a material having higher hardening capacity, $H_c = \frac{\sigma_{UTS}-\sigma_y}{\sigma_y}$ and higher '*n*' needs larger stress for plastic deformation. Here H_c is the hardening capacity, σ_{UTS} is the ultimate tensile strength, and σ_y is the yield strength. A close relationship between FSP, traverse speed, weld zone mechanical properties and dislocation density exists.

The dislocation density (ρ) of tube material has been calculated by (Dhal et al., 2017),

$$\rho = \frac{2\sqrt{3}\varepsilon}{Db} \tag{4.1}$$

where b is the Burgers vector, D is the domain size and ε is the average micro-strain. Burgers vector for aluminium which is an FCC material has been taken to be constant and

is equal to 0.286 nm. The same value was used by (Lee and Huang, 2016) for Al 6061-T6. The domain size and micro strain have been obtained by Williamson-Hall equation (Dhal et al., 2017),

$$BCos\theta = \frac{\lambda K}{D} + 4\varepsilon Sin\theta \quad (4.2)$$

where B is the full width at half maximum (FWHM), θ is the Bragg's angle, K is a material constant whose value is usually taken as 0.9 for FCC materials and λ is the wavelength (0.154060 nm) of the incident radiation and ε is micro-strain. FWHM is calculated by fitting the peak obtained through XRD analysis by Gauss fit. For two different peaks, equation (4.2) is solved to obtain the value of D and ε. Later, putting values of D and ε in equation (4.1), dislocation density value is obtained.

Williamson-Hall plot shows the qualitative behaviour of diffraction peak broadening with FWHM as a function of K, where $K = 2Sin\theta/\lambda$. Here θ and λ are the diffraction angle and wavelength of the X-ray. Strain anisotropy in the conventional Williamson-Hall plot has been rationalized as replacing K by $KC^{1/2}$ in the modified Williamson-Hall plot, where C is the dislocation contrast factor and has been assumed as 0.11 in the present case (value obtained from Woo et al. (2008) by fit). FWHM are plotted as $\Delta K = 2Cos\theta(\Delta\theta)/\lambda$ in 1/nm scale (Woo et al., 2008). Here $\Delta\theta$ is FWHM obtained from (h k l) plot. The slope of modified Williamson-Hall plot quantifies dislocation density. A material having higher dislocation density should have higher slope.

4.1.4 Details of end forming of tubes

End forming experiments have been conducted on specially fabricated tools made of mild steel in an UTM of load capacity 100kN. A 15° tapered tool has been used for tube expansion and reduction. A split die has been used for tube reduction, since the removal of tube was difficult after reduction in a single piece die. Tube beading has been performed on a die having a slot which is slightly larger than the thickness of the tube, so that after beading the tube could be easily taken out of the die. The surface roughness was measured with the help of profilometer and is found to be 5.35±0.87, 4.01±0.44 and 2.84±0.45 μm for tube expansion, tube reduction and tube beading dies respectively. The schematic of the end forming tools showing the complete geometry with dimensions has been shown in Fig. 4.3.

Tube expansion is stopped at the point where tube failed, while reduction and beading have been conducted up to a length of 20 mm and 10 mm respectively for the evaluation of load-progression behaviour and thickness. For thickness measurement, the tube has been taken out of the experimental set-up after every 2 mm of displacement during end forming and thickness has been measured at the deformed end of the processed zone and opposite to the processed zone in the base metal in case of tube expansion and reduction. During tube beading, the thickness has been measured at the peak bulged height of the processed zone and opposite to the processed zone in the base metal zone after every 2 mm of displacement.

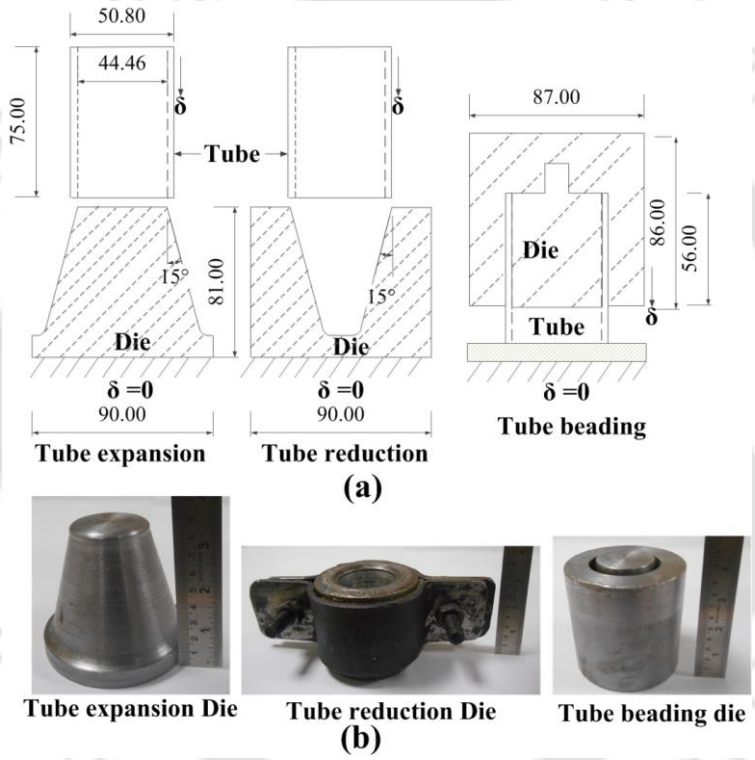

Fig. 4.3 Experimental set-up for end forming operations, (a) schematic of end-forming tools (all dimensions in mm and not to scale), (b) tools used for experiments

4.1.5 Specific energy absorption capacity evaluation

The specific energy absorption capacity per unit mass, kJ/kg (E) is an important parameter indicating the energy absorption capability of the tubes (FSPed or unprocessed). It is a critical performance indicator aiming at lightweight design. Tubes are heavily used in aerospace and spacecraft industries. Here specific energy absorption capacity for tubes has been calculated according to following equation (Yang et al., 2010),

$$E = \frac{W}{\pi \rho L(2tR_0 + t^2)} \quad (4.3)$$

Where W = Energy absorption which can be obtained by integrating deforming force with respect to displacement from zero to displacement corresponding to maximum deformation, ρ = Density of aluminium = 2700 kg/m^3, L = Deformed length of the tube (mm), R_o = Inside radius of the tube (mm), t = Thickness of the tube (mm)

For calculating W, the experimental load curve has been fit into a 3rd order polynomial of the form A + B. x + C. x^2 + D. x^3. It is assumed that higher the order of the fit curve better would be the accuracy. For each fit curve adjusting R-value has been calculated to verify the accuracy of fit curve. It is believed that if the value of adjusting R-square is greater than 0.8, a good fit has been obtained. For an unprocessed tube, thickness of the tube is same as that of the parent metal, but in case of processed tube the thickness of tube has been determined by taking an average of weld zone thickness and unprocessed zone thickness.

4.1.6 FE Simulation of end forming

FE simulation of end forming operations have been done in FE code, ABAQUS (6.17) explicit. The punch and dies for expansion, reduction and beading have been defined as rigid parts, while the tube has been defined as deformable one. A penalty type contact between surfaces have been applied. A constant friction coefficient value of 0.1 has been applied between surfaces. Although friction coefficient has not been evaluated experimentally, a value of 0.1 simulates the friction conditions generally used in metal forming processes. Time period used is 0.0025 s. Element type used is C3D8R and C3D10M. Hexahedral elements have been used for tube and punch, while tetrahedral element is used for die. Amplitude has been provided in tabular format. Punch has been assigned an element size of 4 mm and die has been assigned an element size of 2 mm which is appropriate to define the geometry of die accurately. To evaluate appropriate mesh size for present analysis, an extensive mesh sensitivity analysis has been done for unprocessed tube in case of tube expansion. For this purpose, tube element size is varied between 0.25 mm and 1.5 mm and load evolution pattern is observed at different element sizes. Larger mesh sizes (1mm, 1.25 mm and 1.5 mm) showed a zig-zag and inconsistent load evolution pattern which is not agreeing well with experimental results. In case of mesh sizes, 0.25 mm, 0.5 mm and 0.75 mm, the load evolution obtained are almost same

(Fig. 4.4). However, CPU time spent in case of 0.25 mm mesh size is 842 min, which is quite large as compared to 87 min in case of element size 0.5. Considering computational efficiency, a mesh size of 0.5 has been chosen for end forming simulations which results in 6 elements in the thickness direction and is appropriate for bending involved in beading operation. In the case of processed tubes, since the processed zone is softer and deformation is concentrated more in the processed zone as compared to base metal, a mesh size of 0.4 mm has been assigned to processed zone, while for base metal 0.5 mm element size is retained. The same meshing strategy is followed for reduction and beading as well. During modeling of end forming, the mechanical properties of the raw tube given in Table 4.2 are incorporated for the unprocessed tube and the unprocessed region of the FSPed tubes. For the FSPed zone, the tensile properties are separately evaluated as given in Table 4.5 and incorporated during simulations. The true stress-true strain data are fit using the Hollomon's power law, $\sigma = k\varepsilon^n$ (Hollomon, 1945; Hollomon and Jaffe, 1947), and the obtained flow stress-strain behaviour (Fig. 4.5) is used. The strain hardening curves are extrapolated for larger strains during FE simulations. Actual thickness of raw tube, unprocessed and processed zone thickness in processed tubes have been used during simulations. Table 4.3 summarizes the thickness values incorporated during FE simulations. Punch has been provided required downward vertical displacement to simulate the end forming process.

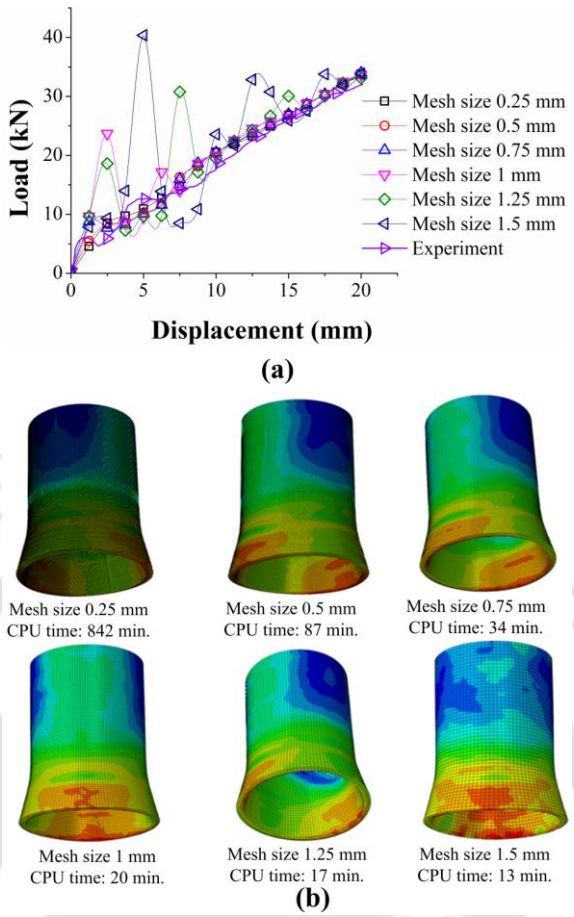

Fig. 4.4 Mesh sensitivity analysis, (a) load-evolution behaviour during tube expansion, and (b) associated simulation images at the last step for different mesh sizes

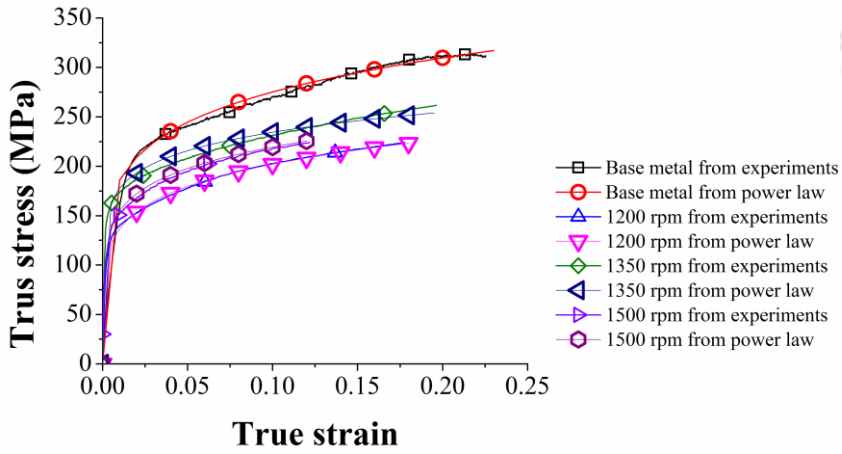

Fig. 4.5 True stress-strain fit used for FE simulations for base metal and FSPed zones at different rotational speeds

Table 4.3 Initial thickness for unprocessed and processed tubes used for end forming simulations

FSPed tube and raw tube thickness (mm)						
Tool rotational speed/Raw tube	Tube expansion		Tube reduction		Tube beading	
	In processed zone	In base metal	In processed zone	In base metal	In processed zone	In base metal
1200 rpm	2.326	3.138	1.984	3.20	2.134	3.17
1350 rpm	1.69	3.174	1.618	3.168	2.038	3.156
1500 rpm	2.058	3.162	1.716	3.112	1.506	3.126
Raw tube	3.16		3.184		3.176	

Hill's 1948 yield function with isotropic hardening has been used to model the plasticity of tubes. Although Hill's 1948 is better suited for steel grades, it is used for Al alloys in the present work. Thuillier et al. (2008) and Thuillier et al. (2011) applied Hill's 1948 yield function to model and analyze the hemming and bending behaviour of Al 6xxx sheets and the results are acceptable. Hence using Hill's 1948 yield function to describe the yielding of Al 6063 T6 tubes is acceptable. In plane stress condition, the six yield factors R_{11}, R_{22}, R_{33}, R_{12}, R_{13} and R_{23} can be calculated using plastic strain ratios r_0 (r_x), r_{45} and r_{90} (r_y) by the following relations (Karajibani et al., 2015),

$$R_{11}= R_{13}= R_{23}=1$$

$$R_{22}=\sqrt{\frac{r_y(r_x+1)}{r_x(r_y+1)}} \tag{4.4}$$

$$R_{33}=\sqrt{\frac{r_y(r_x+1)}{(r_x+r_y)}}$$

$$R_{12}=\sqrt{\frac{3(r_x+1)r_y}{(2r_{45}+1)(r_x+r_y)}}$$

Here 'r' has been calculated only in longitudinal direction of the tube and has been assumed same in other directions. Testing of tensile samples in circumferential direction (transverse) is not done as the specimen needs to be flattened and such flattening can affect the material properties. The value of plastic strain ratio and the value of six yield factors has been shown in Table 4.4. For the present model,

$$r_x(r_0) = r_{45} = r_y(r_{90}) = r \tag{4.5}$$

Table 4.4 Values of plastic strain ratio and anisotropic parameters

Base metal/FSPed zone	Plastic strain ratio *'r'*	R_{11}	R_{22}	R_{33}	R_{12}	R_{13}	R_{23}
Base metal	0.11	1	1	0.744	1.167	1	1
FSPed zone: 1200 rpm	1.726	1	1	1.16	0.96	1	1
FSPed zone: 1350 rpm	0.291	1	1	0.803	1.10	1	1
FSPed zone: 1500 rpm	0.190	1	1	0.771	1.14	1	1

4.1.7 Instability prediction during end forming

Instabilities in the form of neck and crack are observed in expansion and beading respectively**.** It is believed that severe thinning at the edge of the tube is responsible for the instabilities. Instability prediction during tube expansion and tube beading has been done based on thickness strain mapping in the weaker location of the end forming region in comparison to the stronger location of the same material. In reduction, instability is in the form of wrinkling and is observed directly from simulation.

For instability prediction in the case of tube expansion, the element which shows larger thinning at the end formed region in the processed zone is chosen as the unsafe element, whereas the element which shows lesser thinning at the end formed region in the processed zone is chosen as the safe element. A graph is plotted between thickness strain of safe region on X-axis and thickness strain of unsafe region on Y-axis. After a certain displacement, either the thickness strain in the safe region saturates with respect to thickness strain in unsafe region or saturation happens in both the regions. In the first case, a localized thinning occurs, while in the second case, the severe thinning front moves propagating the crack before severe thinning occurs at the edge. The stage at which saturation occurs is seen as the stage of onset of instability during end expansion of tubes. Similar strategy has been followed for instability prediction during end beading. The only difference is that in beading both safe and unsafe regions lie on peak bulged height of base metal region. Unsafe and safe regions are decided by thickness strain contour plot within the same element region in expansion and beading. Fig. 4.6 shows simulation during different end forming operations at a tool rotational speed of 1200 rpm. The unsafe region in case of expansion and beading can be seen (Fig. 4.6a and 4.6c), while wrinkling with overlapping can be observed during end reduction (Fig. 4.6b).

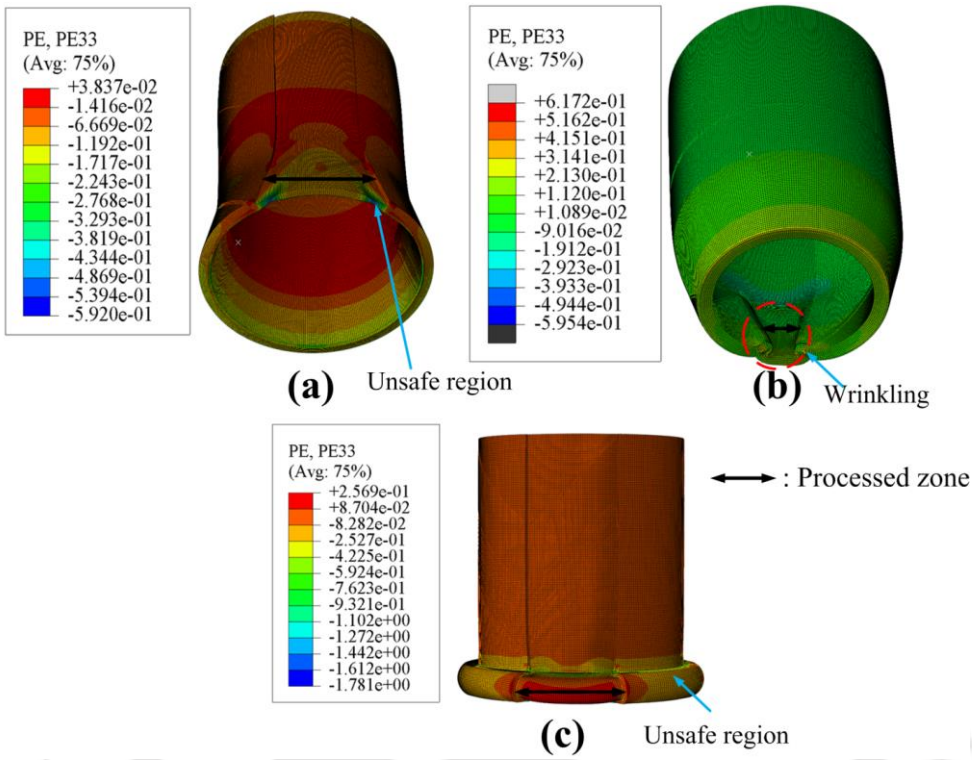

Fig. 4.6 Instability prediction in case of 1200 rpm, (a) end expansion, (b) end reduction, and (c) end beading

. Li et al. (2010) have followed similar strategy as applied in the present work to predict the forming limit diagram of AA5182-O through limit dome height test. Minor and major strains of necking elements show saturation (no further increase) after a certain displacement and this is indicated as stage of onset of localized necking. Paul (2013) predicted theoretical formulations of strain and stress-based FLD by different instability criteria. Naik et al. (2009) proposed four different necking criteria based on strain evolution to predict the forming limit of tailor welded blanks. The necking criteria are based on the fact that the strain evolution in the bulk (or safe region) saturates earlier during forming when compared with straining in the notch (or unsafe) region.

4.2 Results and discussion

In this section, tensile properties of base metal as well as processed zones, hardness distribution across processed zone before and after forming and grain size as well as dislocation density along the processed zone for different cases have been discussed. Later, load evolution and thickness evolution for parent tube and processed tubes during end forming experiments have been discussed. Finally, end forming simulations have been discussed.

4.2.1 Tensile properties and hardness distribution

The tensile behaviour of processed zone at different rotational speeds has been shown in Fig. 4.7. The flow strength of processed zone is lesser with respect to base metal, while an improvement in ductility is observed in case of rotational speed 1350 rpm. Within processed zones, 1350 rpm possesses better mechanical properties as compared to others.

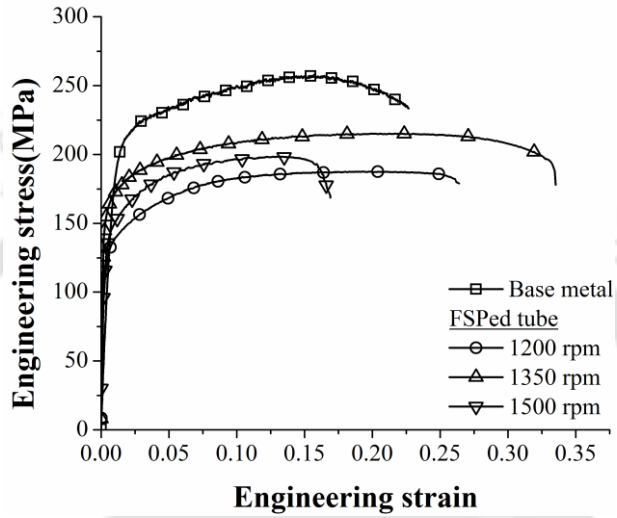

Fig. 4.7 Engineering stress-strain data for FSPed zone specimen at different rotational speeds
(standard deviation in Flow stress: Base metal: 13 MPa, for 1200 RPM: 8 MPa, for 1350 RPM: 22 MPa, for 1500 RPM: 34 MPa)

The tensile properties of the processed zones have been shown in Table 4.5. The strength and ductility related properties are evaluated. The average hardness is represented for strength of the FSPed zone, while elongation and strain hardening exponent for ductility of the FSPed zone (Table 4.5). Hardness of the processed zone is found to be lower than the base metal for all the three rotational speeds, and it is maximum for 1350 rpm with 67.52 VHN.

Table 4.5 Mechanical properties of the FSPed zone at different rotational speeds

Tool rotational speed (ω, rpm)	Average Hardness (VHN) across the processed zone	Yield strength (MPa)	UTS (MPa)	Uniform elongation, at 12.5 mm gauge length	Total elongation, at 12.5 mm gauge length	Strain hardening exponent, n	Strength coefficient, K (MPa)
1200	62.3±4	120±13	187±19	19.4±0.02	25±0.04	0.17±0.01	299±4
1350	67.52±7	153±4	215±25	21.6±0.01	36.4±0.08	0.12±0.04	309±74
1500	64.07±8	130±40	198±60	12.9±0.03	22.1±0.03	0.15±0.02	310±79

Table 4.5 data reveal that the yield strength, ultimate strength (UTS) and strength coefficient of the FSPed zone have decreased when compared to base sheet. The ductility of the processed zone has improved (both uniform and total elongation) in few cases, while in others it has decreased or remained same. The strain hardening exponent of the processed zone is less than the base metal. As said earlier, the hardness of the FSPed zone is measured before and after forming. The motive of measuring hardness after forming is to study the effect of deformation on the processed zone during end forming. The hardness distribution of the processed zone, before forming and after forming, for all the three end forming operations at all rotational speeds has been shown in Fig. 4.8(a-c). The average hardness is given in Table 4.6. From Fig. 4.8(a-c) it is observed that hardness decreases drastically after FSP. A maximum hardness difference of 10 VHN is observed between different zones of processed region (e.g. stirred, TMAZ and HAZ) for any end forming operation for all rotational speeds after FSP. Hardness distribution is showing random behaviour in different zones of processed region. The hardness of softened region (shown by box) in Fig. 4.8(a-c) is mostly lying between 58-70 VHN and maximum hardness is observed at a distance of 7-8 mm from processed centre. The processed zone width increases with the increase of rotational speed before forming. The only exception is for tube expansion, where processed zone width corresponding to 1200 rpm and 1500 rpm is same, whereas in other cases the processed zone width corresponding to 1200 rpm is the lowest (before forming). When the hardness plot reaches the shoulder limit, the hardness increases and reaches to that of base metal hardness.

The hardness of FSPed zone increases after forming and in most of the cases approaches towards base metal hardness which is acceptable from application point of view. The strain hardening during end forming is the main reason for hardness improvement in the processed zone. Behnagh et al. (2012) has described that hardness of aluminium alloys can be improved by strain hardening. Al 5083 has been FSPed in Behnagh et al. work and the average hardness improved slightly as compared to base material because of strain hardening. Al 5083 is a solid-solution hardened Al alloy and strain hardening becomes the reason for hardness improvement, though it is marginal. On the other hand, in the present work, for Al 6063-T6, a precipitation hardening material, it has been demonstrated that the hardness of FSPed zone can be improved by end forming operations as compared to base material, though the FSPed zone is soft after FSP.

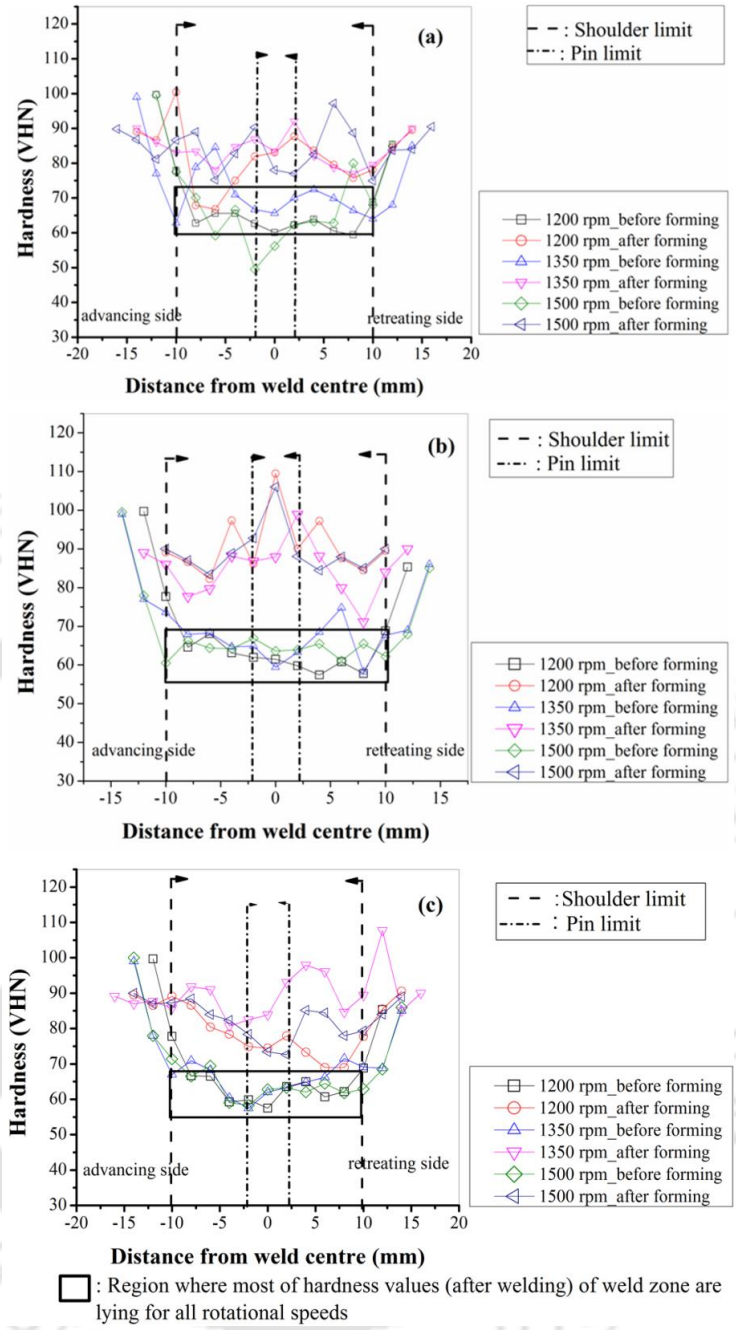

Fig. 4.8 Hardness contour plot in processed zone for all rotational speeds (before forming and after forming) in case of, (a) tube expansion, (b) tube reduction, (c) tube beading (average standard deviation in hardness in processed zone in case of expansion before forming is ±7 and after forming is ±7, in case of reduction before forming is ±4.13 and after forming is ±8.75, in case of beading before forming is ±4 and after forming is ±8.3)

Specifically, in tube reduction, the hardness of FSPed zone is almost same as that of base material. The stirred zone shows maximum hardness for all rotational speeds amongst all zones after tube reduction, while this is not the case with other end forming operations (Fig. 4.8b). After expansion and beading, the maximum hardness for all

rotational speeds is either at the SZ- TMAZ interface or in HAZ towards retreating side of the processed zone. It is also found that hardness variation across different zones of processed region (i.e., SZ, TMAZ and HAZ) is larger after forming as compared to before forming cases for all the end forming operations at different rpms. The effect is prominent in case of reduction and beading as compared to expansion. The stirred zone during reduction of tubes shows even higher hardness at some locations than the base metal for all rotational speeds (Fig. 4.8b). It indicates that in tube reduction operation, the tube undergoes severe strain hardening as compared to tube expansion and beading. Though there is about 8-10 VHN difference between different zones of processed region (before forming and after forming) except for some extreme cases, an average hardness has been evaluated for a processed zone of width 16-18 mm. The average hardness of the processed zone before and after forming at all rotational speeds for all the end forming operations is shown in Table 4.6.

Table 4.6 Hardness (average) of the processed zone before and after end forming at different tool rotational speeds (Base metal hardness: 93.76±13 VHN)

Tool rotational speed (ω, rpm)	Hardness (VHN)					
	Expansion		Reduction		Beading	
	Before forming (H_i)	After forming (H_f)	Before forming (H_i)	After forming (H_f)	Before forming (H_i)	After forming (H_f)
1200	62.52±3	80±17	62.05±5	92.85±12	62.33±4	76.05±8
1350	70.21±10	82.61±7	66.83±5	83.15±10	65.54±6	89.52±8
1500	61.87±10	83.71±8	66.74±10	90.22±9	63.61±5	81±8

Note: Before forming is same as after FSP

It is observed from Table 4.6 that a local material softening occurs in the processed zone after FSP. An average hardness decrement of 33.55 %, 27.98 % and 31.66 % has been observed for tool rotational speeds, 1200 rpm, 1350 rpm and 1500 rpm respectively. Hardness decrease in the FSPed zone of 6xxx Al alloy is mainly dependent on the coarsening and dissolution of strengthening precipitates during thermal cycle of FSP. This is a characteristic of precipitation hardened Al alloy. Similar results have been shown by Moreira et al. (2008) for the same material of almost same thickness. The hardness decrease at the FSPed zone is about 27 % and 32 % on top surface and side surface respectively. The work done by Sato et al. (1999) revealed that for 6063 Al alloy the hardness drastically decreases at the processed zone. It has been observed that the

hardness change depends mainly on the precipitation distribution, and not much on the grain size. It has been revealed that the reduction in the density of needle shaped precipitates and dissolution of precipitates led to softening in the processed zone.

The grain size examination of the FSPed zone has been done at all the rotational speeds (Fig. 4.9(a-d)). Three distinct zones can be identified in the processed zone - stir zone (SZ) consists of fine equiaxed recrystallized grains, thermo-mechanically affected zone (TMAZ) with relatively large elongated grains, and heat affected zone (HAZ).

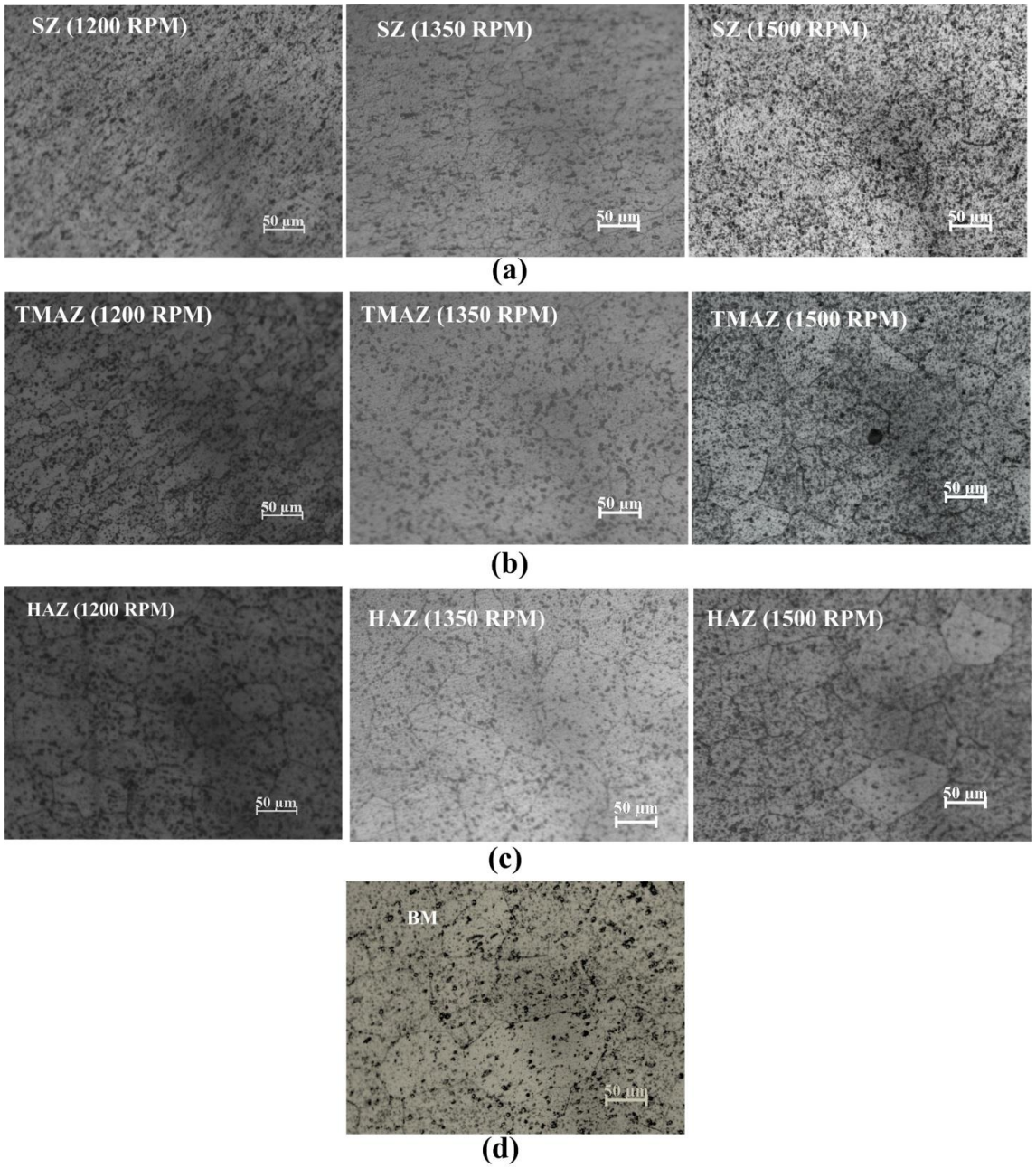

Fig. 4.9 Optical micrographs of different regions of the processed zone at different rotational speeds: (a) SZ at 1200, 1350 and 1500 rpm, (b) TMAZ at 1200, 1350 and 1500 rpm, (c) HAZ at 1200, 1350 and 1500 rpm, (d) Base Metal

TMAZ experiences lesser strain, strain rates and heat input as compared to weld nugget zone and also dynamic recrystallization is absent in this zone. Since TMAZ contains both temperature and deformation during FSP and hence larger elongated grains are observed in TMAZ zone. HAZ only experiences heat during thermal cycle as the name suggests and grain sizes obtained in this zone are similar to that of base metal. In the HAZ the precipitation process continues and it is expected that in this zone precipitation coarsening can take place. Optical micrographs of different zones of processed region at different rotational speeds and for base metal has been shown in Fig. 4.9. It can be concluded from the Fig. 4.9 that the average grain size increases from SZ to TMAZ to HAZ. Coarser grains are observed for base metal (Fig. 4.9d). Due to severe plastic deformation and high temperature, the FSPed zone and in particular stirred zone show grain refinement and dynamic recrystallization.

The average grain size of different regions of the FSPed zone has been shown in Table 4.7. In the stir zone and TMAZ, the grain size increases with the increase of rotational speed, however the difference is insignificant. Sato et al. (2002) have shown similar results. FSW between 6063-T4 and 6063-T5 at 800, 1220 and 2450 rpm were conducted and found that with increase of rotational speed, grain size in SZ increases. It is confirmed that hardness modification in 6063-T6 is dependent on precipitate dissolution rather than on grain size, as different rotational speeds show little effect on the grain size in a particular region.

Table 4.7 Average grain size of different regions of the FSPed zone (Base metal grain size: 91.15±22 μm)

Regions of weld zone	Grain size (μm)		
	1200 RPM	1350 RPM	1500 RPM
SZ	17.4±2	32.25±8	32.25±8
TMAZ	24.6±3	37.8	45.6±11
HAZ	53.4	49.15±6	64.45±15

It is observed from Table 4.6 that there is no significant difference in hardness of the softened region evolved at different rotational speeds. However, maximum hardness of the processed zone is seen at 1350 rpm. Similar results are obtained in the work of Sato et al. (2002) for 6063-T5 material during FSW. They have shown the hardness profile across the processed zone for Al 6063-T5 at three different rotational speeds, i.e., 800 rpm, 1220 rpm and 2450 rpm. The welds are softened around the weld centre and no

significant difference in hardness has been observed resulting from different rotational speeds.

As it has been earlier discussed that hardness of FSPed zone increases after forming in all cases, the degree of hardness change, based on initial hardness, has been defined in terms of hardness index, H (%) as follows:

$$H(\%) = \frac{H_f - H_i}{H_i} \times 100 \quad (4.6)$$

where H (%) is the hardness variation in percentage during deformation, H_f is the final hardness of the FSPed zone after forming, and H_i is the initial hardness of the FSPed zone before forming. For all the end forming operations and at all the rotational speeds, H (%) value has been shown in Fig. 4.10.

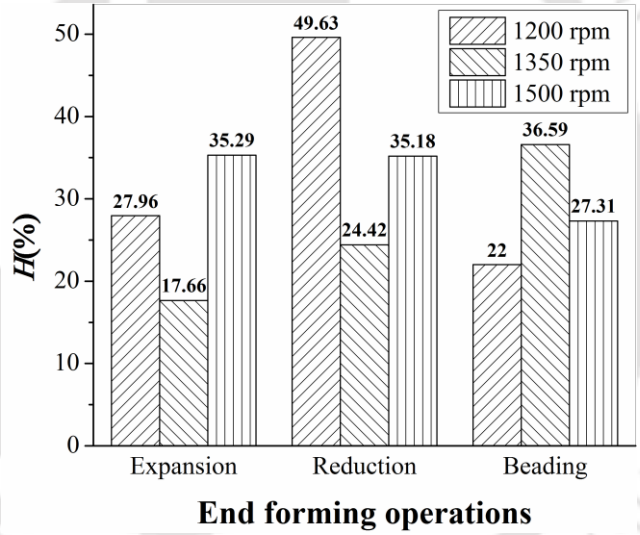

Fig. 4.10 H (%) versus rotational speeds for all end forming operations

H (%) shows sensitiveness to almost all the tool rotational speeds. During expansion, 35 % hardness increment has been observed for tool rotational speed of 1500 rpm. About 49 % hardness increment has been found for the processed zone made at tool rotational speed of 1200 rpm during reduction. Similarly, during beading about 36 % hardness increment has been observed for a tool rotational speed of 1350 rpm. For 1200 and 1500 rpm, H(%) is largest during reduction amongst all end forming operations. For 1350 rpm, H(%) is observed to be highest for tube beading amongst all end forming operations. Expansion and beading also shows significant changes in H(%) for all rotational speeds. With the increase of rpm, from 1200 to 1500 rpm, H(%) first decreases

and then increases for tube expansion and reduction, while it is behaving oppositely for tube beading (e.g. first increases and then decreases), though there is not much difference in the initial hardness of the FSPed zone before forming.

4.2.2 Dislocation density measurement

Fig. 4.11a shows the directly measured X-ray diffraction data. Fig. 4.11b shows the (2 2 0), (3 1 1) and (2 2 2) peak profiles in the SZ for three different tool rotational speeds. It can be observed that peak broadening is slightly different for different rotational speeds which is related to different dislocation densities.

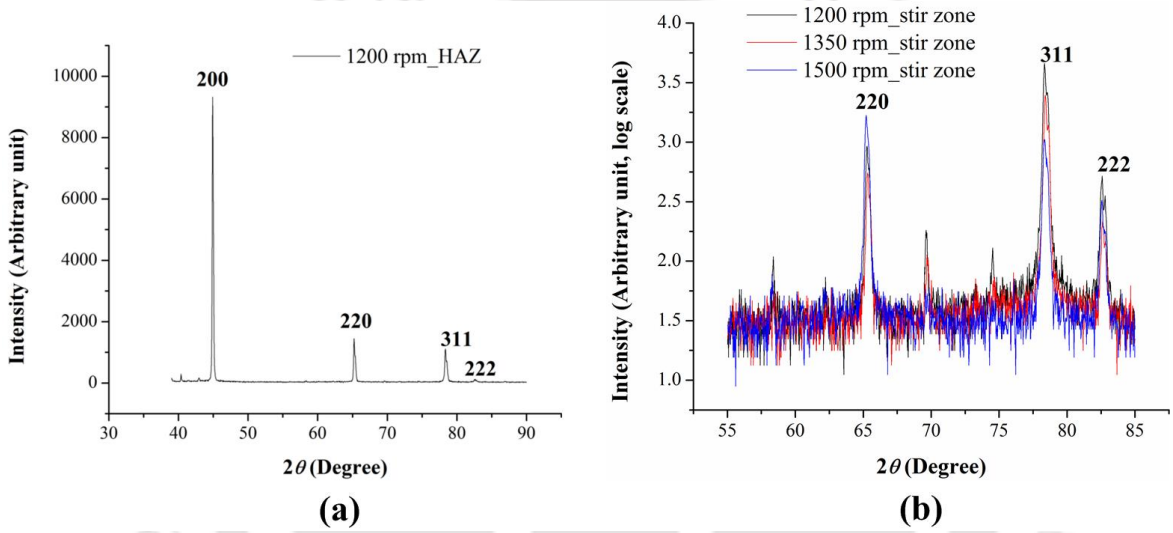

Fig. 4.11 (a) X-ray diffraction peak profile pattern in the HAZ region of FSPed 6063-T6 tubular specimen, (b) peak profiles measured using X-ray diffraction in the stir zone for 1200 rpm, 1350 rpm and 1500 rpm

Modified Williamson-Hall plot for different zones and traverse speeds has been shown in Fig. 4.12. In case of SZ (dynamically recrystallized zone) base metal shows the highest slope between successive peaks as compared to different rotational speeds (Fig. 4.12a). It indicates that base metal has got larger dislocation density as compared to rotational speeds. Within rotational speeds, slope corresponding to rotational speed 1350 rpm is largest, while smallest slope is corresponding to rotational speed 1200 rpm. It means that in case of 1350 rpm largest dislocation density is observed. The strain hardening exponent is minimum in case of 1350 rpm (within rotational speeds) (refer Table 4.2 and Table 4.5).

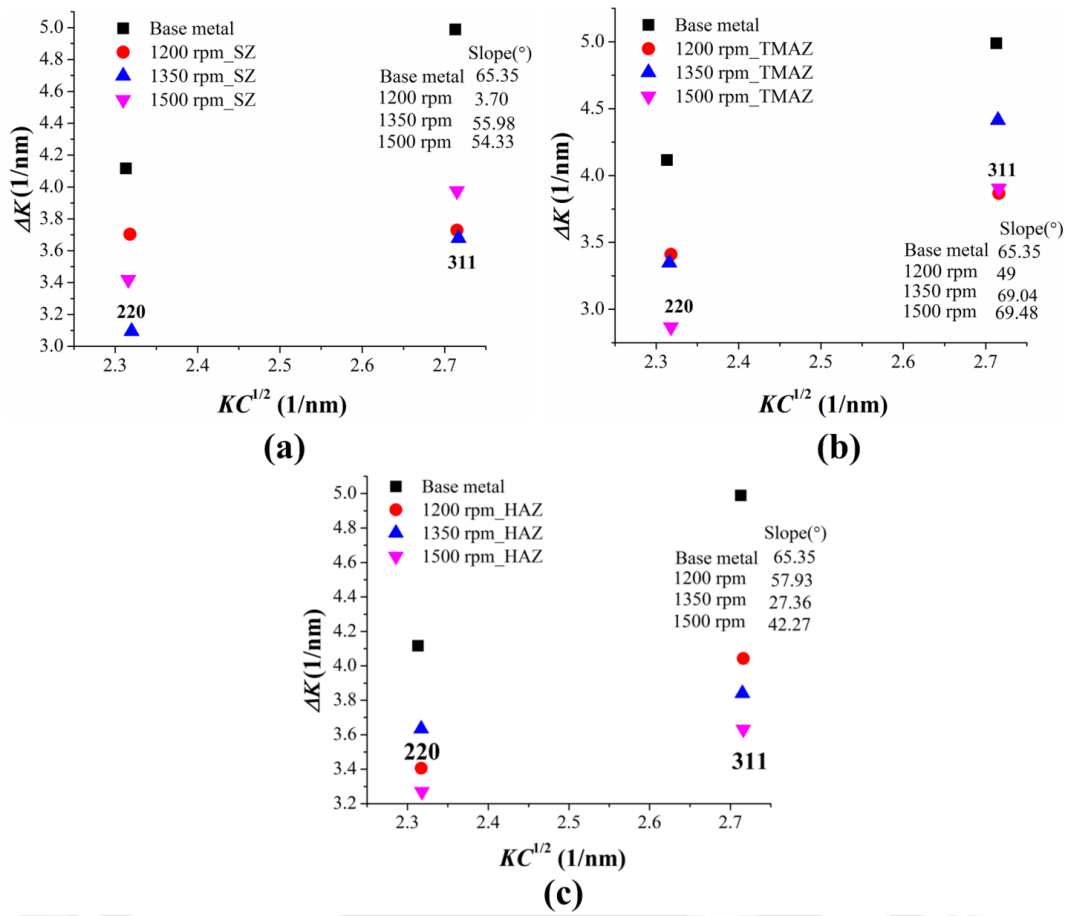

Fig. 4.12 Peak broadening analysis using the modified Williamson-Hall plot in different zones of FSP zone. The FWHM (ΔK) in each (hkl) peak is presented as a function of $KC^{1/2}$ (K=2Sinθ/λ) and C is the dislocation contrast factor

In TMAZ, slope of rotational speeds 1350 rpm and 1500 rpm is larger than that of base metal, while in case of 1200 rpm, slope is almost equal to base metal (Fig. 4.12b). It means that in TMAZ for different rotational speeds larger dislocation density is observed as compared to base metal. Also it can be observed that for rotational speeds 1350 rpm and 1500 rpm slope is almost same. In HAZ region, slope of rotational speeds 1200 rpm and 1500 rpm is comparable with that of base metal, while in case of rotational speed 1350 rpm it is slightly lower than that of base metal (Fig. 4.12c). It suggests that a comparable dislocation density is achieved for different tool rotational speeds in HAZ region and base metal. Similar results have been shown by Woo et al. (2008) for FSWed 6061-T6 alloy. They explained that the low dislocation density in the DXZ can be due to recrystallization at the elevated temperature. The higher dislocation density observed near the boundary between TMAZ and HAZ could be explained by the network structure of

many dislocations in subgrains. HAZ region has got nearly same dislocation density as that of base metal.

Dislocation density at different processing conditions and for different zones has been calculated with the help of equations 4.1 and 4.2 as described in section 4.1.3. Dislocation density for base metal and for different zones at different rotational speeds has been shown in Table 4.8. SZ shows lower dislocation density as compared to base metal, while TMAZ exhibit higher dislocation density for 1350 rpm and 1500 rpm as compared to base metal. For a rotational speed of 1200 rpm a lower dislocation density has been obtained in TMAZ as compared to base metal. The dislocation density obtained in HAZ region for rotational speeds 1350 rpm and 1500 rpm is comparable with that of average dislocation density in base metal, while in case of rotational speed 1200 rpm it is lower than that of the base metal.

Table 4.8 Dislocation density for base metal and for different zones

Rotational speed (rpm)	Dislocation density ($\times 10^{17}$ m^{-2})			Average dislocation density ($\times 10^{17}$ m^{-2}) in processed zone
	SZ	TMAZ	HAZ	
1200	1.70	5.36	2.97	3.34±2
1350	2.94	50.35	6.51	19.93±26
1500	1.72	47.86	7.87	19.15±25
*Base metal Dislocation density: 8.6±0.5 ($\times 10^{17}$ m^{-2})				

As earlier stated, the hardening capacity (H_c) and strain hardening exponent (n) can determine the strain hardening behaviour. Hardening capacity for base metal and processed zone at different rotational speeds and their respective n values has been shown in Table 4.9. H_c is lower for all tool rotational speeds when compared to base metal. Except for tool rotational speed 1200 rpm other rotational speed shows lower n value when compared to base metal while in earlier case it is equal to that of base metal. It means that applied stress required for plastic deformation for base metal is larger as compared to different rotational speeds. Such strain hardening behaviour is typically related to the accumulation and interaction of the dislocations. As rotational speed increases, strain hardening capacity first decreases and then increases. High strain hardening exponent at low rotational speed is because of a low initial dislocation density at lower rotational speed. Williamson Hall plot (Fig. 4.12) confirms the same result.

Table 4.9 H_c and n for base metal and FSPed zone at different rotational speeds

Base metal/Rotational speed	H_c	n
Base metal	0.69	0.17
1200 rpm	0.55	0.17
1350 rpm	0.40	0.12
1500 rpm	0.52	0.15

4.2.3 End forming behaviour

4.2.3.1 Load-displacement behaviour

From the load-displacement behaviour of FSPed tubes and raw tube (Fig. 4.13a, 4.14a, 4.15a), it is observed that load required to deform raw tube (base metal) is more as compared to FSPed tube for all end forming operations. The base metal has larger hardness as compared to the processed zone and hence requires larger load for deformation irrespective of the end forming operations.

In tube expansion operation, it is observed from Fig. 4.13a and 4.13b that the load requirement decreases with increase in rotational speed. There is not much difference between 1200 and 1350 rpm in the load evolution, except in maximum load. The load evolution remains same in all the three cases up to a certain displacement. Only at 1200 rpm, there is a recognizable improvement in displacement at failure and maximum load. The initial hardness of the processed zone is one important factor on which load depends on during forming. However, during end forming, hardness of the processed zone increases, hence change in hardness, H(%), during deformation also play a key role for determining the load during end forming and most of the times the effect of H (%) dominates the initial hardness for load evolution during end forming. The initial hardness and change in hardness index H(%) for FSPed zone made for tube expansion follows the order: $(H_i)_{1500\ rpm}<(H_i)_{1200\ rpm}<(H_i)_{1350\ rpm}$ and $(H\ \%)_{1350\ rpm}<(H\ \%)_{1200\ rpm}<(H\ \%)_{1500\ rpm}$. So, the initial hardness and hardness change is neither highest or lowest for 1200 rpm, rather it lies in between the other two rotational speeds. So due to a combination of mediocre values of initial hardness and hardness index in 1200 rpm, the maximum load is highest for FSPed zone made at 1200 rpm. H (%) for processed zones made at 1350 rpm is minimum as compared to other processed zones (Fig. 4.10) and hence needs lower maximum load for tube expansion. Because of larger strain hardening exponent of processed zone made at 1200 rpm, it is experiencing larger displacement to failure as

compared to other processed zones. On the whole, mainly *H* (%) during deformation and to some extent initial hardness is responsible for determining the load requirement during expansion of tube, while the strain hardening exponent of the weld zone decides the displacement at failure.

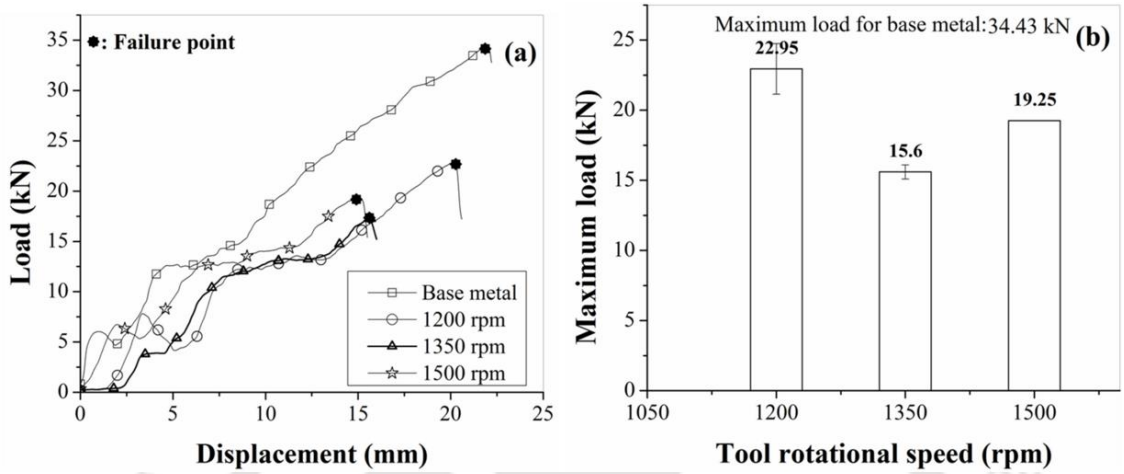

Fig. 4.13 Tube expansion: (a) load-displacement behaviour at different tool rotational speeds, (b) maximum load at different tool rotational speeds (Data show the maximum load)

In the case of tube reduction (Fig. 4.14a), with increase in rotational speed, the load requirement increases. FSPed tube at 1500 rpm needs larger load to deform as compared to the other two. Unlike in tube expansion, there is considerable difference in load requirement throughout the forming in case of tube reduction. The variation in maximum load with rotational speed can be correlated to % change in hardness (Fig. 4.10) and initial hardness before forming. It is seen that the case of 1350 rpm showed the least *H* (%) value (Fig. 4.10) and hence needs lesser maximum load as compared to the other two.

The initial hardness of the processed zone made at 1500 rpm is almost equal to that of 1350 rpm and larger than 1200 rpm (Table 4.6). The change in hardness, *H* %, in case of reduction of tubes follows the order: $(H\ \%)_{1350\ rpm} < (H\ \%)_{1500\ rpm} < (H\ \%)_{1200\ rpm}$, again the load required during tube reduction is determined by the combined effect of initial FSPed zone hardness and *H*(%) of the processed zone during deformation. In this case, tubes made at 1500 rpm requires larger load for forming. It should be noted that the variation in repeatability of maximum load among the three rotational speeds is

considerable. But the effect of rotational speed on the maximum load remains same for both the limits of deviation.

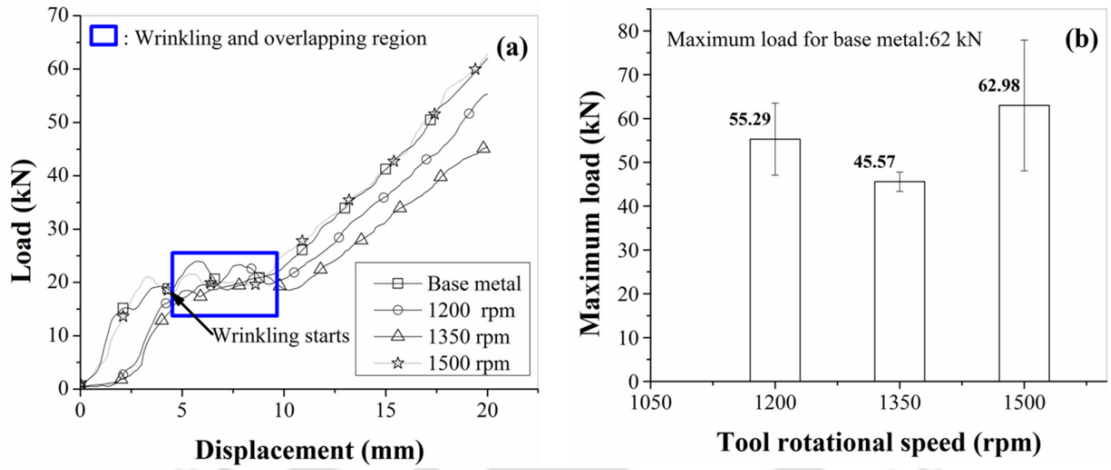

Fig. 4.14 Tube reduction: (a) load-displacement behaviour at different tool rotational speeds, (b) maximum load at different tool rotational speeds (Data show the maximum load)

In the case of tube reduction, a region of constant load is observed for all the rotational speeds between 4 and10 mm of displacement (Fig. 4.14a). The tube wrinkling phenomenon is observed at a displacement of 4 mm for all the rotational speeds, and as the deformation progresses overlapping is also observed in the FSPed zone. Since the deformation between the displacement of 4 to 10 mm is mostly characterized by wrinkling and overlapping, and since these instabilities can occur at the load at which it originates, the evolution of load is not considerable during this phase of deformation. The degree of overlapping, final processed zone width/initial processed zone width, decreases with the increase of rotational speed during this phase and for a tool rotational speed of 1500 rpm full overlapping is observed at a displacement of 10 mm. But the overlapped length is almost half (i.e., 10 mm) of the reduced length (i.e., 20 mm) of tubes for all the rotational speeds at the completion of the process. Hence after a displacement of 10 mm, the deformation is mostly characterized by tube reduction and since reduction requires larger load, an increase in load is observed after a displacement of 10 mm.

During tube beading, the maximum load occurs at 3-4 mm of displacement for different rotational speeds. It is observed that at the start of tube beading, the load requirement is larger and increases rapidly until beading occurs. After the stage, the beading continues in the radial direction for which lesser load is required in all the cases.

Only slight deviation in maximum load is found for all the cases of FSPed tubes (Fig. 4.15). The hardness index (*H* %) during beading of tubes at rotational speed of 1200 rpm, 1350 rpm and 1500 rpm is 22, 36.59 and 27.31 respectively. Though the maximum load is not changing much with rotational speed, the load requirement is larger in case of 1200 rpm and least for 1500 rpm, up to a displacement of 2 mm.

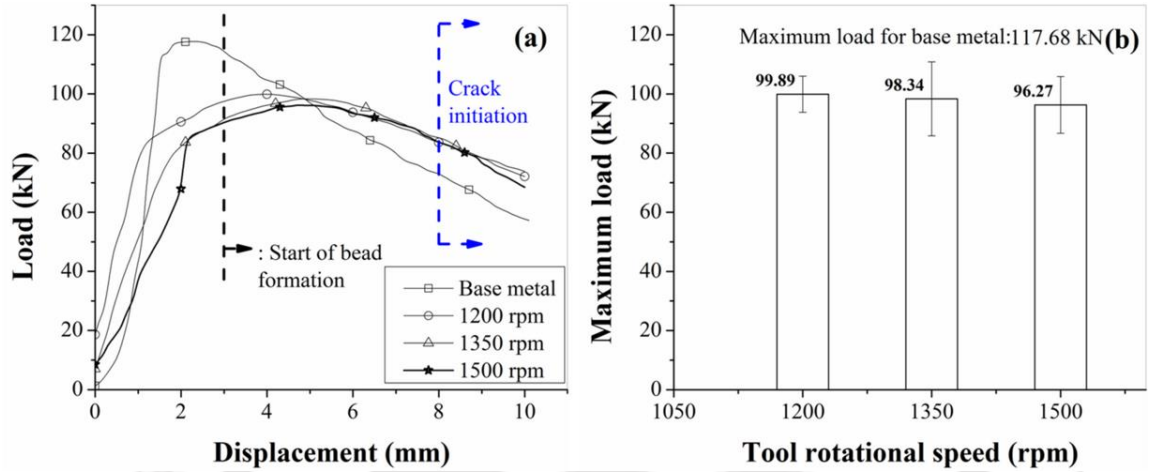

Fig. 4.15 Tube beading: (a) load-displacement behaviour at different tool rotational speeds, (b) maximum load at different tool rotational speeds (Data show the maximum load)

During beading of tubes, fine cracks are observed in base metal region towards the end of deformation, at a displacement of 8-9 mm. It has been observed during thickness measurement of beading of tubes that the thickness of the base metal region in the peak bulged height and the circumferential stretching of the bulged portion of the tube increases in the outward radial direction of the tube and hence cracks are observed along the length direction of the tube in the peak bulged region.

4.2.3.2 Thickness evolution

The thickness evolution in FSPed tubes, both in the processed zone and in base metal, and in the unprocessed tube is shown in Fig. 4.16. In tube expansion, the major thickness change occurs in the FSPed zone, while base metal in FSPed tube as well as the unprocessed tube show insignificant change in thickness (Fig. 4.16a). During tube reduction (Fig. 4.16b), processed zone and base metal in processed tubes and unprocessed tubes, all show thickness change during deformation, but increment in processed zone thickness is more as compared to change in base metal thickness. In case of tube beading (Fig. 4.16c), the processed zone, base metal in processed tube and unprocessed tubes, all

show significant changes in thickness during deformation, but the base metal show more thickness increment as compared to processed zone. Also it is observed that thickness increment of unprocessed tube is less as compared to thickness increment of base metal zone in processed tubes. In summary, tube expansion witnesses thickness reduction, while thickening occurs in the case of tube reduction and beading.

The percentage thinning of processed zone and base metal in processed tube has been evaluated at three different rotational speeds. The final thinning at the last stage of end forming is presented in Fig. 4.17(a, b). The thinning severity (%) is described by,

$$T(\%) = \frac{t_f - t_i}{t_i} \tag{4.7}$$

where T(%) is the thinning severity (%), 't_i' is the initial tube thickness and 't_f' is the final tube thickness.

It is observed that FSPed zone in FSPed tube is more sensitive to thickness change during expansion and is least sensitive during beading. For the same rotational speed, thinning in tube expansion and thickening in tube reduction are severe for FSPed zone of the processed tube as compared to the base material in the same processed tube ((Fig. 4.17(a, b)). For example, at 1200 rpm, about 24 % thinning is seen in the FSPed zone during tube expansion, while it is just about 2 % in base metal. At 1350 rpm, about 44 % thinning of processed zone is seen during tube expansion, while it is less than 1 % in base metal. This is true for 1500 rpm as well. Similar situation exists in the case of tube reduction, except that thickening happens in this case. The FSPed zone shows larger thickening as compared to base metal in tube reduction. But the situation is opposite in tube beading. The base metal shows larger thickening ability than the FSPed zone in all the rotational speeds ((Fig. 4.17(a, b)).

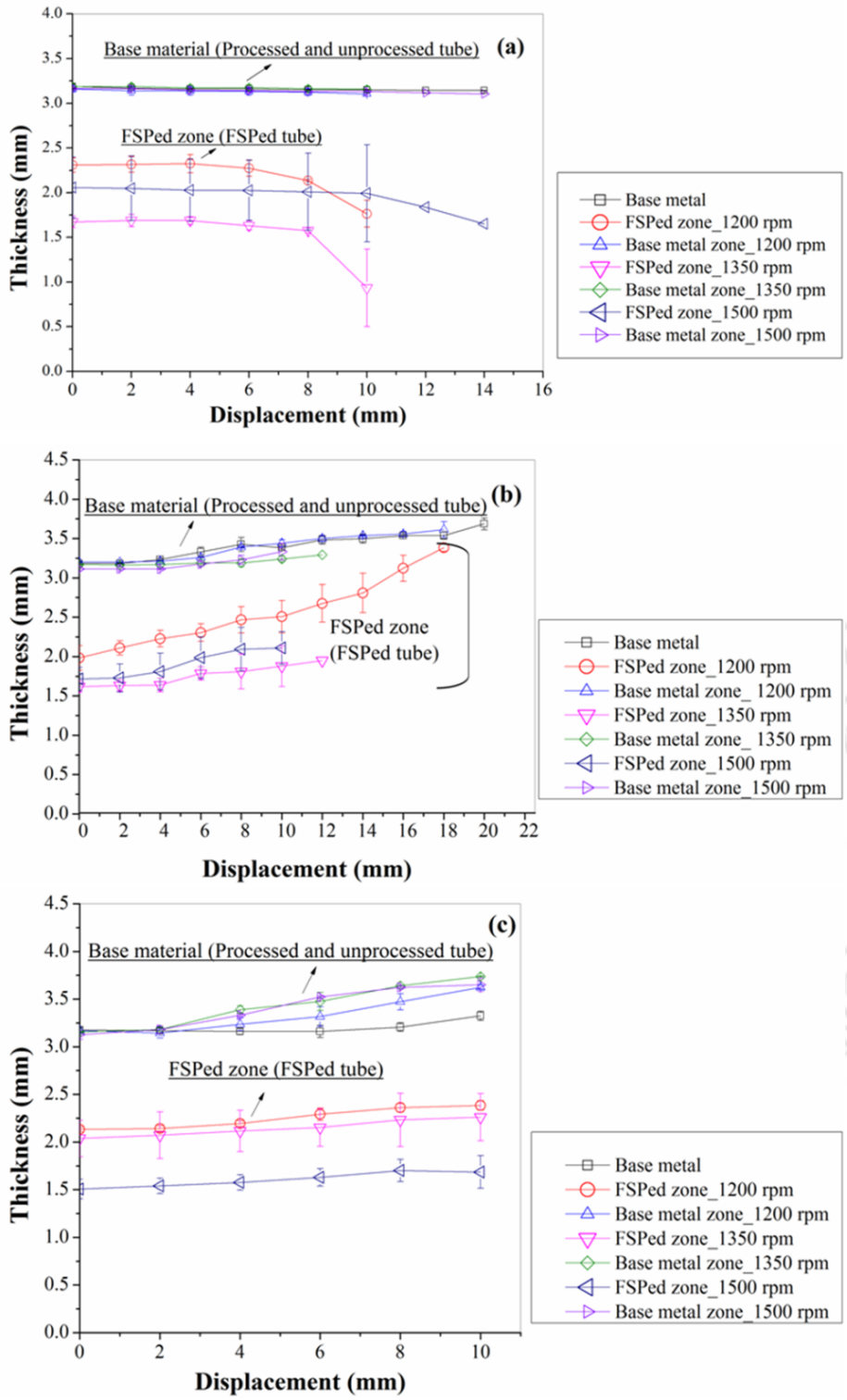

Fig. 4.16 Thickness evolution in FSPed zone and base metal (both in FSPed and unprocessed tube) in case of (a) tube expansion, (b) tube reduction, (c) tube beading

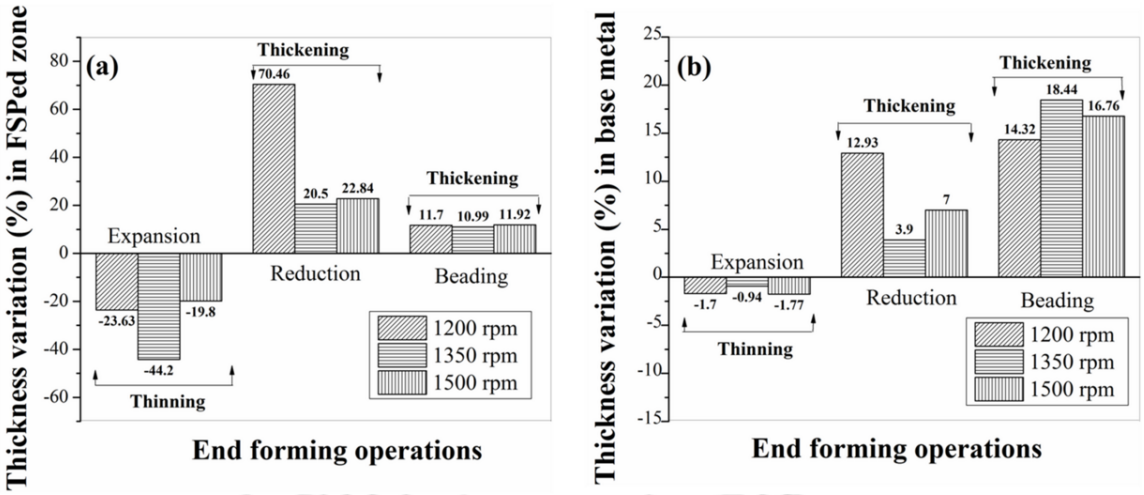

Fig. 4.17 % thickness variation (thinning or thickening) at different rotational speeds (a) in processed zone, and (b) in base metal, of FSPed tube

The strength (or hardness) difference between the FSPed zone and base metal governs the thickness evolution in the case of tube expansion and reduction, as both the operations are either in circumferential tension or circumferential compression modes of deformation. Since the FSPed zone is soft, thinning and thickening is significant in the FSPed zone in comparison to the base material of the same FSPed tube. The strain hardening exponent of the FSPed zone governs the tube thickening phenomenon as compared to base material in tube beading, as bi-axial stretching is expected in the bead forming region. Since the strain hardening exponent of the base material is better than FSPed zone, it shows larger thickening as compared to FSPed zone.

The load-displacement behaviour during end forming operation depends also on the thickness of the FSPed zone after processing. Table 4.10 gives the FSPed zone thickness after FSP for all the cases. The thickness of the processed zone varies between 1.5 and 2.3 mm and depends on the rotational speed, but randomly. The thickness of the processed zone also contributes to the load bearing ability of the FSP tube. FSP tube made at 1350 rpm exhibit lowest initial thickness as compared to 1200 and 1500 rpm is the case of tube expansion and reduction. This in turn has affected the load evolution during tube expansion and reduction, as seen in Fig. 4.13 and Fig. 4.14. But in the case of tube beading, the case of 1500 rpm shows lesser load bearing ability and has got lesser thickness as well (Table 4.10) after FSP, as compared to 1200 and 1350 rpm.

Table 4.10 Thickness of the FSPed zone with respect to end forming behaviour and rotational speed

End forming operations	Initial thickness (average) of the weld zone in welded tube (mm)		
	1200 rpm	1350 rpm	1500 rpm
Tube expansion	2.31	1.674	2.058
Tube reduction	1.984	1.618	1.716
Tube beading	2.134	2.038	1.506

Average thickness deviation: ±0.27 mm

The following are some important observation on the instabilities developed during end forming operations of FSPed and parent tubes.

1) In the case of tube expansion, failure of FSPed tubes occurred at the middle of the processed zone. This is mainly due to the reduction in hardness of the processed zone as compared to the base material of the tube. The softer processed zone is stretched perpendicularly in the circumferential direction during tube expansion and failure is seen at the middle of the weld zone (Fig. 4.18a), where minimum hardness value is witnessed.

2) In tube reduction, since compressive stress acts along the circumferential direction in the FSPed zone, it is pushed away from the die surface in the inward direction. FSPed zone is softer, and as a consequence, wrinkling is seen in the FSPed zone (Fig. 4.18b). It is found that wrinkling starts at a displacement of about 4 mm. Later in the reduction process the wrinkle overlaps. Because of this, measuring thickness in the FSPed zone becomes difficult and hence not measured after a particular stage. The overlapping of wrinkle has been observed in 1200, 1350 and 1500 rpm rotation speeds at a displacement of 18 mm, 10 mm and 12 mm respectively. *H* (%), in 1350 rpm is minimum and hence overlapping occurs easily and at an early stage of 10 mm. In this case, *H* (%) is maximum at 1200 rpm and hence overlapping occurs at a later stage in this case. No wrinkling is observed in the unprocessed tubes.

In the case of tube beading experiments, due to biaxial stretching in the deforming region, cracks are witnessed in the base material part of FSPed tubes and in the unprocessed tube as well. Cracks are located at the bead region of the tube and oriented along the length direction of the tube (Fig. 4.18c). The ductility of the FSPed zone is better than that of base metal and hence cracks are not seen on the FSPed zone. The position of cracks in the base metal of the FSPed tube is random and has no relationship with FSPed zone. Fig.

4.18 describes the mechanism of instabilities developed during the three end forming operations of FSPed tubes.

A comparison between end forming behaviour of unprocessed and FSPed tubes is shown in Fig. 4.19(a-c). The failure in case of processed tube for tube expansion is at the middle of the processed zone and the fracture propagation is almost straight, while in case of unprocessed tube the fracture line is slightly inclined Fig. 4.19a. During reduction, Fig. 4.19b, a uniform reduction without wrinkling is observed in unprocessed tube, while wrinkling is observed in case of FSPed tube. During beading of tubes, larger cracks are observed on the peak bulged height of the base metal in unprocessed tube, while the size of crack is relatively small in base metal part of the FSPed tube Fig. 4.19c.

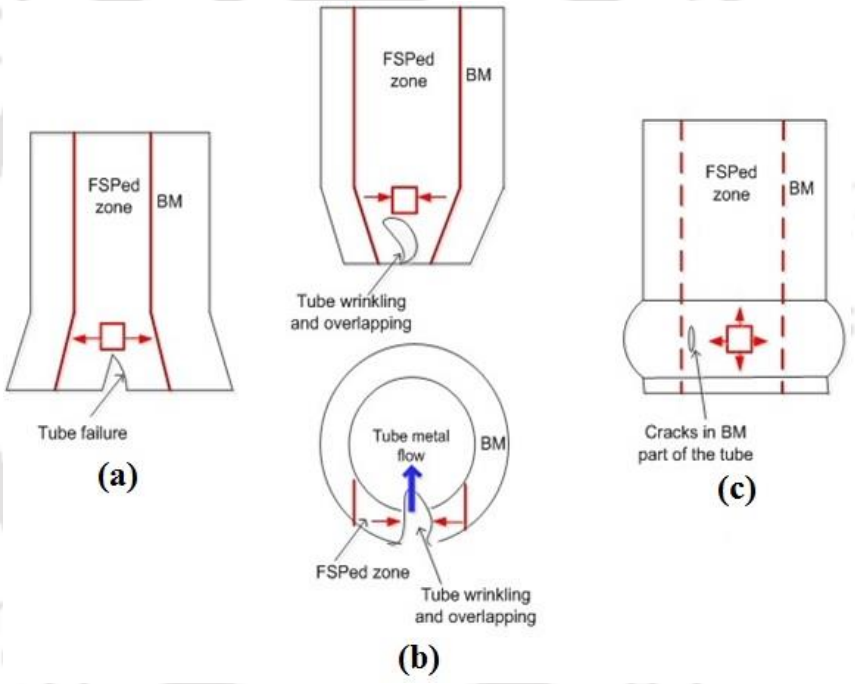

Fig. 4.18 Mechanism of instabilities developed during end forming operations, (a) elemental region stretched circumferentially during tube expansion, (b) elemental region compressed circumferentially during tube reduction, (c) elemental region undergoing biaxial stretching during tube beading.

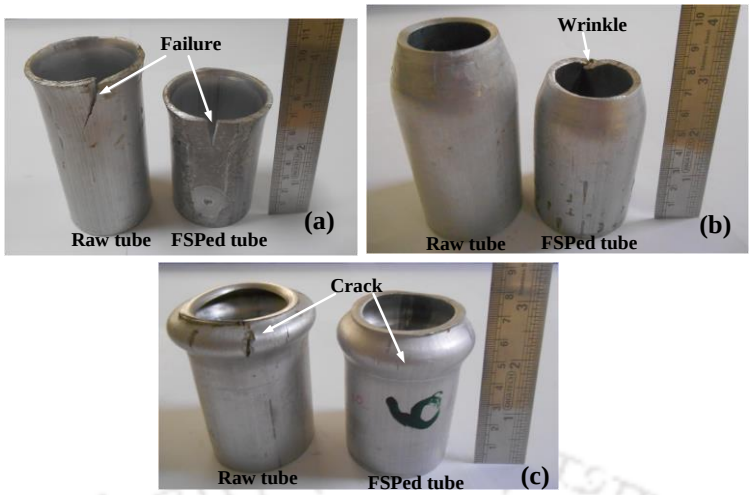

Fig. 4.19 Comparison of end forming behaviour of, (a) tube expansion, (b) tube reduction, (c) tube beading, between unprocessed (left) and FSPed tube (right)

4.2.4 Specific energy absorption

In expansion raw tubes absorb larger energy than processed tubes. In reduction and beading energy absorbed by different FSPed cases is larger than raw tube (Table 4.11). Hence processed tubes can be a better option as far as energy absorption is concerned in case of end reduction and end beading. Within processed tubes, rotational speed 1500 rpm provides better energy absorption capacity as compared to other rotational speeds in different end forming operations. Hence, rotational speed 1500 rpm can be optimized choice within rotational speeds as it gives approximately 7.94 and 20.85 kJ/kg larger energy absorption capacity than raw tube, even in expansion also it reaches towards base metal energy absorption capacity (11 vs 15.27 kJ/kg). In expansion, processed tube fails earlier than raw tube, while there is no wrinkling in raw tube during reduction. In beading crack size obtained in raw tube is larger than that of processed tube. Based on instability developed in raw tube and processed tubes an optimum choice can be made and if possible, processed tubes can be substituted in place of raw tube for better performance as energy absorbing devices in aircraft and shipbuilding industries.

Table 4.11 Coefficients of load curve, R value and energy absorbed

	A	B	C	D	Average thickness of tubes (mm)	Adj. R-square	Specific energy absorbed (*E*) (kJ/kg)
Expansion							
Parent tube	3.55731	1.40775	0.01536	-0.0007	3.19	0.99076	15.27
1200 rpm	-1.08963	2.04916	-0.11328	0.00356	2.73	0.96312	10.73

1350 rpm	-1.53528	1.44579	0.02667	-0.00316	2.43	0.96688	9.26
1500 rpm	0.52941	2.66987	-0.20557	0.0074	2.61	0.9675	10.99
Reduction							
Parent tube	3.88736	4.59669	-0.41516	0.01769	3.164	0.96289	23.43
1200 rpm	-3.51497	5.43679	-0.41462	0.0148	2.59	0.98104	24.43
1350 rpm	-3.4346	5.1036	-0.3892	0.01324	2.39	0.97072	23.35
1500 rpm	4.62365	3.82024	-0.28396	0.01242	2.41	0.97404	31.37
Beading							
Parent tube	-5.95014	78.9564	-15.5023	0.83924	3.204	0.84666	63.48
1200 rpm	32.5587	40.8061	-7.2488	0.36242	2.65	0.9227	81.44
1350 rpm	11.6281	46.2429	-7.44759	0.34805	2.59	0.98305	78.76
1500 rpm	-0.19274	47.5399	-7.09642	0.30583	2.31	0.97738	84.33

4.2.5 Simulation of end forming

Fig. 4.20 and 4.21 shows the thickness strain mapping plot in case of expansion and beading respectively. The displacement at which instability occurs has also been shown in the figure. It can be seen that in case of rotational speed 1200 rpm and 1350 rpm thickness strain saturates in the safe region at a displacement of 19.5 mm, while the same increases in unsafe region (Fig. 4.20).

In these cases a localized thinning occurs as described earlier in section 4.1.7. In case of rotational speed 1500 rpm and in case of base metal thickness strain saturates in both safe and unsafe regions at a displacement of 26 mm and 31.5 mm respectively. In these cases severe thinning front moves propagating the crack before severe thinning occurs at the edge.

In case of beading, thickness strain saturates in safe region, while increases in unsafe region in case of rotational speeds, 1200 rpm, 1350 rpm and 1500 rpm respectively (Fig. 4.21). In these cases localized thinning occurs as described earlier in section 4.1.7. In case of base metal (parent tube) thickness strain saturates in both safe and unsafe regions and hence in this case severe thinning front moves in upward direction before finally crack occurs at the edge. It is also clear from Fig. 4.19 that the crack size obtained in case of parent tube is larger as compared to FSPed tube.

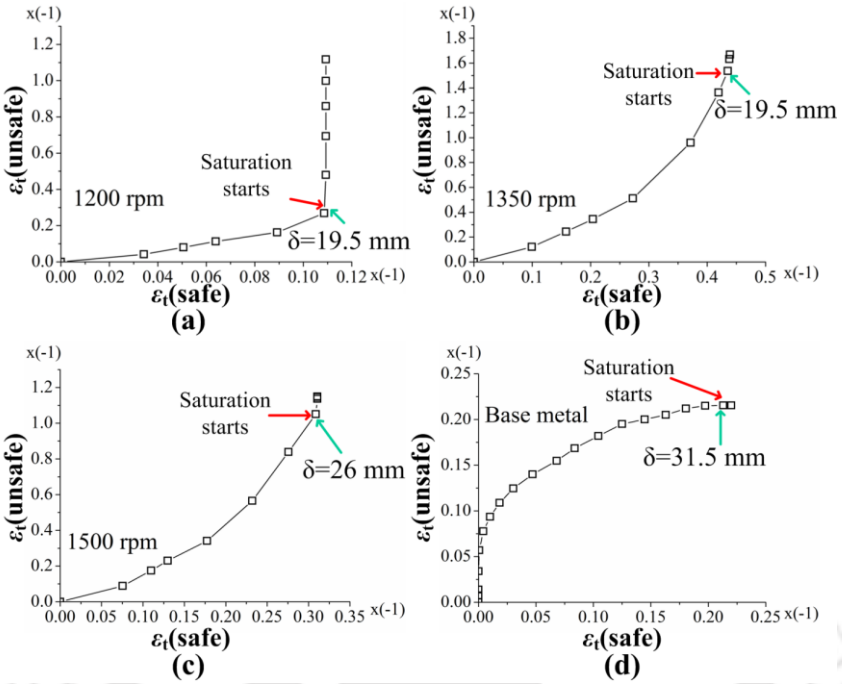

Fig. 4.20 Thickness strain plot in safe region and unsafe region in case of expansion of tubes, (a) 1200 rpm, (b) 1350 rpm, (c) 1500 rpm, and (d) Parent tube (base metal) (thickness strain is actually negative, but shown as positive)

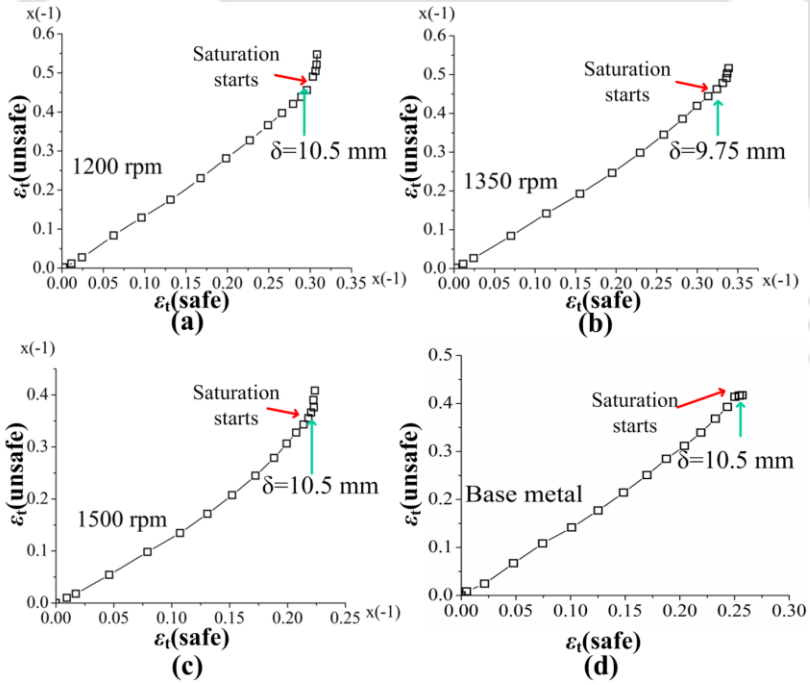

Fig. 4.21 Thickness strain plot in safe region and unsafe region in case of beading of tubes, (a) 1200 rpm, (b) 1350 rpm, (c) 1500 rpm, and (d) Parent tube (base metal) (thickness strain is actually negative in FSPed tubes, but shown as positive)

The displacement at which instability occurs from FE simulation prediction and experiments are summarized in Table 4.12. During end expansion, in case of rotational speeds 1200 rpm and 1350 rpm, a closer match between experimental and numerical prediction is obtained, while in case of parent tube and rotational speed 1500 rpm case a significant difference in displacement is seen. It shows that in these cases (parent tube and 1500 rpm) thickness strain saturation occurs later in expansion during simulation. Modeling conditions (friction coefficient, time period, boundary conditions etc.) can attribute to such difference. In case of end reduction and end beading, an excellent match is observed in displacement at the onset of instability for processed and unprocessed tubes.

Table 4.12 Displacement at which instability occurs for different cases in different end forming operations

Cases (Parent tube/FSPed tube)	End forming operations					
	End expansion		End reduction		End beading	
	Displacement at which instability occurs (mm)					
	Experiment	Simulation	Experiment	Simulation	Experiment	Simulation
Parent tube	22.2	31.5	No wrinkle and overlap		8	10.5
1200 rpm	21	19.5	4	3	8	10.5
1350 rpm	16	19.5	4	3	8	9.75
1500 rpm	15.5	26	4	3	8	10.5

End forming simulation for instability prediction during expansion, reduction and beading has been shown in Figs. 4.22, 4.23 and 4.24 respectively. In case of expansion and beading the image has been shown where instability occurs, while in case of reduction image has been shown at a displacement of 20 mm.

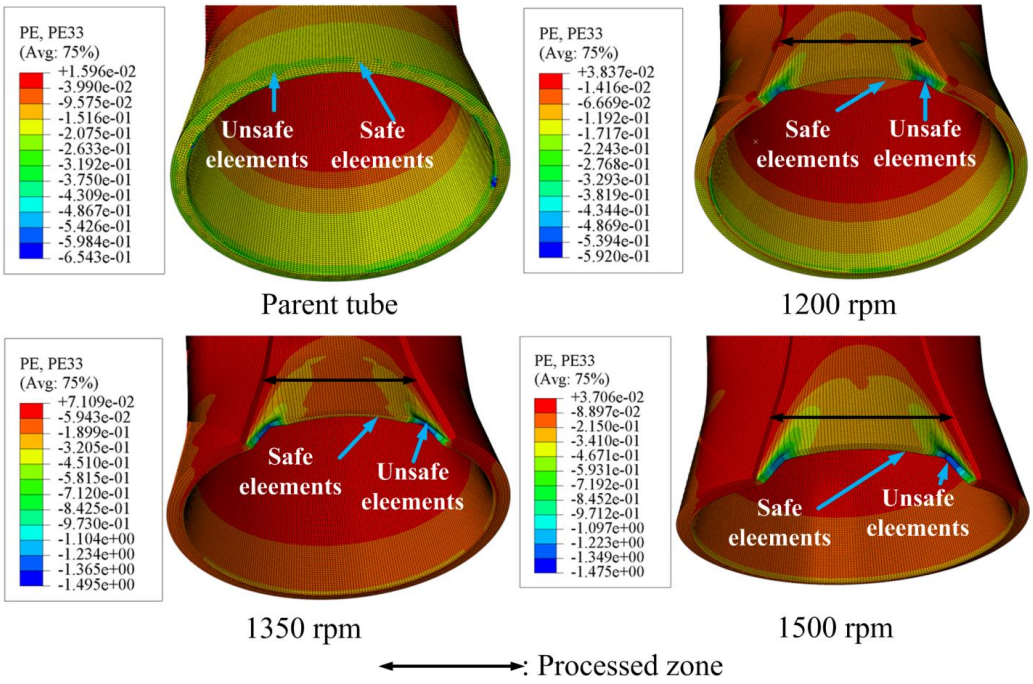

Fig. 4.22 Simulation images where instability occurs for different cases in expansion

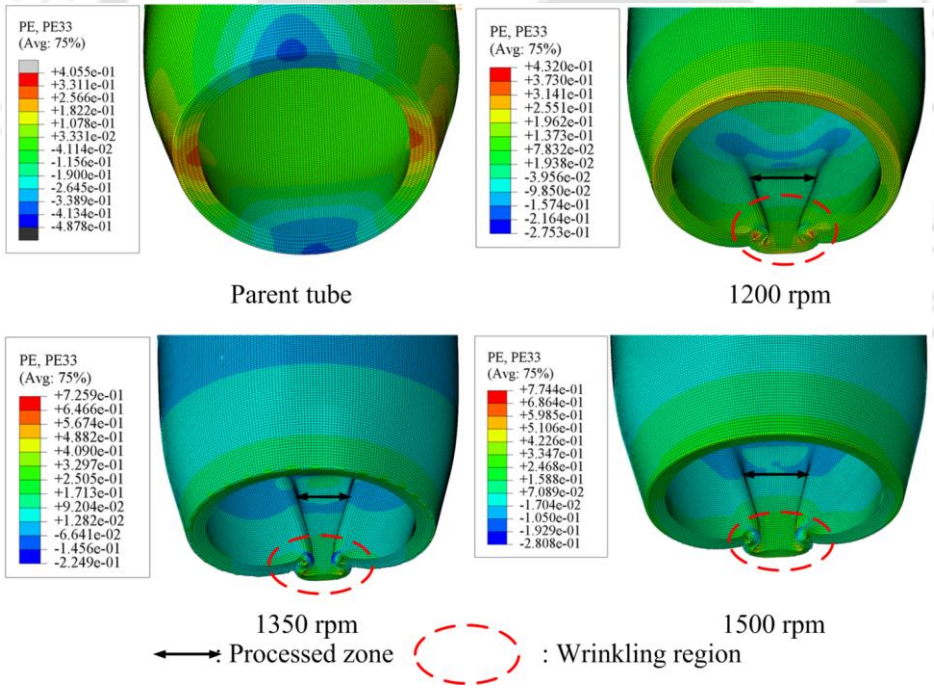

Fig. 4.23 Simulation images for different cases at a displacement of 20 mm in reduction

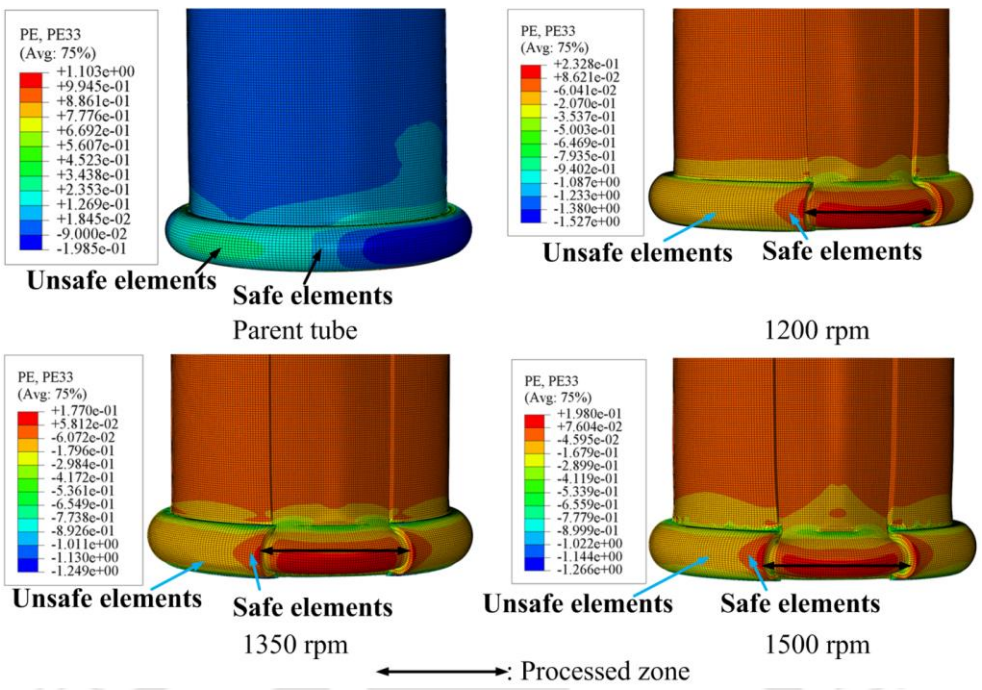

Fig. 4.24 Simulation image for different cases where instability occurs in case of beading

Experimental and predicted load-displacement data for different cases during different end forming operations has been shown in Fig. 4.25. An excellent to good agreement with very minor deviation in load data is observed in case of expansion up to the displacement where actually tube fails in experiments (Fig. 4.25a). In experiments slightly larger load is observed for different cases during experiments as compared to simulations. Wrinkling and overlapping is observed at a lower displacement and load in simulation as compared to experiments for different cases (Fig. 4.25b).

In case of beading, bead initiation occurs almost at the same load in experiments and simulations for different cases (Fig. 4.25c). In experiments after bead initiation load drops for different cases and drop in load continues till the end of deformation process. In simulations, load increases after bead initiation for different FSPed cases. The rate of increment of load for different FSPed cases is larger before bead initiation and towards the end of deformation process (e.g. after 10 mm of displacement). In case of parent tube after bead initiation load remains almost same and increases towards the end of deformation. The difference in load evolution in simulation and experiments, specially in beading operation, for different cases is attributed to modeling conditions such as mismatch in friction coefficient, strain rate and other modelling conditions (time period, mesh size etc.).

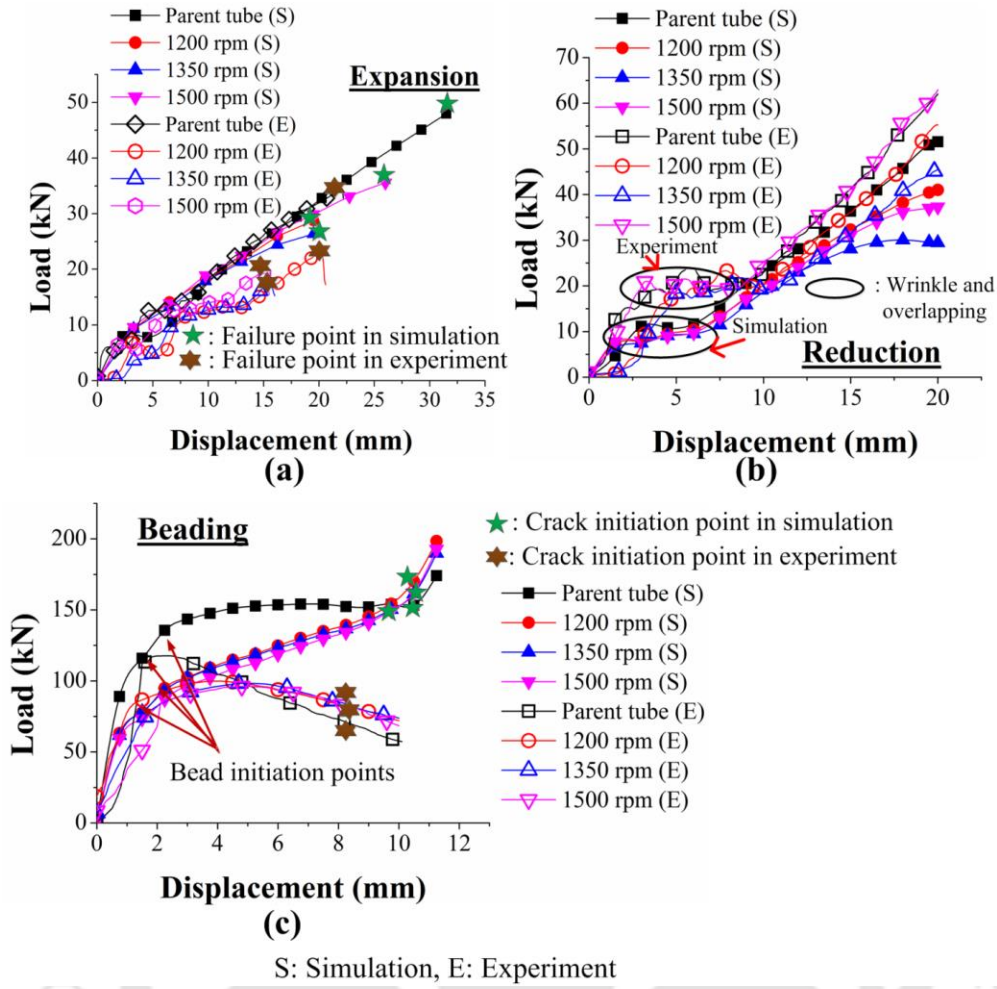

Fig. 4.25 Comparison of load displacement curves for different cases, in case of, (a) end expansion, (b) end reduction, and (c) end beading

4.3 Conclusions

End forming operations such as expansion, reduction and beading of friction stir processed AA 6063-T6 aluminum tubes have been performed to study the effect of tool rotational speed. On the basis of results derived in the present work, the following conclusions are drawn.

1. Hardness of the FSPed zone decreases after processing as compared to parent material. An average hardness decrement of about 34%, 28% and 32% has been observed for tool rotational speeds, 1200 rpm, 1350 rpm and 1500 rpm, respectively. The effect of tool rotational speed on the hardness distribution and grain size of the FSPed zone is insignificant. These results agree well with the existing results on FSP of Al 6063-T6 material.

2. Williamson-Hall plot matches well with *n* values of different cases in different regions of processed zones. A larger average dislocation density in case of rotational speed 1350 rpm results a lower *n* value in this case.

3. The effect of rotational speed on the end expansion and reduction of FSPed tubes is significant, while it is negligible in tube beading. Load at different rotational speeds during expansion and reduction show considerable variation during expansion and reduction, while the variation is minor during tube beading operation. Similarly, thickening and thinning of FSWed zone at different rotational speeds for tube reduction and tube expansion is larger as compared to thickening of FSWed zone for tube beading. The variation in *H*(%) during beading operation is also lower as compared to expansion and reduction.

4. Load evolution obtained during end forming operations like expansion, reduction, and beading of FSPed tube is governed by initial hardness and the hardening index, *H* (%) of the FSPed zone, during forming. The initial thickness of the FSPed zone also decides the load requirement during end forming.

5. FSPed tube requires lesser load to deform as compared to raw tube. The FSPed zone is softer than the raw tube. Hence, the overall load requirement decreases during end forming of FSPed tubes.

6. The thickness evolution in the FSPed zone and base material of the FSPed tube is governed by hardness change, in the case of tube expansion and reduction. The strain hardening exponent difference governs the thickening phenomenon in the case of tube beading. Because of this, thinning and thickening of FSPed zone is larger as compared to base material in tube expansion and reduction, while base material shows larger thickening in tube beading.

7. Mechanical instabilities are observed during tube end forming operations. Failure at the middle of the FSPed zone during tube expansion, wrinkling and overlapping in the FSPed zone during tube reduction, and crack formation during tube beading are observed.

8. Because of lower hardness of the weld zone, tube fails almost at the middle of the weld zone during expansion of tubes, and wrinkling/overlapping occurs at the

FSPed zone during tube reduction. Due to reduced ductility of the base metal, fine cracks are observed at the bead of the base metal during tube beading.

9. The hardness of the FSPed zone approaches that of base metal after end forming operations. This indicates that the end forming operations harden the FSPed tubes. Hence, it is advantageous to use end formed FSPed tube as it requires lower tonnage for part making. However, the mechanical instabilities are prominent in FSPed tubes as compared to raw tube.

10. With respect to the energy absorption capacity, parent tube is better for end expansion applications, while FSPed tube is better for tube reduction and beading. Though there is not much effect of rotational speed on energy absorption in the present work, 1500 rpm is a better choice. Moreover, energy absorption in beading operation is significantly larger as compared to expansion and reduction.

11. FE simulation predictions of load evolution correlate well with experimental data. But for failure/instability prediction, separate thickness strain mapping method has been employed for tube expansion and beading. When experiments are compared, the predicted displacement at failure is acceptable in case of tube beading, while significant difference is observed in tube expansion. In tube reduction, wrinkling is observed in FE simulations almost at the same displacement as that of experiments.

Chapter 5

End forming behaviour of FSPed Al 6063-T6 tubes at different tool traverse speeds

5.1 Methodology

In this section, firstly, methodology of tube FSP and mechanical properties evaluation of base metal and processed zones have been discussed. Dislocation density measurement and end forming experimentation methods have been discussed thereafter. Specific energy absorption methodology and FE simulation methodology have been described at last.

5.1.1 FSP experiments

The methodology of FSP of tube, macrograph examination of processed cross-section and scheme of utilization of tubes at any level of processing parameter have been discussed in Chapter 4 in section 4.1.1. Further, in the present work, the levels of tool traverse speed were decided within defect-free range. From previous experiments of FSW on 6063-T6 Al alloy as described in Chapter 4 in section 4.1.1, it was confirmed that a tool rotational speed of 1150 rpm, tool tilt angle 2° and plunge depth 3 mm resulted in a defect free weld at a traverse speed of 90 mm/min. This information has been utilized in the present work to decide the defect free range for tool traverse speed. In the present work, a tube has been processed from one end to other end with tool traverse speed varied from 30 mm/min at one end to 250 mm/min at the other end with all other parameters such as tool rotational speed, tool plunge depth and tool tilt angle kept constant at 1150 rpm, 3 mm (2.9 mm pin length + 0.1 mm shoulder plunge) and 2° respectively. After completing established procedures for metallographic examination, the macrographs of processed cross-section were captured at a lower magnification of 10×. Later on, microstructural examination has been done at a higher magnification of 20×. Some of the macrographs are shown in Table 5.1.

Table 5.1 Macrographs of processed zone at different traverse speeds

S. No.	Traverse speed (mm/min), Rotational speed, (rpm)	Macrograph of joint cross-section	Observation
1.	50, 1150		Defect fee
2.	92, 1150		Defect free
3.	125, 1150		Defect free
4.	136, 1150		Defective, fine pores
5.	156, 1150	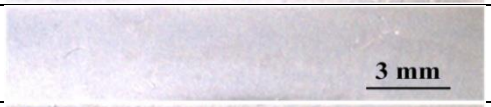	Defect free
6.	200, 1150		Defect free

The macrographs of processed cross-section suggest that there is not much effect of traverse speed on the defect formation, however, fine pores are observed at a processing speed of 136 mm/min. Literature suggest that a larger or smaller traverse speed is not appropriate for a sound processed zone formation because of inadequate heat flow. So traverse speeds of 75 mm/min, 100 mm/min and 125 mm/min were selected for processing trials which lie in the medium range. A fair gap between traverse speeds has been maintained such that their effect on tube processing and end forming could be easily identified.

5.1.2 Details of end forming of tubes

End forming methodology has been described earlier in Chapter 4 is section 4.1.4.

5.1.3 Hardness, tensile properties and grain size

The methodology of evaluating hardness, tensile properties of base metal and processed zones and grain size has been described in Chapter 4 in section 4.1.2.

5.1.4 Specific energy absorption capacity evaluation

The methodology of evaluation of specific energy absorption of processed and unprocessed tubes has been mentioned in Chapter 4 in section 4.1.5.

5.1.5 Dislocation density measurement using X-ray peak profile analysis

The methodology of calculating dislocation density has been mentioned in Chapter 4 in section 4.1.3.

5.1.6 FE simulation of end forming

The methodology of FE simulation has been explained in Chapter 4 in section 4.1.6. Further, during modeling of end forming, the mechanical properties of the raw tube given in Table 5.4 are incorporated for the unprocessed tube and the unprocessed region of the FSPed tubes. For the FSPed zone, the tensile properties are separately evaluated as given in table 5.4 and incorporated during simulations. The true stress-true strain data are fit using the Hollomon's power law, $\sigma = k\varepsilon^n$ (Hollomon, 1945; Hollomon and Jaffe, 1947), and the obtained flow stress-strain behaviour (Fig. 5.1) is used. The power law is used because of its simplicity though Voce law is used for Al alloys and other metals (Sainath et al. (2015), Guo et al. (2013)). The strain hardening curves are extrapolated for larger strains during FE simulations. Actual thickness of raw tube, unprocessed and processed zone thickness in processed tubes have been used during simulations. Table 5.2 summarizes the thickness values incorporated during FE simulations. Punch has been provided required downward vertical displacement to simulate the end forming process.

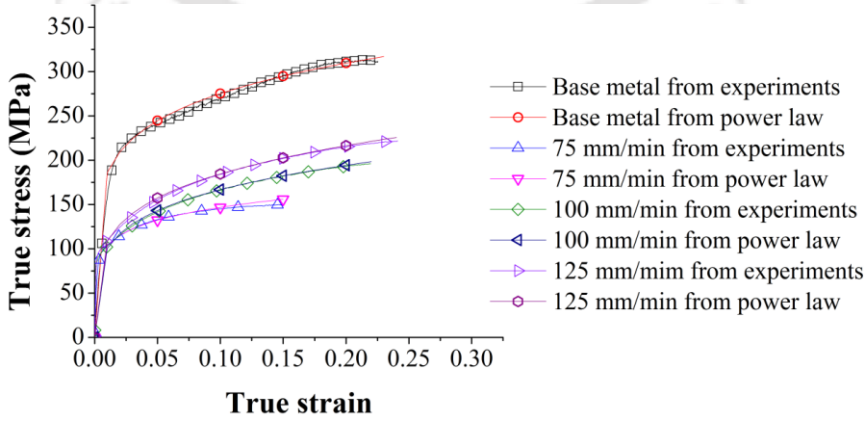

Fig. 5.1 True stress-strain fit used for FE simulations for base metal and FSPed zones for different traverse speeds

Table 5.2 Initial thickness for unprocessed and processed tubes used for end forming simulations

FSPed tube and raw tube thickness (mm)						
Traverse speed/Raw tube	Tube expansion		Tube reduction		Tube beading	
	In processed zone	In base metal	In processed zone	In base metal	In processed zone	In base metal
75 mm/min	2.196	3.174	2.496	3.156	2.484	3.156
100 mm/min	2.154	3.132	2.46	3.158	2.66	3.166
125 mm/min	2.042	3.202	2.47	3.138	2.406	3.166
Raw tube	3.19		3.164		3.204	

Table 5.3 summarizes the '*r*' value and the six yield factors R_{11}, R_{22}, R_{33}, R_{12}, R_{13} and R_{23} for base metal as well as FSPed zones made at different traverse speeds according to equation 4.4 as described in section 4.1.6 in Chapter 4. Here '*r*' has been calculated only in longitudinal direction of the tube and has been assumed same in other directions. Testing of tensile samples in circumferential direction (transverse) is not done as the specimen needs to be flattened and such flattening can affect the material properties. For the present model,

$$r_x(r_0) = r_{45} = r_y(r_{90}) = r \tag{5.1}$$

Table 5.3 Values of plastic strain ratio and anisotropic parameters

Base metal/FSPed zone	Plastic strain ratio *'r'*	R_{11}	R_{22}	R_{33}	R_{12}	R_{13}	R_{23}
Base metal	0.11	1	1	0.744	1.167	1	1
FSPed zone: 75 mm/min	0.52	1	1	0.8722	1.056	1	1
FSPed zone: 100 mm/min	0.45	1	1	0.8522	1.069	1	1
FSPed zone: 125 mm/min	0.86	1	1	0.9657	1.012	1	1

Base metal and processed zone are anisotropic in nature which is confirmed from plastic strain ratio '*r*' values. So it is believed that Hill's 1948 yield function which has been used to calculate values shown in Table 5.3 will provide acceptable results over von-Mises yield function which is meant for isotropic material. Table 5.3 values are incorporated as input during FE simulations of end forming.

5.1.7 Instability prediction during end forming

The methodology of instability prediction has been explained in Chapter 4 in section 4.1.7.

5.2 Results and discussion

In this section, mechanical properties of base metal and processed zones have been discussed initially. A discussion on dislocation density and microstructural changes into different regions of processed zones has been presented thereafter. Characterization of end forming behaviour through load displacement analysis of tubes, thickness evolution of tubes and specific energy absorption capacity of tubes has been shown later on. Finally, end forming simulations have been discussed.

5.2.1 Tensile behaviour and hardness distribution

The tensile behaviour of processed zone at different traverse speeds has been shown in Fig. 5.2. It has been observed that with the increase of traverse speed, strength, ductility and strain hardening exponent of the processed zone increases. With the increase of traverse speed, the heat input to the processed zone decreases. As a result, a strong processed zone having larger flow stress is obtained at a higher traverse speed. When compared with base material, the strength (UTS) of the FSPed tube has decreased in all cases, while formability has improved in case of traverse speed 125 mm/min.

The hardness distribution across the processed zone has been shown in Fig. 5.3(a-c). The hardness distribution suggests that material softening has occurred, because of heat experienced by the processed zone during FSP. The hardness in different regions of processed zone, i.e., stirred zone (SZ), heat affected zone (HAZ) and thermomechanically affected zone (TMAZ) varies between 55–70 VHN after FSP for different cases. A reduction in hardness after FSP in the processed zone is responsible for a lower flow strength of processed zones made at different traverse speeds. The hardness has improved after end forming operations. Although a hardness variation of 10-20 VHN has been observed at different regions of processed zones for any case (before forming or after forming), an average hardness has been calculated for the whole processed zone of width 16-18 mm, and has been presented in Table 5.5.

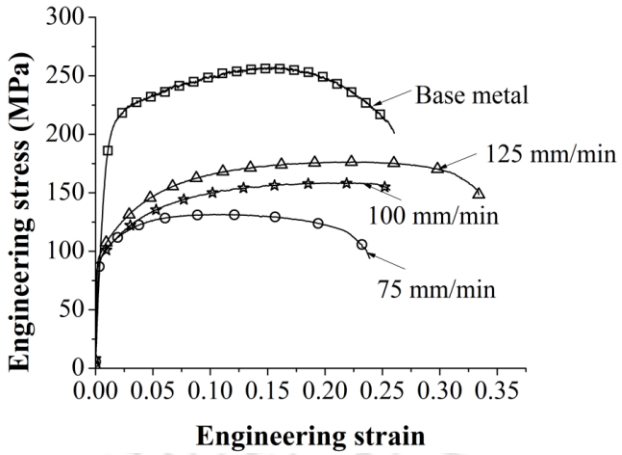

Fig. 5.2 Engineering stress-strain data for FSPed zone specimen at different traverse speeds
(standard deviation in Flow stress: Base metal:13 MPa, for 75 mm/min: 15 MPa, for 100 mm/min: 9 MPa, for 125 mm/min: 38 MPa)

Table 5.4 Mechanical properties of base metal and processed zone made at different traverse speeds

Traverse speed (mm/min) /Base metal	Yield strength (MPa)	Ultimate tensile strength (MPa)	Uniform elongation (%), at 12.5 mm gauge length	Total elongation (%), at 12.5 mm gauge length	Strain hardening exponent, *n*	Strength coefficient, *K* (MPa)
75	88.62±6	131.46±10	11±1	24±1	0.15±0.01	207.35±30
100	89.16±10	158.54±11	22±0.2	24±0.2	0.22±0.02	276.83±9
125	93.75±22	176.48±40	22±2	35±8.2	0.23	313.37±70
Base metal	152±11	258±12	20±0.6	31±0.02	0.17±0.01	407±13

The hardness of the FSPed zone decreases by about 32.98 %, 33.59 % and 32.65 % in case of traverse speeds 75 mm/min, 100 mm/min and 125 mm/min respectively (Table 5.5). Moreira et al. (2008) has reported a similar decrement in processed zone hardness after FSP for AA6063-T6. In their work AA 6063-T6 has been friction stir welded and a hardness decrement of about 27 % and 32 % has been observed in the upper surface and in the side surface of the FSW region. Sato et al. (1999) FSWed 6 mm thick AA6063-T5 sheet and found that hardness decreases drastically in the weld zone. It was observed that all the precipitates have dissolved in the softened region because of a larger temperature observed in the precipitate free region (402°C) as compared to 201°C in in the base metal region which is quite high and responsible for dissolution of all precipitates in the softened region. This phenomenon ultimately causes a decrease in hardness in the weld region. This is a characteristic of precipitation based hardened aluminium alloy.

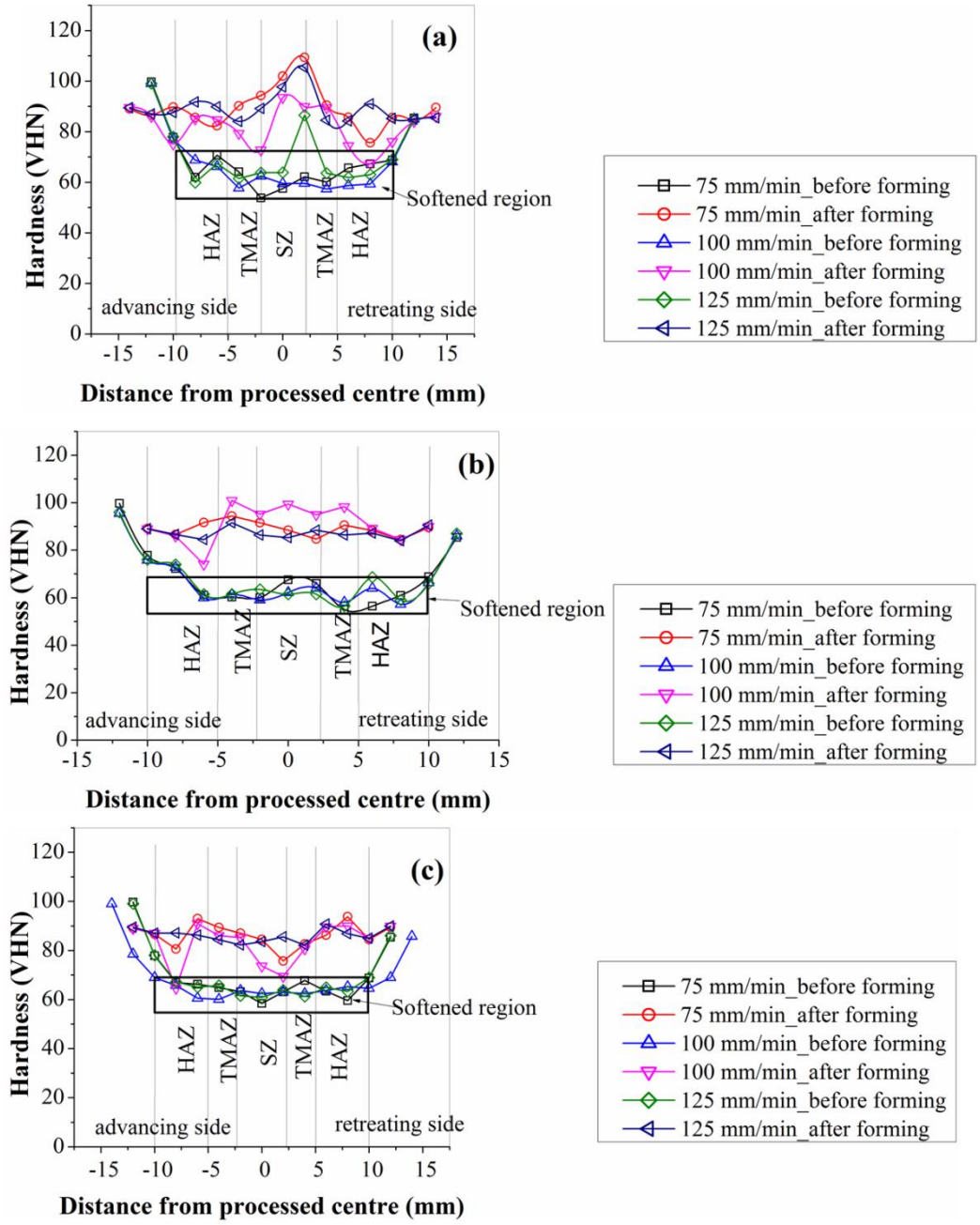

Fig. 5.3 Hardness plot across the processed zone before forming and after forming in case of, (a) tube expansion, (b) tube reduction, (c) tube beading
(average standard deviation for hardness in weld zone in case of expansion before forming is ±6 and after forming is ±8, in case of reduction before forming is ±4 and after forming is ±4, in case of beading before forming is ±2 and after forming is ±4)

Table 5.5 Hardness of the processed zone before forming and after forming (Base metal hardness: 93.76 ± 13 VHN)

Traverse speed (mm/min)	Hardness (VHN)					
	Expansion		Reduction		Beading	
	Before forming *, H_i	After forming, H_f	Before forming*, H_i	After forming, H_f	Before forming*, H_i	After forming, H_f
75	62.61±5	90.08±9	62.18±3	89.92±3	63.72±3	85.86±5
100	61.07±4	80.67±8	62.05±3	93.16±9	63.67±3	81.23±10
125	62.56±3	90.02±7	63.05±5	87.10±2	63.75±2	85.42±3

*Before forming is equivalent to after FSP

Hardening of FSPed zone after end forming is primarily due to strain hardening during end forming. Lee et al. (2002) applied accumulative roll bonding (ARB) process to a 6061 aluminum alloy and observed a hardness increase through the thickness of the specimen. This is explained as work hardening due to larger redundant strains induced between roll surface and specimen. Similar work hardening has been observed in the present work in FSPed zone.

Microstructural images of different regions of processed zone has been shown in Fig. 5.4. The main purpose of the microstructural examination is to observe the grain size changes in the processed zone. Three distinct regions, i.e., SZ, TMAZ and HAZ, based on grain size, have been identified at each traverse speed in the processed zone. The stir zone shows smaller grain size at all traverse speeds, while HAZ shows larger grain size. Due to severe plastic deformation and recrystallization taking place at high temperature, the grain size is smaller in SZ when compared with other regions of the processed zone. A coarser grain size approaching to that of the base metal grain size has been noticed in HAZ. This region is only affected by the thermal cycle and deformation is almost absent in this region. A combined effect of deformation and thermal effect results in elongated equi-axed grains in TMAZ. However, recrystallization is usually absent in this region because of lesser heat produced. A combination of varying thermal effect and plastic deformation is responsible for grain size variation across processed zone. However, no direct correlation is seen between grain size and hardness after FSP. Table 5.6 compares the average grain size at different regions of FSP zone.

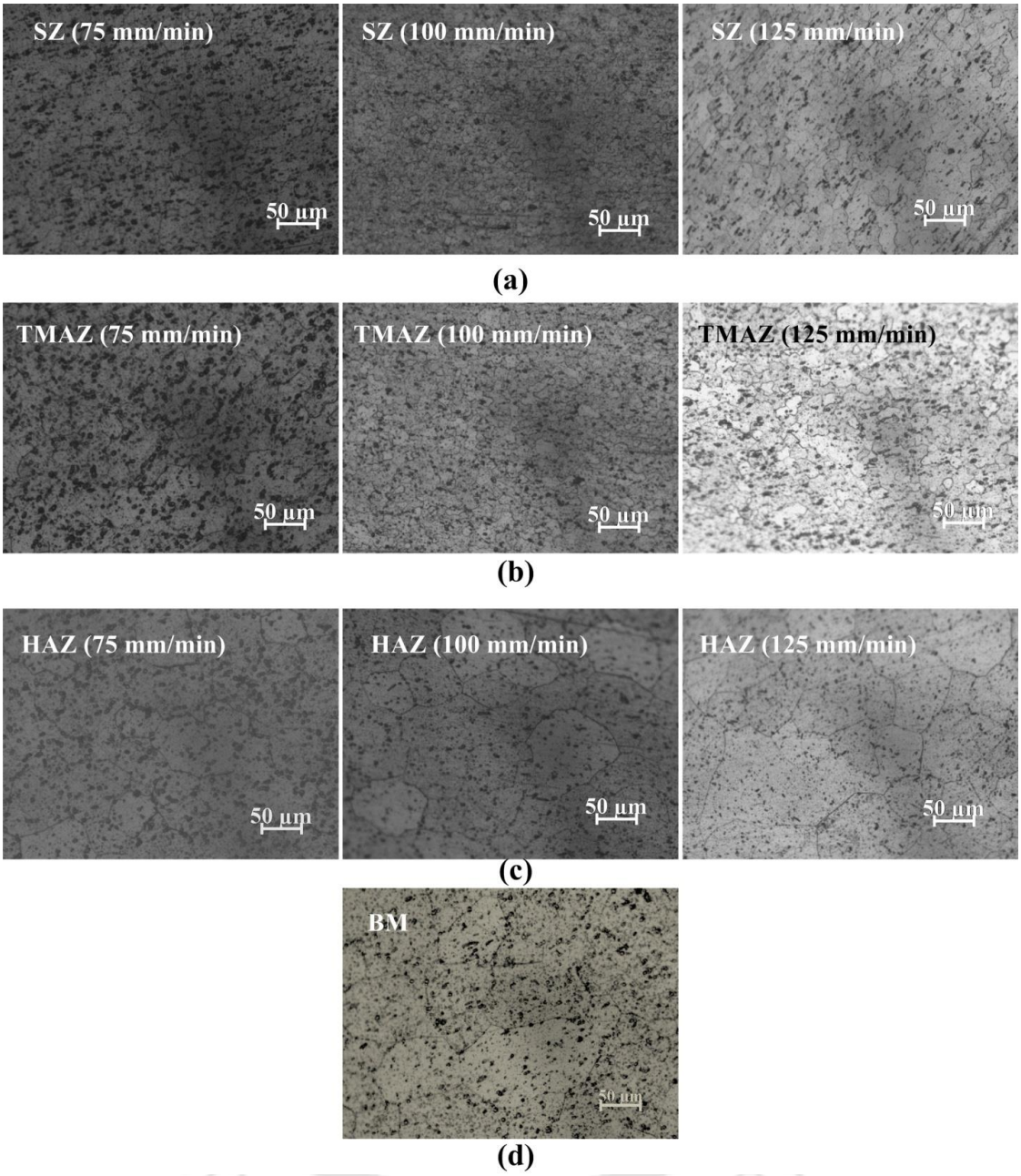

Fig. 5.4 Microstructural images of different regions of FSPed zone at varied traverse speeds: (a) SZ at 75 mm/min, 100 mm/min and 125 mm/min, (b) TMAZ at 75 mm/min, 100 mm/min and 125 mm/min, (c) HAZ at 75 mm/min, 100 mm/min, and 125 mm/min, and (d) Base metal (BM)

Table 5.6 Average grain size of different regions of FSPed zone at different traverse speeds (Base metal grain size: 91.15±22)

Traverse speed (mm/min)	Grain size (µm)		
	SZ	TMAZ	HAZ
75	24.6±3	29.25±4	58.45±7
100	17.4±2	24.6±3	76.65±18
125	24.6±3	24.62±3	64.50±15

Hardness index, H (%), based on initial hardness and change in hardness, during end forming operations has been proposed as follows:

$$H(\%) = \frac{H_f - H_i}{H_i} \times 100 \quad (5.2)$$

where H_i is the initial hardness (after FSP) and H_f is the final hardness (after forming). It is concluded from Fig. 5.5 that the hardness change is more sensitive to tube expansion and tube reduction as compared to tube beading. However, all the end forming operations show considerable variation in H, at all the traverse speeds. Tube reduction shows considerable change in hardness (or H) in almost all cases causing severe strain hardening as compared to the other end forming operations.

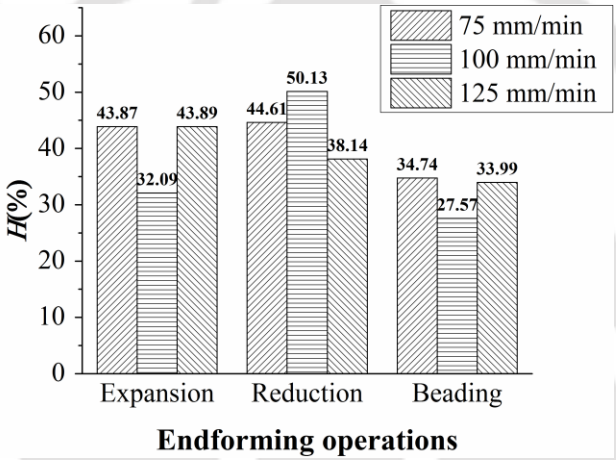

Fig. 5.5 H % versus end forming operations at varying traverse speeds

5.2.2 Dislocation density changes

Fig. 5.6a shows the directly measured X-ray diffraction peak data. The indices of each (h k l) peak are presented for the FCC Al alloy. Fig. 5.6b shows the (2 2 0), (3 1 1) and (2 2 2) peak profiles in the SZ for three different tool traverse speeds. The peak broadening is slightly different for different traverse speeds which is related to different dislocation densities.

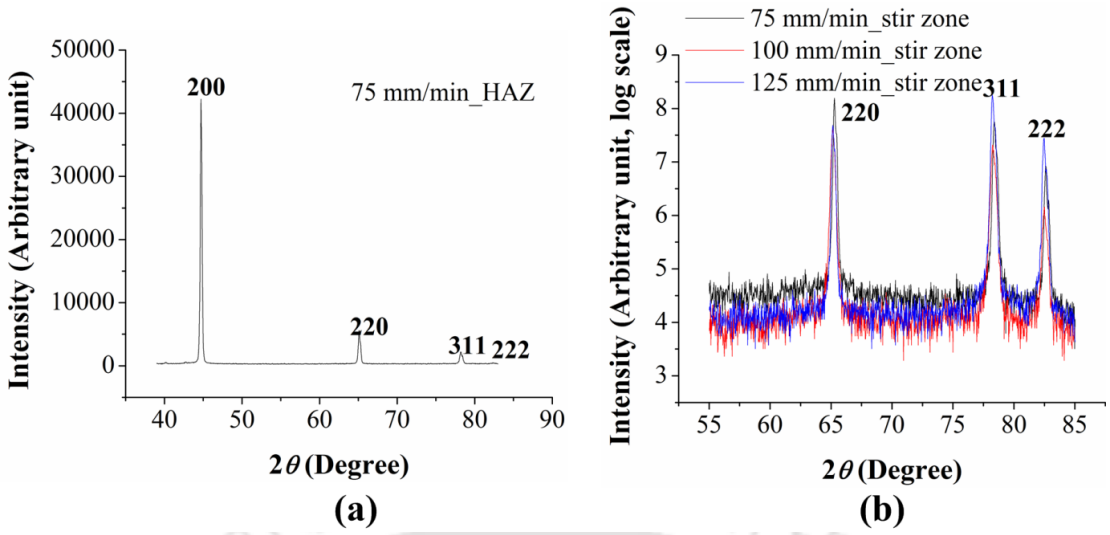

Fig. 5.6 (a) X-ray diffraction peak profile pattern in the HAZ region of FSPed zone made at 75 mm/min, (b) peak profiles measured using X-ray diffraction in the SZ for 75 mm/min, 100 mm/min and 125 mm/min tool traverse speeds

Modified Williamson-Hall plot for different zones and traverse speeds has been shown in Fig. 5.7. In case of SZ (Fig. 5.7a), the base metal shows the highest slope between successive peaks as compared to different traverse speeds which means that base metal has higher dislocation density as compared to stir zone. As traverse speed increases, slope decreases indicating a decrease in dislocation density. The dislocation density decrease indicates improvement in strain hardening exponent with increase in traverse speed (refer Table 5.4).

The TMAZ made at different traverse speeds exhibit larger slope (Fig. 5.7b) as compared to the base metal except 125 mm/min. In this case, the slope is closer to the base metal. It means that TMAZ for different traverse speeds possesses either a larger or at par dislocation density as compared to base metal. Moreover, as the traverse speed increases, the slope decreases indicating a decrease in dislocation density. In case of 75 mm/min, the slope observed is largest among cases indicating a larger dislocation density in this case.

In HAZ region, the slopes of base metal and traverse speeds are comparable (Fig. 5.7c). It suggests that dislocation density in base metal and HAZ region are almost same for different traverse speeds. Similar results have been shown by Woo et al. (2008) for FSWed 6061-T6 alloy. They explained that the low dislocation density in the DXZ can be due to recrystallization at the elevated temperature. The higher dislocation density

observed near the boundary between TMAZ and HAZ could be explained by the network structure of many dislocations in sub-grains. HAZ region has got nearly same dislocation density as that of base metal in Woo et al. (2008) work as well.

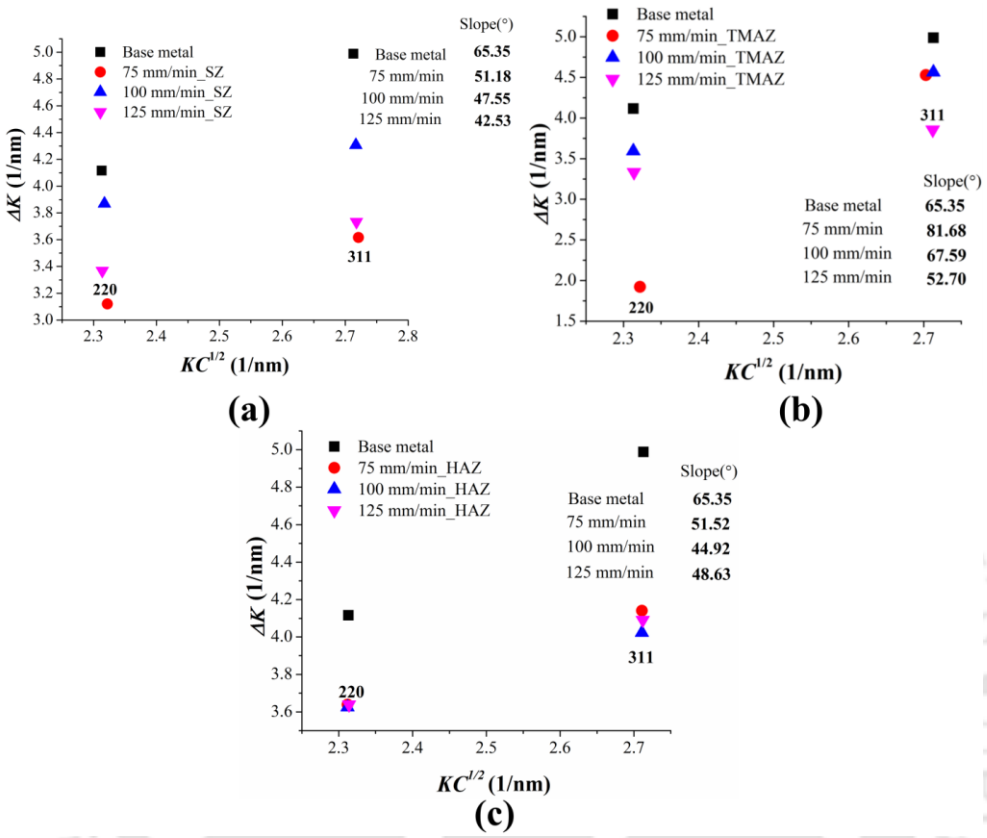

Fig. 5.7 Peak broadening analysis using the modified Williamson-Hall plot for (a) SZ, (b) TMAZ, (c) HAZ, of FSP zone. The FWHM (ΔK) in each (hkl) peak is presented as a function of $KC^{1/2}$ (K=2Sinθ/λ) and C is the dislocation contrast factor

Dislocation densities at different processing conditions and for different zones has been calculated with the help of equations 4.1 and 4.2 as described in section 4.1.3 in Chapter 4 and are summarized in Table 5.7. SZ shows lower dislocation density as compared to base metal, while TMAZ exhibit higher dislocation densities at 75 and 100 mm/min traverse speeds as compared to base metal. A larger value of dislocation density in the case of 75 mm/min and hence a reduced ductility are acceptable. For a traverse speed of 125 mm/min, a lower dislocation density has been obtained in TMAZ. A considerable variation in dislocation density in TMAZ has been observed for different traverse speeds. The dislocation density obtained in HAZ region is comparable with that of average dislocation density in base metal.

Table 5.7 Dislocation density for base metal and for different zones

Traverse speed (mm/min)	Dislocation density ($\times 10^{17}$ m^{-2})			Average dislocation density ($\times 10^{17}$ m^{-2}) in FSPed zone
	SZ	TMAZ	HAZ	
75	1.60	513.68	5.29	173.52±294
100	8.12	27.79	7.37	14.42±11.57
125	6.40	2.14	6.39	4.97±2.45
*Base metal dislocation density: 8.6±0.5 ($\times 10^{17}$ m^{-2})				

Hardening capacity (H_c) for base metal and processed zone at different traverse speeds and their respective n values has been shown in Table 5.8. For 75 mm/min traverse speed, H_c and n are lesser as compared to base metal. On the other hand, for 100 mm/min and 125 mm/min, H_c and n are larger as compared to base metal. Moreover, both H_c and n increases with increase in traverse speed. The same is depicted in Fig. 5.2 with 125 mm/min case showing higher ductility and almost same plastic stress slope with respect to the base metal. High strain hardening exponent n at higher traverse speed is because of low dislocation density at higher traverse speed. Williamson Hall plot (Fig. 5.6) and Table 5.8 confirm the same result.

Table 5.8 H_c and n for base metal and FSPed zones at different traverse speeds

Base metal/FSPed zone	H_c	n
Base metal	0.69	0.17
75 mm/min.	0.48	0.15
100 mm/min.	0.77	0.22
125 mm/min.	0.88	0.23

5.2.3 End forming behaviour

5.2.3.1 Load-displacement behaviour

The load-displacement behaviour in case of tube expansion, tube reduction and tube beading has been shown in Fig. 5.8. The load requirement for base metal is found to be larger than the FSPed tube for all the end forming operations because of larger hardness (or strength) of base metal (Fig. 5.8(a-c)). The load-displacement behaviour in case of tube expansion correlates with the results obtained from the tensile test of processed zone (Fig. 5.8a). FSPed zone having larger strength needs larger load to deform. The load requirement for all the FSPed zones is almost same with very minor deviation, up to a displacement of 16 mm. The FSPed tube corresponding to a traverse speed of 75 mm/min and 100 mm/min fails at an early stage (e.g. at about 16 mm of

displacement). However, displacement and load at failure is found to be maximum for FSPed tube made at 125 mm/min. Larger strain hardening exponent in case of 125 mm/min is responsible for this. In summary, the tensile strength of the joint determines the load requirement, while strain hardening exponent governs the displacement to failure for processed tubes, in tube expansion.

The load-displacement behaviour for tube reduction has been shown in Fig. 5.8b. A small difference in load is observed throughout the reduction process among all the traverse speeds. However, the maximum load for deformation increases with respect to increase in traverse speed (Fig. 5.8b). Processed zone having larger flow strength require larger load for deformation. However, a larger load requirement in case of traverse speed 100 mm/min as compared to other traverse speeds except last few displacement can be attributed to a larger *H* (Fig. 5.5) in this case. Wrinkling phenomena is observed at a displacement of 4 mm during reduction of tubes. A softer processed zone is pushed more towards inside (centre of die) as compared to base metal and as a result wrinkling in FSPed zone is observed. A region of constant load is observed within displacement range of 4-10 mm (Fig. 5.8b). In this region the deformation is mainly governed by wrinkling initially and by overlapping later on. For this mode of deformation a lesser load is required. After a displacement of 10 mm, the mode of deformation is mainly reduction, and for reduction process larger load is required and hence after that a monotonic rise in load is observed.

The load-displacement curve for tube beading (Fig. 5.8c) suggest that with the increase of traverse speed the load required for bead formation increases. There is considerable difference in load requirement among the tubes fabricated at different traverse speed up to a displacement of 5 mm. At about 5 mm, maximum load is reached for all the cases (processed tubes) and there is not much variation in maximum load among the processed tubes (Fig. 5.8c). There is significant difference after maximum load during load reduction in the displacement range of 5-10 mm. The FSPed tubes made at 75 mm/min and 125 mm/min behave in a similar manner throughout the process. Fine cracks are observed at the base material of the FSPed tube at the end of the beading process (e.g. at a displacement of 8 mm) at the peak of bulged region. Due to reduced ductility, fine cracks are observed in the base metal.

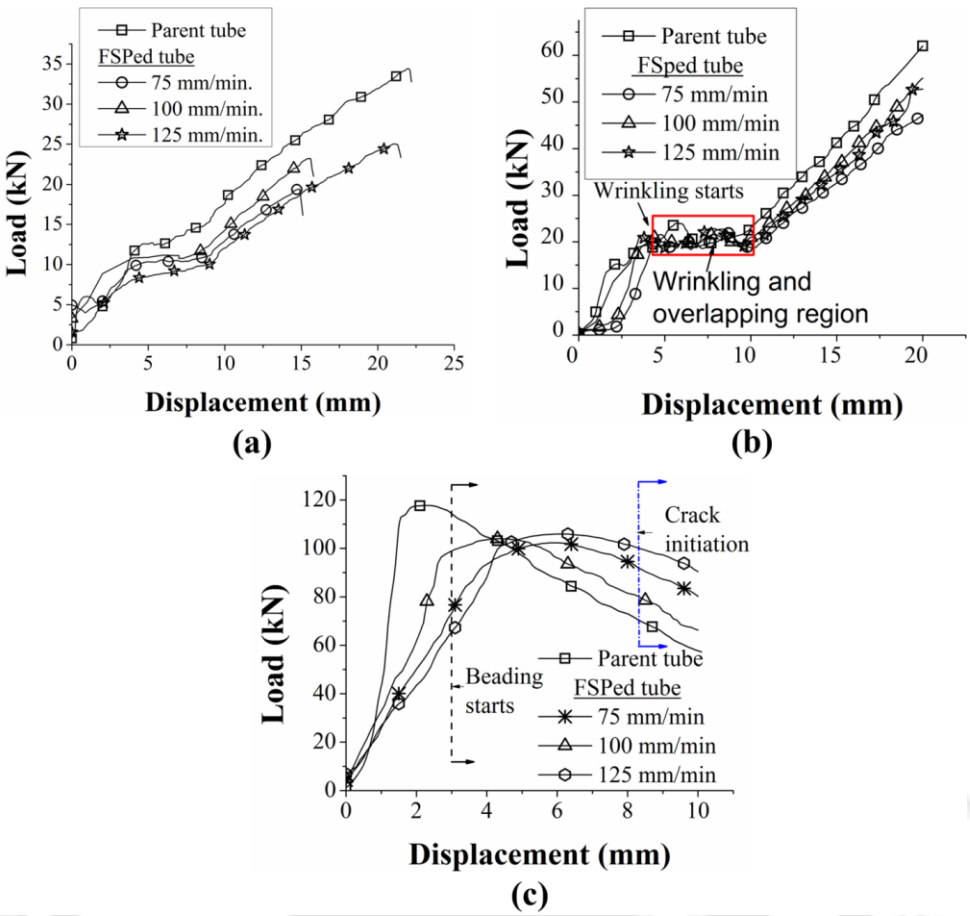

Fig. 5.8 Load evolution for processed and unprocessed tubes in case of, (a) end expansion, (b) end reduction, and (c) end beading

5.2.3.2 Thinning evolution

Thinning evolution of unprocessed tube, FSPed zone and base metal in the FSPed tubes has been shown in Fig. 5.9(a-c). The FSPed zone during tube expansion thins down significantly, while the thickness change in base metal of processed tube and in unprocessed tube is insignificant (Fig. 5.9a). During tube reduction and beading, a considerable thickening, is observed in FSPed zone and base metal of the processed tubes and in unprocessed tubes (Fig. 5.9(b, c)). Thickness evolution during tube end forming can be represented as, $T(\%)$, using following equation:

$$T\ (\%) = \frac{t_f - t_i}{t_i} \tag{5.3}$$

where T (%) is the percentage variation in thickness of tubes, t_i is the initial tube thickness and t_f is the final tube thickness. If T (%) is negative thinning takes place and when it is positive thickening takes place.

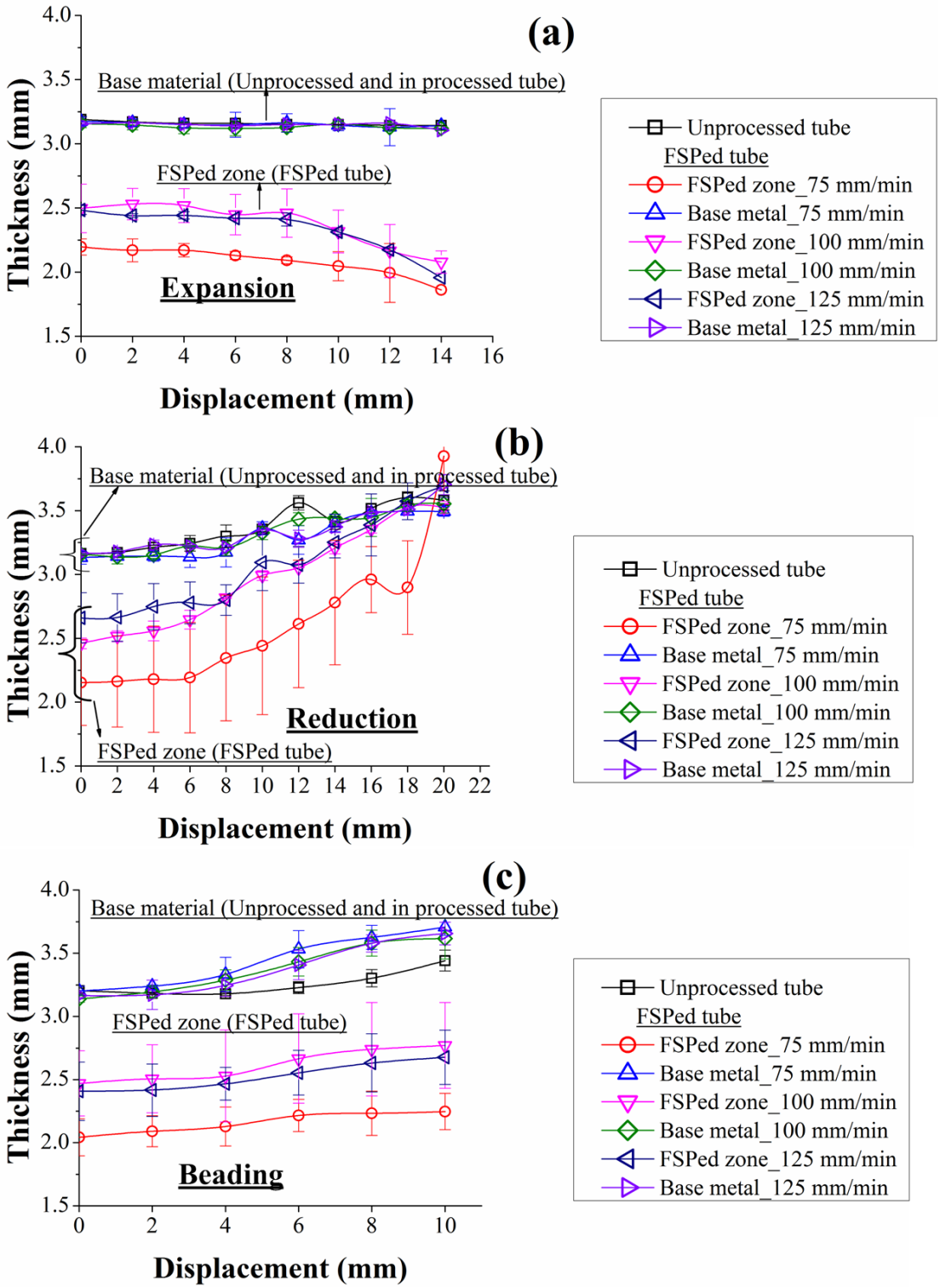

Fig. 5.9 Thickness evolution for (a) tube expansion, (b) tube reduction, (c) tube beading in processed tube (processed zone and base metal zone) and unprocessed tube

As the traverse speed increases, the thinning (%) of FSPed zone increases in case of tube expansion. With increase in traverse speed ductility improves and hence *T* also improves. Since the processed zone is softer as compared to base metal, thinning in the processed zone is larger as compared to base metal (Fig. 5.10(a, b)).

In tube reduction, thickening of processed zone for all traverse speeds is higher than the thickening of the corresponding base metal. A softer processed zone as compared to base metal is responsible for this. As the traverse speed increases, *T* of FSPed zone decreases. FSPed zone having lesser strength has thickened more, while the corresponding base metal zone has thickened less (Fig. 5.10(a, b)).

In beading, the thickening of base metal is larger than the thickening of processed zone for all the traverse speeds. Actually beading is a combination of bending and circumferential bulging in outward direction. *T* of processed zone and corresponding base metal zone is decided based on their relative strength and ductility. A random behaviour in *T* of processed zone and base metal zone has been observed for different traverse speeds (Fig. 5.10(a, b)). However, a minor difference in *T* is observed for processed zones and corresponding base metal zones made at different traverse speeds.

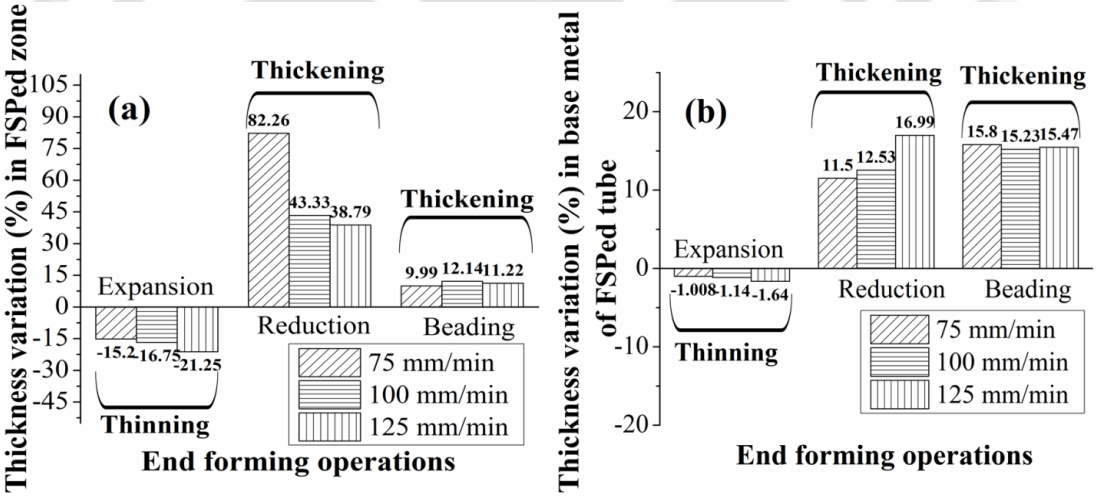

Fig. 5.10 Thickness variation (thinning or thickening) during end forming behaviour in, (a) FSPed zone, (b) base metal, of FSPed tube

The following are some of the important observations drawn from the present work for the processed and unprocessed tubes.

1. Tube is found to fail at the middle of the processed zone during tube expansion. Because of circumferential stretching, failure is seen in the softer FSPed zone, and not in the harder base material. In unprocessed tube failure line is slightly inclined (Fig. 5.11a).

2. During reduction of tubes, the circumferential compressive stresses are acting on the tube surface as a result wrinkling and overlapping is seen in a softer FSPed zone, while no such wrinkling is observed in unprocessed tube (Fig. 5.11b).

3. A higher hardness and reduced ductility of base metal as compared to FSPed zone is responsible for crack formation at the peak bulged height of FSPed tube in beading. The cracks formed in the unprocessed tube are larger as compared to cracks formed in processed tubes (Fig. 5.11c).

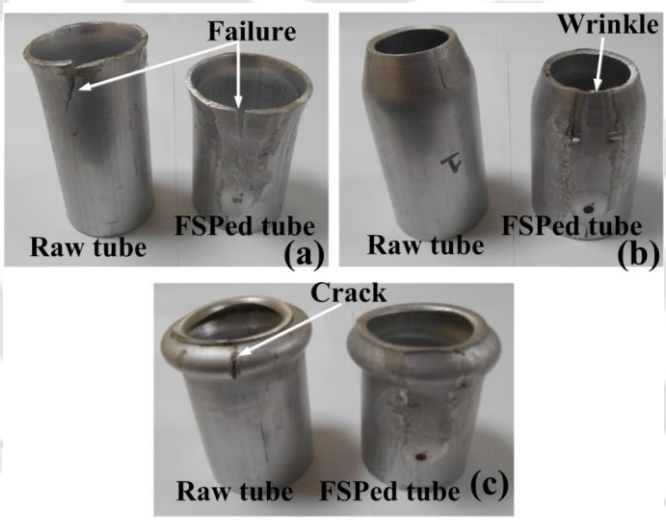

Fig. 5.11 Comparison of end forming behaviour of, (a) tube expansion, (b) tube reduction, (c) tube beading, between unprocessed tube (left) and FSPed tube (right)

5.2.4 Specific energy absorption

Specific energy absorbed has been calculated for parent tubes and processed tubes at different traverse speeds during different end forming operations according to equation 4.3 as described in section 4.1.5 in Chapter 4. Coefficients of fit equation, the specific energy absorbed for variety of tubes, adjusting R-square and thickness of tubes have been shown in Table 5.9.

The adj. R-square is more than 0.95 in all the cases except for parent tube during beading. Hence it can be said that a good fit of load-displacement curve has been obtained. The specific energy absorbed (*E*) is more for parent tube as compared to processed tubes during expansion. In tube reduction, *E* is almost same for FSPed tube and parent tube. In case of beading, *E* for processed tubes is more as compared to base metal. The results imply that the FSPed tubes can be used in tube reduction and tube beading applications in place of raw parent Al tubes with lesser load requirement for deformation. In the case of tube expansion applications, parent Al tube would be better. Though this is the case, *E* of FSPed tube made at 125 mm/min traverse speed is approaching that of the parent tube, 15.27 kJ/kg vs 12.13 kJ/kg, making it as another choice for tube expansion applications. But the main issue with FSPed tube restricting its use is instability developed for which instability prediction at design stage is required. However, utilization of FSPed tube in crash condition require no such designing.

Table 5.9 Coefficients of fit equation for load-displacement curve, average thickness of the tubes, adjusting R-square and specific energy absorbed during end forming

	A	B	C	D	Average thickness of tubes (mm)	Adj. R-square	Specific energy absorbed (*E*) (kJ/kg)
Expansion							
Parent tube	3.55731	1.40775	0.01536	-0.0007	3.19	0.99	15.27
75 mm/min	3.3026	1.92836	-0.18331	0.00883	2.685	0.97	10.68
100 mm/min	5.32356	0.57736	0.0202	0.00131	2.826	0.97	11.26
125 mm/min	2.48592	1.0439	-0.0057	0.00041	2.82	0.98	12.13
Reduction							
Parent tube	3.88736	4.59669	-0.41516	0.01769	3.164	0.96	23.43
75 mm/min	-3.80066	5.81386	-0.4692	0.0158	2.643	0.95	22.15
100 mm/min	-1.7043	5.67861	-0.47957	0.01745	2.809	0.96	23.14
125 mm/min	9.01538	2.81002	-0.2546	0.01166	2.913	0.96	22.73
Beading							
Parent tube	-5.95014	78.9564	-15.5023	0.83924	3.204	0.84	63.48
75 mm/min	-4.12382	35.8580	-3.4203	0.06405	2.622	0.99	74.2
100 mm/min	-7.50709	54.5903	-8.29428	0.3579	2.804	0.96	70.03
125 mm/min	-0.31876	27.5918	-1.32713	-0.05817	2.786	0.98	71.04

5.2.5 Prediction of end forming behaviour

In tube expansion, after failure at the end formed edge of the tube, deformation is concentrated for crack development in upward vertical direction. So once crack is initiated at the edge of tubes (both in processed and unprocessed tubes) no further thinning is observed in both safe and unsafe regions (Fig. 5.12(a-d)). Hence thickness

strain saturates in both safe and unsafe regions after instability is observed. The displacement at which saturation starts for the processed tubes and unprocessed tube during end expansion of tubes has been shown in (Fig. 5.12(a-d)).

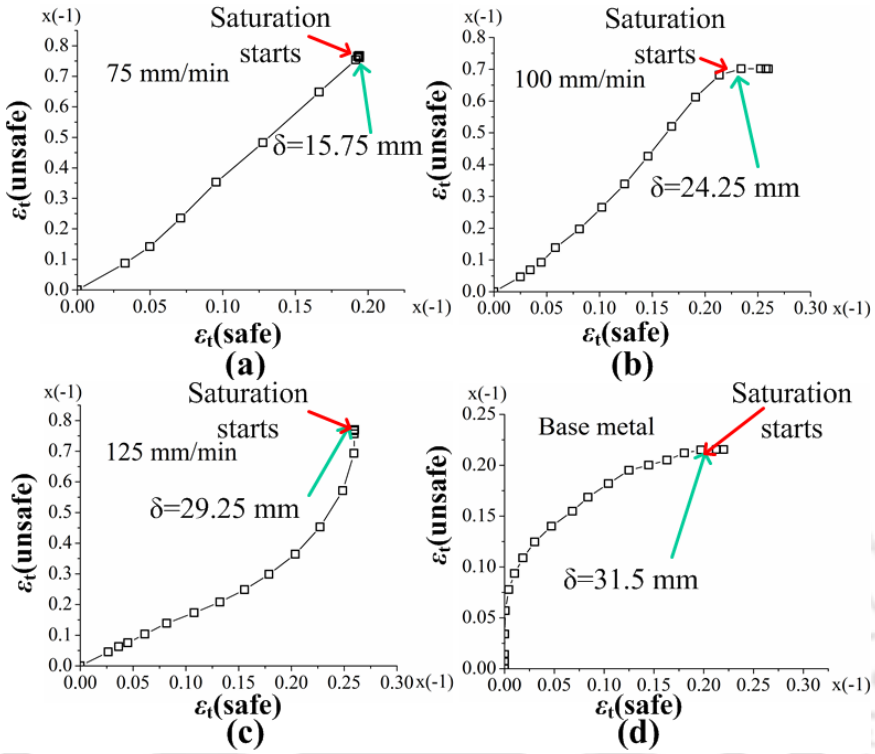

Fig. 5.12 Thickness strain plot safe region and unsafe region in case of expansion of tubes, (a) 75 mm/min, (b) 100 mm/min, (c) 125 mm/min, and (d) Parent tube (base metal) (thickness strain is actually negative, but shown as positive)

In case of end beading of tubes, once crack is initiated (onset of instability) further displacement causes crack propagation rather than bead development as a result of which thickness strain saturates in safe and unsafe regions. Here it should be noted that thinning of tube is observed in the base metal region for processed tubes, while thickening of tube is observed for unprocessed tube because of bending locally. Fig. 5.13(a-d) shows the thickness strain plot between safe vs unsafe region in case of end beading for processed and unprocessed tubes.

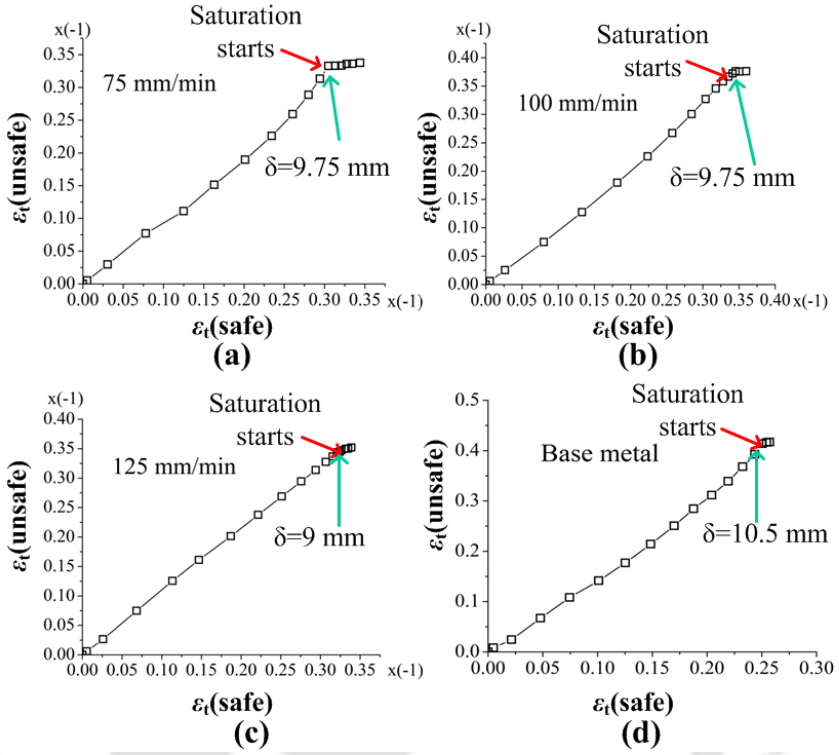

Fig. 5.13 Thickness strain in safe region versus thickness strain in unsafe region in case of beading of tubes, (a) 75 mm/min, (b) 100 mm/min, (b) 125 mm/min, and (d) Parent tube (base metal) (In FSPed tubes thickness strain is actually negative, but shown as positive)

The displacement at which instability occurs from FE simulation prediction and experiments are summarized in Table 5.10. During end expansion, a significant difference in displacement is observed for the onset of instability, except 75 mm/min case. It shows that thickness strain saturation occurs later in expansion during simulation. Modeling conditions (friction coefficient, time period, boundary conditions etc.) can attribute to such difference. In case of end reduction and end beading, an excellent match is observed in displacement at the onset of instability for processed and unprocessed tubes.

Table 5.10 Displacement at onset of instability in experiments and prediction

Cases (Parent tube/FSPed tube)	End expansion		End reduction		End beading	
	Displacement at which instability occurs (mm)					
	Experiment	Simulation	Experiment	Simulation	Experiment	Simulation
Parent tube	22.2	31.5	No wrinkling		8	10.5
75 mm/min	15.1	15.75	4.5	4.5	8	9.75
100 mm/min	16.2	24.75	4.4	4.5	8	9.75
125 mm/min	21.7	29.25	3.7	3	8	9

The instability developed during different end forming operations for traverse speed 75 mm/min has been shown in Fig. 5.14. In expansion and beading the image has been shown where instability occurs, while in reduction the image has been shown at the last stage of displacement (i.e., 20 mm). Similarly instability is seen in other traverse speeds and parent tube as well during simulation.

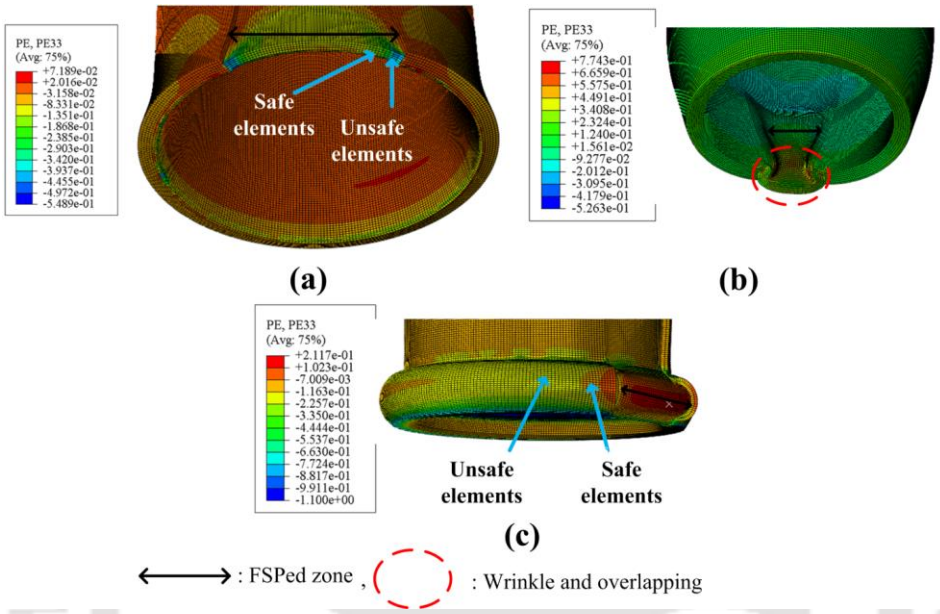

Fig. 5.14 Instability development for traverse speed 75 mm/min in case of, (a) end expansion, (b) end reduction, and (c) end beading

Experimental and predicted load evolution has been compared for different cases (Fig. 5.15). The stage at which thickness strain saturation occurs is shown indicating onset of instabilities in case of expansion and beading. In case of FE simulations, instability is observed later as compared to experiments for tube expansion (Fig. 5.15a). Load evolution is almost identical for experimental and simulation trials up to a displacement at which failure is seen in experiments. After that, a monotonic increase in load is observed in case of simulations until failure occurs.

In end reduction of tubes (Fig. 5.15b), a good comparison between experimental and numerical load has been observed after a displacement of 10 mm. Up to 10 mm displacement, a lower load has been observed in numerical trials. This region is attributed to wrinkling and overlapping. Wrinkling also happens slightly earlier in simulation as compared to experiments. Load obtained in experimental trials is marginally larger than numerical trials. Load evolution obtained in numerical trials is significantly larger as

compared to experimental cases in tube beading for different cases (Fig. 5.15c). In simulation, for parent tubes, load is almost constant after bead initiation and at the later stage of displacement load drops slightly, while for processed tubes, after bead initiation load continuously increases. In experiments, load drops after bead intiation for processed as well as unprocessed tube. The gradient of load drop is larger in case of unprocessed tubes as compared to processed tubes.

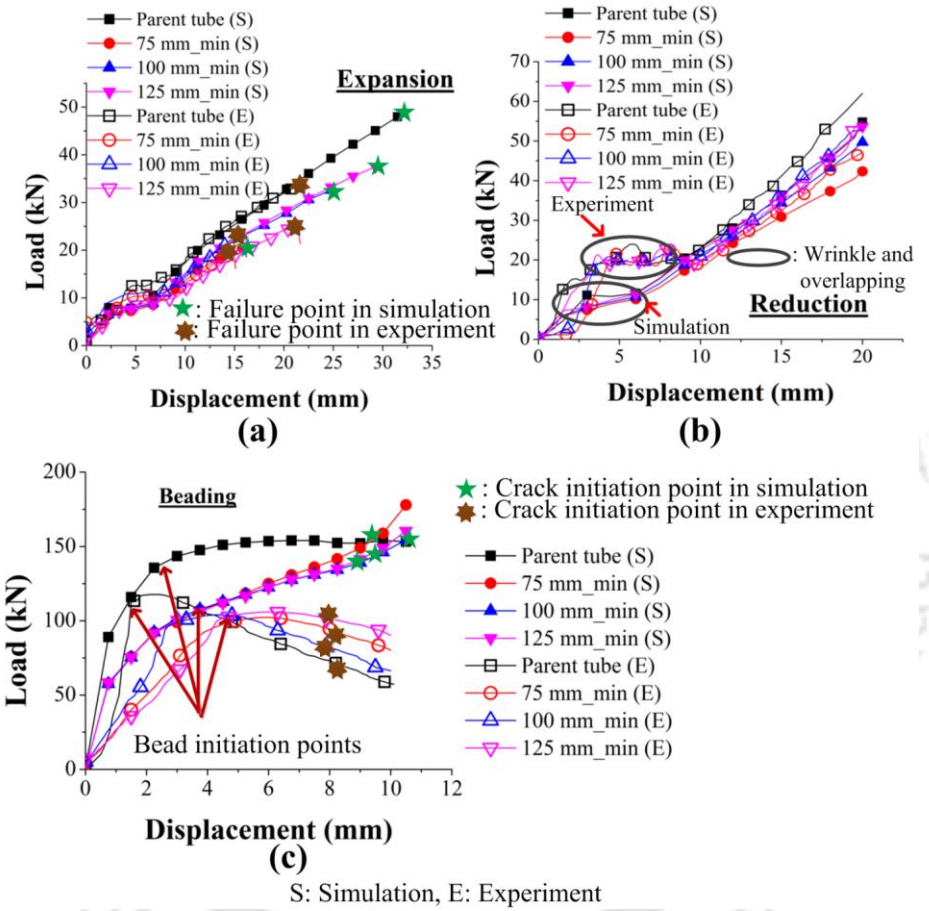

Fig. 5.15 Comparison of load evolution between numerically and experimentally obtained data for processed and unprocessed tubes in case of end, (a) expansion, (b) reduction, and (c) beading

5.3 Conclusions

A comprehensive analysis on end expansion, end reduction, and end beading of FSPed Al 6063-T6 tubes at different traverse speeds have been performed through experiments and FE simulations. Important conclusions drawn from the present work are as follows:

1. The traverse speed during FSP affects the tensile behaviour and end forming behaviour of the tubes significantly. The yield strength and tensile strength of the FSPed zone is found to be lower as compared to base metal, while the elongation and strain hardening exponent *n* are either equal to or larger than the base metal. The reduction in strength is because of thermal softening of the processed zone. The hardness of the FSPed zone is also reduced as compared to base metal, and effect of traverse speed is random.

2. All the tensile properties increase with increase in traverse speed. The strength of the FSPed zone improves because of reduction in heat flux at higher traverse speed, while *n* increases because of reduction in average dislocation density with increase in traverse speed.

3. Hardness of the FSPed zone increases during end forming for all end forming operations and traverse speeds. Strain hardening is believed as the main reason for increase in hardness. Hardness increment during end expansion and end reduction is larger as compared to end beading for all the traverse speeds.

4. During end forming operations, the raw tube needs larger load to deform as compared to FSPed tubes for different end forming operations. With increase in traverse speed, the load requirement in FSPed tubes increases. The strength of the processed zone is found to be responsible for this. The results suggest the usage of FSPed tubes in place of raw Al tube for end forming applications, with proper optimization of FSP parameters like traverse speed.

5. Significant thickening is observed in the processed zone during end reduction and end beading, while thinning of the processed zone is observed during end expansion. Wrinkling during reduction, and bending during beading are responsible for thickening. Circumferential stretching is responsible for thinning in tube expansion.

6. Instabilities like longitudinal crack in the FSPed zone during end expansion, wrinkling and overlapping during end reduction, and crack in the base metal of the FSPed tube during tube beading are observed. The same is seen during raw tube end forming, except that there is no wrinkling in tube reduction. This suggests that the FSPed tubes should be used cautiously for tube reduction applications.

7. With respect to the energy absorption capacity, parent tube is better for end expansion applications, while FSPed tube is acceptable for tube reduction and beading. Though there is not much effect of traverse speed on energy absorption in the present work, 125 mm/min is a better choice, as it delivers a stronger and ductile FSPed zone. Moreover, energy absorption in beading operation is significantly larger as compared to expansion and reduction.

8. FE simulation predictions of load evolution correlate well with experimental data. But for failure/instability prediction, separate thickness strain mapping method has been employed for tube expansion and beading. When experiments are compared, the predicted displacement at failure is acceptable in case of tube beading, while significant difference is observed in tube expansion. In tube reduction, wrinkling is observed in FE simulations almost at the same displacement as that of experiments.

Chapter 6

End forming behaviour of FSPed Al 6063-T6 tubes at different tool pin profiles

6.1 Methodology

In this section, the methodology for FSP of tubes has been discussed initially. Experiments on end forming of tubes has been presented after that. Further, procedure for hardness measurement, grain size evaluation, tensile properties measurement, specific energy absorption capacity and dislocation density measurement are presented. Finally, FE simulation of end forming of tubes has been elaborated.

6.1.1 FSP of tubes

The methodology of FSP of tubes, macrograph examination and scheme of utilization of tubes has been discussed in section 4.1.1 in Chapter 4.1.

In the present work, tools with different pin profiles have been used for FSP. Tools are made of H13 raw tool steel. All the tools have cylindrical shoulder with flat surface having same diameter and length of 25 mm. Different pin profiles fabricated for FSP purpose are tapered cylindrical pin (TCP), straight cylindrical pin (SCP) and stepped cylindrical pin (STP). The length of the pin is kept constant at 2.9 mm. For tapered cylindrical pin, the base diameter of pin is 4.5 and free end diameter is 2.45 mm. For straight cylindrical pin, pin diameter is 4.5 mm throughout its length. For stepped cylindrical pin, the whole length of pin is divided into equal halves. For first half length (base side) diameter is 4.5 mm and for the next half length (free end side) diameter is 2.45 mm. The schematic of the tools has been shown in Fig. 6.1. Similar pin profiles are used by (Elangovan and Balasubramanian, 2008) and (Elangovan et al., 2008a) as well. Otherwise, published literature comparing the effect of different pin profiles on FSPed zone of 6000 Al alloys is scarce. In the present work, STP has been introduced besides taking TCP and SCP from the existing literature. In STP, each step acts as a shoulder for the next step which helps in material to flow downward and fills the pin bottom. This phenomenon results in improved mechanical properties and minimization of tunnel defects (Arab et al., 2016), and prompted authors to choose STP as the third option.

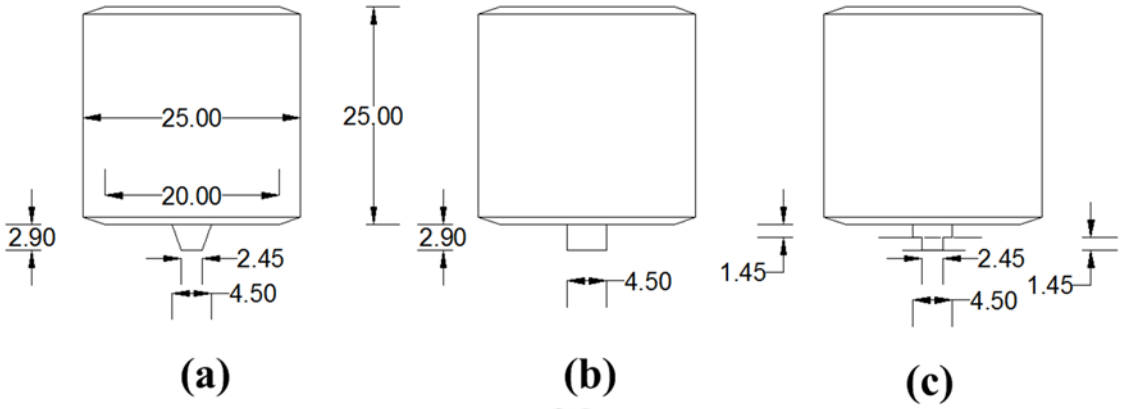

Fig. 6.1 Schematic and dimensions of tools used for FSP (a) TCP, (b) SCP, and (c) STP (all dimensions in mm)

For the present work, a tool rotational speed of 1350 rpm, tool traverse speed of 90 mm/min, tool tilt angle of 2° and tool plunge depth of 3 mm were used. Hence plunge depth includes insertion of 2.9 mm pin length and 0.1 mm shoulder length inside the tube. The interaction between shoulder and workpiece is necessary so that more frictional heat is generated which results in sufficient plasticization of the materials. This phenomenon increases the material movement around the tool pin and helps in removing tunnel defect (Dehghani et al., 2013). A 2.9 mm pin length allows insertion of 0.1 mm shoulder length and is found to be appropriate for the present work. At these conditions, a defect free weld has been obtained for TCP as described in section 4.1.1 in Chapter 4. Later, at these conditions, a defect free weld has been obtained for SCP and STP as well. The quality of the processed zone has been obtained by observing the macrostructure. The macrographs of the processed cross-section of different pin profiles have been captured at a low magnification of 7× and have been shown in Table 6.1. Later for grain size evaluation, microstructural images have been captured at a higher magnification of 20× into different zones of processed region.

Table 6.1 Macrographs of processed samples for different pin profiles

S. No.	Pin profile	Macrograph of FSPed zone cross-section	Quality of weld
1	TCP	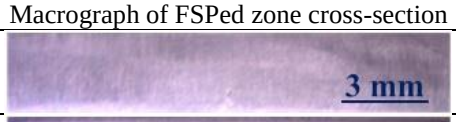	Defect free
2	SCP		Defect free
3	STP		Defect free

6.1.2 End forming experiments

The methodology of end forming experiments has been discussed in section 4.1.4 in Chapter 4.

6.1.3 Hardness distribution, tensile properties and grain size

The methodology of hardness distribution and grain size evaluation have been discussed in section 4.1.2 in Chapter 4.

Further, the mechanical properties of the base metal and processed zones have been evaluated in an UTM machine (INSTRON) of load capacity 100 kN. The dimensions of the tensile specimen for processed zones are, gauge width: 16 mm, gauge length: 12.5 mm, shoulder length: 35 mm, shoulder width: 24 mm and total length: 90.5 mm. To avoid any discrepancy in tensile test, tensile coupons from base metal have been fabricated with same dimensions. The tensile tests have been performed at a cross head speed of 1 mm/min. With the help of load-displacement data and initial dimensions of the gauge section, engineering stress and strain have been evaluated. True stress-strain curve has been generated after that. Later, by following standard procedures, mechanical properties such as yield strength, elongation (uniform and total), ultimate tensile strength, strain hardening exponent 'n' and strength coefficient 'K' have been calculated as per ASTM E8/E8M standard. Plastic strain ratio 'r' (ratio of true width strain and true thickness strain) has been calculated for base metal and FSPed zone at different conditions. Tensile testing has been performed only along the longitudinal directions (along the FSP directions) for FSPed zone, while the same has been done in longitudinal, transverse and at 45° directions for base metal, as per ASTM E517-000 standard.

6.1.4 Specific energy absorption capacity

The methodology of specific energy absorption capacity of processed as well as unprocessed tubes has been discussed in section 4.1.5 in Chapter 4.

6.1.5 Dislocation density measurement using X-ray peak profile analysis

The methodology of dislocation density measurement using X-ray peak profile analysis has been discussed in section 4.1.3 in Chapter 4.

6.1.6 Finite element simulation of end forming

The methodology of finite element simulation of end forming has been discussed in section 4.1.6 in Chapter 4. Further, the actual thicknesses of unprocessed zone and FSPed zone which have been incorporated during end forming simulations has been shown in Table 6.2.

Table 6.2 Actual thicknesses (mm) incorporated in end forming FE simulation

Pin profiles/ Raw tube	Tube expansion		Tube reduction		Tube beading	
	In FSPed zone	In base metal	In FSPed zone	In base metal	In FSPed zone	In base metal
TCP	2.48	3.16	2.90	3.09	2.80	3.07
SCP	2.81	3.10	2.56	3.09	2.96	3.03
STP	2.26	3.10	2.35	3.14	2.62	3.20
Raw tube	3.18		3.20		3.16	

The mechanical properties of base metal and FSPed zone corresponding to different pin profiles have been shown in Table 6.4. These values have been incorporated as material properties during end forming simulations. The true stress-strain curves are fit using the Hollomon's power law, $\sigma = k\varepsilon^n$ (Hollomon, 1945; Hollomon and Jaffe, 1947) for different cases (Fig. 6.2). The true stress-strain curves have been extrapolated for larger strain values during FE simulations.

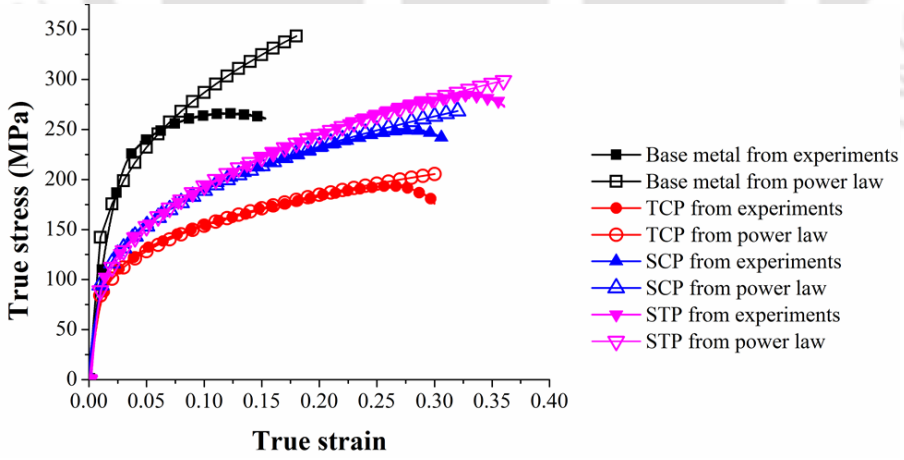

Fig. 6.2 Experimental and fit true stress-strain curves for base metal and FSPed zones

Table 6.3 summarizes the '*r*' value and the six yield factors R_{11}, R_{22}, R_{33}, R_{12}, R_{13} and R_{23} for base metal as well as FSPed zones made at different traverse speeds according to equation 4.4 as described in section 4.1.6 in Chapter 4. Here '*r*' has been calculated in longitudinal direction (along the processing direction) for processed zones. For base metal

'*r*' has been calculated in longitudinal, transverse and at 45° directions. For the present model in processed zone,

$$r_x(r_0) = r_{45} = r_y(r_{90}) = r \quad (6.1)$$

Table 6.3 *r* and other anisotropic input data

Base metal/FSPed zone	Plastic strain ratio '*r*'	R_{11}	R_{22}	R_{33}	R_{12}	R_{13}	R_{23}
Base metal	$r_0 = 1.53$	1	0.72	0.77	0.82	1	1
	$r_{90} = 0.47$						
	$r_{45} = 0.80$						
FSPed zone: TCP	0.65	1	1	0.91	1.03	1	1
FSPed zone: SCP	0.42	1	1	0.84	1.07	1	1
FSPed zone: STP	1.30	1	1	1.07	0.98	1	1

Base metal and FSPed zone corresponding to different pin profiles are anisotropic in nature (Table 6.3) as their values deviates from unity. Hence, it is believed that Hill's yield function which has been used to model plasticity of tubes will provide better results over von-Mises yield function which is meant particularly for isotropic materials.

6.1.7 Instability prediction during end forming

The methodology of instability prediction during end forming has been discussed in section 4.1.7 in Chapter 4.

6.2 Results and discussion

In this section, tensile properties of unprocessed and processed zones, hardness evaluation of the FSPed zone before and after forming, and microstructures at different regions of FSPed zone for different pin profiles have been discussed at the start of the section. Further, load evolution and thinning evolution during end forming for different pin profiles have been presented. Finally, the predicted load evolution and instabilities are validated with experimental results.

6.2.1 Tensile behaviour, hardness distribution and grain size

Tensile behaviour of base metal and processed zone for different tool geometries has been shown in Fig. 6.3. Individual mechanical properties of the FSPed zone and base metal are given in Table 6.4. FSPed zones exhibit lower yield strength and tensile strength as compared to base metal, while ductility improved for FSPed zones. The

strength of FSPed tube in case of TCP, SCP and STP has decreased by about 37 %, 20 % and 13 % as compared to unprocessed tube (base metal). Ductility has increased by 28.5 %, 20 % and 32.15 % in case of TCP, SCP and STP as compared to unprocessed tube (base metal). The *n* value of FSPed zone is either same or larger than that of base metal for SCP and STP, while it is lower in case of TCP. On the whole, *n* of FSPed zone varies within a range closer to that of base metal. STP shows larger tensile strength and elongation among various pin profiles.

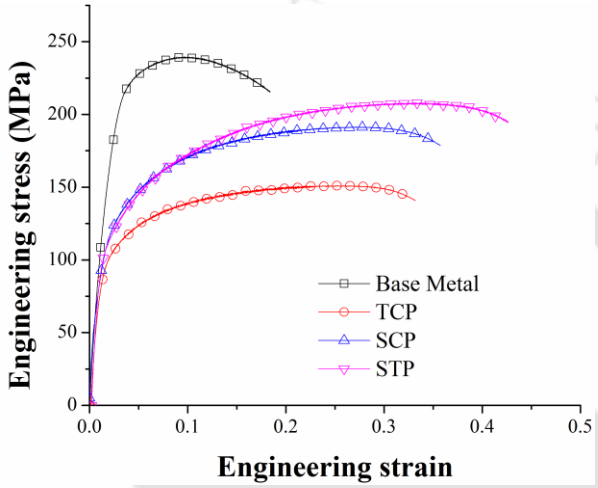

Fig. 6.3 Tensile behaviour of base metal and FSPed zones for different tool geometries (standard deviation in flow stress: base metal: 1 MPa , TCP: 8 MPa , SCP: 17 MPa, STP: 29 MPa)

Table 6.4 Mechanical properties of base metal and FSPed zone made at different tool geometries

Base Metal/Tool pin profiles	Yield strength (MPa)	Tensile strength (MPa)	Uniform elongation (%), at 12.5 mm gauge length	Total elongation (%), at 12.5 mm gauge length	Strain hardening exponent, *n*	Strength coefficient, *K* (MPa)
Base Metal	122.31±8	239.84±1	9.48±0.1	28±8	0.30±0.01	579.02±20
TCP	50.21±16	151.09±5	25.8±9	36±7	0.26±0.1	282.14±8
SCP	66.27±3	191.59±19	27.1±6	33.6±4	0.30±0.01	378.18±28
STP	51.06±35	208.68±18	34.19±1	37±2	0.33±0.01	422.57±30

The hardness distribution across the FSPed zone has been shown in Fig. 6.4(a-c). Hardness decreases after FSP for different tool pin profiles. Heat input experienced during FSP causes material softening. Hardness lies between 46-70 VHN across different zones for different tool geometries after FSP. FSPed zone softening is larger in case of SCP and TCP as compared to STP for different end forming operations. Similar trend has

been observed in tensile strength with TCP and SCP as compared to STP (Table 6.4). A very minor difference in hardness is seen across different zones of FSPed region in case of SCP and TCP.

Similar FSPed zone softening after FSP has been observed by Moreira et al. (2008). In their work, 3 mm thick plates of AA 6063-T6 has been FS welded. A hardness decrease of about 27 % and 32 % was found in the top surface and side surface. Sato et al. (1999) has confirmed similar results for a 6 mm thick AA 6063-T5 plate. It was observed that friction heating and plastic flow during friction stir welding create a fine recrystallized grain structure and a softened region around the weld centre. Further, it has been explained that since 6063 Al is a precipitation-hardenable alloy, mechanical properties are significantly related to the volume fraction, size and distribution of precipitates. Micrographs suggested dissolution of all precipitates in the softened region in their work.

In the present work, micrographs at different regions of FSPed zone at different pin profiles suggest that precipitate dissolution is more in case of TCP and SCP as compared to STP (Fig. 6.5). Hence FSPed zone softening is more in case of TCP and SCP as compared to STP resulting in larger strength of STP as compared to TCP and SCP. Moreover, in the existing literature comparison of FSPed zone strength for TCP and SCP is available, but not for STP. Elangovan and Balasubramanian (2008) showed that strength of FSPed zone is affected by tool pin profile and shoulder diameter in case of AA 6061 aluminum alloy. For fixed conditions of rotational speed, 1200 rpm, welding speed, 1.25 mm/sec and axial force, 7 kN, SCP showed better yield and tensile strengths as compared to TCP for a shoulder diameter of about 18 mm. At a larger diameter of 21 mm, TCP showed better yield and tensile strengths. Hence it can be said that keeping all other parameters constant, change in shoulder diameter affects the strength of the processed zone for a pin profile. In the present work, SCP shows larger strength at 25 mm shoulder diameter as compared to TCP for AA 6063-T6 which is acceptable.

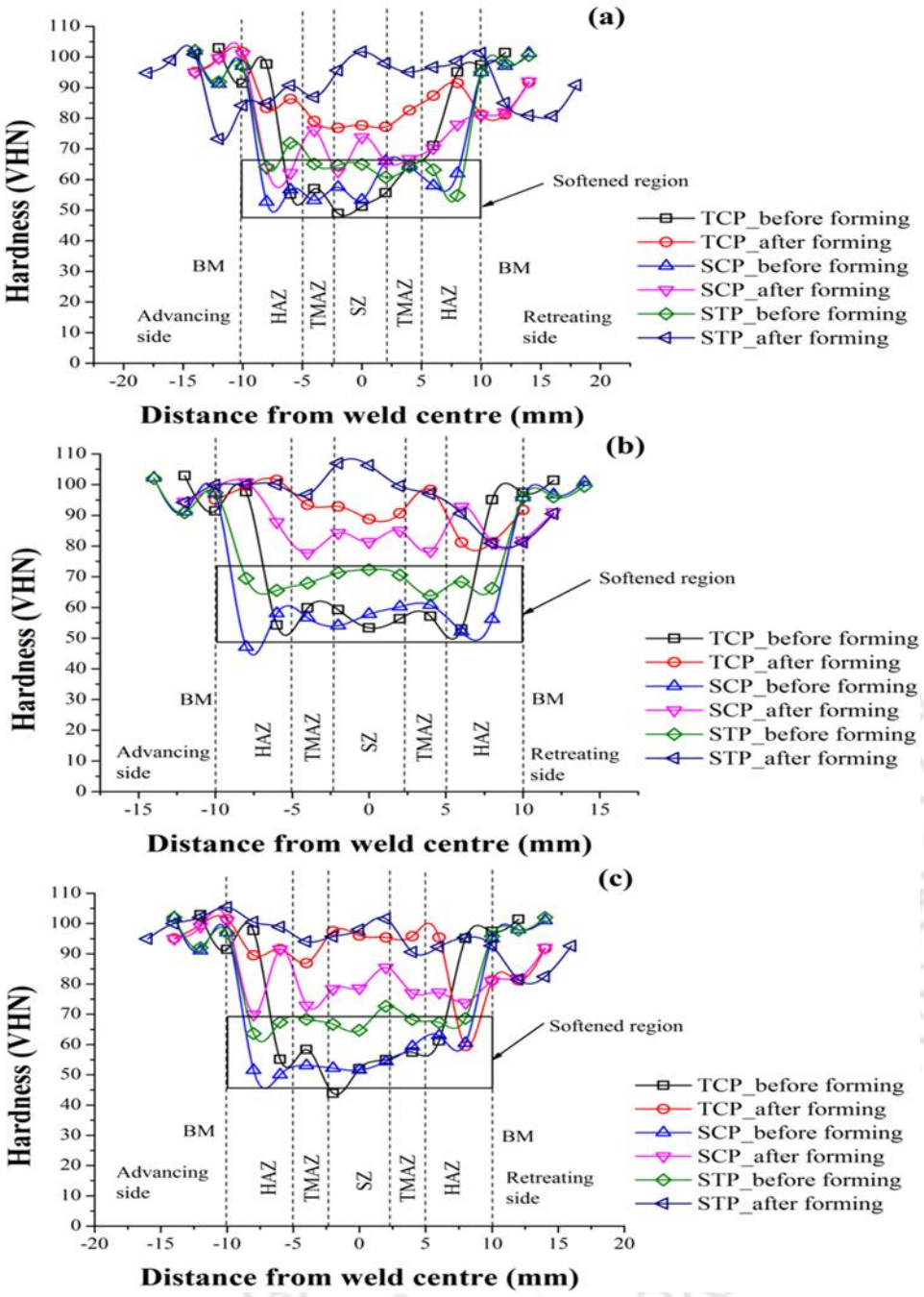

Fig. 6.4 Hardness variation across the FSPed zone before forming and after forming in case of, (a) tube expansion, (b) tube reduction, (c) tube beading
(average standard deviation for hardness in FSPed zone in case of expansion, before forming is ± 6 and after forming is ±12, in case of reduction, before forming is ±7 and after forming is ±9, in case of beading, before forming is ±7 and after forming is ±11)

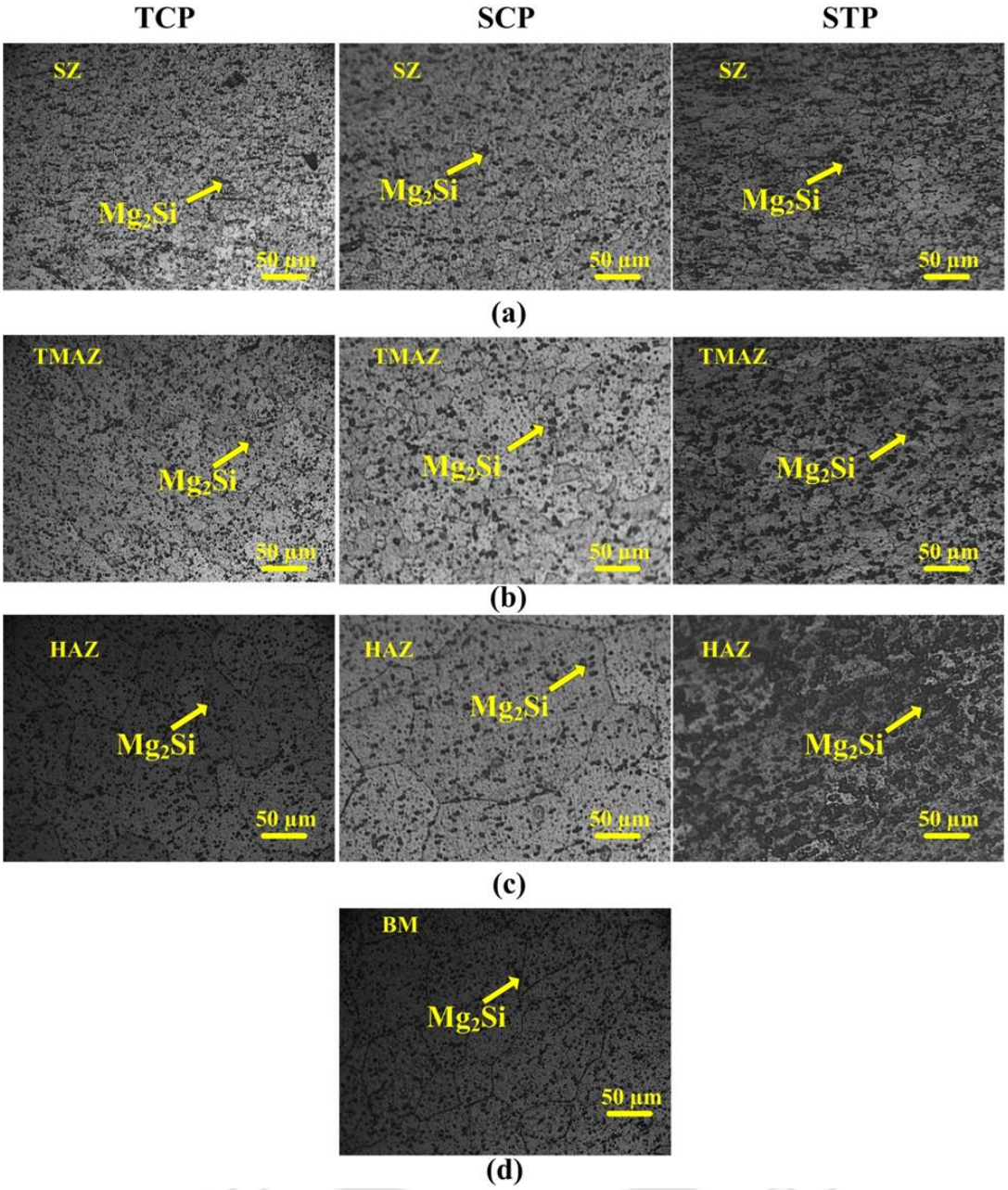

Fig. 6.5 Microstructures of different zones of FSPed region at different tool geometries: (a) SZ for TCP, SCP and STP, (b) TMAZ for TCP, SCP and STP, (c) HAZ for TCP, SCP and STP, and (d) base metal

Hardness increases after forming for all tool geometries in all end forming operations (Fig. 6.4(a-c)). For various end forming operations, STP provided larger hardness and SCP provided lower hardness. TCP is in between these two pin profiles. Here hardness increases due to strain hardening during end forming operations. Juijerm et al. (2006) found hardness increase during rolling due to strain hardening. They applied deep rolling under different aging conditions for precipitation hardened AA 6110 and

studied the residual stress and work hardening states near the surface by X-ray diffraction methods.

An average hardness has been calculated across the FSPed zone of width 16-18 mm (Table 6.5). In case of TCP and SCP, hardness of processed zone is almost same after FSP. Similar results have been shown by (Elangovan et al., 2008b). In case of STP, a larger hardness with a difference of approximately 10 VHN is obtained as compared to TCP and SCP. Hardness index, *H* (%) has been shown in Fig. 6.6. *H* (%) is larger in the case of reduction as compared to expansion and beading, except in few FSPed cases, showing a larger strain hardening in reduction as compared to other cases. In STP cases, the *H* (%) is almost same in all the three end forming operations. Among various tool geometries, *H* (%) is larger in case of TCP, and lower in case of SCP, except in few cases.

Table 6.5 Hardness of the processed zone before and after forming (BM hardness: 92 ± 3)

Tool pin profiles	Hardness (VHN)					
	Expansion		Reduction		Beading	
	Before forming *, H_i	After forming, H_f	Before forming*, H_i	After forming, H_f	Before forming*, H_i	After forming, H_f
TCP	57.63±8	82.46±5	55.45±2	92.2±3	54.71±6	89.73±12
SCP	56.97±6	68.82±6	55.89±4	83.90±4	55.04±5	78.33±7
STP	63.74±4	91.67±8	68.38±3	96.81±9	67.54±3	96.82±4

(* Before forming is same as after FSP)

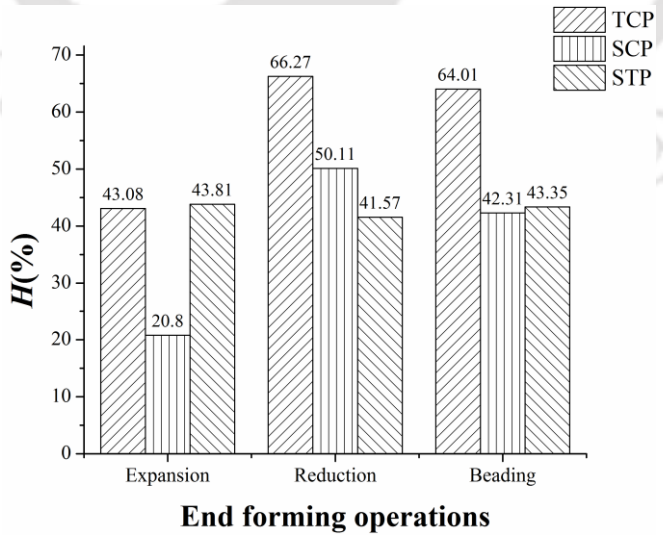

Fig. 6.6 *H* (%) during different end forming operations and tool geometries

A lower grain size in seen in SZ (Fig. 6.5a). Because of temperature rise and severe plastic deformation, dynamic recrystallization takes place in the SZ which reduces the grain size (Fig. 6.5a). Elongated grains are observed in TMAZ (Fig. 6.5b). TMAZ experiences both temperature and plastic deformation, and recrystallization is usually absent in this zone because of insufficient mechanical strain. HAZ experiences thermal cycle, whereas plastic deformation is absent in this zone (Fig. 6.5c). Appreciable variation in grain size and distribution of strengthening particles (Mg_2Si) can be seen in the micrographs (Fig. 6.5(a-d)). Base metal consists of larger elongated grains with uniform distribution of strengthening particles throughout the matrix. The density of strengthening precipitates has decreased in FSPed zone as compared to base metal. Cui et al. (2013) states that in precipitation hardening aluminium alloys like AA 6061-T4, precipitates are dissoluted during FSW, while during cooling of the FSPed zone reprecipitation of strengthening phases occur. These precipitates corrode during etching and possibly create holes which is seen as black particles in the micrographs.

Fig. 6.7 shows the average grain size in different regions of FSPed region. The pin profile does not show any influence in changing the grain size in SZ and TMAZ, while significant influence in HAZ is seen. Moreover, HAZ has larger grains as compared to SZ and TMAZ, and approaches that of base metal. In HAZ, a relatively smaller grain is observed for STP as compared to base metal and other pin profiles.

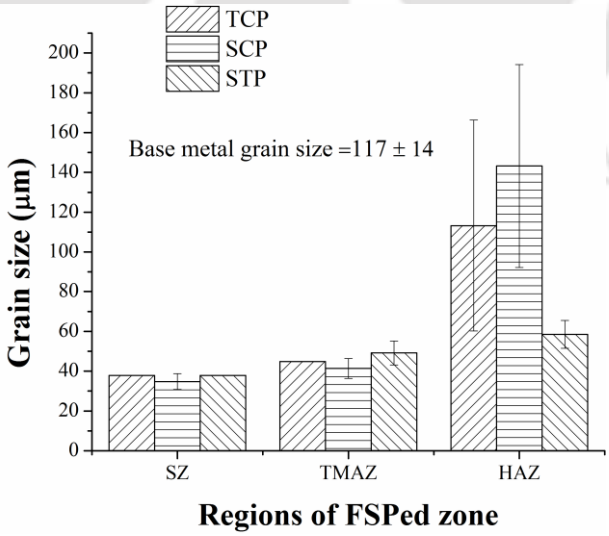

Fig. 6.7 Grain size at FSPed zone for different tool geometries

6.2.2 Dislocation density changes

Fig. 6.8 shows the (2 0 0), (2 2 0) and (3 1 1) peak profiles in the SZ for three different tool geometries. The peak broadening is different for different tool geometries which is related to different dislocation densities.

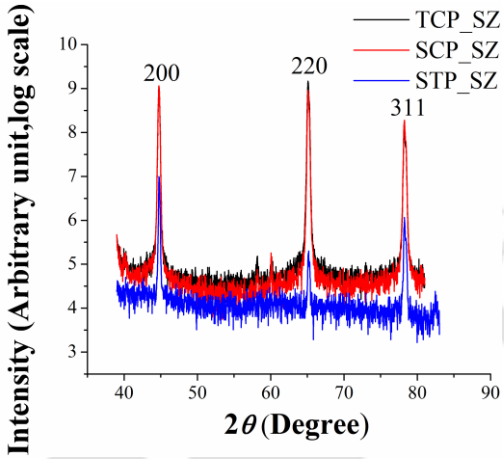

Fig. 6.8 X-ray diffraction peak profile in the stir region of FSPed zone made by TCP, SCP and STP

Modified Williamson-Hall plot for FSPed zones and pin profiles has been shown in Fig. 6.9. In case of SZ (Fig. 6.9a), the base metal shows the similar slope with TCP and SCP, whereas STP shows significantly lower slope when compared to base metal and other pin profiles. It means that base metal has nearly same dislocation density as compared to SZ of TCP and SCP. On the other hand, STP generates lower dislocation density in the SZ as compared to base metal. FSP zone having lower *n* value shows larger slope indicating a larger dislocation density.

The TMAZ made at different tool pin profiles exhibits larger slope (Fig. 6.9b) as compared to the base metal. However, the slopes corresponding to different pin profiles are almost same in HAZ region and is comparable with base metal (Fig. 6.9c). It suggests that dislocation density is also comparable. Similar results have been shown by Woo et al. (2008) for FSWed 6061-T6 alloy. They explained that the higher dislocation density observed near the boundary between TMAZ and HAZ could be explained by the network structure of many dislocations in subgrains. HAZ region has got nearly same dislocation density as that of base metal in Woo et al. (2008) work as well.

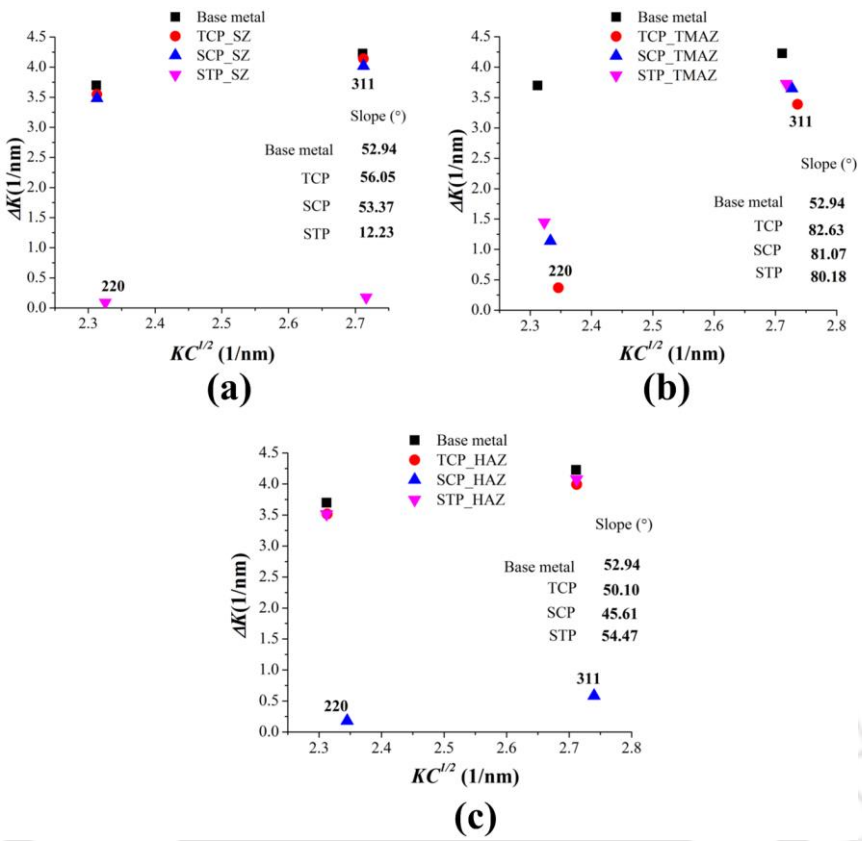

Fig. 6.9 Peak broadening analysis using the modified Williamson-Hall plot for, (a) SZ, (b) TMAZ, and (c) HAZ of FSP zone

Dislocation densities at different pin profiles and for different FSPed zones have been calculated with the help of equations 4.1 and 4.2 as described in section 4.1.3 and Chapter 4 and are summarized in Table 6.6. SZ shows lower dislocation density as compared to base metal, while TMAZ exhibit larger dislocation densities in all cases. The dislocation density obtained at HAZ is comparable with that of the base metal except in the case of SCP.

Table 6.6 ρ for base metal and for various FSPed zones

Pin profiles	ρ ($\times 10^{17}$ m^{-2})			Average ρ ($\times 10^{17}$ m^{-2}) in FSPed zone
	SZ	TMAZ	HAZ	
TCP	0.8	570	5.55	192±327
SCP	3.02	249	14.07	88±139
STP	0.54	423	2.48	142±243
*Base metal ρ: 5.22±0.8 ($\times 10^{17}$ m^{-2})				

Hardening capacity (H_c) for base metal and processed zone at different pin profiles and their respective n values have been shown in Table 6.7. For all pin profiles

H_c is larger as compared to base metal. This is clear from Fig. 6.3 depicting the flow stress change for various pin profiles with respect to base metal. The SZ with lower dislocation density as compared to base metal is responsible for equal or larger *n* values in case of FSPed zone (Table 6.6). TCP generates FSPed zone with lower *n* because of larger dislocation density (Table 6.6 and 6.7), while the other two show better *n* values with reduced ρ.

Table 6.7 H_c and *n* for base metal and FSPed zone at different pin profiles

Base metal/pin profiles	H_c	*n*
Base metal	0.96	0.30
TCP	2	0.26
SCP	1.89	0.30
STP	3.08	0.33

6.2.3 End forming operations

6.2.3.1 Load-displacement behaviour

Load-displacement behaviour during different end forming operations has been shown in Fig. 6.10-6.12 for different tool geometries and for unprocessed tubes. For parent tube the load observed is larger than that of processed tubes for different end forming operations because of larger overall strength of the raw tube. Within different tool geometries, load and displacement at failure is lower for TCP in case of expansion (Fig. 6.10), whereas it is higher for STP. Load experienced by tubes geometries is proportional to their tensile strength, i.e., larger is the flow strength, larger is the load experienced. For different tool geometries, displacement at failure depends on '*n*'. Cases with larger *n* have larger displacement at failure also. *H*(%) is also larger in case of STP, and hence larger load is obtained in this case. It can be said that load evolution depends on overall flow strength of the FSPed zone, and displacement at failure is dependent on *n* of FSPed zones. *H*(%) is also responsible for load evolution up to certain extent in FSPed tubes during end expansion.

In the case of end reduction, a minor load difference has been observed for different pin geometries throughout the end forming operation (Fig. 6.11). Lower load is observed for SCP, and higher load for TCP. TCP also shows maximum *H* (%) among all pin profiles. Within a displacement of 5-10 mm, either load drops or remains constant, for different tool geometries, which is because of initiation of wrinkling in the FSPed zone.

Wrinkle formation occurs due to softening of FSPed zone as compared to base metal because of circumferential compression. During wrinkle formation, load requirement is lesser as compared to end reduction process, and hence, a reduction in load is experienced. Later, overlapping is also observed in the wrinkled region. Within 5-10 mm displacement, wrinkling is predominant, and after that end reduction occurs along with continuation of wrinkling, and overlapping in the FSPed region. Hence beyond 10 mm displacement load increases monotonically for different tool geometries.

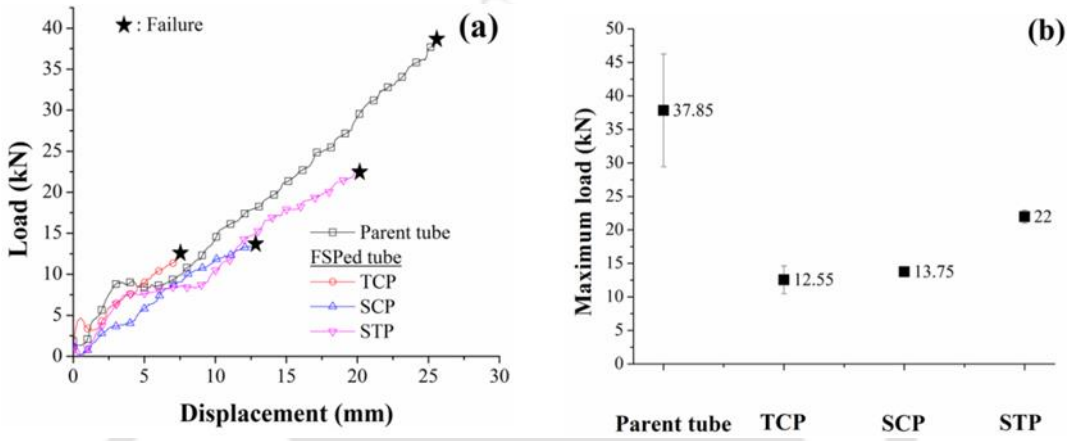

Fig. 6.10 (a) Load-displacement behaviour at different pin profiles, (b) maximum load variation for tube expansion

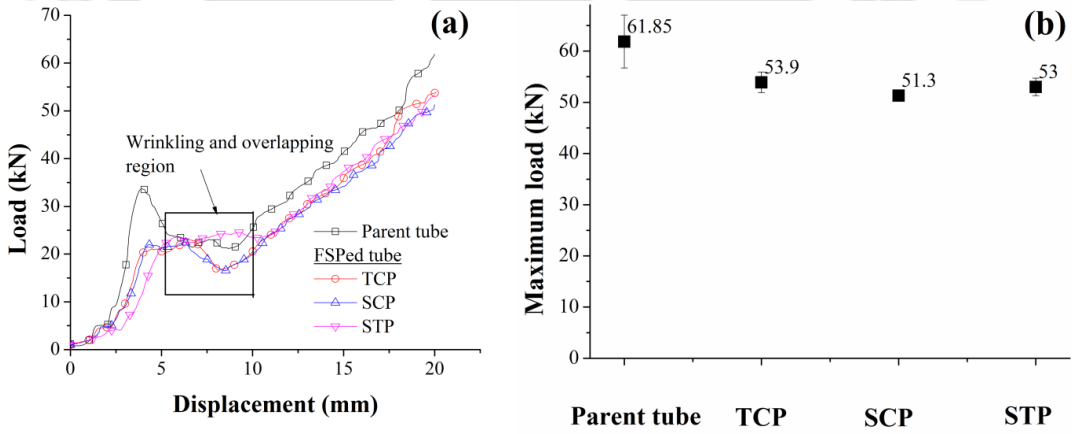

Fig. 6.11 (a) Load-displacement behaviour at different pin profiles, (b) maximum load variation for tube reduction

In the end beading of tubes, load monotonically increases until bead initiates (Fig. 6.12). After that a reduction in load is observed for unprocessed tube. For FSPed tubes, either load remains constant or slightly decreases as in TCP case. Bead initiation occurs at an early stage of 2-3 mm displacement for processed and unprocessed tubes. Maximum

load for bead initiation is observed for parent tube among all cases because of larger flow strength of base metal as compared to FSPed tubes. Lower load for bead Initiation is observed for TCP where as higher load is observed for STP, though there is not much difference. The load requirement coincides with change in flow strength of FSPed zone for various pin profiles summarized in Table 6.4.

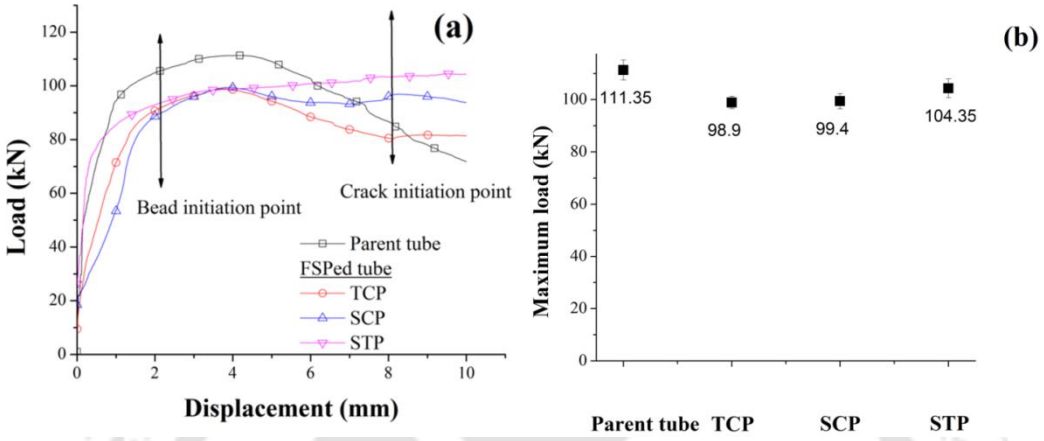

Fig. 6.12 (a) Load-displacement behaviour at different pin profiles, (b) maximum load variation for tube beading

6.2.3.2 Thickness evolution

Thickness evolution at the end of the tube during end forming has been shown in Fig. 6.13(a-c). Processed zone shows larger thinning as compared to unprocessed zones for different tool geometries (Fig. 6.13a) and unprocessed tube in tube expansion. Processed zone is softer than the unprocessed zone. A softer processed zone is more sensitive to thickness reduction, and hence larger thinning is observed in the processed zone. STP shows larger thinning among all pin profiles because of larger ductility.

The FSPed zone and unprocessed zone in FSPed tube and raw tube show thickening during end reduction (Fig. 6.13b). Thickening shown by processed zone is larger than that of unprocessed zone due to softening of FSPed zone. During end reduction material accumulates in the FSPed zone along circumferential direction. As a result of which, firstly, wrinkling occurs, and later on, overlapping is witnessed. Because of this phenomena thickening observed in FSPed zone is severe as compared to the unprocessed zone of the same tube.

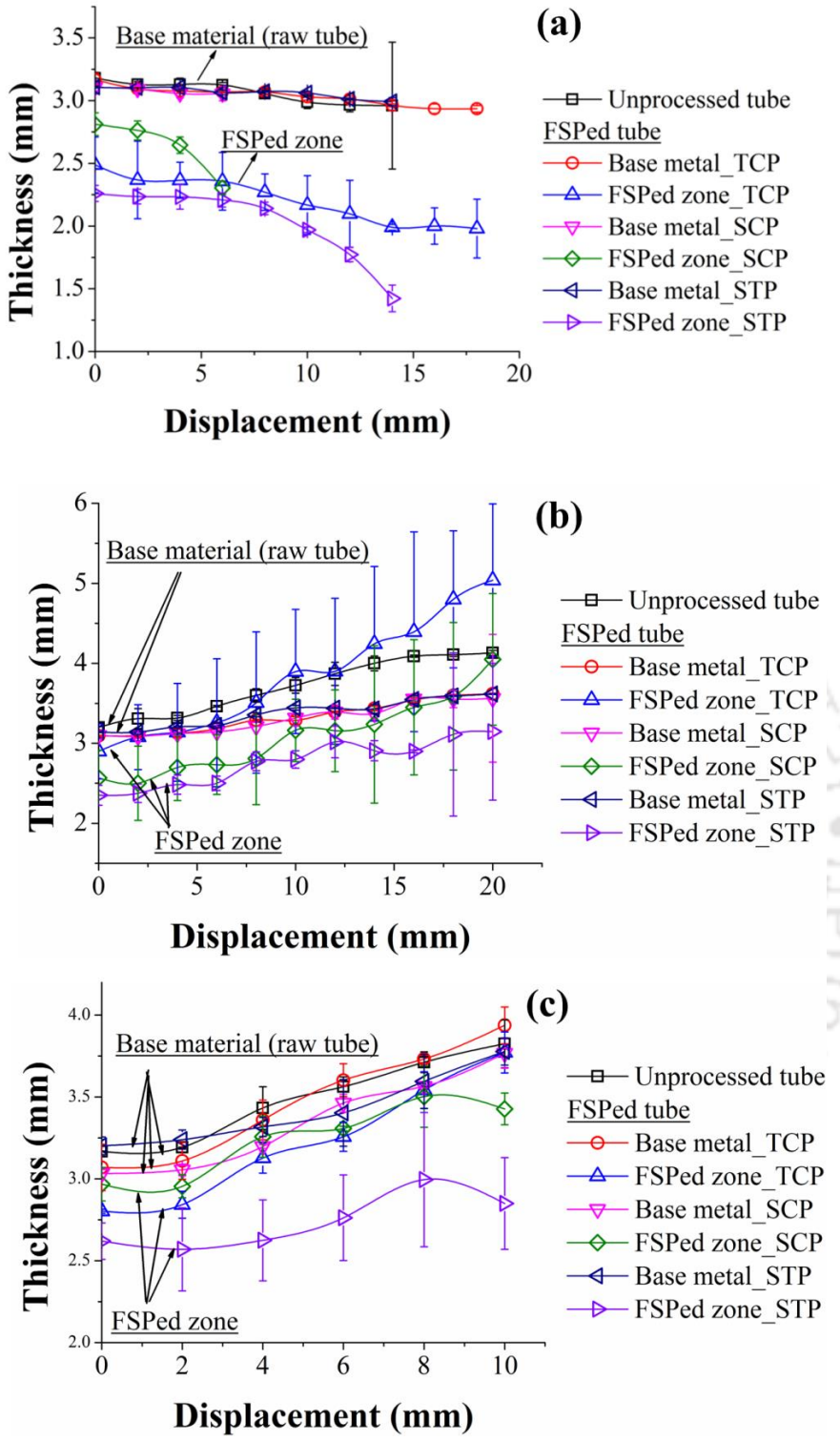

Fig. 6.13 Thickness evolution for (a) tube expansion, (b) tube reduction, (c) tube beading in processed tube (processed zone zone and base metal zone) and unprocessed tube

In case of end beading, thickening is observed both in the FSPed zone and unprocessed zones of processed tube, as well as in raw tubes (Fig. 6.13c). Beading process is a combination of bending and bulging process. Initially tube bends during compression of tube against the bottom plate and die, and then bulging starts because of restricted unsupported length of tube. Thickening of processed and unprocessed zones shows prominence of tube compression process during end beading. The quality of thickening depends on the relative strength of FSPed zone and unprocessed zone. A softer FSPed zone corresponding to TCP shows larger thickening as compared to other FSPed zones made by other pin profiles.

Tube thinning is lesser in base metal zone as compared to processed zones for different tool geometries in case of end expansion (Fig. 6.14(a, b)). Thickening in FSPed zone is larger for TCP and is lower for STP in case of end reduction (Fig. 6.14(a, b)). The zone which has lesser flow strength has thickened more. Base metal thickening remains unaffected for different tool geometries in this case. In case of tube beading, thickening of processed zone and base metal thickening follows the order, TCP > SCP > STP. FSPed zone thickening seen in TCP is larger than that of corresponding base metal thickening during end forming, while an opposite situation is observed in case of other pin profiles. A softer FSPed zone has thickened more.

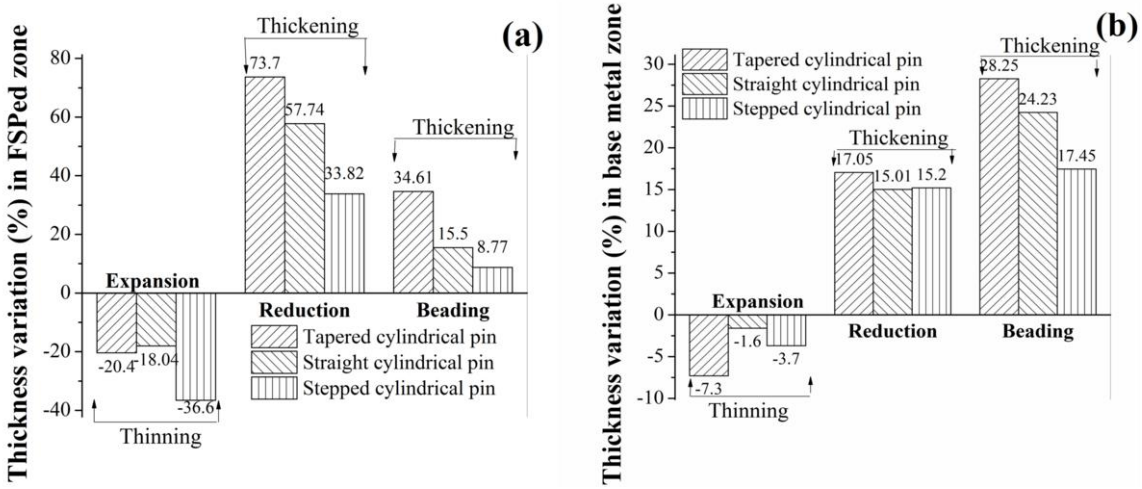

Fig. 6.14 Thickness variation for different tool geometries: (a) in FSPed zone, and (b) in base metal zone

6.2.4 Instabilities observed during end forming experiments

Instabilities have been observed during end forming operations. During end expansion, tube mostly fails at the middle of the FSPed zone. The fracture line is straight in case of processed tube, whereas in case of raw tube, it is slightly inclined (Fig. 6.15a). During end reduction of tubes, wrinkling and overlapping has been observed in the middle of the processed zone. No such wrinkling and overlapping is observed for raw tube (Fig. 6.15b). During tube end beading, fine cracks have been observed on the bulged region of the base metal zone. In case of raw tube, crack observed is quite large (Fig. 6.15c).

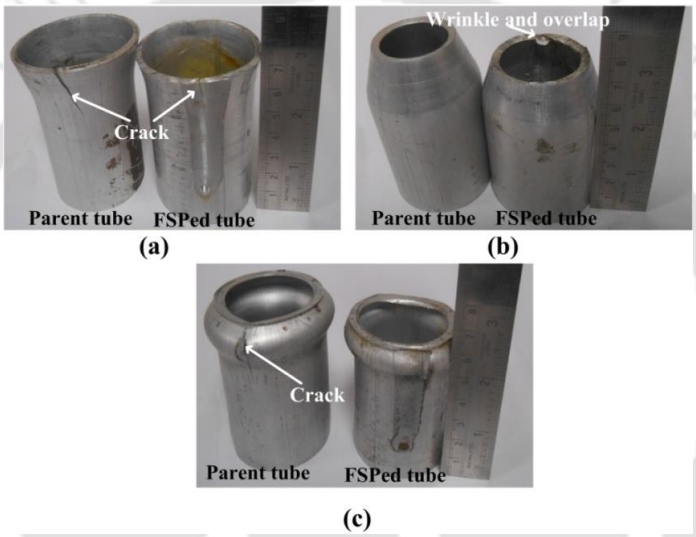

Fig. 6.15 Instabilities developed during, (a) tube expansion, (b) tube reduction, and (c) tube beading

6.2.5 Energy absorbed during end forming

The coefficients of load curve (A, B, C, D), average thickness of tubes, adjusting R –square and specific energy absorbed by the tubes have been shown in Table 6.8. The adjusting R-square value is more than 0.94 which means that a good fit has been obtained between actual load curve and curve from fit equation. The specific energy absorbed by the tubes for different tool geometries is closer to that of the parent tube in case of reduction and beading. In case of STP, it is larger than that of the parent tube making it an appropriate choice for energy absorbers in aircraft and ship building industries. In tube expansion, the FSPed tube fabricated by STP performs equivalent to that of raw tube. Hence STP can be a better option in fabricating FSPed tubes for end forming operations.

However, occurrence of instabilities can restrict its use in industries, specifically in end expansion and reduction. In end expansion, failure occurs in FSPed tubes well before raw tube, while there is no wrinkling during end reduction of raw tube.

Table 6.8 Specific energy absorbed by the tubes during end forming operations

Raw tube/Pin profiles	A	B	C	D	Average thickness of tubes (mm)	Adj. R-square	Specific energy absorbed (*E*) (kJ/kg)
Expansion							
Parent tube	2.991	0.99503	0.01235	0.00012	3.18	0.99	14.6
TCP	3.24346	0.1525	0.33475	-0.02653	2.82	0.97	6.5
SCP	0.28137	0.83467	0.08674	-0.00558	2.95	0.99	6.2
STP	1.32287	1.17924	-0.02498	0.00101	2.68	0.97	13.3
Reduction							
Parent tube	-0.19024	6.93699	-0.6163	0.02171	3.20	0.90	23.5
TCP	-1.00977	5.40937	-0.45652	0.0168	2.99	0.95	21.3
SCP	-0.00226	4.91174	-0.39761	0.01448	2.83	0.94	22
STP	-4.44121	6.09844	-0.45026	0.01474	2.74	0.96	23.7
Beading							
Parent tube	54.3099	36.5216	-6.71528	0.32739	3.16	0.91	74.7
TCP	29.6791	44.1669	-8.49456	0.4671	2.93	0.95	71.9
SCP	20.1375	45.2972	-8.0145	0.43217	3	0.95	72.9
STP	67.9467	16.7014	-2.73967	0.1469	2.91	0.87	83.4

6.2.6 Numerical analysis of end forming

6.2.6.1 Mesh sensitivity analysis

An extensive mesh sensitivity analysis for end expansion of tube has been done (Fig. 6.16). Tube element size has been varied between 0.25 mm and 1.50 mm. For mesh size of 1 mm, 1.25 mm and 1.50 mm, a zig-zag load pattern has been obtained which is not appropriate for a continuously expanding tube. On the other hand, almost same load evolution has been obtained for mesh sizes 0.25 mm, 0.50 mm and 0.75 mm. The load evolution obtained from simulation for 0.25 mm, 0.50 mm and 0.75 mm agrees well with that of from experiments. CPU time observed for mesh size of 0.25 mm is significantly larger as compared to that obtained for 0.50 mm and 0.75 mm. For a mesh size of 0.50 mm CPU time observed is 50 min. In this case, 6 elements in thickness direction has been obtained. Hence, considering computational efficiency, a mesh size of 0.50 mm has been chosen for present end forming simulation and analysis. A mesh size of 0.40 mm has been chosen for the softer FSPed zone in case of processed tubes which is appropriate to capture finer details of the deformation and instabilities of the FSPed zone.

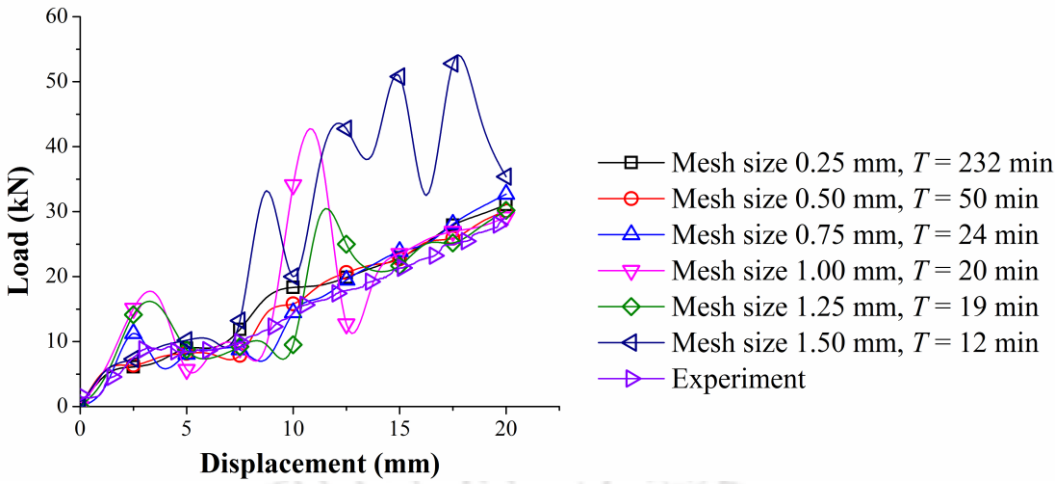

Fig. 6.16 Mesh sensitivity analysis for end expansion for parent tube

6.2.6.2 Prediction of instabilities by strain mapping method

In case of tube expansion, thickness strain in safe region does not increase, but increases in unsafe region after certain displacement. The displacement at which saturation occurs in safe region is shown in Fig. 6.17(a-d). In case of beading of tubes, after some displacement saturation takes place in the safe region (Fig. 6.18(a-d)). At this displacement, instability is believed to occur.

Table 6.9 summarizes the displacement at which instability occurs in case of experiment and FE simulation. A fair agreement is observed in displacement at which instability occurs in case of experiments and simulations for reduction and beading. However, in case of expansion, instability occurs late during simulation as compared to experiments. For processed tube, difference is larger as compared to unprocessed tube. Modeling conditions such as friction coefficient, time period, boundary conditions etc. can attribute to such difference in displacement.

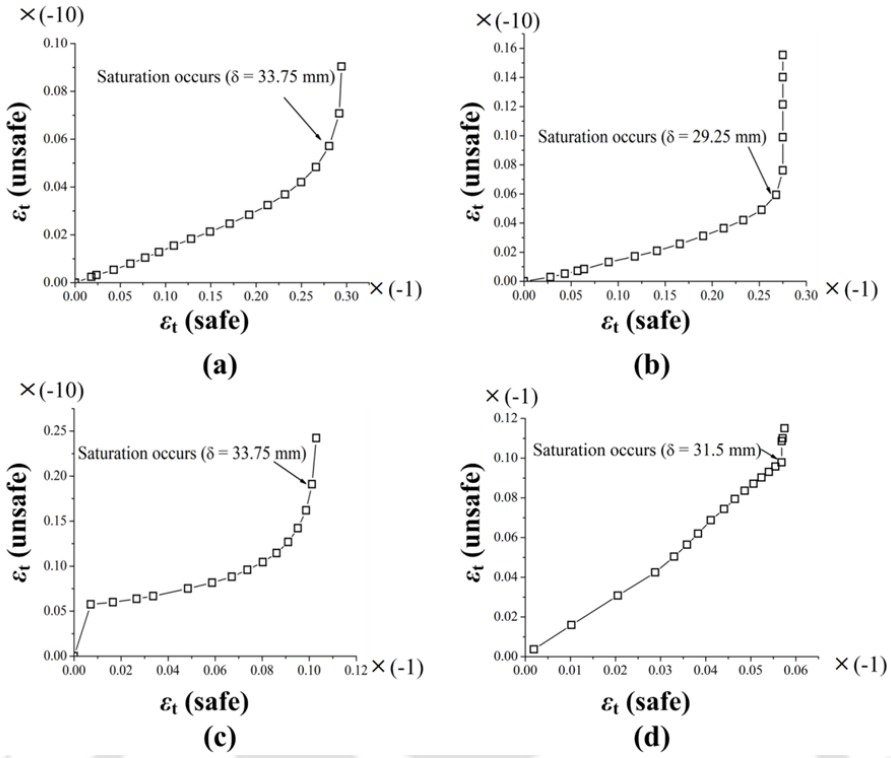

Fig. 6.17 Instability prediction during tube expansion, (a) TCP, (b) SCP, (c) STP, and (d) for parent tube (base metal) (thickness strain is actually negative, but shown here as positive)

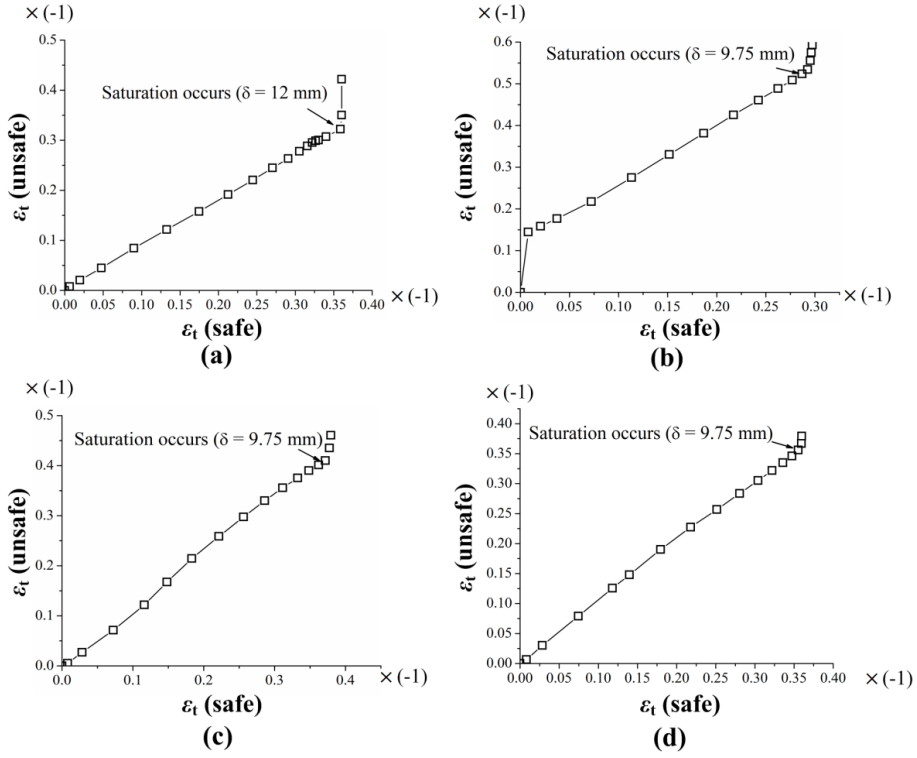

Fig. 6.18 Instability prediction during tube beading, (a) TCP, (b) SCP, (c) STP, and (d) parent tube (base metal) (thickness strain is actually negative, but shown here as positive)

Table 6.9 Prediction of displacement at onset of instability and experimental validation

Cases	Displacement at which instability occurs (mm)					
	End expansion		End reduction		End beading	
	Experiment	Prediction	Experiment	Prediction	Experiment	Prediction
Parent tube	25.48	31.5	No wrinkle and overlap		8	9.75
TCP	7.69	33.75	5	3	8	12
SCP	12.65	29.25	4.5	4.5	8	9.75
STP	20.1	33.75	5	3	8	9.75

Fig. 6.19 shows the instability developed during end forming simulation in STP. In expansion and beading the image is shown where instability is seen, while in reduction the image has been shown at the last stage of displacement, i.e., 20 mm. Similar pattern of instability development has been observed for other pin profiles and raw tube during FE simulation.

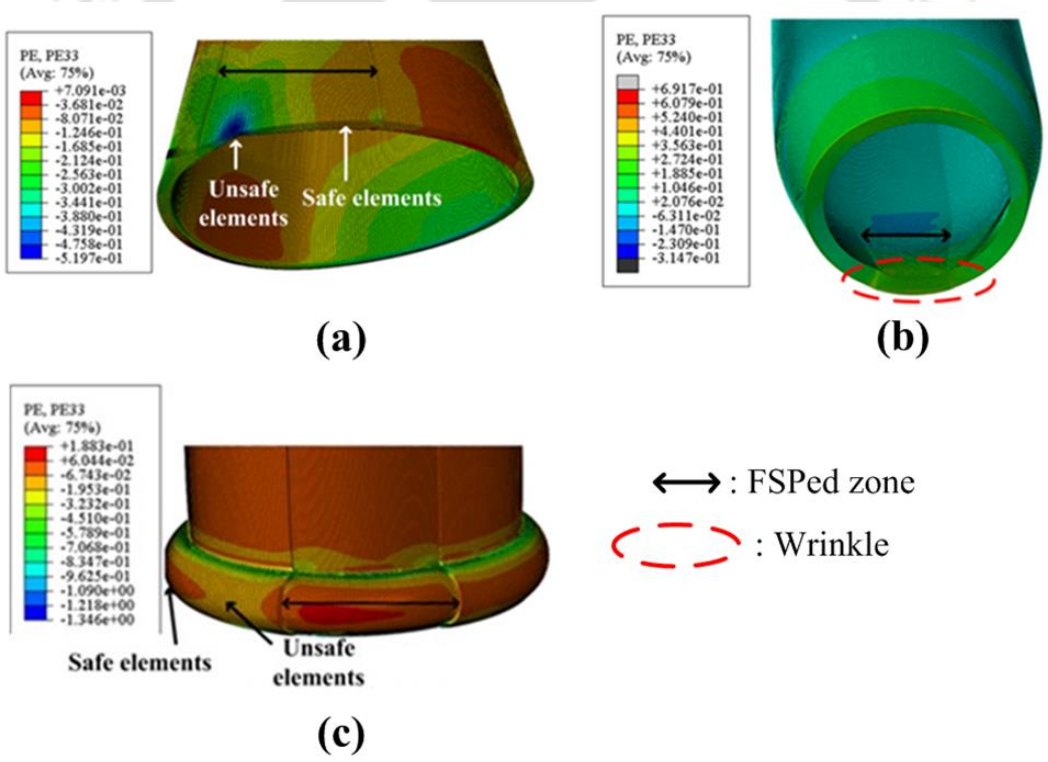

Fig. 6.19 Instability development during end forming in case of STP during, (a) end expansion, (b) end reduction, and (c) end beading

A comparison between experimental and FE simulation load-displacement data has been shown in Fig. 6.20. A good agreement is observed between experimental and predicted data until failure (Fig. 6.20a). Load evolution obtained by experiments and FE simulations agree well for end reduction. The load requirement from experiments is

slightly larger than from simulations. Wrinkling is observed at an early stage, at a relatively lower load in FE simulation as compared to experiments (Fig. 6.20b). In beading, load evolution obtained in case of experiment and simulation is slightly different after bead initiation (Fig. 6.20c). During FE simulations, load evolution shows an increasing trend after bead initiation for different cases. However, bead initiation occurs at almost same displacement when FE simulation data and experiments are compared.

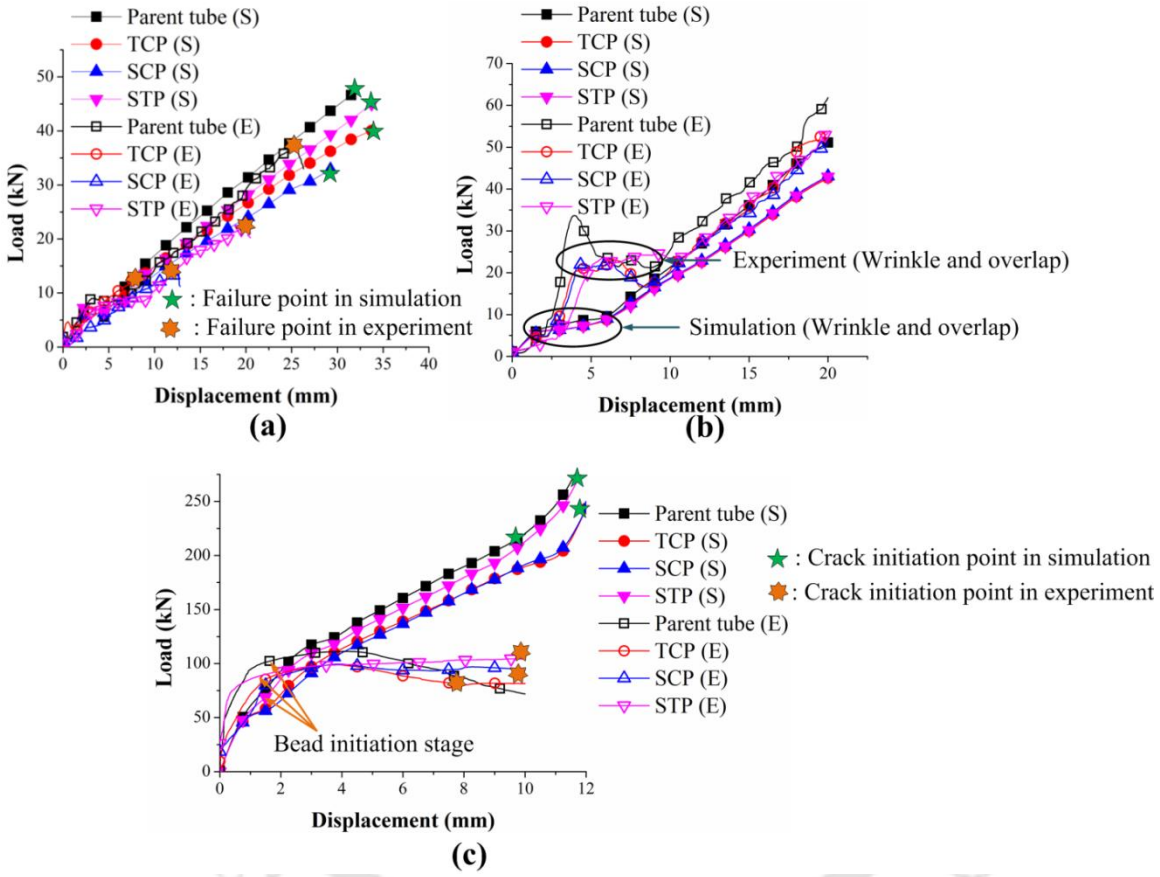

Fig. 6.20 Comparison between load evolution from experiments and simulations in case of, (a) end expansion, (b) end reduction, and (c) end beading (S: FE simulation, E: Experiment)

Multiple FSP of tubes can also be performed for enhancement in energy absorption to avoid crash severity of tubes. The same can be predicted by FE simulations. FSP of longer tubes of 1m length is also practically feasible and end forming can be studied with modification in the mandrel and base plate.

6.3 Conclusions

The main aim of the present work is to understand the effect of pin profiles on the end forming performance of FSPed Al 6063 T6 tubes. The end forming behaviour has

been predicted by FE simulations as well. The following are the conclusions drawn from the results:

1. The strength and hardness of the FSPed zone are lower than that of raw tube material. Because of this, the overall load requirement during end expansion, end reduction and end beading has reduced when compared to that required for the raw tube. Moreover, STP generated stronger FSPed zone as compared to other pin profiles. There is not much difference in the load evolution among pin profiles in case of end reduction, while FSPed tubes fabricated by STP bears larger load as compared to other two pin profiles in the case of end expansion and beading, which correlates with the tensile test results.

2. The ductility of FSPed zone has improved as compared to the raw tube material. This is due to the reduction in dislocation density in the stir zone after FSP. Such correlation is not observed during end forming, as the displacement at failure during end reduction and end beading is at par with that of raw tube, while it is reduced in case of end expansion. Among the pin profiles, the FSPed zone made by STP shows larger ductility due to lower dislocation density in the stir zone. Because of this, the FSPed tube shows larger displacement at failure during end expansion as compared to other pin profiles. Such difference is not observed in end reduction and end beading.

3. Hardness of the FSPed zone improves after end forming due to strain hardening. Hardening index is larger in case of reduction as compared to expansion and beading for all the pin profiles, with few exceptions. TCP shows largest hardening index among different pin profiles for all the end forming operations, while STP shows similar hardening index for with respect to end forming operations.

4. Thinning in FSPed zone during end expansion depends on the ductility of the FSPed zone in end expansion. As a result, thinning is larger in case of FSPed zone made by STP. Thickening in FSPed zone in case of reduction and beading depends on flow strength of FSPed zone. A weaker FSPed zone, like in case of TCP, has thickened more, while stronger FSPed zone, like in case of STP, has thickened less.

5. The FSPed tubes perform equal to that of raw tubes in terms of energy absorption during end beading and end reduction, while it is not so in end expansion. This demonstrates the suitability of FSPed Al tubes for end reduction and end beading applications. All the three pin profiles show similar performance during end beading and end reduction, while it is STP that performs better during end expansion.

6. Instabilities in the form of longitudinal crack in the FSPed zone during end expansion, wrinkling and overlapping during end reduction, and crack in the base metal of the FSPed tube during tube beading are witnessed. On the other hand, there is no wrinkling in tube reduction suggesting that the FSPed tubes should be used cautiously for tube reduction applications, though energy absorption is acceptable.

7. Load evolution in case of expansion and reduction matches well between experimental and predicted results for raw tube and FSPed tubes. A significant difference is observed in beading, specifically after bead initiation. The displacement at failure in reduction and beading matches well when experimental and predicted results are compared, while in expansion, a significant difference is observed. There is window for improving the modeling conditions during end expansion prediction.

8. STP is a better choice when the flow strength, and ductility of the FSPed zone, and end forming of FSPed tubes are referred. However, thinning is larger in case of FSPed zone made by STP during end expansion. TCP is a better choice when hardening index is referred. Hence, choosing pin profiles should be done cautiously depending on the tube applications.

Chapter 7

End forming behaviour of FSPed Al 6063-T6 tubes at different tool plunge depths

7.1 Methodology

In this section, FSP of tubes has been discussed initially. The procedure of conducting end forming experiments has been described. Evaluation of hardness, grain size, and tensile properties of FSPed zone have been described after that. Evaluation of specific energy absorption and dislocation density have been described. At last, FE simulation of end forming has been discussed with details of strain mapping method of instability prediction.

7.1.1 FSP of tubes

The methodology of FSP of tubes, macrograph examination and scheme of utilization of tubes have been discussed in section 4.1.1 in Chapter 4. Further, the range of plunge depths within which a defect free processed zone is obtained has been decided. Constant FSP parameters used are, tool rotational speed: 1350 rpm, tool traverse speed: 90 mm/min, and tool tilt angle: 2°. At these set of process parameters and at a plunge depth of 3 mm, defect free processed zone has been obtained as described in section 4.1.1 in Chapter 4. To decide a defect free range, plunge depth has been varied between 2.70 mm and 3.05 mm, by keeping the other parameter constant. Macrostructures have been obtained at a lower magnification of 7× to decide whether the FSPed zone is defective or not. Etching is done with Keller's reagent (H_2O: 95 ml, HNO_3: 2.5 ml, HF: 1.5 ml, HCl: 1 ml) to reveal the microstructures. Micrographs have been obtained at a higher magnification of 20× and 80×. Macrographs at different plunge depths have been shown in Table 7.1.

At plunge depths between 2.70 mm and 2.85 mm, and at 3.05 mm, defective FSPed zone has been obtained. Khan et al. (2015) work suggests that defects are formed at a lower plunge depth because of inadequate material flow, while the defects are minimized at higher plunge depths as suggested by Dehghani et al. (2013). Between 2.90 mm and 3.00 mm, defect free FSPed zones are obtained as shown in Table 7.1. Hence

plunge depths of 2.90 mm, 2.95 mm and 3.00 mm have been chosen for final FSP of tubes.

Table 7.1 Macrographs of joint cross-section at different plunge depths

S. No	Plunge depth (mm)	Macrograph of the joint cross-section	Quality of the weld
1.	2.70	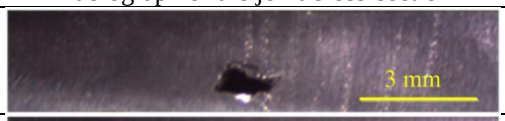	Defective, tunnel defect
2.	2.77	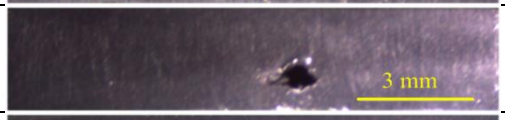	Defective, tunnel defect
3.	2.85		Defective, rough surface
4.	2.90		Defect free
5.	2.95		Defect free
6.	3.00		Defect free
7.	3.05		Defective, tunnel defect

7.1.2 Tube end forming

The methodology of end forming of tubes has been discussed in section 4.1.4 in Chapter 4.

7.1.3 Hardness, tensile properties and grain size evaluation

The methodology of hardness distribution and grain size evaluation has been discussed earlier in section 4.1.2 in Chapter 4, while methodology of tensile properties evaluation has been discussed in section 6.1.3 in Chapter 6.

7.1.4 Specific energy absorption capacity

The methodology of specific energy absorption capacity has been discussed earlier in section 4.1.5 in Chapter 4.

7.1.5 Dislocation density measurement using X-ray peak profile analysis

The methodology of dislocation density measurement using X-ray peak profile analysis has been discussed in section 4.1.3 in Chapter 4.

7.1.6 FE simulation of end forming

FE simulation methodology has been discussed in section 4.1.6 in Chapter 4, while mesh sensitivity analysis of tube has been discussed in section 6.2.6.1 in Chapter 6.

In simulation, the FSPed zone properties and base metal properties mentioned in Table 7.4 are provided. The true stress-true strain data are fit using the Hollomon's power law, $\sigma = k\varepsilon^n$ (Hollomon and Jaffe, 1947; Hollomon, 1945), and the obtained flow stress-strain behaviour (Fig. 7.1) is used during simulations to define the constitutive behaviour. The strain hardening curves are extrapolated for larger strains during FE simulations. The actual thicknesses of the base metal region and the processed region (Table 7.2) have been incorporated in the FE simulations for different plunge depths.

Table 7.2 Initial thickness of the raw and processed tubes used for end forming simulations

FSPed tube and raw tube thickness (mm)						
Plunge depth/Raw tube	Tube expansion		Tube reduction		Tube beading	
	in FSPed zone	in base metal	In FSPed zone	In base metal	In FSPed zone	In base metal
2.90 mm	2.88	3.13	3.20	3.13	3.12	3.15
2.95 mm	1.98	3.13	3.29	3.15	1.83	3.14
3.00 mm	2.50	3.15	2.66	3.125	2.895	3.12
Raw tube	3.18		3.20		3.16	

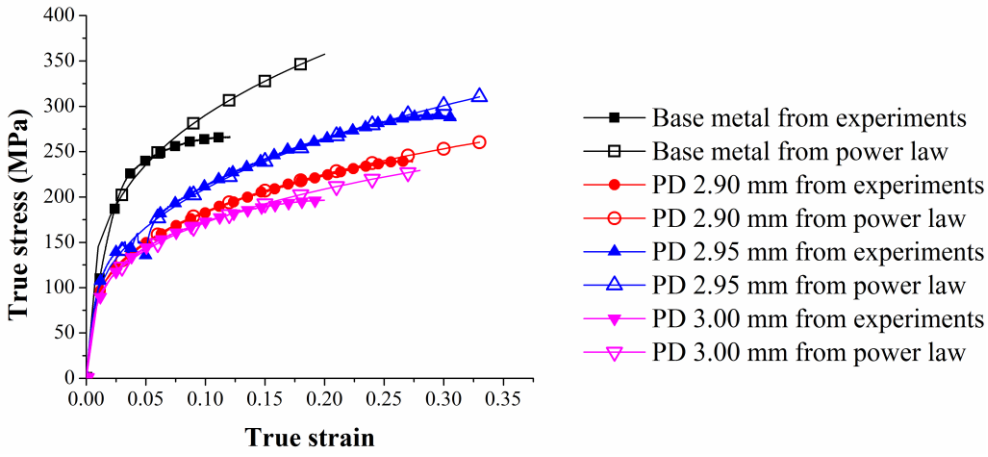

Fig. 7.1 True stress-strain fit curves used for base metal and processed zones at different plunge depths

Table 7.3 summarizes the '*r*' value and the six yield factors R_{11}, R_{22}, R_{33}, R_{12}, R_{13} and R_{23} for base metal as well as FSPed zones made at different traverse speeds according to equation 4.4 as described in section 4.1.6 in Chapter 4. Here '*r'* has been calculated in longitudinal direction (along the processing direction) for processed zones. For base metal '*r*' has been calculated in longitudinal, transverse and at 45° directions. For the present model in processed zone,

$$r_x(r_0) = r_{45} = r_y(r_{90}) = r \tag{6.1}$$

Table 7.3 Values of *r* and anisotropic parameters

Base metal/FSPed zone	Plastic strain ratio *'r'*	R_{11}	R_{22}	R_{33}	R_{12}	R_{13}	R_{23}
Base metal	*r* (0°)=1.53	1	0.72	0.77	0.82	1	1
	r (90°)=0.47						
	r (45°)=0.80						
FSPed zone: 2.90 mm	0.72	1	1	0.92	1.02	1	1
FSPed zone: 2.95 mm	0.17	1	1	0.76	1.14	1	1
FSPed zone: 3.00 mm	0.69	1	1	0.92	1.03	1	1

The anisotropic properties given in Table 7.3 are incorporated during FE simulations of end forming operation. Base metal and processed zone are anisotropic in nature which is confirmed from '*r*' values. So it is believed that Hill's 1948 yield function which is used to model plasticity of tubes will deliver acceptable results over von-Mises yield function which is meant for isotropic material.

7.1.7 Instability prediction during end forming

The methodology of instability prediction during end forming has been discussed in section 4.1.7 in Chapter 4.

7.2 Results and discussion

In this section, the influence of plunge depth on the tensile behaviour, hardness distribution after FSP and after end forming and grain size has been discussed in the initial part. After that, dislocation density changes at the FSPed zone in comparison to the base metal have been discussed. The effect of plunge depths on load and thickness evolution, and instabilities development has been presented in the next section. Finally, the FE predicted results are highlighted.

7.2.1 Tensile behaviour, hardness and grain size distribution

Tensile behaviour of base metal and processed zones for different plunge depths has been shown in Fig. 7.2. The flow strength has decreased and ductility has improved in FSPed zones when compared with the base metal. Tensile strength has decreased by about 22.5 %, 8 % and 32 % for 2.9 mm, 2.95 mm and 3.00 mm plunge depths. On the other hand, for plunge depths 2.90 mm and 2.95 mm the ductility has increased by about 7 % and 21 %. In case of 3 mm, it has decreased slightly. Strain hardening exponent of base metal and 2.90 mm plunge depth is almost same. For plunge depth 2.95 mm, it is slightly larger than that of base metal, and it is slightly lower than that of base metal in case of plunge depth 3 mm (Table 7.4).

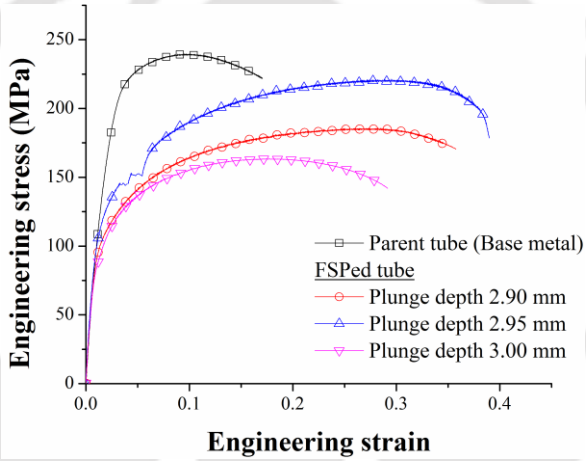

Fig. 7.2 Engineering stress-strain curves for base metal and FSPed zones made at different plunge depths
(standard deviation in flow stress: base metal: 1 MPa , plunge depth of 2.90 mm: 8 MPa, plunge depth of 2.95 mm: 2 MPa, plunge depth of 3.00 mm: 29 MPa)

Table 7.4 Mechanical properties of base metal and FSPed zone made at different plunge depths (Base metal hardness: 92±3)

Base metal/ plunge depths	Yield stress (MPa)	Ultimate tensile strength (MPa)	Uniform strain (%), at 12.5 mm gauge length	Total strain (%), at 12.5 mm gauge length	Strain hardening exponent, *n*	Strength coefficient, *K* (MPa)
Base metal	122.31±8	239.84±1	9.48±0.1	28±8	0.30±0.01	579.02±20
2.90 mm	83.63±1	185.83±8	27.40±4	30±4	0.293±0.01	359.02±18
2.95 mm	93.76±2	221.33±5	29.46±4	34±3	0.328±0.01	447.36±22
3.00 mm	73.11±2	163.41±35	17.74±8	25.6±7	0.279±0.03	327.47±69

Hardness distribution across FSPed zone after FSP and after end forming has been shown in Fig. 7.3(a-c). Hardness decreases after FSP for different plunge depths due to heat experienced during FSP. Hardness decrease is larger in case of plunge depths 2.90 mm and 3.00 mm as compared to plunge depth 2.95 mm. Hardness lies in a range of 45-80 VHN for different plunge depths across different zones, after FSP.

El-Rayes and El-Danaf (2012) FSWed AA 6082–T651 using different combinations of feed rates (90, 140 and 224 mm/min) and tool rotational speeds (850, 1070 and 1350 rpm). Microhardness distribution on the transverse section of welded sample showed that for different combination of process parameters softening occurs in stir zone and further softening occurs in TMAZ. Sato et al. (1999) revealed that the weld zone has softened after FSW of AA 6063-T5 and all precipitates dissoluted in the weld zone spanning over a distance of 8.5 mm from the weld centre. Similarly, in the present work, because of different levels of dissolution of precipitates with respect to heat flux induced due to different levels of plunge depths, the hardness and flow strength of the FSPed zone decreased with respect to base metal. This is clear from flow strength in Table 7.4 and hardness distribution in Fig. 7.3.

Hardness increases after end forming for all the plunge depths. The hardness improvement in case of 2.90 mm plunge depth after end beading is insignificant. Plunge depth of 2.90 mm shows the lowest hardness, while plunge depth 2.95 mm shows the highest hardness with a difference of about 30-40 VHN in this case. It can also be said that plunge depth of 2.90 mm shows lower hardness, and plunge depth of 2.95 mm shows higher hardness for all the end forming operations. In end expansion and reduction, the hardness after forming, for 2.95 mm and 3.00 mm plunge depth are close to each other in most of the processed zone region. The main reason for hardness increment during end forming is strain hardening.

Dutkiewicz and Litynska (2002) showed that AA 6013 and AA 6xxx (1.09 % Mg, 0.9 % Si, 0.1 % Fe and 1.1 % Cu by wt.) showed a hardness increase of 40 VHN and 30 VHN when thickness is reduced from 30 % to 90 % during cold rolling process. It shows that hardness increases during cold rolling because of strain hardening in their work. Average hardness has been determined for a processed zone of width 16-18 mm for different plunge depths and end forming operations and has been shown in Table 7.5.

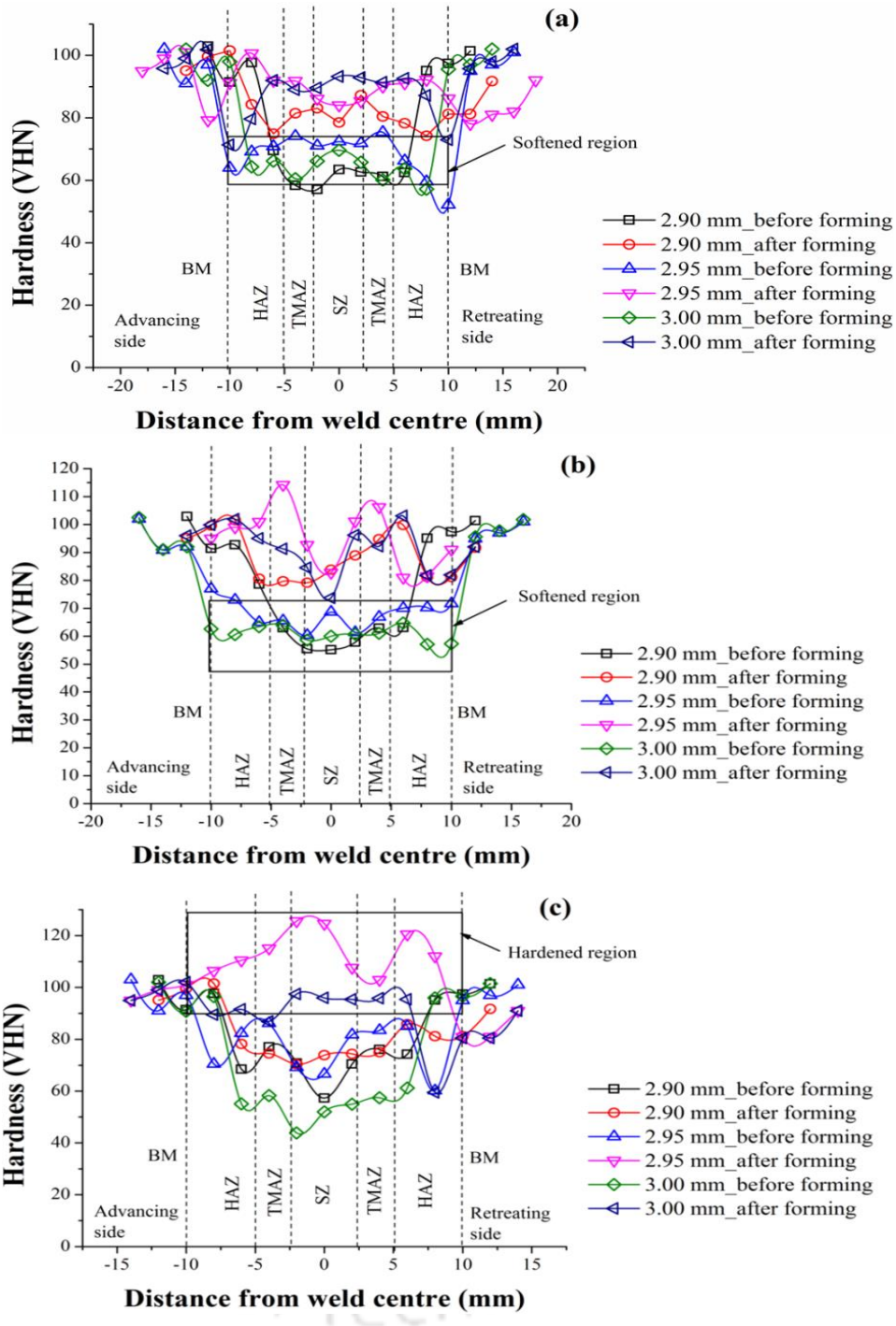

Fig. 7.3 Hardness plot across the processed zone before forming and after forming in case of, (a) tube expansion, (b) tube reduction, and (c) tube beading
(average standard deviation for hardness in processed zone in case of expansion before forming is ±6, and after forming is ±7, in case of reduction before forming is ±6, and after forming is ±11, in case of beading before forming is ±7, and after forming is ±20)

Table 7.5 Average hardness of the processed zone for different plunge depths and end forming operations

Plunge depth (mm)	Average hardness (VHN)					
	Expansion		Reduction		Beading	
	Before forming *, H_i	After forming, H_f	Before forming*, H_i	After forming, H_f	Before forming*, H_i	After forming, H_f
2.90	62.08±4	80.26±4	62.3±8	86.67±8	70.64±2	76.02±5
2.95	67.86±7	88.31±6	68.15±5	99.41±12	76.12±10	113.91±8
3.00	63.70±4	86.51±8	60.91±3	90.85±9	63.04±5	72.6±10

* Here before forming is same as that of after FSP

The variation in *H* with respect to different plunge depths and end forming operations has been shown in Fig. 7.4. A systematic improvement in *H* is observed with increase in plunge depths in case of expansion and reduction. But, in case of beading, larger *H* is observed for the plunge depth of 2.95 mm. End reduction shows larger *H* for all the plunge depths indicating larger strain hardening as compared to end expansion and beading. Only exception is when FSPed zone made at 3 mm and 2.95 mm in case of reduction and beading. They perform equally when *H* is compared (Fig. 7.4).

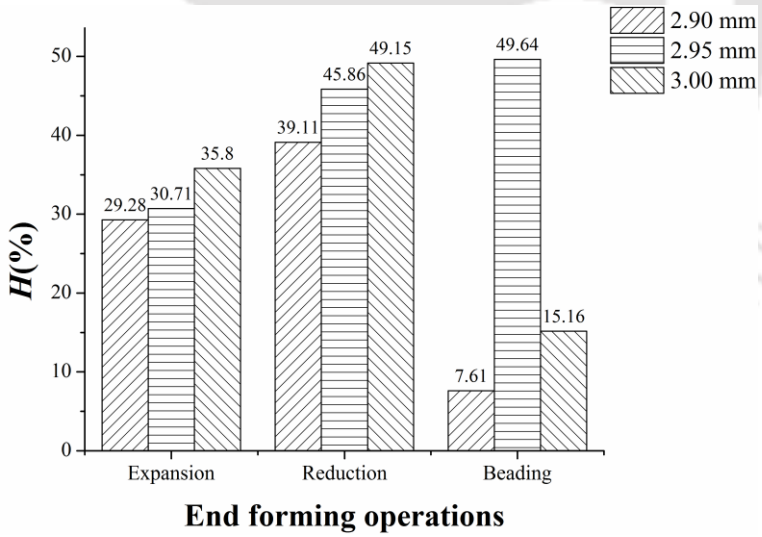

Fig. 7.4 Variation in *H* with respect to different plunge depths and end forming operations

Optical microstructures of different FSPed zones made at different plunge depths has been shown in Fig. 7.5(a-d). SZ shows lower and uniform grain size as compared to TMAZ and HAZ (Fig. 7.5a). In TMAZ larger elongated grains as compared to SZ are observed (Fig. 7.5b). In HAZ and base metal almost similar grain size pattern is observed (Figs. 7.5c and 7.5d).

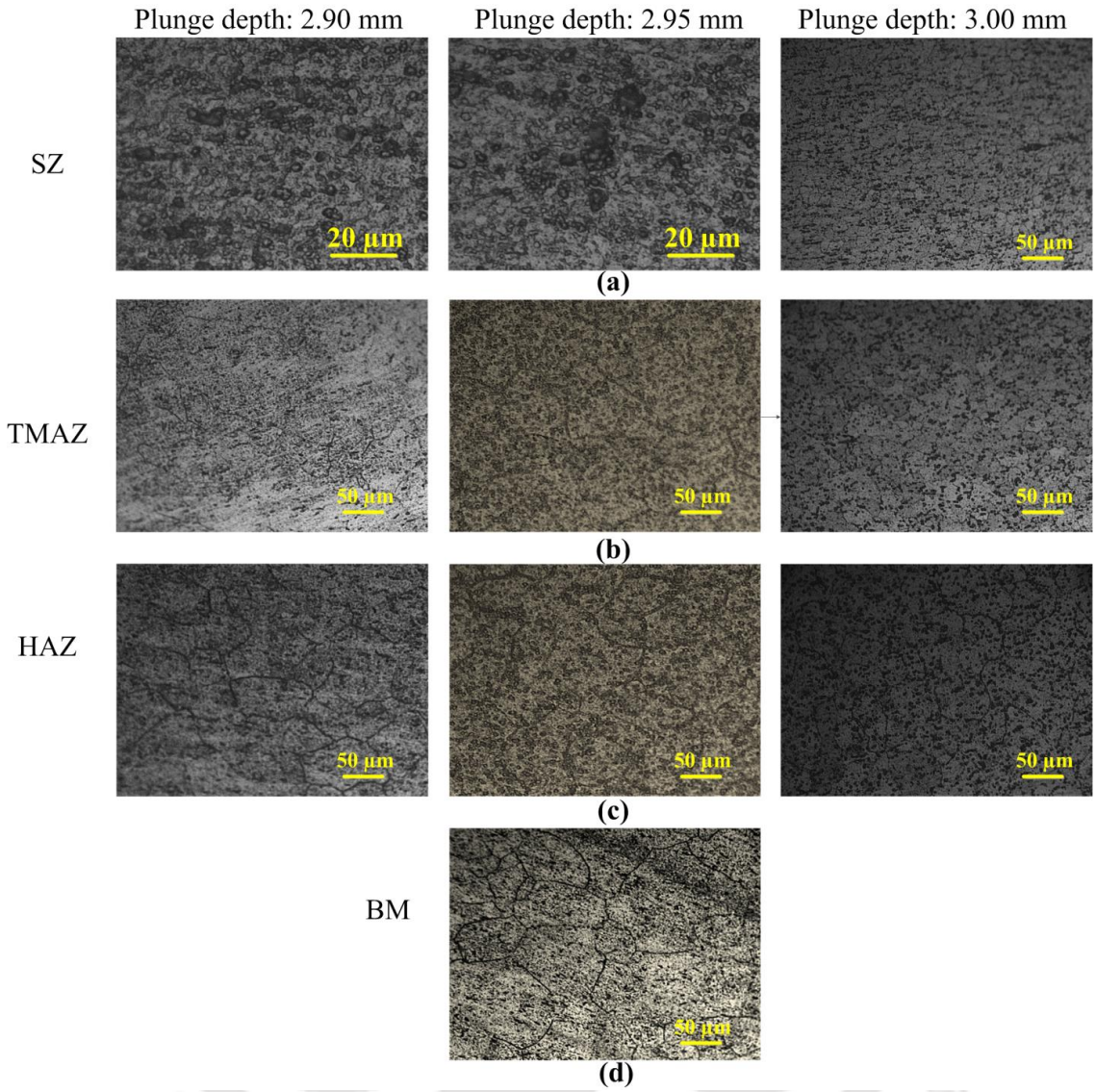

Fig. 7.5 Optical microstructures of FSPed zone at different plunge depths: (a) SZ for 2.90 mm, 2.95 mm and 3.00 mm, (b) TMAZ for 2.90 mm, 2.95 mm and 3.00 mm, (c) HAZ for 2.90 mm, 2.95 mm and 3.00 mm, and (d) Base metal

Due to severe plastic deformation and friction heating, recrystallization takes place in SZ, while TMAZ usually experiences no recrystallization because of insufficient deformation strain. HAZ experiences only thermal cycle. A varying plastic deformation and heat experienced in different zones influences the grain size. Within different zones, plunge depth of 2.95 mm shows lower grain size as compared to other zones (Fig. 7.6). It can be seen that precipitate dissolution (Mg_2Si), within zones, is less in case of 2.95 mm as compared to other plunge depths. It means that lesser heat has been experienced in case of 2.95 mm which results in a harder processed zone in case of 2.95 mm as compared to other plunge depths (Fig. 7.5(a-c)). In precipitation hardening aluminium alloys

strengthening particles (Mg_2Si) dissolute during heating cycle and reprecipitate when cooling of the processed zone occurs. These particles are seen as black after etching. In etching these particles corrode with the etching solution (Cui et al., 2013).

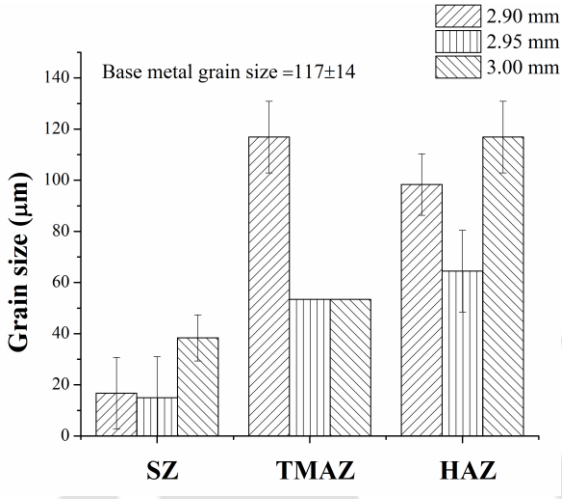

Fig. 7.6 Grain size changes at different FSPed zones made at varying plunge depths

7.2.2 Dislocation density changes in the FSPed zone

The directly measured X-ray diffraction peak data has been shown in Fig. 7.7. The indices for each (h k l) peak are presented for the FCC Al alloy (Fig. 7.7a). Fig. 7.7b shows the (200), (220) and (311) peak profiles in the TMAZ for different plunge depths. Peak broadening is slightly different for different plunge depths at different (h k l) peak.

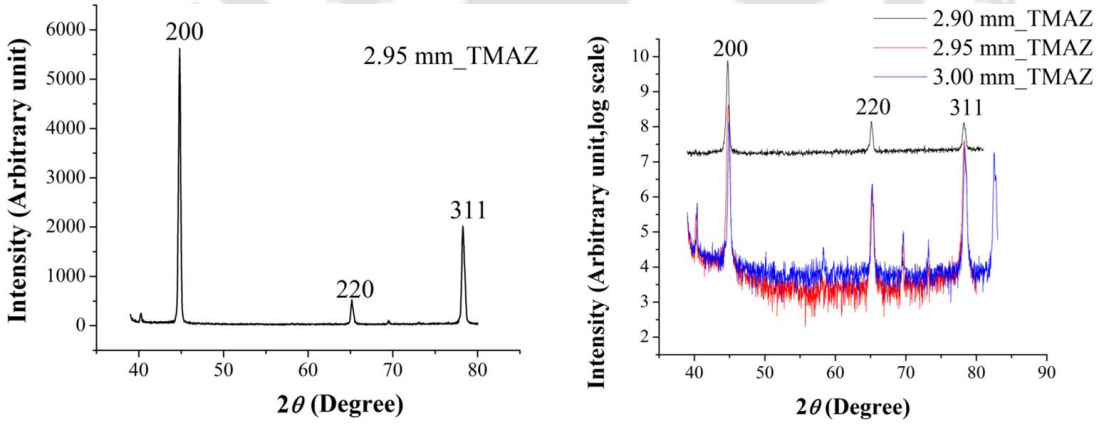

Fig. 7.7 (a) X-ray diffraction peak profile pattern in the TMAZ of FSPed zone made at plunge depth of 2.95 mm, (b) peak profiles measured in the TMAZ for 2.90 mm, 2.95 mm and 3.00 mm plunge depths

Modified Williamson-Hall plot for different zones and plunge depths has been shown in Fig. 7.8. Base metal has larger slope in the SZ as compared to different plunge

depths (Fig. 7.8a). It means that base metal has larger dislocation density as compared to FSPed zones made at different plunge depths. Dissolution of precipitate in the SZ is a major reason of a lower dislocation density in the zone. Among different plunge depths, slope corresponding to plunge depth of 2.95 mm is lower, while it is higher for 3.00 mm plunge depth. For 2.90 mm, the slope lies between the two. It can be concluded that the SZ made at 2.95 mm plunge depth exhibits lower dislocation density as compared to other plunge depths and hence a larger *n* value, while SZ made at the plunge depth of 2.9 mm has dislocation density in between that of 2.95 mm and 3 mm indicating moderate *n* value.

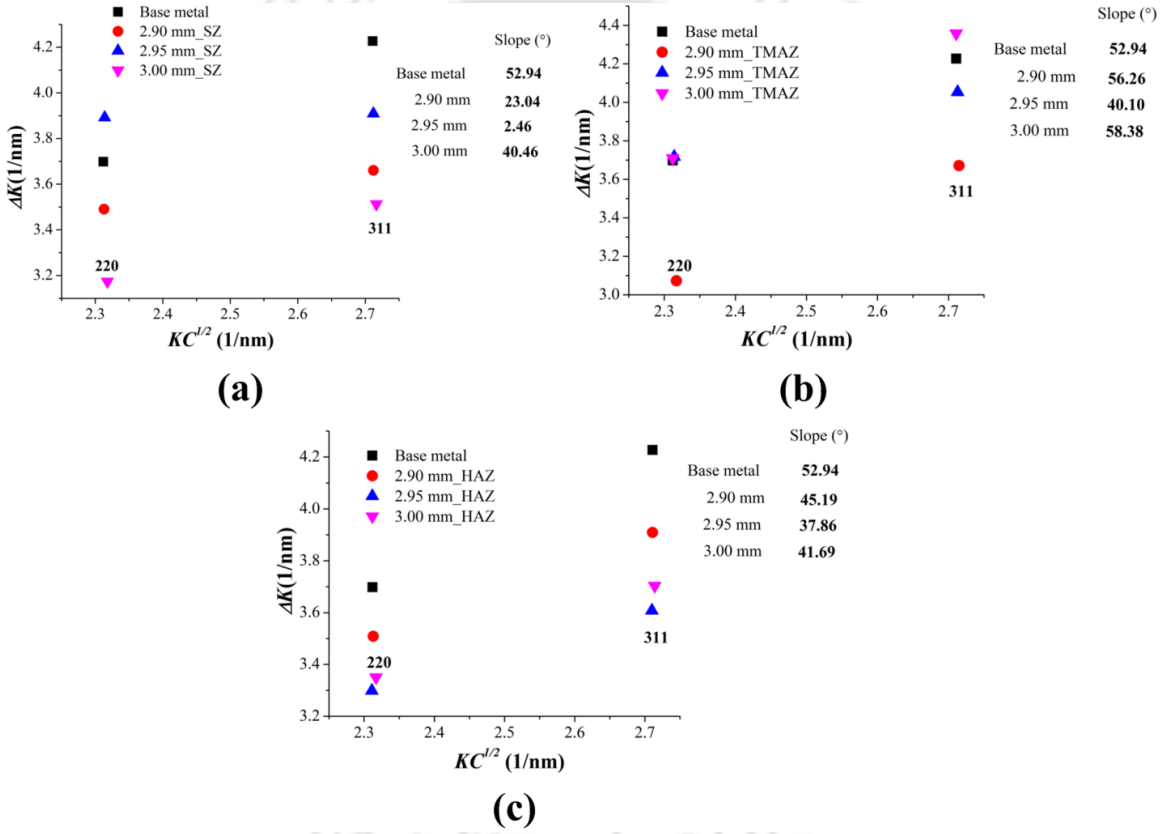

Fig. 7.8 Peak broadening analysis using the modified Williamson-Hall plot for (a) SZ, (b) TMAZ, (c) HAZ, of FSP zone. The FWHM (ΔK) in each (hkl) peak is presented as a function of $KC^{1/2}$ (K=2Sinθ/λ) and C is the dislocation contrast factor

TMAZ exhibits larger dislocation density as compared to base metal (Fig. 7.8b). Among plunge depths, lower dislocation density is observed for 2.95 mm plunge depth and higher dislocation density is observed for 3.00 mm plunge depth and hence *n* value is higher for 2.95 mm plunge depth as compared to 3.00 mm plunge depth. The dislocation density characteristics of TMAZ generated at a plunge depth of 2.9 mm fall in between.

The change in dislocation density with respect to different zones correlates with the change in *n* value in these zones. Similar results have been shown by Woo et al. (2008) during FSW of AA6061-T6 alloy. HAZ exhibits almost same dislocation density as that of base metal (Fig. 7.8c). Woo et al. (2008) presented similar results.

The dislocation density has been calculated according to equations 4.1 and 4.2 as described in section 4.1.3 in Chapter 4 and are shown in Table 7.6. SZ shows lower dislocation density in case of plunge depth of 2.95 mm and 3.00 mm as compared to base metal. In case of 2.90 mm plunge depth, it is closer to base metal. In TMAZ, in case of plunge depth of 2.90 mm, dislocation density is slightly less as compared to base metal. HAZ shows similar dislocation density as compared to base metal. Plunge depth of 2.95 mm generates SZ with larger *n* value because of considerable reduction in dislocation density. The dislocation density at 2.9 mm plunge depth is closer to that of base metal, and hence *n* is almost same as of base metal (Table 7.6 and Table 7.7).

Table 7.6 Dislocation density for base metal and for different zones

Plunge depth (mm)	ρ ($\times 10^{17}$ m^{-2})			Average ρ ($\times 10^{17}$ m^{-2}) in FSPed zone
	SZ	TMAZ	HAZ	
2.90	6.72	2.78	7.5	5.6±25
2.95	0.8	9.2	6.03	5.34±4
3.00	3.78	52	6.90	20±27
*ρ of base metal: 5.22±0.8 ($\times 10^{17}$ m^{-2})				

Table 7.7 H_c and *n* for base metal and FSPed zone at different plunge depths

Base metal/plunge depth	H_c	*n*
Base metal	0.96	0.30
2.90 mm	1.22	0.29
2.95 mm	1.36	0.33
3.00 mm	1.23	0.28

'H_c' and '*n*' are larger in case of plunge depth of 2.95 mm when compared with other cases (Table 7.7). This indicates that larger plastic deformation and ductility characterize the deformation in case of plunge depth 2.95 mm (Fig. 7.2). The FSPed zones made at 2.90 mm and 3.00 mm plunge depths behave almost same with H_c and *n* varying within a small range. However, the ductility is better in the case of 2.90 mm as depicted in Fig. 7.2 with slightly larger *n*.

7.2.3 End forming behaviour

7.2.3.1 Load-displacement behaviour

Load-displacement behaviour for different end forming operations and at different plunge depths are depicted in Figs. 7.9-7.11. For tube expansion larger load is observed in case of unprocessed tube because of larger strength as compared to FSPed tubes made at different plunge depths. The displacement at failure is also better in case of raw tube. In case of FSPed tubes, larger load is observed for plunge depth of 3.00 mm and smaller for plunge depth of 2.90 mm. Larger *H* is also observed in case of plunge depth of 3.00 mm, and is smaller in the case of plunge depth of 2.90 mm. Hence it can be said that, hardening index (*H*) during end expansion decides the maximum load requirement, rather than the raw mechanical properties of the FSPed zone. It is also believed that the enhanced ductility of the FSPed zone will enhance the failure levels of the FSPed tubes. But because of the edge cracking behaviour of FSPed zone, onset of instability occurs at an early stage, reducing its failure levels, as compared to the raw tube. Larger the failure load, larger is the displacement at failure (Fig. 7.9). This is true in case of FSPed tubes, and even when these are compared with raw tube, in case of tube expansion. When plunge depths are compared, larger the plunge depth, larger is the displacement at failure, indicating that a larger plunge depth is desirable for fabricating FSPed tubes, specifically for tube expansion applications.

In reduction, in case of processed tubes, larger load is observed in case of plunge depth of 2.95 mm and lower load in case of plunge depth of 3.00 mm (Fig. 7.10), but the variation is within a small range of ±5 kN. Load initially rises up to a displacement of 5 mm and after that remains almost constant up to a displacement of 10 mm. Within the displacement range, wrinkling occurs. Because of a softer FSPed zone, during wrinkling, material is pushed inwards. Material accumulation happens in this region circumferentially. As a result, at a later stage, overlapping occurs in this region. During wrinkling and overlapping, a constant and lower load levels are observed, and after that, the reduction process continues, increasing the load monotonically (Fig. 7.10a).

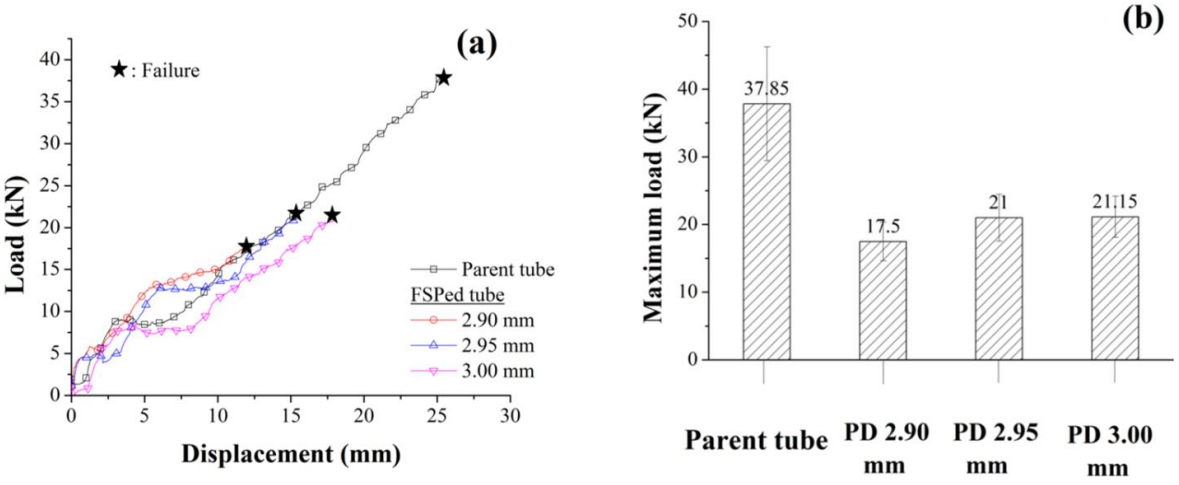

Fig. 7.9 (a) Load-displacement behaviour at different plunge depths, (b) maximum load for parent tube and FSPed tubes at different plunge depths for tube expansion

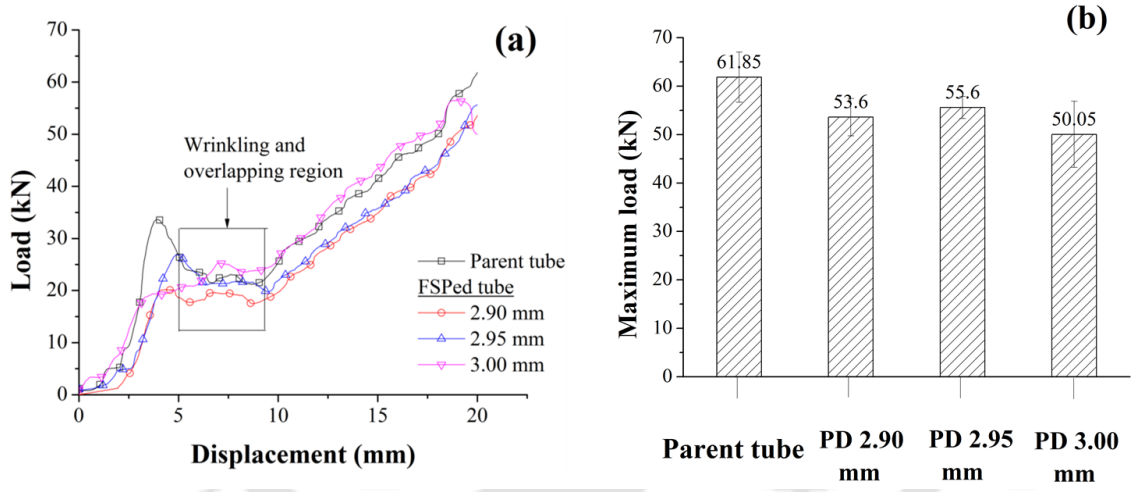

Fig. 7.10 (a) Load-displacement behaviour at different plunge depths, (b) maximum load for parent tube and FSPed tubes made at different plunge depths for tube reduction

Load increases continuously for parent tube and FSPed tubes made at different plunge depths till beading starts. Beading starts at a displacement of 3-5 mm (Fig. 7.11). The FSPed tubes bear lesser load at the same displacement when compared with the raw tube. This is because of the softer FSPed zones. After bead initiation, the load drops. But the gradient of load drop in case of parent tube is larger as compared to FSPed tubes. At the end of the load drop, at about 9 mm displacement, crack occurs. This indicates that crack initiation occurs at a lower load in case of raw tube as compared to FSPed tubes. All the FSPed tubes perform equally and at par with raw tube, when maximum load bearing ability is referenced. The performance varies within ±5 kN range.

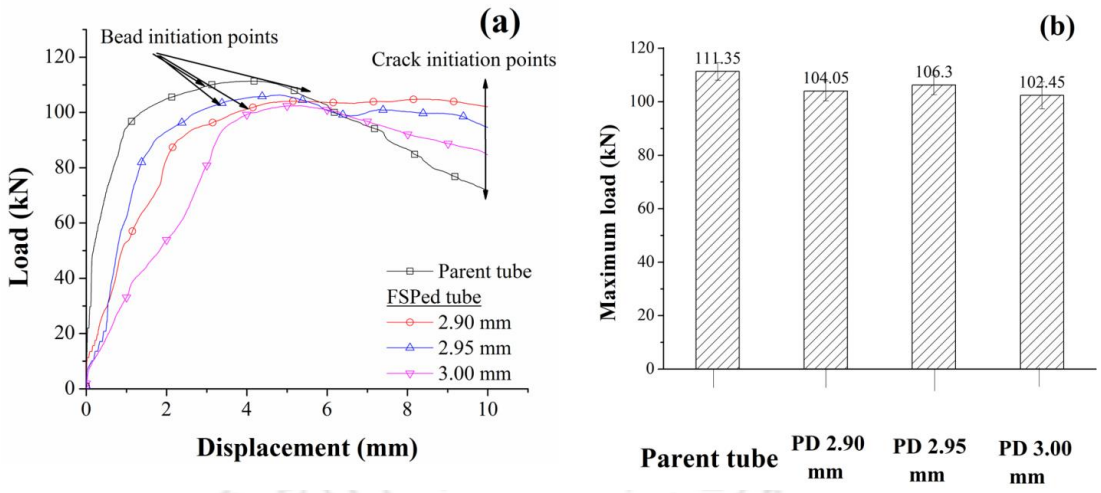

Fig. 7.11 (a) Load-displacement behaviour of the FSPed tubes made at different plunge depths, (b) maximum load for parent tube and FSPed tubes, for tube beading

7.2.3.2 Thickness evolution

Thickness evolution for unprocessed tubes, and for processed and unprocessed zones in processed tubes has been shown in Fig. 7.12. In case of end expansion, thinning is observed for processed and unprocessed zones in processed tubes as well as for raw tubes for different plunge depths (Fig. 7.12a). Thinning is severe for different processed zones. It is almost equal and larger for plunge depth 2.95 mm and 3.00 mm as compared to plunge depth 2.90 mm.

Thickening is observed for unprocessed tube as well as processed and unprocessed zones of processed tubes for different plunge depths in reduction (Fig. 7.12b). Processed zone thickening is more as compared to base metal thickening in the same tube. Because of overlapping phenomena thickening severity is more in processed zones as compared to unprocessed zones. FSPed zone corresponding to plunge depths 2.90 mm and 3.00 mm has thickened more as compared to plunge depth 2.95 mm.

Thickening is observed for unprocessed tube as well as processed and unprocessed zone of the processed tube for different plunge depths (Fig. 7.12c) except for processed zone made at plunge depth 3.00 mm where thinning is seen in case of beading. Base metal thickening is more for different plunge depths as compared to corresponding FSPed zones. Beading is a combination of bending and bulging operation. Initially the unsupported length of the tube bends and after that due to insufficient height of

unsupported length, tube bulges. Relative strength of processed and unprocessed zones decides the thickening or thinning of material in this case.

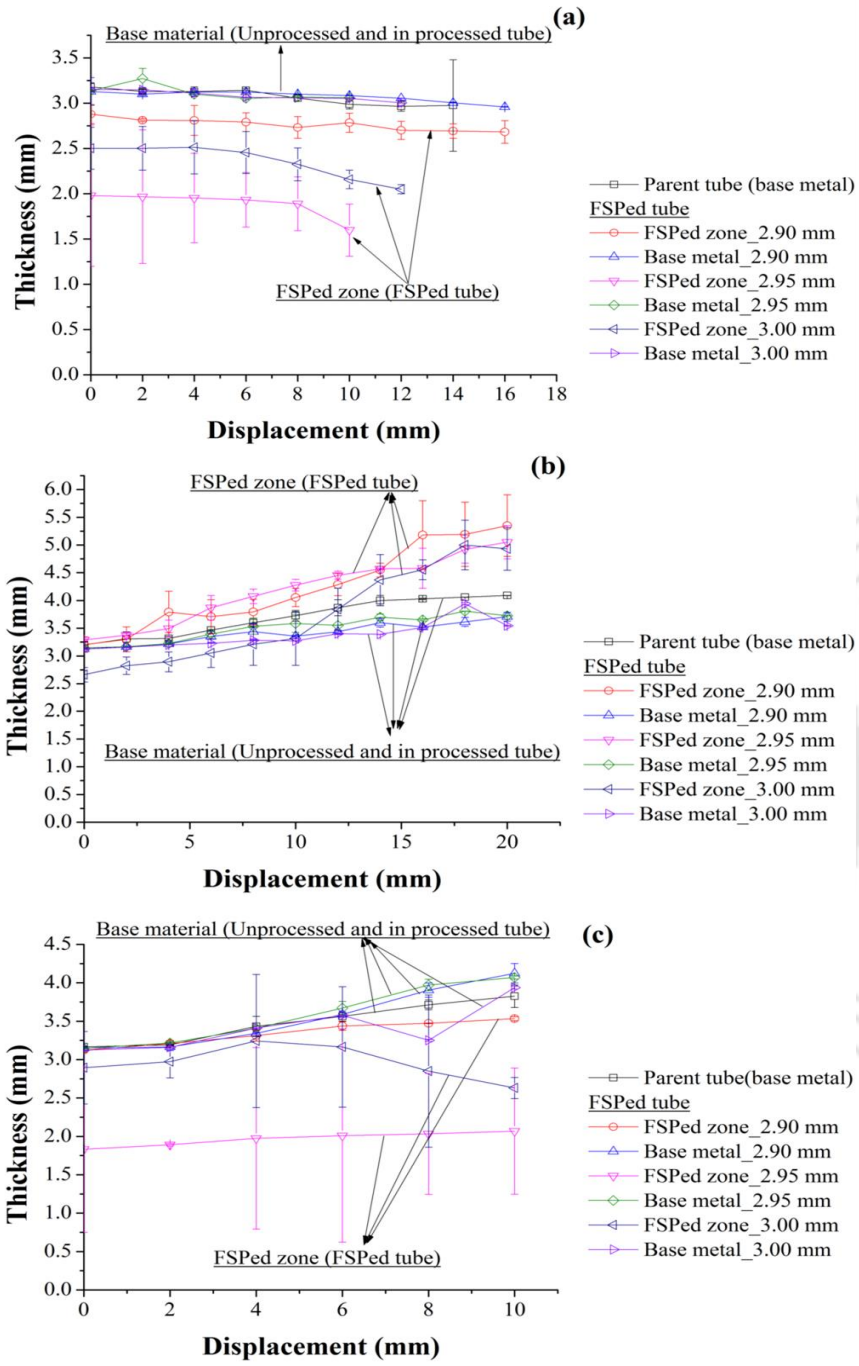

Fig. 7.12 Thickness evaluation in unprocessed tube and in processed zones and unprocessed zones of processed tubes in case of, (a) end expansion, (b) end reduction, and (c) end beading

7.2.4 Instabilities in end forming operations

During different end forming operations instabilities have been observed at all plunge depths. Tube fails mostly at the middle of the processed zone in case of expansion. A softer processed zone is more sensitive to circumferential stretching and hence failure is observed at the middle of the processed zone. For the processed tube the failure line is almost straight, while in case of unprocessed tube failure line is oblique (Fig. 7.13a). In case of end reduction wrinkling and overlapping has been observed in the middle of the weld zone. Material accumulation takes place in this zone and as a result of which wrinkling and overlapping is observed in this region. Wrinkling and overlapping is absent in the case of unprocessed tube (Fig. 7.13b). A harder base metal zone as well as more thickening in the base metal zone as compared to processed zone is responsible for crack generation in the base metal zone in case of end beading (Fig. 7.13c). In case of processed tube, cracks generated are of smaller sizes, while in case of unprocessed tubes cracks are larger.

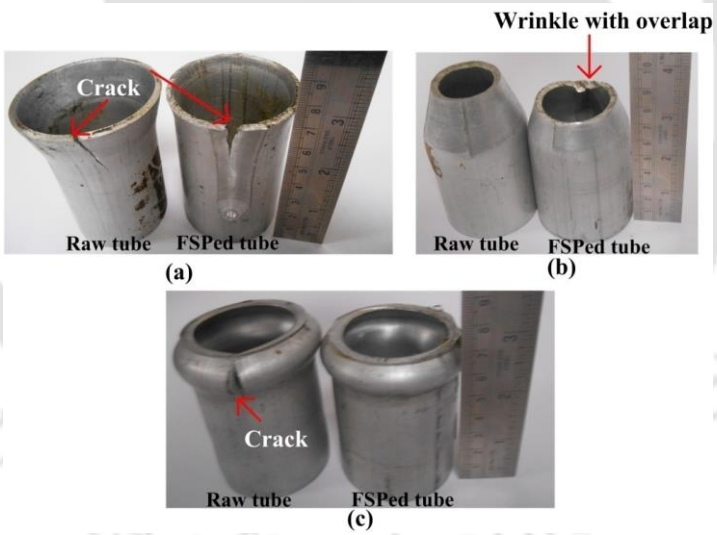

Fig. 7.13 Instabilities in, (a) end expansion, (b) end reduction, and (c) end beading

7.2.5 Energy absorbed during end forming

Energy absorbed for different plunge depths and end forming operations have been shown in Table 7.8. The energy absorbed by different end forming operations follows the following order: Beading > Reduction > Expansion. In case of beading of tubes, processed tubes are proved to be good energy absorbers as compared to unprocessed tubes except at the plunge depth of 3.00 mm. In tube reduction, FSPed tubes

perform at par with raw tube. Hence, FSPed tubes can be used as energy absorbers in case of beading and in reduction as compared to unprocessed tubes. However, plunge has to be optimized for achieving desirable performance. For tube expansion applications, the raw tubes are better as compared to FSPed tubes. Though this is the case, the plunge depth of 2.95 mm can be considered for FSP, while other FSP parameters can be optimized to enhance its applicability for end expansion applications. However, instability incurred during forming can be a problem and can restrict applications of FSPed tubes.

Table 7.8 Coefficients of load curve A, B, C and D, adjusting R-square, average thickness of tubes and specific energy absorbed for different cases

Plunge depths/Parent tube	A	B	C	D	Average thickness of tubes (mm)	Adj. R-square	Specific energy absorbed (*E*) (kJ/kg)
Expansion							
Parent tube	2.991	0.99503	0.01235	0.00012	3.18	0.99	14.68
2.90 mm	1.56946	2.80796	-0.1958	0.00558	3.00	0.98	9.40
2.95 mm	1.30203	2.43268	-0.19287	0.00778	2.56	0.95	11.70
3.00 mm	1.24908	1.61219	-0.1042	0.00443	2.83	0.96	9.71
Reduction							
Parent tube	-0.19024	6.93699	-0.6163	0.02171	3.20	0.90	23.90
2.90 mm	-1.52674	4.87166	-0.37545	0.01379	3.17	0.96	21.80
2.95 mm	-3.56093	6.76013	-0.57864	0.01962	3.22	0.95	20.10
3.00 mm	2.52897	3.97576	-0.19356	0.00088	2.89	0.97	25.50
Beading							
Parent tube	54.3099	36.5216	-6.71528	0.32739	3.17	0.92	74.74
2.90 mm	11.8851	46.1241	-7.25375	0.36091	3.14	0.98	73.93
2.95 mm	19.8741	48.9286	-8.4856	0.44443	2.49	0.92	93.70
3.00 mm	-3.47637	42.1787	-5.25529	-0.00923	0.19	0.98	30.55

7.2.6 Prediction of load and instability during end forming

It has been seen from Fig. 7.14 that after certain displacement thickness strain in safe region saturates, i.e., does not increase, while thickness strain in unsafe region increases. Here processed region is the region of instability. It can be seen that plunge depths of 2.90 mm and 2.95 mm fail at larger displacement as compared to 3 mm. 2.90 mm and 2.95 mm plunge depths have generated FSPed zones with larger *n* as compared to 3 mm, and hence larger displacement to failure is observed. Similarly, strain mapping for tube beading has been shown in Fig. 7.15. In this case both the safe and unsafe regions are in the unprocessed region of FSPed tube.

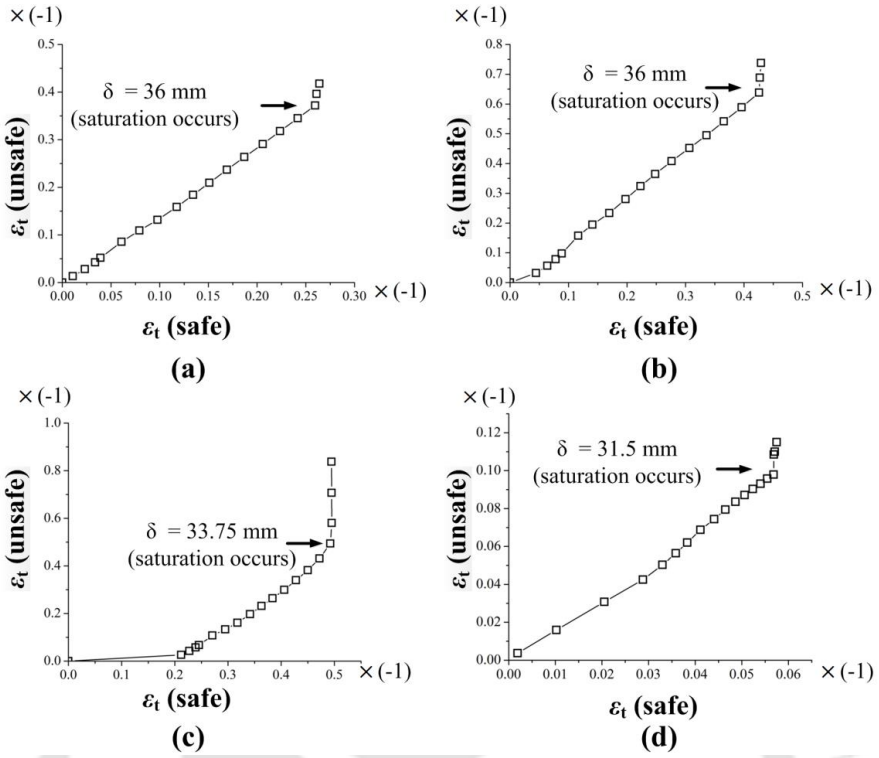

Fig. 7.14 Strain mapping method to predict instability during tube expansion, (a) plunge depth 2.90 mm, (b) plunge depth 2.95 mm, (c) plunge depth 3.00 mm, (d) base metal (thickness strain is actually negative, but shown as positive)

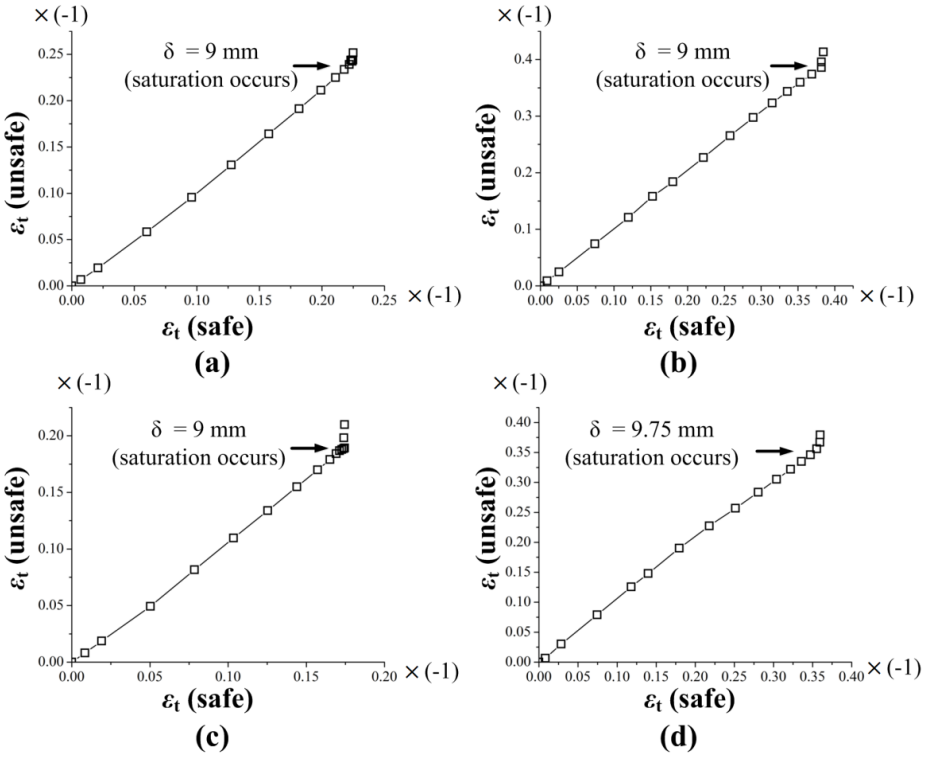

Fig. 7.15 Strain mapping method to predict instability during tube beading, (a) plunge depth 2.90 mm, (b) plunge depth 2.95 mm, (c) plunge depth 3.00 mm, and (d) base metal (thickness strain is actually negative, but shown as positive)

Table 7.9 summarizes the displacement at which instability occurs. In case of reduction and beading, the displacement at which instability occurs in prediction agrees well with the experimental data and the effect of plunge depth is insignificant. The same is observed in Fig. 7.10 and 7.11. A fair difference in displacement at failure is observed between experimental data and FE simulation prediction, in case of tube expansion. It is believed that modeling conditions, friction coefficient, boundary conditions etc. contribute to such difference in the prediction of instability in tube expansion.

Fig. 7.16 shows instabilities developed during simulations for different end forming operations in case of plunge depth 2.90 mm. Here images in case of expansion and beading is shown at that point where instability is seen. In reduction the image at last stage of displacement, i.e, 20 mm is shown. Wrinkle formation is very less in this case. Instabilities have been observed for other cases in the similar manner.

Table 7.9 Displacement at which instability occurs at varying plunge depths and end forming operations

Cases (Parent tube/plunge depths)	End expansion		End reduction		End beading	
	Displacement at which instability occurs (mm)					
	Experiment	Simulation	Experiment	Simulation	Experiment	Simulation
Parent tube	25.48	31.5	No wrinkle and overlap		8	9.75
2.90 mm	11.66	36	5	3	10	9
2.95 mm	15.37	36	4.5	4.5	10	9
3.00 mm	18.04	33.75	5	3	10	9

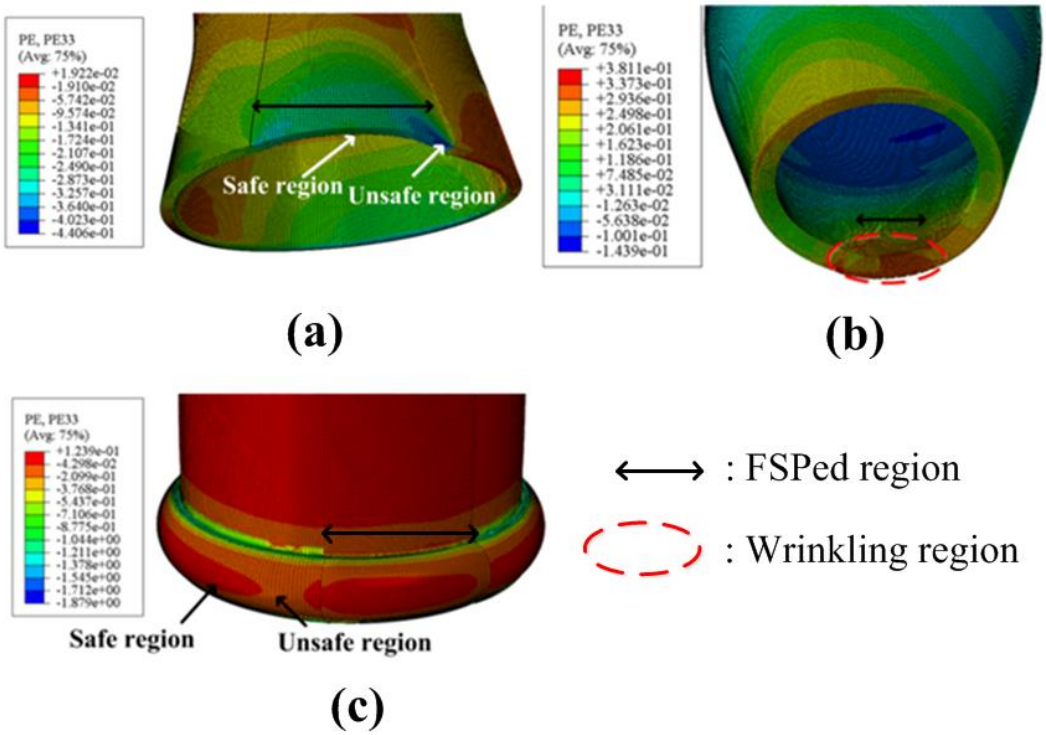

Fig. 7.16 Instabilities developed during simulations in case of plunge depth 2.90 mm, (a) end expansion, (b) end reduction, and (c) end beading

A comparison between experimental and numerical load curves for different plunge depths and end forming operations has been shown in Fig. 7.17. A fair agreement in load-displacement curves has been observed for experimental and numerical load curves for different plunge depths up to the displacement where tube fails in the experiment in case of expansion (Fig. 7.17a). In case of end reduction of tubes the load difference between experimental and numerical trials throughout the deformation process is minor for experimental and numerical trials with a slightly larger load in case of experiments as compared to simulations. The difference is larger in case of plunge depth 3 mm (Fig. 7.17b). In simulations, wrinkling occurs early as well as at a lower load as compared to experiments. Load evolution pattern in case of beading operation is significantly different for experimental and numerical trials for different cases after bead initiation process. Load increases at a rapid rate up to bead initiation for both experimental and numerical trials. In experimental trials, after bead initiation load either drops slightly or remains almost constant, whereas in simulation load increases monotonically up to the end of the process (Fig. 7.17c).

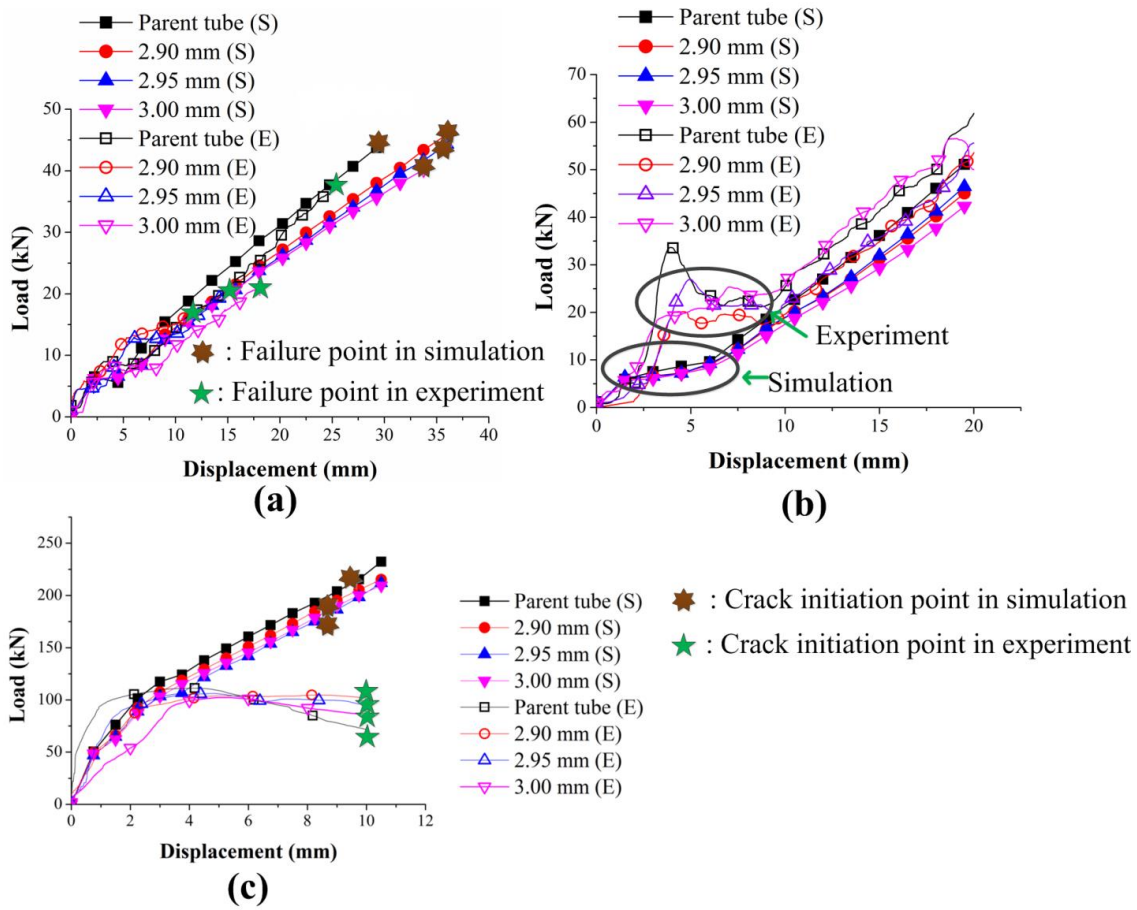

Fig. 7.17 Comparison between experimental and numerical load curves in case of, (a) end expansion, (b) end reduction, and (c) end beading (S: Simulation, E: Experiment)

7.3 Conclusions

End forming operation of friction stir processed aluminum tubes AA 6063-T6 have been performed successfully in the present work. End forming simulation has been conducted successfully and encouraging results have been obtained.

1. Flow strength of FSPed zone is lesser as compared to base metal. Ductility of FSPed zone improves in case of plunge depth 2.90 mm and 2.95 mm, while slightly decreases in case of plunge depth 3 mm. Among different plunge depths 2.95 mm shows largest flow strength as well as ductility.

2. Hardness of FSPed zone decreases after FSP, while increases after forming. The decrease is due to heat experienced in FSP process, while increase is due to strain hardening. Most ductile FSPed zone (2.95 mm) has got largest *n* and lowest dislocation density.

3. Largest hardening index, *H*(%) is observed in case of reduction as compared to other end forming operations for different plunge depths. Only exception is 2.95 mm, where it is slightly less than the maximum value. Plunge depth 2.90 mm shows lesser *H*(%) as compared to other plunge depths in different end forming operations.

4. Unprocessed tube needs larger load to deform as compared to FSPed tubes because of larger strength. *H*(%) is responsible for load evolution in processed tubes in expansion. A minor difference in load evolution is observed for different processed tube cases in reduction and beading. Though FSPed zone having larger strength, needed larger load to deform.

5. FSPed zone made at 2.95 mm has thinned more as compared to other plunge depths because of larger ductility. FSPed zone having lower flow strength has thickened more as compared to that of FSPed zone having larger flow strength. In beading FSPed zone made at 3 mm experiences thinning, while other FSPed zones experience almost equal thickening.

6. Beading absorbs larger energy as compared to expansion and reduction for raw and FSPed tubes. In beading, plunge depths 2.95 mm, while in reduction, plunge depth 3.00 mm absorbs larger energy than raw tube. In other cases comparable energy is absorbed between raw tubes and processed tubes during reduction and beading. In expansion parent tube absorbs larger energy than FSPed tubes.

7. Load evolution matches well in expansion and reduction, while in beading significant difference in load evolution is observed after bead initiation when experimental and predicted load data are compared. With respect to instability prediction FE simulation results and experimental results matches well in case of reduction and beading, while a difference is seen in expansion. Simulation strategy is the main cause for this difference.

Chapter 8

Conclusions and scope of future work

8.1 Conclusions

The following conclusions are drawn from the present work:

Joining of metallic structures

- A simple and novel method of joining a tube to a sheet through end curling has been proposed and the same has been successfully demonstrated in lab scale. Die groove radius and friction conditions are found to significantly affect the joint quality. The FE simulation results are validated with experimental results. Though good agreement has been obtained, it is suggested to incorporate a failure criterion in FE simulations to improve the prediction accuracy.
- Pull-out test for strength evaluation of end formed joint between a tube and a sheet at different angular planes has been conducted successfully and has been compared with the joints made by welding. The performance of end formed joint in terms of maximum load is better when flat die is used, while the welded joint performed better when inclined dies are used. 3D FE simulation of pull-out tests show a significant difference in load-displacement data between experiments and predictions. This implies that such models should be used cautiously for joint strength prediction.
- A novel method of joining of two steel tubes using tube end forming has been proposed based on FE simulations. Successful validation of the proposed joining method has been done experimentally through some selected cases. Circular arc radius and projected height of punch are found to significantly affect the joint quality. Predicted load evolution data matches well with experimental data. Strength evaluation of fabricated end formed joints has been compared with welded tube-tube joint. The strength of end formed joint compared well with welded joint. Later FE simulation of joining of longer tubes has been done to check the feasibility. It is suggested that it can be achieved by few minor modifications in the existing process.

Comparison of end forming of FSP tubes and raw tube during end forming

- End forming operations such as expansion, reduction and beading of FSP AA 6063-T6 tubes have been conducted at different tool rotational speeds, tool traverse speeds, tool pin profiles and tool plunge depths. Unprocessed tubes have larger strength as compared to processed tubes and hence need larger load to deform as compared to processed tubes during end forming. In expansion, thinning is larger in FSPed zone as compared to base metal. Processed zone having larger ductility shows larger thinning. For example, FSPed zone made at 1350 rpm tool rotational speed, 125 mm/min tool traverse speed, STP pin profile and 2.95 mm tool plunge depth possess larger ductility and hence undergoes larger thinning. In reduction, thickening is larger in FSPed zone as compared to base metal. A weaker processed zone has thickened more. In this context, FSPed zone made at 1200 rpm tool rotational speed, 75 mm/min tool traverse speed, TCP pin profile and 3 mm tool plunge depth experience larger thickening in respective cases. In beading, base metal thickening is larger as compared to FSPed zone for most of the cases. Relative strength of FSPed zone and base metal zone, and *n* value of FSPed zone and base metal zone are responsible for this. The effect of tool rotational speed and tool traverse speed on processed zone thickening and base metal thickening is insignificant. In case of different pin profiles, FSPed zone having lesser strength and corresponding base metal zone has thickened more, while in case of different plunge depths, FSPed zone made at plunge depth 3 mm thins down. In other cases for different plunge depths (processed zones and base metal zones) thickening is seen, though not following any trend.

- In expansion, parent tubes absorb larger energy during end forming as compared to FSPed tubes for different process parameters and their levels. In beading and reduction, the specific energy absorption by FSPed tubes varies within a close range as compared to that by parent tubes. End formed tubes, specifically in bead formation and reduction cases can potentially replace raw tube as energy absorbers in shipbuilding and aircraft industry. These tubes can also be utilized in minimizing damage in vehicles during crash conditions.

- Processed tubes mostly fails at the middle of the FSPed zone in end expansion, while wrinkling and overlapping is observed in the FSPed zone in end reduction.

A softer processed zone as compared to base metal zone is responsible for these instability in expansion and reduction. Strain hardening exponent of FSPed zone is responsible for displacement to failure in expansion in case of different rotational speeds, traverse speeds and pin profiles. Processed zone having larger *n* value needs larger displacement to failure in case of these parameters during expansion. In end beading, fine cracks are observed at the peak height of the bulged region in processed tubes. Larger hardness and reduced ductility of base metal as compared to FSPed zone is responsible for this. In unprocessed tube, during reduction, no wrinkling is observed, while in beading, crack size is larger in unprocessed tube as compared to processed tubes.

- A minor difference in experimental and predicted load-displacement data is observed in expansion and reduction of different cases. In beading, a significant difference in load value is observed after bead initiation for different process parameters between experimental and predicted load-displacement data. The displacement at which instability occurs, matches very well in reduction and beading for different cases between experimental and predicted data, while in expansion, a significant difference is seen.

Influence of FSP parameters on processed zone mechanical behaviour and end forming

- Strength of FSPed zone decreases with respect to base metal in all cases, while ductility of FSPed zone improves in many cases. Hardness decreases along the processed zone after FSP, while it improves in the processed zone during end forming. Slope of Willamson-Hall plot for dislocation density measurement in different zones of processed region correlates well with the '*n*' values of respective cases. In Willamson-Hall plot any material or region having larger slope possesses larger dislocation density. Further, a larger dislocation density is believed as the main reason for lower *n* value. In this context, tool rotational speed 1350 rpm, tool traverse speed 75 mm/min, tool pin profile TCP and tool plunge depth 3 mm possesses larger dislocation density and lower *n* in case of different rotational speeds, traverse speeds, pin profiles and plunge depths.

- Three different zones namely, stirred zone (SZ), thermomechanically affected zone (TMAZ), and heat affected zone (HAZ) have been identified according to the grain size. Different magnitude of plastic deformation and heat experienced at different zones are responsible for variation in grain size. No direct correlation is seen between grain size and hardness in different zones of processed region as the base metal is precipitation hardening type. SZ shows lower dislocation density as compared to other zones and base metal. The dislocation density in TMAZ is larger than SZ, HAZ and base metal in most of the cases. HAZ shows similar dislocation density as that of base metal. The results agree with available results.

- For tubes processed at different rotational speeds desirable mechanical properties are obtained at a tool rotational speed of 1350 rpm. The ductility in this case is better than the base metal. A combination of initial hardness and hardening index, *H*, of the FSPed zone is responsible for load evolution in case of expansion and reduction. FSPed zone having initial hardness and hardening index, *H*, lying in the moderate range yields larger maximum load among rotational speeds in these cases. The effect of rotational speed in case of beading is insignificant. A minor deviation of ±1.5 kN is observed in maximum load for different rotational speeds during beading. Here load drops for different cases after bead initiation.

- FSPed zone made at traverse speed of 125 mm shows better mechanical properties as compared to other FSPed zones. Infact, all the tensile properties improve with increase in traverse speed. The ductility in case of 125 mm/min traverse speed has improved with respect to base metal. With increase in traverse speed, maximum load requirement in FSPed tube increases for different end forming operations. However, in case of beading operation the maximum load requirement for different traverse speeds lies within a limit of ±1.5 kN. In beading, load drops for different cases after bead initiation up to the end of deformation process.

- FSPed zones made at different pin profiles exhibit larger ductility as compared to base metal. Better mechanical properties are obtained in case of STP as compared to TCP and SCP. Load requirement in processed tubes, in case of expansion and beading, depend on tensile strength of the processed zone in terms of maximum load requirement. In beading, load requirement remains almost same after beading starts and shows an increasing trend towards the end of deformation for processed

tubes only. In case of parent tube, load drops after beading starts. In case of reduction, load evolution with respect to different processed tube cases are almost similar with a minor deviation of ±1kN in maximum load requirement.

- Plunge depth of 2.95 mm exhibits desirable mechanical properties. Plunge depth 2.90 mm and 2.95 mm possess better ductility as compared to base metal. In different end forming operations the effect of plunge depth on load evolution is minor with a deviation of ±1.70 kN, ± 2.30 kN, ± 1.57 kN in maximum load in case of expansion, reduction and beading respectively. However, the load requirement in terms of maximum load depends on FSPed zone strength in reduction and beading, while in expansion it depends on hardening index. In beading, in processed tubes, load remains same after bead initiation till the end of reformation. In case of parent tube, load drops after beading starts.

8.2 Scope of future work

The following recommendations could be applied to future work in this area:

- In the present work, novel methods of joining of a tube to a sheet and a tube to a tube have been proposed. The workpiece material used here is 'steel'. In place of both workpiece materials as steel different materials can be tried. For example, tube material may belong to steel grade and sheet material may belong to aluminium grade or vice versa. Even polymers can be tried for joining.

- Joining of longer tubes have been proposed for which basic principle remains same as that of joining of shorter tubes. It has been shown that slight modification in the proposed method for joining of shorter tubes is good enough for joining of longer tubes also. However, the proposed method for joining of longer tubes need to be demonstrated experimentally.

- The work has been restricted by proposing methods for joining of a tube to a sheet and tube to a tube. The work can be extended further with some more methods of joining which will provide new understanding in the field of mechanical joining. Joining of rod to a sheet or a rod to a rod can be attempted.

- Analytical model for joining of a tube to a tube or a tube to a sheet can be developed. In this field, mathematical models for joining of tubes has been attempted which has not been included in the present thesis.

- 3D modelling for pull-out test of tube-sheet joints has been performed in the present work. The modelling method needs to be improved for the better accuracy of predicted result taking experiments as reference.

- FSP of tubes has been conducted in the present work. The experimental set-up needs to be simplified which can minimize the experimental efforts during FSP process.

- The effect of tool rotational speed, tool traverse speed, tool pin profile and tool plunge depth has been studied in the present work. Further there are other parameters such that tool tilt angle and axial load which effect can also be studied during FSP process.

- A single-line single-pass processing strategy of tubes has been adopted in the present work. The work can be extended to multi-line single-pass, single-line multi-pass or multi-line multi-pass processing of tubes.
- Hill's 1948 yield function has been used in the FE simulation of end forming of aluminium tubes. Anisotropic yield function meant for aluminium alloys like Barlat 89 or YLD2000 should be incorporated in the model for better results.
- Further, the predicted results through end forming simulations can be improved with proper implementation of strain rate and friction coefficient.

Appendix

Finite element discretization using Arbitrary Lagrangian Eulerian formulation (ALE)

The arbitrary Lagrangian Eulerian description is an extension of both classical Lagrangian and Eulerian ones. The grid points are not constrained to remain fixed in space (as in Eulerian description) or to move with material points (as in Lagrangian description), but have their own motion governing equations. In such a description, material points are represented by a set of Lagrangian coordinates $\vec{X}$, spatial points with a set of Eulerian coordinates $\vec{x}$ and reference points (grid points) with a set of arbitrary coordinates $\vec{\xi}$.

At time t, a special point $\vec{x}$ is simultaneously the image of a material point $\vec{X}$ by the material motion $\vec{x} = \vec{\Psi}(\vec{\xi}, t)$.

The material velocity $\vec{v}$ of the particles is obtained using a classical material $\dot{()}$ derivative, while the grid velocity $\vec{\hat{v}}$ is obtained after the introduction of a mixed $\ddot{()}$ derivative which must be interpreted as the "time" variation of a physical quantity for a given grid point.

$$\vec{v} = \dot{\vec{x}} = \frac{\partial \vec{x}}{\partial t}\Big|_{\vec{X}} = cte \text{ and } \vec{\hat{v}} = \ddot{\vec{x}} = \frac{\partial \vec{x}}{\partial t}\Big|_{\vec{\xi}} = cte \quad (1)$$

All physical quantities are computed at spatial points $\vec{x}$ and *t*. All observation laws must be expressed taking into account the grid motion during the simulation.

Conservation laws in ALE description

Conservative laws in a form almost identical to those of the Eulerian description is used. According to the following relation $\dot{()} = \ddot{()} + \vec{c}\,\Delta()$ where $\vec{c} = \vec{v} - \vec{\hat{v}}$ is the so-called convective velocity and Δ is the gradient operator, all Eulerian conservation laws (mass, momentum and energy) can be re-written according to the ALE description as following:

$$\ddot{\rho} + \vec{c}\,\Delta\rho + \rho\, div\, \vec{v} = 0 \quad (2)$$

$$\rho\,\ddot{\vec{v}} + \rho\,\vec{c}\,\Delta\vec{v} = \vec{f} + div\,\sigma \quad (3)$$

$$\rho\,\ddot{e} + \rho\,\vec{c}\,\Delta e = \sigma : D \quad (4)$$

Where ρ is the mass density, $\vec{f}$ are the body forces, σ is the Cauchy stress tensor, e is the specific internal energy, D is the strain rate tensor. In such a description, the ALE form may be considered as an automatic and continuous re-zoning method.

Spatial discretization

In finite element approximation, all dependent variables are defined as functions of element coordinates. The ALE domain is subdivided into elements and for element *e*, the ALE coordinates are given by $\xi = \xi_1 N_1$ where *N* are the geometrical shape functions of element *e*. In view of spatial discretization of mass, momentum and energy equations (2)-(4) by the finite element method, a classic variational form is obtained by multiplying these equations respectively by a set of weighing function (ρ^*, v_i^*, e^*) over the spatial domain R_x. Employing the divergence theorem, the variational forms associated with these equations, and finally, using the Galerkin approach, one obtain the corresponding discretized equations,

$$M^\rho \ddot{\rho} + L^\rho \rho + K^\rho \rho = 0 \quad (5)$$

$$M^v \ddot{v} + L^v v + f^{int} = f^{ext} \quad (6)$$

$$M^e \ddot{e} + L^e e = r \quad (7)$$

where M^ρ, M^v, M^e are the generalized mass matrices for corresponding variables in (5)-(7) respectively; L^ρ, L^v, L^e are the generalized convective matrices: K^ρ is the stiffness matrix for density; f^{int} is the internal force vector; f^{ext} is the external force vector; *r* is the generalized energy source vector.

Four nodes quadrilateral elements with a reduced integration scheme have been used for the discretization of the problem in 2D simulations while 8 node brick elements with also a reduced integration scheme are used in 3D.

References

Abaqus/Expicit: Advanced topics (Lecture 2) Copyright 2005 ABAQUS, Inc.

Abramowicz, W., Jones, N., 1984. Dynamic axial crushing of circular tubes. International Journal of Impact Engineering. 2, 263-281

Ahmad, Z., Thambiratnam, D.P., 2009a. Crushing response of foam-filled conical tubes under quasi-static axial loading. Materials and Design. 30, 2393-2403

Ahmad, Z., Thambiratnam, D.P., 2009b. Dynamic computer simulation and energy absorption of foam-filled conical tubes under axial impact loading. Computers and Structures. 87, 186-197

Ahmed, S., Saha, P., 2018. Development and testing of fixtures for friction stir welding of thin aluminium sheets. Journal of Materials Processing Technology. 252, 242-248

Ahmed, S., Shubhrant, A., Deep, A., Saha, P., 2015. Development and analysis of butt and lap welds in micro-friction stir welding (μFSW). In: Narayanan, R.G., Dixit, U.S. (Eds.), Advances in Material Forming and Joining, 5th International and 26th All India Manufacturing Technology, Design and Research Conference, AIMTDR 2014, Springer, New Delhi, India, 295-306

Aktarer, S.M., Sekban, D.M., Kuckomeroglu, T., Pursek, G., 2019. Microstructure, mechanical properties and formability of friction stir welded dissimilar materials of IF-steel and 6061 Al alloy. International Journal of Minerals, Metallurgy and Materials. 26(6), 722-731

Al-Fadhalah, K.J., Almazrouee, A.I., Aloraier, A.S., 2014. Microstructure and mechanical properties of multi-pass friction stir processed aluminum alloy 6063. Materials and Design. 53, 550-560

Almeida, B.P.P., Alves, M.L., Rosa, P.A.R., Brito, A.G., Martins, P.A.F., 2006. Expansion and reduction of thin-walled tubes using a die: experimental and theoretical investigation. International Journal of Machine Tools and Manufacture. 46, 1643-1652

Alves, L.M., Gameiro, J., Silva, C.M.A., Martins, P.A.F., 2017a. Sheet-bulk forming of tubes for joining applications. Journal of Materials Processing Technology. 240, 154-161

Alves, L.M., Afonso, R.M., Silva, C.M.A., Martins, PA.F., 2018a. Joining tubes to sheets by boss forming and upsetting. Journal of Materials Processing Technology. 252, 773-781

Alves, L.M., Afonso, R.M., Silva, C.M.A., Martins, P.A.F., 2018b. Joining sandwich composite panels to tubes. Proceedings of the Institution of Mechanical Engineers, Part L: Journal of Materials: Design and Applications.0(0), 1-10

Alves, L.M., Silva, M.B., Martins, P.A.F., 2011a. Fabrication of small size seamless reservoirs by tube forming. International Journal of Pressure Vessels and Piping. 88, 239-247

Alves, L.M., Afonso, R.M., Silva, C.M.A., Martins, P.A.F., 2017b. Boss forming of annular flanges in thin-walled tubes. Journal of Materials Processing Technology. 250, 182-189

Alves, L.M., Martins, P.A.F., 2009. Understanding invert forming of thin-walled ploy vinyl chloride tubes using a die based on mechanical flow formulation. Materials and Manufacturing Processes. 24, 1398-1404

Alves, L.M., Martins, P.A.F., 2013. Single-stroke mechanical joining of sheet panels to tubular profiles. Journal of Manufacturing Processes. 15, 151-157

Alves, L.M., Martins, PA.F., 2010. Forming of thin-walled tubes into toroidal shells. Journal of Materials Processing Technology. 210, 689-695

Alves, L.M., Nielsen, C.V., Silva, C.M.A., Martins, PA.F., 2017c. Joining end-to-end tubing of dissimilar materials by forming. International Journal of Pressure Vessels and Piping. 149, 24-32

Alves, L.M., Pardal, T.C.D., Martins, P.A.F., 2010. Nosing thin-walled tubes into axisymmetric seamless reservoirs using recyclable mandrels. Journal of Cleaner Production. 18, 1740-1749

Alves, L.M., Pimentel, M.M., Silva, C.M.A., Martins, P.A.F., 2018c. Towards joining by plastic buckling of hollow polyvinylchloride profiles. Proceedings of the Institution of Mechanical Engineers, Part L: Journal of Materials: Design and Applications. 232(7), 592-601

Alves, L.M., Silva, C.M.A., Martins, P.A.F., 2017d. Joining of tubes by internal mechanical locking. Journal of Materials Processing Technology. 242, 196-204

Alves, L.M., Silva, C.M.A., Martins, PA.F., 2014. End-to-end joining of tube by plastic instability. Journal of Materials Processing Technology. 214, 1954-1961

Alves, L.M., Dias, E.J., Martins, P.A.F., 2011b. Joining sheet panels to thin-walled tubular profiles by tube end forming. Journal of Cleaner Production. 19, 712-719

Alves, M.L., Almeida, B.P.P., Rosa, P.A.R., Martins, P.A.F., 2006. End forming of thin-walled tubes. Journal of Materials Processing Technology. 177, 183-187

Arab, S.M., Jahromi, S.A.J., Zebarjad, S.M., 2016. The effect of friction stir processing by stepped tools on the microstructure, mechanical properties and wear behaviour of a Mg-Al-Zn alloy. Journal of Materials Engineering and Performance. 25, 4587-4597

Aval, H.J., 2015. Influence of pin profile on the mechanical and microstructural behaviors in dissimilar friction stir welded AA6082-AA7075 butt joint. Materials and Design. 67, 413-421

Azarakhsh, S., Ghamarian, A., 2017. Collapse behaviour of thin-walled conical tube clamped at both ends subjected to axial and oblique loads. Thin-Walled Structures. 112, 1-11

Balasubramanian, V., 2008. Relationship between base metal properties and friction stir welding process parameters. Materials Science and Engineering A. 480, 397-403

Banabic, D., 2010. Sheet metal forming processes: constitutive modelling and numerical simulation, Springer-Verlag Berlin Heidelberg, pp. 45-52

Barcellona, A., Buffa, G., Fratini, L., Palmeri, D., 2006. On microstructural phenomena occurring in friction stir welding of aluminium alloys. Journal of Materials Processing Technology. 177, 340-343

Barenji, R.V., 2016. Effect of tool traverse speed on microstructure and mechanical performance of friction stir welded 7020 aluminum alloy. Proceedings of the Institution of Mechanical Engineers, Part L: Journal of Materials: Design and Applications. 230(2), 663-673

Behnagh, R.A., Givi, M.K.B., Akbari, M., 2012. Mechanical properties, corrosion resistance, and microstructural changes during friction stir processing of 5083 aluminum rolled plates. Materials and Manufacturing Processes. 27, 636-640

Buffa, G., Ducato, A., Fratini, L., 2011. Numerical procedure for residual stresses prediction in friction stir welding. Finite Elements in Analysis and Design. 47, 470-476

Buffa, G., Hua, J., Shivpuri, R., Fratini, L., 2006. Design of friction stir welding tool using the continuum based FEM model. Materials Science and Engineering A. 419, 381-388

Carlone, P., Palazzo, G.S., 2013. Influence of process parameters on microstructure and mechanical properties in AA2024-T3 friction stir welding. Metallography, Microstructure, and Analysis. 2, 213-222

Charit, I., Mishra, R.S., 2003. High strain rate superplasticity in a commercial 2024 Al alloy via friction stir processing. Materials Science and Engineering A. 359, 290-296

Chen, B., Chen, K., Hao, W., Liang, Z., Yao, J., Zhang, L., Shan, A., 2015. Friction stir welding of small-dimension Al3003 and pure Cu pipes. Journal of Materials Processing Technology. 223, 48-57

Chen, C.M., Kovacevic, R., 2003. Finite element modeling of friction stir welding-thermal and thermomechanical analysis. International Journal of Machine Tools and Manufacture. 43, 1319-1326

Chen, Y.C., Fujii, H., Tsumura, T., Kitagawa, Y., Nakata, K., Ikeuchi, K., Matsubayashi, K., Michishita, Y., Fujiya, Y., Katoh, J., 2009. Friction stir processing of 316L stainless steel plate. Science and Technology of Welding and Joining. 14(3), 197-201

Choi, W.M., Kwon, T.S., Jung, H.S., Kim, J.S., 2012. Influence of impact velocity on energy absorption characteristics and friction coefficient of expansion tube. International Journal of Crashworthiness. 17(6), 621-629

Colegrove, P.A., Shercliff, H.R., 2003. Experimental and numerical analysis of aluminium alloy 7075-T7351 friction stir welds. Science and Technology of Welding and Joining. 8(5), 360-368

Colegrove, P.A., Shercliff, H.R., 2005. 3-Dimensional CFD modelling of flow round a threaded friction stir welding tool profile. Journal of Materials Processing Technology. 169, 320-327

Cui, L., Yang, X., Xie, Y., Hou, X., Song, Y., 2013. Process parameter influence on defects and tensile properties of friction stir welded T-joints on AA6061-T4 sheets. Materials and Design. 51, 161-174

Cui, S., Chen, Z.W., Robson, J.D., 2010. A model relating tool torque and its associated power and specific energy to rotation and forward speeds during friction stir welding/processing. International Journal of Machine Tools and Manufacture. 50, 1023-1030

Daxner, T., Rammerstorfer, F.G., Fischer, F.D., 2005. Instability phenomena during the conical expansion of circular cylindrical shells. Computer methods in Applied Mechanics and Engineering. 194, 2591-2603

Dehghani, M., Amadeh, A., Mousavi, S.A.A.A., 2013. Investigations on the effects of friction stir welding parameters on intermetallic and defect formation in joining aluminum alloy to mild steel. Materials and Design. 49, 433-441

Dhal, A., Panigrahi, S.K., Shunmugam, M.S., 2017. Insight into the microstructural evolution during cryo-severe plastic deformation and post-deformation annealing of aluminum and its alloys. Journal of Alloys and Compounds. 726, 1205-1219

DiPaolo, B.P., Tom, J.G., 2009. Effects of ambient temperature on a quasi-static axial-crush configuration response of thin-wall, steel-box components. Thin-walled structures. 47, 984-997

Dutkiewicz, J., Litynska, L., 2002. The effect of plastic deformation on structure and properties of chosen 6000 series aluminium alloys. Materials Science and Engineering A. 324, 239-243

Elangovan, K., Balasubramanian, V., 2008. Influence of tool pin profile and tool shoulder diameter on the formation of friction stir processing zone in AA6061 aluminium alloy. Materials and Design. 29, 362-373

Elangovan, K., Balasubramanian, V., Valliappan M., 2008a. Effect of tool pin profile and tool rotational speed on mechanical properties of friction stir welded AA6061 aluminium alloy. Materials and Manufacturing Processes. 23, 251-260

Elangovan, K., Balasubramanian, V., Valliappan, M., 2008b. Influences of tool pin profile and axial force on the formation of friction stir processing zone in AA 6061 aluminum alloy. The International Journal of Advanced Manufacturing Technology. 38, 285-295

El-Domiaty, A., 1997. Curling of thin tubes: analytical and experimental study. Journal of Materials Engineering and Performance. 6(4), 481-495

El-Rayes, M.M., El-Danaf, E.A., 2012. The influence of multi-pass friction stir processing on the microstructural and mechanical properties of aluminum alloy 6082. Journal of Materials Processing Technology. 212, 1157-1168

Fratini, L., Buffa, G., 2005. CDRX modelling in friction stir welding of aluminium alloys. International Journal of Machine Tools and Manufacture. 45, 1188-1194

Ghamarian, A., Zarei, H.R., Abadi, M.T., 2011. Experimental and numerical crashworthiness investigation of empty and foam-filled end-capped conical tubes. Thin-Walled structures. 49, 1312-1319

Golezani, A.S., Barenji, R.V., Heidarzadeh, A., Pouraliakbar, H., 2015. Elucidating of tool rotational speed in friction stir welding of 7020-T6 aluminum alloy. The International Journal of Advanced Manufacturing Technology. 81, 1155-1164

Goncalves, A., Alves, L.M., Martins, P.A.F., 2014. Inclined tube-sheet plastically deformed joints. Steel Research International. 85(1), 67-75

Gouveia, B.P.P., Alves, M.L., Rosa, P.A.R., Martins, PA.F., 2006. Compression beading and nosing of thin-walled tubes using a die: experimental and theoretical investigation. International Journal of Mechanics and Materials in Design. 3, 7-16

Guo, J., Zhao, S., Murakami, R-I., Ding, R., Fan, S., 2013. Modeling the hot deformation behavior of Al alloy 3003. Journal of Alloys and Compounds. 566, 62-67

Gupta, P.K., Sahu, R.R., 2013. Experimental and numerical studies on the tube contraction using a conical-cylindrical die. The Journal of Strain Analysis for Engineering Design. 48(8), 482-493

Hariri, M.B., Shiri, S.G., Yaghoubinezhad, Y., Rahvard, M.M., 2013. The optimum combination of tool rotational rate and traveling speed for obtaining the preferable corrosion behavior and mechanical properties of friction stir welded AA5052 aluminum alloy. Materials and Design. 50, 620-634

Hashmi, M.S.J., 2006. Aspects of tube and pipe manufacturing processes: meter to nanometer diameter. Journal of Materials Processing Technology. 179, 5-10

Heidler, N., Schenk, C., Harnisch, G., Risse, S., Schubert, G., Eberhardt, R., Tunnermann, A., 2012. Contact-free exhaust system for vacuum compatible gas bearing guides. Precision Engineering. 36, 37-43

Hollomon, J,H., 1945. Tensile deformation. Transaction of American Institute of Mechanical Engineering. 162, 268–277

Hollomon, J.H., Jaffe, L.D., 1947. Ferrous metallurgical design: design principles for fully hardened steel. J. Wiley &Sons, Inc., New York. 84-85

Hu, Z.L., Wang, X.S., Pang, Q., Huang, F., Qin, X.P., Yuan, S.J., Hua, L., 2015. Experimental and numerical study on hydroforming characteristics of friction stir welded aluminum alloy tubes. The International Journal of Advanced Manufacturing Technology. 80, 959-969

Hua, F.A., Yang, Y.S., Zhang, Y.N., Guo, M.H., Guo, D.Y., Tong, W.H., Hu, Z.Q., 2005. Three-dimensional finite element analysis of tube spinning. Journal of Materials Processing Technology. 168, 68-74

Huang, X., Lu, G., Yu, T. X., 2002. On the axial splitting and curling of circular metal tubes. International Journal of Mechanical Sciences. 44, 2369-2391

Huang, Y.-M., Huang, Y.-M., 2001. Elasto-plastic finite-element analysis of the axisymmetric tube-flaring process with conical punch. The International Journal of Advanced Manufacturing Technology. 18, 390-398

Hwang, Y-M., Kang, Z-W., Chiou, Y-C., Hsu, H-H., 2008. Experimental study on temperature distributions within the workpiece during friction stir welding of aluminum alloys. International Journal of Machine Tools and Manufacture. 48, 778-787

Imam, M., Biswas, K., Racherla, V., 2013. Effect of weld morphology on mechanical response and failure of friction stir welds in a naturally aged aluminium alloy. Materials and Design. 44, 23-34

Jafarian, N., Rezvani, M.J., 2019. Crushing behavior of multi-component conical tubes as energy absorber: A comparative analysis between end-capped and non-capped conical tubes. Engineering Structures. 178, 128-135

Jeswiet, J., Geiger, M., Engel, U., Kleiner, M., Schikorra, M., Duflou, J., Neugebauer, R., Bariani, P., Bruschi, S., 2008. Metal forming progress since 2000. CIRP Journal of Manufacturing Science and Technology. 1, 2-17

Jianguo, Y., Makoto, M., 2005. An experimental study on spinning of taper shape on tube end. Journal of Materials Processing Technology. 166, 405-410

Juijerm, P., Altenberger, I., Scholtes, B., 2006. Fatigue and residual stress relaxation of deep rolled differently aged aluminium alloy AA6110. Materials Science and Engineering A. 426, 4-10

Kang, S.H., Vasudevan, M., Noh, S., Jin, H.J., Jang, J., Kim, T.K., 2016. Friction stir welding of F/M ODS steel plug and F/M ODS steel tube. Fusion Engineering and Design. 109-111, 182-185

Karajibani, E., Fazli, A., Hashemi, R., 2015. Numerical and experimental study of formability in deep drawing of two-layer metallic sheets. The International Journal of Advanced Manufacturing Technology. 80, 113-121

Karrech, A., Seibi, A., 2010. Analytical model for the expansion of tubes under tension. Journal of Materials Processing Technology. 210, 356-362

Khan, N.Z., Siddiquee, A.N., Khan, Z.A., Shihab, S.K., 2015. Investigations on tunnelling and kissing bond defects in FSW joints for dissimilar aluminum alloys. Journal of Alloys and Compounds. 648, 360-367

Khodabakhshi, F., Arab, S.M., Svec, P., Gerlich, A.P., 2017. Fabrication of a new Al-Mg/graphene nanocomposite by multi-pass friction-stir processing: dispersion, microstructure, stability and strengthening. Materials Characterization. 132, 92-107

Kim, D-K., Lee, S., 1999. Impact energy absorption of 6061 aluminum extruded tubes with different cross-sectional shapes. Materials and Design. 20, 41-49

Kim, Y.G., Fujii, H., Tsumura, T., Komazaki, T., Nakata, K., 2006. Three defect types in friction stir welding of aluminum die casting alloy. Materials Science and Engineering A. 415, 250-254

Kitamura, K., Hirota, K., Ukai, Y., Matsunaga, K., Osakada, K., 2012. Cold joining of rotor shaft with flange by using plastic deformation. CIRP Annals-Manufacturing Technology. 61, 275-278

Kitazawa, K., 1993. Criteria for outward curling of tubes. Transactions of the ASME. 115, 466-471

Kumar, K., Kailas, S.V., 2008. The role of friction stir welding tool on material flow and weld formation. Materials Science and Engineering A. 485, 367-374

Kumar, K., Kailas, S.V., Srivatsan, T.S., 2008. Influence of tool geometry in friction stir welding. Materials and Manufacturing Processes. 23(2), 188-194

Kumar, S., 2008. Technology of metal forming processes, Prentice-Hall of India Private Limited, New Delhi, pp. 57-58

Kurt, A., Uygar, I., Cete, E., 2011. Surface modification of aluminium by friction stir processing. Journal of Materials Processing Technology. 211, 313-317

Lammlein, D.H., Gibson, B.T., DeLapp, D.R., Cox, C., Strauss, A.M., Cook, G.E., 2011. The friction stir welding of small-diameter pipe: an experimental and numerical proof of concept for automation and manufacturing. Proceedings of the Institution of Mechanical Engineers, Part B: Journal of Engineering Manufacture. 226, 383-398

Leal, R.M., Leitao, C., Loureiro, A., Rodrigues, D.M., Vilaca, P., 2008. Material flow in heterogeneous friction stir welding of thin aluminium sheets: effect of shoulder geometry. Materials Science and Engineering A. 498, 384-391

Leal, R.M., Loureiro, A., 2008. Effect of overlapping friction stir welding passes in the quality of welds of aluminium alloys. Materials and Design. 29, 982-991

Lee, S.H., Saito, Y., Sakai, T., Utsunomiya, H., 2002. Microstructures and mechanical properties of 6061 aluminum alloy processed by accumulative roll - bonding. Materials Science and Engineering A. 325, 228-235

Lee, W-S., Huang, Y-C., 2016. Mechanical properties and dislocation substructure of 6061-T6 aluminum alloy impacted at cryogenic temperatures. Materials Transactions. 57(3), 344-350

Leu, D-K., 2000. The curling characteristics of static inside-out inversion of metal tubes. International Journal of Machine Tools and Manufacture. 40, 65-80

Li, B., Nye, T.J., Wu, P.D., 2010. Predicting the forming limit diagram of AA 5182-O. The Journal of Strain Analysis for Engineering Design. 45, 255-273

Liu, X., Lan, S., Ni, J., 2014. Analysis of process parameters effects on friction stir welding of dissimilar aluminium alloy to advanced high strength steel. Materials and Design. 59, 50-62

Lu, Y-H., 2004. Study of tube flaring ratio and strain rate in the tube flaring process. Finite elements in Analysis and Design. 40, 305-318

Luo, Y.H., Huang, Z.W., Zhang, X.L., 2007. FEM analysis of external inversion and energy absorbing characteristics of inverted tubes. Journal of Materials Processing Technology. 187-188, 279-282

Ma, Z.Y., Sharma, S.R., Mishra, R.S., 2006. Effect of friction stir processing on the microstructure of cast A356 aluminum. Materials Science and Engineering A. 433, 269-278

Maamoun, A.H., Veldhuis, S.C., Elbestawi, M., 2019. Friction stir processing of AlSi10Mg parts produced by selective laser melting. Journal of Materials Processing Technology. 263, 308-320

Maggiolini, E., Tovo, R., Susmel, L., James, M.N., Hattingh, D.G., 2016. Crack path and fracture analysis in FSW of small diameter 6082-T6 aluminum tubes into tension-torsion loading. International Journal of Fatigue. 92, 478-487

Mandal, S., Rice, J., Elmustafa, A.A., 2008. Experimental and numerical investigation of the plunge stage in friction stir welding. Journal of Materials Processing Technology. 203, 411-419

Masmoudi, M., Ketata, H., Krichen, A., 2016. External curling process of thin tubes: finite element and experimental investigation. The International Journal of Advanced Manufacturing Technology. 87, 3169-3184

Mastanaiah, P., Sharma, A., Reddy, G.M., 2018. Role of hybrid tool pin profile on enhancing welding speed and mechanical properties of AA2219-T6 friction stir welds. Journal of Materials Processing Technology. 257, 257-269

Mehta, K.P., Badheka, V.J., 2015. Influence of tool design and process parameters on dissimilar friction stir welding of copper to AA 6061-T651 joints. The International Journal of Advanced Manufacturing Technology. 80, 2073-2082

Mehta, K.P., Badheka, V.J., 2016. Effects on tilt angle on the properties of dissimilar friction stir welding copper to aluminum. Materials and Manufacturing Processes. 31, 255-263

Mehta, K.P., Badheka, V.J., 2017. Hybrid approaches of assisted heating and cooling for friction stir welding of copper to aluminum joints. Journal of Materials Processing Technology. 239, 336-345

Mishra, R.S., Ma, Z.Y., 2005. Friction stir welding and processing. Materials Science and Engineering R. 50, 1-78

Mishra, R.S., Ma, Z.Y., Charit, I., 2003. Friction stir processing: a novel technique for fabrication of surface composite. Materials Science and Engineering A. 341, 307-310

Mishra, R.S., Mahoney, M.W., 2001. Friction stir processing: a new grain refinement technique to achieve high strain rate superplasticity in commercial alloys. Materials Science Forum. 357-359, 507-514

Mohamed, F.A., El-Abden, S.Z., Abdel-Rahman, M., 2005. A rotary flange forming process on the lathe using a ball-shaped tool. Journal of Materials Processing Technology. 170, 501-508

Mohebbi, M.S., Akbarzadeh, A., 2010. Experimental study and FEM analysis of redundant strains in flow forming of tubes. Journal of Materials Processing Technology. 210, 389-395

Moreira, P.M.G.P., Oliveira, F.M.F.D., De Castro, P.M.S.T., 2008. Fatigue behaviour of notched specimens of friction stir welded aluminum alloy 6063-T6. Journal of Materials Processing Technology. 207, 283-292

Moshwan, R., Yusof, F., Hassan, M.A., Rahmat, S.M., 2015. Effect of tool rotational speed on force generation, microstructure and mechanical properties of friction stir welded Al-Mg-Cr-Mn (AA 5052-O) alloy. Materials and Design. 66, 118-128

Movahedinia, H., Mirnia, M.J., Elyasi, M., Baseri, H., 2018. An investigation on flaring process of thin-walled tubes using multistage single point incremental forming. The International Journal of Advanced Manufacturing Technology. 94, 867-880

Mugada, K.K., Adepu, K., 2018. Influence of ridges shoulder with polygonal pins on material flow and friction stir welding characteristics of 6082 aluminum alloy. Journal of Manufacturing Processes. 32, 625-634

Nagel, G.M., Thambiratnam, D.P., 2004. A numerical study on the impact response and energy absorption of tapered thin-walled tubes. International Journal of Mechanical Sciences. 46. 201-216

Naik, B.S., Ramulu, P.J., Narayanan, R.G., 2009. Application of a few necking criteria in predicting the forming limit of unwelded and tailor-welded blanks. The Journal of Strain Analysis for Engineering Design. 45, 79-96

Pantale, O., 1996. Modelisation et simulation tridimensionnelles de la coupe des metaux. Ph. D. thesis, Universite de Bordeaux I, School

Pantale, O., Bacaria, J-L., Dalverny, O., Rakotomalala, R., Caperaa, S., 2004. 2D and 3D numerical models of metal cutting with damage effects. Computer Methods in Applied Mechanics and Engineering. 193, 4383-4399

Paul, S.K., 2013. Theoretical analysis of strain- and stress-based forming limit diagrams. The Journal of Strain Analysis for Engineering Design. 48(3), 177-188

Peel, M., Steuwer, A., Preuss, M., Withers, P.J., 2003. Microstructure, mechanical properties and residual stresses as a function of welding speed in aluminium AA5083 friction stir welds. Acta Materialia. 51, 4791-4801

Pervez, T., Qamar, S.Z., Al-Abri, O.S., Khan, R., 2012. Experimental and numerical simulation of in-situ tube expansion for deep gas wells. Materials and Manufacturing Processes. 27, 727-732

Praveen Kumar, A., Shrivaathsav, S., 2019. Influence of forming parameters on the crash performance of capped cylindrical tubes using LS-DYNA follow-on simulations. International Journal on Interactive Design and Manufacturing. 13, 1215-1232

Rajabiehfard, R., Darvizeh, A., Alitavoli, M., Ansari, R., Maghdouri, E., 2018. Experimental, numerical and analytical investigations into the internal inversion of mild steel tubes under high velocity axial impact using a die. Thin-Walled structures. 125, 21-37

Rakotomalala, R., Joyot, P., Touratier, M., 1993. Arbitrary Lagrangian-Eulerian thermomechanical finite-element model of material cutting. Communications in Numerical Methods in Engineering. 9, 975-987

Ramesh, R., Dinaharan, I., Kumar, R., Akinlabi, E.T., 2017. Microstructure and mechanical characterization of friction stir welded high strength low alloy steels. Materials Science and Engineering A. 687, 39-46

Ramulu, P.J., Narayanan, R.G., Kailas, S.V., 2013. Forming limit investigation of friction stir welded sheets: influence of shoulder diameter and plunge depth. The International Journal of Advanved Manufacturing Technology. 69, 2757-2772

Rana, H., Badheka, V., 2018. Influence of friction stir processing conditions on the manufacturing of Al-Mg-Zn-Cu alloy/boron carbide surface composite. Journal of Materials Processing Technology. 255, 795-807

Rezaei, B., Niknejad, A., Assaee, H., Liaghat, G.H., 2015. Axial splitting of empty and foam-filled circular composite tubes-an experimental study. Archives of Civil and Mechanical Engineering. 15, 650-662

Rodrigues, D.M., Loureiro, A., Leitao, C., Leal, R.M., Chapparo, B.M., Vilaca, P., 2009. Influence of friction stir welding parameters on the microstructural and mechanical properties of AA 6016-T4 thin welds. Materials and Design. 30, 1913-1921

Rosa, P.A., Rodrigues, J.M.C., Martins, P.A.F., 2004. Internal inversion of thin-walled tubes using a die: experimental and theoretical investigation. International Journal of Machine Tools and Manufacture. 44, 775-784

Rosa, P.A.R., Rodrigues, J.M.C., Martins, P.A.F., 2003. External inversion of thin-walled tubes using a die: experimental and theoretical investigation. International Journal of Machine Tools and Manufacture. 43, 787-796

Sabari, S.S., Malarvizhi, S., Balasubramanian, V., 2016. Influence of tool traverse speed on tensile properties of air cooled and water cooled friction stir welded AA2519-T87 aluminium alloy joints. Journal of Materials Processing Technology. 237, 286-300

Sainath, G., Choudhary, B.K., Christopher, J., Samuel, E.I., Mathew, M.D., 2015. Applicability of Voce equation for tensile flow and work hardening behaviour of P92 ferritic steel. International Journal of Pressure Vessels and Piping. 132-133, 1-9

Salari, E., Jahazi, M., Khodabandeh, A., Ghasemi-Nanesa, H., 2014. Influence of tool geometry and rotational speed on mechanical properties and defect formation in friction stir lap welded 5456 aluminum alloy sheets. Materials and Design. 58, 381-389

Sato, Y.S., Kokawa, H., 2001. Distribution of tensile property and microstructure in friction stir weld of 6063 aluminum. Metallurgical and Materials Transactions A. 32A, 3023-3031

Sato, Y.S., Kokawa, H., Enomoto, M., Jogan, S., Hashimoto, T., 1999. Precipitation sequence in friction stir weld of 6063 aluminum during aging. Metallurgical and Materials Transactions A. 30A, 3125-3130

Sato, Y.S., Urata, M., Kokawa, H., 2002. Parameters controlling microstructure and hardness during friction-stir welding of precipitation-hardenable aluminum alloy 6063. Metallurgical and Materials Transactions A. 33A, 625-635

Sekban, D.M., Aktarer, S.M., Purcek, G., 2019. Friction stir welding of low-carbon shipbuilding steel plates: microstructure, mechanical properties and corrosion behaviour. Metallurgical and Materials Transactions A. 50A, 4127-4140

Sekhon, G.S., Gupta, N.K., Gupta, P.K., 2003. An analysis of external inversion of round tubes. Journal of Materials Processing Technology. 133, 243-256

Shakeri, M., Salehghaffari, S., Mirzaeifar, R., 2007. Expansion of circular tubes by rigid tubes as impact energy absorbers: experimental and theoretical investigation. International Journal of Crashworthiness. 12(5), 493-501

Silva, C.M.A., Nielsen, C.V., Alves, L.M., Martins, P.A.F., 2015. Environmentally friendly joining of tubes by their ends. Journal of Cleaner Production. 87, 777-786

Sinclair, P.C., Longhurst, W.R., Cox, C.D., Lammlein, D.H., Strauss, A.M., Cook, G.E., 2010. Heated Friction stir welding: an experimental and theoretical

investigation into how preheating influences process forces. Materials and Manufacturing Processes. 25, 1283-1291

Song, M., Kovacevic, R., 2003. Thermal modeling of friction stir welding in a moving coordinate system and its validation. International Journal of Machine Tools and Manufacture. 43, 605-615

Spena, P.R., Maddis, M.D., Lombardi, F., Rossini, M., 2015. Investigation on resistance spot welding of TWIP steel sheets. Steel Research International. 86(12), 1480-1489

Sun, Z.C., Yang, H., 2006. Free deformation mechanism and change of forming mode in tube inversion under conical die. Journal of Materials Processing Technology. 177, 171-174

Sun, Z.C., Yang, H., 2007. Study on forming limit and feasibility of tube axial compressive process. Journal of Materials Processing Technology. 187-188, 292-295

Susmel, L., Hattingh, D.G., James, M.N., Tovo, R., 2017. Multiaxial fatigue assessment of friction stir welded tubular joints of Al 6082-T6. International Journal of Fatigue. 101, 282-296

Tan, C.J., Chong, W.T., Hassan, M.A., 2013. End formation of a round tube into a square section having small corner radii. Journal of Materials Processing Technology. 213, 1465-1474

Tan, C-J., Purbolaksono, J., Chong, W-T., 2015. Forming box-shaped ends in circular tubes. International Journal of Precision Engineering and Manufacturing. 16(9), 1975-1981

Tarigopula, V., Langseth, M., Hopperstad, O.S., Clausen, A.H., 2006. Axial crushing of thin-walled high-strength steel sections. International Journal of Impact Engineering. 32, 847-882

Thankachan, T., Soorya Prakash, K., 2017. Microstructural, mechanical and tribological behaviour of aluminum nitride reinforced copper surface composites fabricated through friction stir processing route. Materials Science and Engineering A. 688, 301-308

Thuillier, S., Maout, N.L., Manach, P.Y., 2011. Influence of ductile damage on the bending behaviour of aluminium alloy thin sheets. Materials and Design. 32, 2049-2057

Thuillier, S., Maout, N.L., Manach, P.Y., Debois, D., 2008. Numerical simulation of the roll hemming process. Journal of Materials Processing Technology. 198, 226-233

Toktas, A., Toktas, G., 2012. Effect of welding parameters and aging process on the mechanical properties of friction stir-welded 6063-T4 Al alloy. Journal of Materials Engineering and Performance. 21(6), 936-945

Tongne, A., Desrayaud, C., Jahazi, M., Feulvarch, E., 2017. On material flow in friction stir welded Al alloys. Journal of Materials Processing Technology. 239, 284-296

Turk, B.H., Harrison, J., Sextro, R.G., 1991. Performance of radon control systems. Energy and Buildings. 17, 157-175

Tutunchilar, S., Haghpanahi, M., Givi, M.K.B., Asadi, P., Bahemmat, P., 2012. Simulation of material flow in friction stir processing of a cast Al-Si alloy. Materials and Design. 40, 415-426

Ulysse, P., 2002. Three-dimensional modeling of the friction stir-welding process. International Journal of Machine Tools and Manufacture. 42, 1549-1557

Vijay, S.J., Murugan, N., 2010. Influence of tool pin profile on the metallurgical and mechanical properties of friction stir welded Al-10wt.% TiB_2 metal matrix composite. Materials and Design. 31, 3585-3589

Wang, X.S., Hu, Z.L., Yuan, S.J., Hua, L., 2014. Influence of tube spinning on formability of friction stir welded aluminum alloy tubes for hydroforming supplication. Materials Science and Engineering A. 607, 245-252

Wang, Z., Lu, J., Wang, Z.R., 2001. Numerical and experimental research of the cold upsetting-extruding of tube flanges. Journal of Materials Processing Technology. 110, 28-35

Woo, W., Balogh, L., Ungar, T., Choo, H., Feng, Z., 2008. Grain structure and dislocation density measurements in a friction-stir welded aluminum alloy using X-ray peak profile analysis. Materials Science and Engineering A. 498, 308-313

Xia, Q., Xiao, G., Long, H., Cheng, X., Yang, B., 2014. A study of manufacturing tubes with nano/ultrafine grain structure by stagger spinning. Materials and Design. 59, 516-523

Yang, J., Luo, M., Hua, Y., Lu, G., 2010. Energy absorption of expansion tubes using a conical-cylindrical die: experiments and numerical simulation. International Journal of Mechanical Sciences. 52, 716-725

Yeh, F-H., 2007. Study of tube flaring forming limit in the tube flaring process. The Journal of Strain Analysis for Engineering Design. 42, 315-324

Yu, X., Qiu, X., Yu, T.X., 2016. Theoretical model of metal tube inversion over circular dies. International Journal of Mechanical Sciences. 108-109, 23-38

Yuan, S.J., Hu, Z.L., Wang, X.S., 2012a. Evaluation of formability and material characteristics of aluminum alloy friction stir welded tube produced by a novel process. Materials Science and Engineering A. 543, 210-216

Yuan, S.J., Hu, Z.L., Wang, X.S., 2012b. Formability and microstructural stability of friction stir welded Al alloy tube during subsequent spinning and post weld heat treatment. Materials Science and Engineering A. 558, 586-591

Zapata, J., Toro, M., Lopez, D., 2016. Residual stresses in friction stir dissimilar welding of aluminum alloys. Journal of Materials Processing Technology. 229, 121-127

Zhang, Q., Jin, K., Mu, D., 2014. Tube/tube joining technology by using rotary swaging forming method. Journal of Materials Processing Technology. 214, 2085-2094

Zhu, X.K., Chao, Y.J., 2004. Numerical simulation of transient temperature and residual stresses in friction stir welding of 304L stainless steel. Journal of Materials Processing Technology. 146, 263-272

Zhu, Y., Chen, G., Chen, Q., Zhang, Q., Shi, Q., 2016. Simulation of material plastic flow driven by non-uniform friction force during friction stir welding and related direct prediction. Materials and Design. 108, 400-410

Zimmer, S., Langlois, L., Laye, J., Bigot, R., 2010. Experimental investigation of the influence of the FSW plunge processing parameters on the maximum generated force and torque. The International Journal of Advanced Manufacturing Technology. 47, 201-205

Zoghi, H., Arezoodar, A.F., Sayeaftabi, M., 2013. Enhanced finite element analysis of material deformation and strain distribution in spinning of 42CrMo steel tubes at elevated temperature. Materials and Design. 47, 234-342

Publications from the present work

International Journals

1. Agrawal, A.K., Narayanan, R.G., 2017. Joining of a tube to a sheet through end curling. Journal of Materials Processing Technology. 246, 291-304. http://dx.doi.org/10.1016/j.jmatprotec.2017.03.035

2. Agrawal, A.K., Narayanan, R.G., Kailas. S.V., 2017. End forming behaviour of friction stir processed Al 6063-T6 tubes at different tool rotational speeds. The Journal of Strain Analysis For Engineering Design. 52(7), 434-449. https://doi.dox.org/10.1177/0309324717724662

3. Agrawal, A.K., Narayanan, R.G., 2018. Pull-out tests on tube to sheet joints fabricated by end forming. Journal of Constructional Steel Research. 144, 186-197. https://doi.org/10.1016/j.jcsr.2018.01.027

4. Agrawal, A.K., Narayanan, R.G., Kailas, S.V., 2018. End forming behaviour of friction stir processed aluminum tubes at different tool traverse speed. Materials Today: Proceedings. 5, 27100-27106. https://doi.org/10.1016/j.matpr.2018.09.016

5. Agrawal, A.K., Narayanan, R.G., Kailas, S.V., 2019. Experimental evaluation and prediction of friction stir processed Al 6063 T6 tubes at different tool traverse speeds. The International Journal of Advanced Manufacturing Technology. https://doi.org/10.1007/s00170-019-04068-4

International Conferences

1. Agrawal, A.K., Narayanan, R.G. A novel method of joining sheet with tube: Modelling and Analyses, Proceedings of the 17th ISME Conference, IIT Delhi, New Delhi, October 3-4, 2015. (Paper No. ISME-M-019)

2. Agrawal, A.K., Narayanan, R.G., Kailas, S.V. End forming behaviour of friction stir processed aluminium tubes at different tool traverse speed. e-Proceedings of the International Conference on Advances in Materials & Manufacturing (ICAMM 2016), Hyderabad, Osmania University and DRDL Hyderabad Joint organizers, December 8-10 2016, Part 2: pp 173-179

3. Agrawal, A.K., Narayanan, R.G., Kailas, S.V. Thickness evolution during end forming operations of friction stir processed AA 6063-T6 tubes at different tool geometries (AIMTDR 2018), Anna University, Chennai, 13th -15th December, 2018 (Paper ID: 11292)